

Nr. 302

Jens-André Paffenholz

Direct geo-referencing of 3D point clouds  
with 3D positioning sensors

HANNOVER 2012

---

Diese Arbeit ist gleichzeitig veröffentlicht in:  
Deutsche Geodätische Kommission bei der Bayerischen Akademie der Wissenschaften,  
Reihe C, Nr. 689, München 2012, ISBN 978-3-7696-5101-0, ISSN 0065-5325, [www.dgk.badw.de](http://www.dgk.badw.de)



Nr. 302

Direct geo-referencing of 3D point clouds  
with 3D positioning sensors

Von der Fakultät für Bauingenieurwesen und Geodäsie  
der Gottfried Wilhelm Leibniz Universität Hannover  
zur Erlangung des Grades

**DOKTOR-INGENIEUR (Dr.-Ing.)**

genehmigte Dissertation  
von

**Dipl.-Ing. Jens-André Paffenholz**

geboren am 07. Januar 1981 in München

HANNOVER 2012

---

Prüfungskommission

Vorsitzende:

Prof. Dr.-Ing. habil. Monika Sester, Hannover

Hauptreferent:

Prof. Dr.-Ing. habil. Hansjörg Kutterer, Frankfurt a. M.

Korreferenten:

Prof. Dr.-Ing. Andreas Eichhorn, Darmstadt

Prof. Dr.-Ing. Steffen Schön, Hannover

Tag der Einreichung der Arbeit: 14. Juni 2012

Tag der mündlichen Prüfung: 13. September 2012

## Abstract

A broad range of scientific, administrative, industrial and private users demand for detailed three dimensional (3D) spatial data with typical applications in, for instance, as-built documentation, construction engineering, navigation applications and forensic investigations. The acquisition of 3D spatial data is conveniently performed by means of laser range sensors which provide immediately numerous 3D object points. These 3D point clouds are obtained in the local coordinate system of the Light Detection and Ranging (LiDAR) sensor which is also known as laser scanner. In order to capture a complete view of objects, multiple sites are necessary. Aforementioned applications frequently demand, besides a common local coordinate system, the transformation into a global coordinate system (*geo-referencing*). For a time-saving and efficient provision of geo-referenced 3D point clouds, sophisticated methodologies are required to obtain the parameters for the transformation.

The main objective of this thesis is the development of an *efficient methodology for the determination of parameters and its uncertainty measures for the direct geo-referencing of 3D point clouds acquired by stationary laser scanners*. This objective is addressed by a prototypic Multi-Sensor System (MSS) and a novel algorithm to perform the geo-referencing of 3D point clouds considering uncertainty measures.

The developed MSS is established by the fusion of a laser scanner and Global Navigation Satellite System (GNSS) equipment. The use of only physically attached sensors to the laser scanner and the waiver of auxiliary control points leads to a time-saving, simultaneous acquisition of 3D point clouds and its geo-reference information, i. e., *direct geo-referencing*.

The novel algorithm is fundamentally based on the motion modelling of the MSS in an Extended Kalman Filter (EKF). The circular motion of the laser scanner about its vertical axis is exploited to obtain time series of 3D positions by means of GNSS equipment eccentrically installed on the laser scanner. These time series enable a redundant estimation of the transformation parameters and their variance matrices which increase the fidelity and reliability of the proposed approach. The prediction and filtering of the 3D trajectories are realised by two distinct variants of modelling the system. First, *states and adaptive parameters* are considered in a single antenna scenario. Here, the benefit can be stated by the verification possibility of MSS specific parameters which are usually obtained by separate calibration procedures. Second, *constraints among the states* are taken into account by a dual antennas scenario. The constant velocity of the circular motion and the distance between the two GNSS antennas are considered as constraints.

The geo-referenced 3D point clouds are supplemented with uncertainties induced by the transformation parameters (*transformational uncertainty*) as well as the laser scanner (*positional uncertainty*). Both uncertainties are jointly propagated to the geo-referenced 3D point clouds. The result is a *geo-referenced stochastic 3D point cloud* which provides spatial and supplemental stochastic information. In addition, an optimisation of transformation parameters by an Iterative Closest Point (ICP) based matching (*Gref-ICPHe3*) is proposed which utilises both kinds of uncertainties and also incorporates the uncertainties of the relative transformation parameters within the iterative matching.

The potential of the developed methodology is shown in practical experiments for both system modelling approaches (single and dual antennas scenario). The results show good coincidence of overlapping regions from different sites and differences of only a few centimetres with respect to known control point coordinates. Owing to the use of one set of transformation parameters for the geo-referencing of the entire 3D point cloud, each 3D point cloud is consistent. It can be stated that the main influencing factor of the proposed geo-referencing approach is the heading and its uncertainty. As expected, the heading and its uncertainty is strongly related to the baseline length used for the heading determination.

The proposed methodology with the introduced MSS and novel algorithm is suitable for the above-mentioned laser scanning applications. In addition, optimal initial values with uncertainty information for matching algorithms can be obtained. The provision of the geo-referenced stochastic 3D point clouds is efficient and paves the way for rigorous consideration of the entire uncertainty budget of a 3D point cloud also for subsequent analysis like, e. g., estimation of geometric primitives.

**Keywords:** geo-referencing, Kalman filter, light detection and ranging, LiDAR, 3D point cloud, registration, sensor fusion, terrestrial laser scanning, uncertainty

## Kurzfassung

Eine Reihe wissenschaftlicher, öffentlicher, kommerzieller und privater Nutzer benötigt umfangreiche 3D Daten für typische Anwendungen, beispielsweise in den Bereichen as-built Dokumentation, Bauwesen, Navigation und für forensische Untersuchungen. Die Erfassung von 3D Daten kann effizient mit laserbasierten Entfernungsmesssensoren erfolgen, die unmittelbar 3D Objektpunkte zur Verfügung stellen. Diese 3D Punktwolken liegen im lokalen Koordinatensystem des Light Detection and Ranging (LiDAR) Sensors, auch als Laserscanner bekannt, vor. Zur Erfassung von Objekten sind in der Regel mehrere Standpunkte notwendig. Dabei erfordern die meisten Anwendungen, neben einem gemeinsamen lokalen System, die Transformation in ein globales Koordinatensystem (*Geo-Referenzierung*).

Das Ziel dieser Arbeit ist die Entwicklung einer *effizienten Methode zur Bestimmung von Parametern und ihren Unsicherheitsmaßen für die direkte Geo-Referenzierung von 3D Punktwolken, die mit stationären Laserscannern erfasst wurden*. Zur Erfüllung dieses Ziels werden ein Multi-Sensor System (MSS) und ein Algorithmus zur Geo-Referenzierung mit Berücksichtigung der Unsicherheit entworfen.

Das entwickelte MSS entsteht durch die Kombination eines Laserscanners und GNSS Ausrüstung. Der ausschließliche Gebrauch von unmittelbar am Laserscanner adaptierten Sensoren und der Verzicht auf zusätzliche Kontrollpunkte führen zu einer zeitsparenden, zeitgleichen Erfassung von 3D Punktwolken und ihres räumlichen Bezugs (*direkte Geo-Referenzierung*).

Der neuartige Algorithmus beruht im Wesentlichen auf der Modellierung der Bewegung des MSS in einem Extended Kalman Filter. Die kreisförmige Bewegung des Laserscanners um seine Stehachse wird genutzt um Zeitreihen von 3D Positionen durch die exzentrisch auf dem Laserscanner installierte GNSS Ausrüstung zu erhalten. Diese Zeitreihen ermöglichen eine redundante Bestimmung der Transformationsparameter und ihrer Varianzmatrizen, wodurch die Genauigkeit und Zuverlässigkeit des vorgeschlagenen Ansatzes erhöht wird. Die Prädiktion und Filterung der 3D Trajektorien wird für zwei unterschiedliche Systemmodellierungen realisiert. Zum einen werden die *Systemzustände und adaptiven Parameter* in einem Einzel-Antennen-Szenario bestimmt. Hier ist als Vorteil die Überprüfbarkeit von MSS-spezifischen Parametern zu nennen, die sonst nur im Rahmen einer getrennten Kalibrierung erfolgen kann. Zum anderen werden *Bedingungen zwischen den Systemzuständen* in einem Doppel-Antennen-Szenario berücksichtigt. Die konstante Geschwindigkeit der kreisförmigen Bewegung und die Entfernung zwischen den zwei GNSS Antennen werden als Bedingungen eingeführt.

Die geo-referenzierten 3D Punktwolken werden mit Unsicherheitsmaßen ergänzt, die durch die Transformationsparameter (*Transformationsunsicherheit*) sowie den Laserscanner (*Sensorunsicherheit*) hervorgerufen werden. Beide Unsicherheitsmaße werden auf die geo-referenzierten 3D Punktwolken fortgepflanzt. Das Ergebnis sind *geo-referenzierte, stochastische 3D Punktwolken*, die neben räumlichen zusätzlich stochastische Informationen enthalten. Darüber hinaus wird eine Optimierung von Transformationsparametern durch einen ICP basierten Matchingalgorithmus (*Gref-ICPHe3*) vorgeschlagen, der beide Arten von Unsicherheiten verwendet und zusätzlich die Unsicherheiten der relativen Transformationsparameter während des iterativen Matching berücksichtigt.

Das Potenzial der entwickelten Methode wird für beide Systemmodelle (Einzel- und Doppel-Antennen-Szenario) anhand praktischer Beispiele gezeigt. Die Ergebnisse zeigen eine gute Übereinstimmung für überlappende Regionen von verschiedenen Standpunkten und Differenzen von wenigen Zentimetern im Vergleich zu Kontrollpunktkoordinaten. Aufgrund der Nutzung identischer Transformationsparameter für die Geo-Referenzierung der gesamten 3D Punktwolke ist diese in sich konsistent. Als Haupteinflussfaktoren auf das Ergebnis haben sich die azimutale Orientierung und ihre Unsicherheit herausgestellt. Dabei ist die Orientierungsbestimmung, wie erwartet, abhängig von der Länge der Basislinie zwischen den beiden Antennen.

Die entwickelte Methode, bestehend aus MSS und Algorithmus, ist für die oben genannten Anwendungen sehr gut geeignet. Zusätzlich können optimale Startwerte mit Unsicherheitsmaßen für die Nutzung in iterativen Matchingalgorithmen bestimmt werden. Die Bereitstellung geo-referenzierter, stochastischer 3D Punktwolken ist effizient. Sie ermöglicht die Berücksichtigung des gesamten Unsicherheitshaushaltes auch für weitere Analysen, wie bei der Bestimmung von geometrischen Primitiven.

**Schlüsselworte:** Geo-Referenzierung, Kalman Filter, 3D Punktwolke, Registrierung, Sensorfusion, Terrestrisches Laserscanning, Unsicherheit

# Contents

<b>1. Introduction</b>	<b>15</b>
1.1. Motivation and objectives	15
1.2. Reader's guide	17
<b>2. Basics of terrestrial laser scanning and geo-referencing methods</b>	<b>19</b>
2.1. Terrestrial laser scanning	19
2.1.1. Distinction of stationary and mobile terrestrial laser scanning	19
2.1.2. Stationary laser scanner	21
2.1.3. Ranging principle	21
2.1.4. Scanning mechanism	23
2.2. Geo-referencing of 3D point clouds	24
2.2.1. Terminology and the state of research	24
2.2.2. Direct geo-referencing of 3D point clouds	28
2.2.3. Registration of 3D point clouds by means of matching algorithms	31
2.2.4. Sensor candidates for a direct geo-referencing procedure	33
2.3. Uncertainty consideration in terrestrial laser scanning	41
2.3.1. Measurement errors and evaluation of uncertainties in measurements	41
2.3.2. Classification of the error budget in terrestrial laser scanning	42
2.3.3. Positional uncertainty	43
2.3.4. Transformational uncertainty	45
<b>3. Basics of discrete-time recursive state-space and transversal filtering</b>	<b>47</b>
3.1. Recursive parameter estimation	47
3.1.1. Gauss-Markov model	48
3.1.2. Gauss-Helmert model	48
3.1.3. Recursive least-squares estimation in Gauss-Markov model	49
3.1.4. Transformation of Gauss-Helmert model into Gauss-Markov model	50
3.1.5. Parameter elimination in Gauss-Markov model	50
3.2. Recursive state-space filtering	51
3.2.1. Discrete-time linear Kalman filter	51
3.2.2. Non-linearities in state-space equations	54
3.2.3. Smoothing algorithms in the Kalman filter framework	56
3.2.4. Joint estimation of states and adaptive parameters	58
3.2.5. Kalman filtering with constraints	58
3.3. Transversal prediction and filtering by means of least-squares collocation	60
3.3.1. Estimation of covariance functions	61
3.3.2. Least-squares collocation	62
<b>4. Conceptual design and realisation of a multi-sensor system</b>	<b>63</b>
4.1. Conceptual design of a multi-sensor system for direct geo-referencing purposes	63
4.2. Prototypic realisation of the conceptual design	64
4.2.1. Sensors in the multi-sensor system	65

4.2.2.	GNSS analysis strategy . . . . .	68
4.2.3.	Conception of an algorithm to derive the transformation parameters . . . . .	70
4.3.	Investigations of the multi-sensor system's components . . . . .	72
4.3.1.	Laser scanner and wing support structure to mount additional sensors . . . . .	72
4.3.2.	GNSS equipment . . . . .	74
4.3.3.	Inclinometers . . . . .	78
4.3.4.	Multi-sensor system calibration . . . . .	79
4.3.5.	Concluding remarks and uncertainty assessment . . . . .	80
<b>5.</b>	<b>Novel methodology for geo-referencing of 3D point clouds</b>	<b>83</b>
5.1.	Transformation parameters from 3D circle estimation . . . . .	83
5.2.	Motion modelling of the multi-sensor system in recursive state-space filters . . . . .	84
5.2.1.	Process equation . . . . .	85
5.2.2.	Measurement equation . . . . .	90
5.2.3.	Proposed algorithm for direct geo-referencing of 3D point clouds . . . . .	91
5.3.	Optimisation of transformation parameters considering uncertainties . . . . .	94
<b>6.</b>	<b>Results of practical investigations</b>	<b>97</b>
6.1.	Analyses of high resolution 3D trajectories for direct geo-referencing purposes . . . . .	98
6.1.1.	Modelling of the multi-sensor system's motion in recursive state-space filters . . . . .	98
6.1.2.	Transversal prediction and filtering by means of least-squares collocation . . . . .	102
6.1.3.	Concluding remarks . . . . .	104
6.2.	Positional uncertainty . . . . .	105
6.3.	Direct geo-referencing by means of the novel algorithm . . . . .	107
6.3.1.	Saxon Steed data set . . . . .	107
6.3.2.	Geodetic Institute data set . . . . .	110
6.4.	Optimisation of transformation parameters by means of Gref-ICPHe3 . . . . .	113
<b>7.</b>	<b>Conclusions and outlook</b>	<b>117</b>
7.1.	Conclusions . . . . .	117
7.2.	Outlook . . . . .	119
	<b>References</b>	<b>121</b>
	<b>A. Supplementary material</b>	<b>129</b>
	<b>B. Specifications of the used sensors in this thesis</b>	<b>133</b>
	<b>Curriculum vitae</b>	<b>135</b>



## List of Figures

2.1. Coordinate systems and laser scanner observables in the context of direct geo-referencing. . . . .	25
2.2. Sensor candidates for a direct geo-referencing procedure. . . . .	34
2.3. Sketch of PCC (PCO and associated PCV) for an eccentrically rotating antenna. . . . .	37
2.4. Stereographic plot of the absolute GPS L1 PCC for the Javad GrAnt G3T antenna. . . . .	37
2.5. Circular polarisation of a satellite signal. . . . .	37
2.6. PWU effect of an azimuthally rotating GNSS antenna. . . . .	37
3.1. Illustration of smoothing by means of forward and backward filtering. . . . .	57
4.1. Prototypic realisation of the MSS. . . . .	66
4.2. Comparison of epoch-wise and filter-based solution for 3D position estimation. . . . .	69
4.3. Analyses of the influence of the wing support structure on the rotation of the laser scanner. . . . .	73
4.4. Parameters of the static and kinematic experiments with the GNSS equipment. . . . .	74
4.5. DD analyses for two specific satellites on two different DOYs. . . . .	76
4.6. GPS satellites constellation DOY025 and PCC analyses of GPS L1 signals. . . . .	76
4.7. Analyses of static and kinematic experiments in the coordinate domain. . . . .	77
4.8. Inclinator measurements for different rotation speeds of the laser scanner. . . . .	78
4.9. Sketch of the MMS calibration in the laboratory. . . . .	80
4.10. Unique spatial reference for sensors of the MSS. . . . .	80
5.1. States and adaptive parameters for motion modelling. . . . .	86
5.2. States with constraints and control input for motion modelling. . . . .	88
5.3. Uncertainty aspects in the direct geo-referencing of 3D point clouds. . . . .	92
5.4. Optimisation of transformation parameters by means of Gref-ICPHe3. . . . .	94
6.1. Data sets used in the experimental studies. . . . .	97
6.2. Single antenna scenario – Saxon Steed data set: State $\mathbf{p}^{G,o}$ . . . . .	99
6.3. Single antenna scenario – Saxon Steed data set: State $\kappa^L$ and adaptive parameters. . . . .	100
6.4. Dual antennas scenario – Geodetic Institute data set: State $\mathbf{p}^{G,d/o}$ . . . . .	101
6.5. Dual antennas scenario – Geodetic Institute data set: Demonstration of the impact of state constraints. . . . .	102
6.6. Dual antennas scenario – Geodetic Institute data set: Standard deviations of observations, filtered and constrained estimates of the north-component. . . . .	102
6.7. Determination of covariance functions exemplary for the trajectory of $\mathbf{p}^{G,d}$ . . . . .	103
6.8. Cofactor matrices of the collocation estimates. . . . .	104
6.9. Filtering and prediction of the 3D trajectory of $\mathbf{p}^{G,d}$ by means of LSC and EKF. . . . .	105
6.10. Positional uncertainty – Geodetic Institute data set: Separation of the 3D point cloud acquired from P1 into planar regions. . . . .	106
6.11. Positional uncertainty – Geodetic Institute data set: Positional uncertainty in the $P$ -frame for 3D point cloud acquired from P1. . . . .	106
6.12. Single antenna scenario – Saxon Steed data set: Geo-referenced 3D point clouds of the three sites around the sculpture of the Saxon Steed. . . . .	107

---

6.13. Single antenna scenario – Saxon Steed data set: Comparison of 3D point clouds of S2 and S3. . .	108
6.14. Dual antennas scenario – Geodetic Institute data set: Standard deviation of the heading $\sigma_{\kappa}^{P5}$ obtained by the constrained positions and the smoothed, constrained positions. . . . .	110
6.15. Dual antennas scenario – Geodetic Institute data set: Overview of the geo-referenced 3D point clouds of the two sites. . . . .	111
6.16. Dual antennas scenario – Geodetic Institute data set: Top view of the tower building and zoom of the cylindrical shape of P9 of the two geo-referenced 3D point clouds. . . . .	111
6.17. Dual antennas scenario – Geodetic Institute data set: Analyses of geometric primitives in the geo-referenced 3D point clouds. . . . .	112
6.18. Dual antennas scenario – Geodetic Institute data set: Positional and transformational uncertainty of 3D point clouds of P1 and P5. . . . .	113
6.19. Single antenna scenario – Saxon Steed data set: Positional and transformational uncertainty of 3D point clouds of S2 and S3. . . . .	114
6.20. Single antenna scenario – Saxon Steed data set: Results of the Gref-ICPHe3 applied to the geo-referenced stochastic 3D point clouds of S2 and S3. . . . .	115
6.21. Single antenna scenario – Saxon Steed data set: Geo-referenced stochastic 3D point cloud of S2 with respect to S3 after the use of Gref-ICPHe3. . . . .	116
B.1. Individual PCC of GPS L1 and GPS L2 for the Javad GrAnt G3T antenna. . . . .	134

## List of Tables

4.1. Requirements for a MSS for direct geo-referencing purposes and proposals to fulfil them. . . . .	64
4.2. Sensors with their specifications and tasks in the MSS. . . . .	66
4.3. Comparison of epoch-wise and filter-based solution for 3D position estimation. . . . .	69
5.1. Aim, states, observations and output of different system modelling approaches. . . . .	85
5.2. Calculation steps of the novel algorithm for the single and the dual antennas scenario. . . . .	91
6.1. Data sets with their main characteristics used throughout the experimental studies. . . . .	98
6.2. Single antenna scenario – Saxon Steed data set: Control point differences. . . . .	109
6.3. Dual antennas scenario – Geodetic Institute data set: Coordinate differences calculated by known pillar coordinates and estimated cylinder centre points. . . . .	112
B.1. Technical data Z+F IMAGER 5006. . . . .	133
B.2. Technical data Schaevitz LSOC-1 °. . . . .	133
B.3. Specifications and parameters of GNSS equipments. . . . .	134

## List of Algorithms

2.1. ICP algorithm. . . . .	32
2.2. Calculation of positional uncertainty. . . . .	45
3.1. KF algorithm with its fundamental calculation steps. . . . .	53
3.2. Rauch-Tung-Striebel smoother. . . . .	57
4.1. Conception of an algorithm to derive the transformation parameters. . . . .	72
5.1. Direct geo-referencing considering uncertainty measures. . . . .	93
5.2. Iterative matching by means of Gref-ICPHe3. . . . .	95



## List of Acronyms

<b>Acronym</b>	<b>Meaning</b>	<b>Section</b>
aEKF	Adaptive Extended Kalman Filter	3.2, 5.2, 6.1
AM	Amplitude Modulation	2.1, 2.3, A.3
ARP	Antenna Reference Point	2.2, 4.2, 4.3
CAD	Computer-Aided Design	1.0
CCR	Corner Cube Reflector	4.3
CN/0	Signal Strength	4.3
CODE	Center for Orbit Determination in Europe	2.2
CW	Continuous Wave	2.1, 2.3, A.3
DD	Double-Differences	4.3
DoF	Degrees of Freedom	2.2, 3.2, 4.1
DOY	Day of Year	4.2, 4.3
EDM	Electronic Distance Measurement	2.1, 2.2
EKF	Extended Kalman Filter	0.0, 1.1, 2.2, 3.0, 3.2, 4.2, 5.0, 5.2, 6.0, 6.1, 7.0, 7.1
EKPF	Extended Kalman Particle Filter	3.2
ESA	European Space Agency	2.2
ESOC	European Space Operations Centre	2.2
ETRS89	European Terrestrial Reference System 1989	1.1, 2.2, 4.3, 5.2, 6.1, 6.3
FM	Frequency Modulation	2.1
FoV	Field of View	2.1
GHM	Gauss-Helmert Model	2.2, 3.0, 3.1, 3.3, 5.1–5.3, 6.1, 7.1, A.2
GLONASS	Globalnaja Nawigazionnaja Sputnikowaja Sistema	2.2, 4.2, 4.3, 6.0
GMM	Gauss-Markov Model	2.2, 3.0, 3.1, 4.2, 5.1, 5.2
GNSS	Global Navigation Satellite System	0.0, 1.1, 1.2, 2.1–2.3, 3.1, 3.3, 4.0–4.3, 5.0–5.2, 6.0, 6.1, 6.3, 7.0–7.2, B.3
GPS	Global Positioning System	2.2, 4.2, 4.3, 6.0, B.3
GUM	Guide to the Expression of Uncertainty in Measurement	2.3
ICP	Iterative Closest Point	0.0, 2.2, 5.0, 5.3, A.2
IGS	International GNSS Service	2.2
IMU	Inertial Measurement Unit	2.1–2.3, 4.1, 4.2
ITRF05	International Terrestrial Reference Frame 2005	4.3, 6.3
k-TLS	Kinematic Terrestrial Laser Scanning	2.1
kd-tree	k-Dimensional Binary Search Tree	2.2, 5.3
KF	Kalman Filter	1.1, 1.2, 2.2, 3.0, 3.2, 4.1–4.3, 5.1

<b>Acronym</b>	<b>Meaning</b>	<b>Section</b>
LiDAR	Light Detection and Ranging	0.0, 1.0, 2.0–2.2
LOP	Law of Propagation of Uncertainties	1.1, 2.3, 3.1–3.3, 5.2, 6.4
LSC	Least-Squares Collocation	1.2, 3.0, 3.3, 5.2, 6.0, 6.1, 7.1
MC	Monte Carlo	2.3, 3.2
MEMS	Microelectromechanical Systems	2.2
MLS	Mobile Laser Scanning	1.1, 2.1, 2.2, 7.1
MMS	Mobile Mapping System	1.1, 2.1, 2.2
MSS	Multi-Sensor System	0.0, 1.2, 2.2, 3.2, 4.0–4.3, 5.0, 5.2, 6.0–6.4, 7.0–7.2
NEU	North-, East- and Up-axes	4.2, 4.3, 5.2, 6.3
NMEA	National Marine Electronics Association	4.2
PCC	Phase Centre Corrections	2.2, 4.3, 6.0, B.3
PCO	Phase Centre Offsets	2.2, 4.3, B.3
PCV	Phase Centre Variations	2.2, 4.3, B.3
PDF	Probability Density Function	3.2
PF	Particle Filter	3.2
PPP	Precise Point Positioning	2.2
PPS	Puls Per Second	2.2, 4.2
PWU	Phase Wind Up	2.2, 4.3
RANSAC	Random Sample Consensus	2.2
RINEX	Receiver Independent Exchange Format	4.3
RTK	Real-time Kinematic	2.2
RTOS	Real-Time Operating System	4.2
SIFT	Scale-Invariant Feature Transform	2.2, 2.3
SLAM	Simultaneous Localization And Mapping	1.0, 2.1, 2.2
SMC	Sequential Monte Carlo	3.2
SURF	Speeded-Up Robust Features	2.2
SVD	Singular Value Decomposition	2.2, 5.1, A.2
TLS	Terrestrial Laser Scanning	1.2, 2.0–2.3, 4.1, 4.3, 6.3, 7.2, A.3
TOF	Time-of-Flight	2.1, A.3
UKF	Unscented Kalman Filter	3.2
UT	Unscented Transformation	3.2
UTM	Universal Transverse Mercator	1.1, 2.2, 5.2, 6.1, 6.3
UWB	Ultra Wide Band	1.1, 2.2
VCE	Variance Component Estimation	3.2, 7.2
VCM	Variance Covariance Matrix	2.2, 2.3, 3.1–3.3, 4.2, 5.1–5.3, 6.1, 6.4, 7.0–7.2
Z+F	Zoller + Fröhlich	1.1, 2.1, 4.2, 4.3, 6.0, 6.2, A.3, B.1

## List of Symbols

<b>Notation</b>	<b>Meaning</b>	<b>Section</b>
$\alpha$	elevation angle observable of the laser scanner	2.2
$\beta$	horizontal direction observable of the laser scanner	2.2
$\rho$	range observable of the laser scanner	2.1, 2.2
<i>G</i> -frame	Absolute or global coordinate system with known geodetic datum	2.2, 5.2, 5.3
<i>L</i> -frame	Local sensor-defined coordinate system, defined by the principal axes of the laser scanner	2.2, 2.3, 4.2, 5.2, 6.2
<i>P</i> -frame	Individual point coordinate system	2.3, 6.2
$\mathbf{p}^G$	3D point $[x^G \ y^G \ z^G]^T$ in the <i>G</i> -frame	2.2
$\mathbf{p}^L$	3D point $[x^L \ y^L \ z^L]^T$ in the <i>L</i> -frame	2.2
$\mathbf{R}_L^G$	rotation matrix $\in \mathbb{R}^{3 \times 3}$ between <i>L</i> -frame and <i>G</i> -frame	2.2
$\kappa$	heading: spatial angular direction with respect to the <i>z</i> -axis	2.2
$\mathbf{t}_L^G$	translation vector $\in \mathbb{R}^{3 \times 3}$ between <i>L</i> -frame and <i>G</i> -frame	2.2

## List of mathematical Symbols

<b>Notation</b>	<b>Definition</b>	<b>Equation</b>
$E\{\cdot\}$	expectation operator	3.2
$V(\cdot)$	variance operator	3.46
$\text{tr}(\cdot)$	trace operator	3.13
$k$	epoch index in recursive estimation, filtering, prediction and smoothing	3.11
$n_u$	number of known input parameters	3.18
$n_w$	number of condition equations	3.7
$n_x$	number of unknown (state) parameters	3.2
$n_y$	number of observations	3.2
$\mathbf{H}$	full rank $n_y \times n_x$ design (measurement) matrix	3.3, 3.7, 3.23, 3.33
$\mathbf{f}$	real-valued differentiable function of $\mathbf{x}$ and $\mathbf{y}$ / non-linear dynamic model	3.6, 3.31
$\mathbf{h}$	real-valued differentiable function of $\mathbf{x}$	3.2, 3.32
$\sigma_0^2$	(unknown) variance of the unit weight	3.2, 3.24
$\mathbf{v}$	measurement error (residual) vector	3.2, 3.23, 3.45
$\mathbf{x}$	unknown parameter vector / state vector $\in \mathbb{R}^{n_x}$	3.2, 3.19
$\mathbf{y}$	observation vector $\in \mathbb{R}^{n_y}$	3.2, 3.23
$\mathbf{P}$	weight matrix of observations	3.2
$\mathbf{Q}_{\hat{\mathbf{x}}\hat{\mathbf{x}}}$	cofactor matrix of $\hat{\mathbf{x}}$	3.5
$\mathbf{Q}_{\mathbf{y}\mathbf{y}}$	cofactor matrix of $\mathbf{y}$	3.2
$\Sigma_{\mathbf{y}\mathbf{y}}$	regular variance covariance matrix of $\mathbf{y}$	3.2
$\mathbf{U}$	full rank $n_w \times n_y$ coefficient (condition) matrix	3.7

<b>Notation</b>	<b>Definition</b>	<b>Equation</b>
$\Delta \mathbf{x}$	truncated parameter vector	3.3
$\Delta \mathbf{y}$	truncated observation vector	3.3
$\mathbf{k}$	vector of Lagrange multipliers	3.8, 3.53
$\mathbf{w}$	vector of inconsistencies / model disturbances $\in \mathbb{R}^{n_w}$	3.7
$\hat{\mathbf{x}}$	estimated parameter vector	3.5
$\mathbf{B}_{k+1,k}$	known input gain	3.19, 3.33
$\mathbf{K}$	Kalman gain	3.12, 3.14, 3.25, 3.26
$\mathbf{Q}_{\mathbf{i}\mathbf{i}_{k+1}}$	cofactor matrix of $\mathbf{i}_{k+1}$ at time $k+1$	3.28
$\mathbf{Q}_{\mathbf{w}\mathbf{w}_k}$	cofactor matrix of $\mathbf{w}_k$ at time $k$	3.20
$\mathbf{Q}_{\hat{\mathbf{x}}\hat{\mathbf{x}}_{k+1}^+}$	cofactor matrix of $\hat{\mathbf{x}}_{k+1}^+$ at time $k+1$	3.27
$\mathbf{Q}_{\hat{\mathbf{x}}\hat{\mathbf{x}}_{k+1}^-}$	cofactor matrix of $\hat{\mathbf{x}}_{k+1}^-$ at time $k+1$	3.22
$\mathbf{S}_{k+1,k}$	coefficient matrix of disturbing variables	3.19, 3.33
$\mathbf{T}_{k+1,k}$	transition matrix	3.19, 3.33
$\mathbf{i}$	innovations vector	3.12, 3.25
$\sigma_{0w}^2$	a priori variance factor of the process noise	3.20
$\mathbf{u}_k$	known input vector $\in \mathbb{R}^{n_u}$ at time $k$	3.19
$\mathbf{w}_k$	process error vector $\in \mathbb{R}^{n_x}$ at time $k$	3.19
$\hat{\mathbf{x}}_{k+1}^+$	filtered state vector at time $k+1$	3.25, 3.35
$\hat{\mathbf{x}}_{k+1}^-$	predicted state vector at time $k+1$	3.21, 3.34
$\mathbf{D}$	known $s \times n_x$ constant, full rank matrix	3.39
$\mathbf{Q}_{\tilde{\mathbf{x}}\tilde{\mathbf{x}}_{k+1}^+}$	cofactor matrix of $\tilde{\mathbf{x}}_{k+1}^+$ at time $k+1$	3.42
$\mathbf{W}$	weighting matrix (KF with constraints)	3.41
$\mathbf{d}$	known $s \times 1$ vector with $s$ constraints	3.39
$\mathbf{g}$	known non-linear function of the constraints	3.43, 3.44
$\tilde{\mathbf{x}}_{k+1}^+$	constrained state vector at time $k+1$	3.41
$C_\xi$	empirical autocovariance function	3.47
$C_{\xi\eta}$	empirical cross-covariance function	3.49
$K_\xi$	empirical autocorrelation function	3.48
$K_{\xi\eta}$	empirical cross-correlation function	3.49
$\mathbf{Q}_{\hat{\mathbf{s}}\hat{\mathbf{s}}}$	cofactor matrix of $\hat{\mathbf{s}}$	3.55
$\mathbf{Q}_{\hat{\mathbf{s}}'\hat{\mathbf{s}}'}$	cofactor matrix of $\hat{\mathbf{s}}'$	3.56
$\mathbf{Q}_{\hat{\mathbf{v}}\hat{\mathbf{v}}}$	cofactor matrix of $\hat{\mathbf{v}}$	3.54
$\mathbf{R}$	$n_y \times (r - n_y)$ matrix of known coefficients	3.45
$\mathbf{s}'$	predicted signal vector $\in \mathbb{R}^{(r-n_y)}$	3.46
$\mathbf{s}$	signal vector $\in \mathbb{R}^{(r-n_y)}$	3.45



# 1. Introduction

Three dimensional (3D) spatial data acquisition, its interpretation and fast availability to users are important factors in today's information-dominated world. These topics related to 3D spatial data are investigated by a multitude of research disciplines such as geodesy, architecture, computer vision, engineering, infrastructure planning and robotics. In addition to the scientific users, a range of administrative, industrial and private users demand for detailed 3D spatial data. Typical applications are as-built and cultural heritage documentation, the generation of 3D city models, facility management, construction engineering, navigation applications and forensic investigations. As a result, geo-information products provide nowadays geodetic location, digital mapping and terrain models simply via internet. While this information was traditionally available only to specific scientific and governmental users.

Information for 3D geodetic mapping purposes is often acquired by both, digital cameras and laser range sensors, which are generally called Light Detection and Ranging (LiDAR) sensors or laser scanners (Mikhail et al., 2001, Vosselman and Maas, 2010). The determination of 3D object point coordinates with cameras requires multiple images. The local object's coordinates are obtained by space resection based on least-squares adjustment with conditions and rigorous uncertainty analysis (Luhmann et al., 2006). In computer vision and robotics, different approaches with projective geometry and outlier detection are utilised, e.g., Simultaneous Localization And Mapping (SLAM), which are popular for the development of indoor mapping with low-cost autonomous vehicles (e.g., Nüchter, 2009). In case of laser scanners, the distance between the laser scanner and an object is actively measured with laser beams and, simultaneously, the horizontal and vertical angles towards the object are acquired. By implication, the measurement principle of laser scanners is equivalent to those of total stations. The spherical coordinates are transformed to the Cartesian coordinates in the same manner.

One of the major advantages of laser scanners over digital cameras is the immediate data acquisition in 3D space. The 3D coordinates are determined without post-processes of resection by multiple images in order to obtain the depth information of objects. Advantages of digital cameras are their range-independent, high resolution and their moment shot acquisition procedure within a few milliseconds (Mikhail et al., 2001, Vosselman and Maas, 2010). With appropriate sensor calibration (e.g., Lichti and Skaloud, 2010), terrestrial laser scanners provide millions of 3D object points with millimetres-precision within a few minutes of acquisition time. Therefore, 3D point clouds are popular for the production of 3D models within Computer-Aided Design (CAD) software for planning, documentation and monitoring of architectural, cultural heritage and infrastructure objects. In order to capture a complete view of objects, multiple sites are necessary and, subsequently, they are required to transform into a common local and global coordinate system (e.g., Lichti and Skaloud, 2010).

## 1.1. Motivation and objectives

The required parameters for the transformation of local 3D point clouds of single sites to common local and global coordinate systems (e.g., European Terrestrial Reference System 1989 (ETRS89) combined with the Universal Transverse Mercator (UTM) projection) are traditionally obtained by pre-surveyed control points (with known geodetic datum), i.e., indirect geo-referencing. Often, appropriate control points have to be determined in an independent survey which is a time-consuming task. In the last years, research has been conducted on more sophisticated variants of the efficient and time-saving determination of the transformation parameters. These direct geo-referencing variants utilise a minimal number of control points and additional sensors which are frequently attached to the laser scanner. Telescopes (e.g., Lichti and Gordon, 2004) and Global Navigation Satellite System (GNSS) equipments (e.g., Reshetyuk, 2009, Wilkinson et al., 2010) are typically used for

the position and orientation determination. The fusion between laser scanners and digital cameras as well as sensors, which gather geo-reference information, is common for Mobile Mapping Systems (MMSs), installed in either vehicles or aircraft (cf. Barber et al., 2008, Puente et al., 2011). The term Mobile Laser Scanning (MLS) is common for applications with laser scanners installed on moving platforms.

*The first objective of this thesis is the development of an innovative approach to obtain the required parameters for the transformation of the local sensor-defined 3D point cloud of a stationary laser scanner to an absolute coordinate system without the use of auxiliary control points.* In this research the sensor fusion aspect from the MLS domain is seized upon and should be transferred to the stationary usage of laser scanners.

In the stationary laser scanning domain only a rare number of approaches exploit the aforementioned sensor fusion for the geo-referencing task. The majority of approaches (Lichti and Gordon, 2004, Reshetyuk, 2009, Scaioni, 2005) still demand pre-surveyed control points, in particular for the orientation (heading) determination. On the contrary, the position of the laser scanner is directly obtained by, e. g., GNSS equipment on the laser scanner site (Mårtensson et al., 2012, Reshetyuk, 2009). Supports for position determination of the laser scanner are also provided by almost all laser scanner manufacturer (e. g., Leica Geosystems, Heerbrugg, Switzerland; Riegl, Horn, Austria; Trimble, Sunnyvale, CA, USA and Zoller + Fröhlich (Z+F), Wangen im Allgäu, Germany). Approaches which are based on two eccentrically installed GNSS antennas with respect to the laser scanner's rotation axis are capable to determine both, position and orientation (Paffenholz and Kutterer, 2008, Wilkinson et al., 2010).

The approaches mentioned above indicate the potential of an efficient determination of the transformation parameters for direct geo-referencing purposes. Nonetheless, some drawbacks exist: First, regarding the time-saving aspect, a reduced number of required control points compared to the traditional indirect methodology can be noted. Even though the reduced number of control points can lead to less redundancy, fidelity and reliability. Second, the geo-reference information is often gathered separately from the 3D point cloud acquisition, whereupon the simultaneous acquisition would further optimise the on-site work flow. Third, in terms of panoramic-type laser scanners, valuable information of the circular motion of the laser scanner about its vertical axis is neglected.

*This thesis aims for the fusion between a stationary laser scanner and GNSS equipment. The GNSS equipment is proposed to be physically attached to the laser scanner to pave the way for a simultaneous, continuous data acquisition. The circular motion of the laser scanner should be exploited for the estimation of the transformation parameters by means of recursive state-space filtering.* Owing to the often occurring non-linearities in the modelling of the motion of vehicles (here the laser scanner's circular motion), the Kalman Filter (KF) technique and its variants, which are capable to handle non-linearities (e. g., the Extended Kalman Filter (EKF)), are proposed to use. The main advantage of KF over traditional recursive parameter estimation is the consideration of an explicit motion model. Although, the transferability of the proposed approach to GNSS-denied scenarios should be, with minimum effort, envisaged with a substitution of the GNSS equipment to 3D positioning sensors, such as total stations, laser trackers or indoor positioning methods, e. g., Ultra Wide Band (UWB).

*The second objective is the supplementation of the geo-referenced 3D point clouds with both, laser scanner and geo-reference uncertainties.* The availability of the full stochastic information of 3D point clouds is beneficial for subsequent analyses like, e. g., extraction of geometric primitives or application of matching algorithms. Many research studies have been conducted on the topic of laser scanner uncertainties, calibration and error modelling (e. g., Bae et al., 2009, Lichti et al., 2005, Schulz, 2007, Soudarissanane et al., 2011). The reason can be seen in the active measurement principle of laser scanners where the interaction with the environment and the object itself has an impact on the measurement quantities. At this point it should be noted that separate laser scanner investigations and calibrations are out of the thesis's scope. The aim is to provide uncertainty measures for the transformation parameters and their joint propagation with uncertainties induced by the laser scanner to the geo-referenced 3D point clouds. In contrast to laser scanner uncertainties those of the transformation parameters are rarely considered in direct geo-referencing approaches. That is simply because this information

(especially related to an absolute coordinate system) is not always available.

*To achieve the aim of the second objective, the state-space filtering of the GNSS time series (obtained for the circular motion of the laser scanner) is suitable to provide uncertainty measures. Their joint propagation with uncertainty measures of laser scanners can be realised by applying the Law of Propagation of Uncertainties (LOP) to the transformation equation.* In addition, the transformation parameters can be redundantly estimated by means of GNSS time series which increases the fidelity and reliability of the results.

**The thesis's main objective is the development of an *efficient methodology for the determination of parameters and its uncertainty measures for the transformation of 3D point clouds* acquired by stationary laser scanners to a common local or an absolute coordinate system. It is proposed to use only physically attached sensors to the laser scanner and the waiver of external or auxiliary control points is stated.** This leads to a time-saving and simultaneous acquisition of 3D point clouds and its geo-reference information, i. e., direct geo-referencing. Moreover, the geo-referenced 3D point cloud should be supplemented with uncertainties induced by the transformation parameters as well as the laser scanner.

## 1.2. Reader's guide

The thesis is structured as follows. Chapter 2 provides the basic theory of 3D point clouds and geo-referencing methods. In addition, the consideration of uncertainty in Terrestrial Laser Scanning (TLS) is addressed. Chapter 3 familiarises the reader with the basic theory of discrete-time recursive state-space and transversal filtering. In particular, recursive parameter estimation, KF technique and prediction and filtering by Least-Squares Collocation (LSC) are introduced. In Chapter 4, the conceptual design and prototypic realisation of a Multi-Sensor System (MSS) for geo-referencing purposes are explained in detail. Furthermore, investigations of the MSS's components are discussed. Detailed descriptions of the proposed methodology for geo-referencing of 3D point clouds with GNSS equipment are given in Chapter 5. Subsequently, results of analytical investigations of the two previous chapters are discussed in Chapter 6. Chapter 7 concludes the thesis and gives an outlook for future research work.



## 2. Basics of terrestrial laser scanning and geo-referencing methods

This chapter familiarises the reader with the basics of 3D point clouds gathered by the Terrestrial Laser Scanning (TLS) technique and geo-referencing methods. In Section 2.1.1, the TLS technique (also referred to as Light Detection and Ranging (LiDAR)) is considered in terms of their stationary usage, as proposed in this thesis, and their mobile usage. Similarities and differences of both acquisition scenarios are clearly stated. Section 2.1.2 introduces laser scanners (short for terrestrial laser scanners) with focus on their stationary usage on tripods. The ranging principle and the scanning mechanism of laser scanners are outlined in Section 2.1.3 and Section 2.1.4, respectively, along with a recall of the corresponding error sources.

Section 2.2 introduces the geo-referencing of 3D point clouds acquired by stationary laser scanners. Section 2.2.1 defines the terminology used throughout this thesis before turning to the state of research in geo-referencing of 3D point clouds. In Section 2.2.2, the methodology of direct geo-referencing is discussed in detail since this is the fundamental background of this thesis. In the direct geo-referencing methodology, the required transformation parameters are typically obtained by physically attached sensors to the laser scanner. The estimation of transformation parameters by means of matching algorithms is outlined in Section 2.2.3. An overview of sensor candidates for position and orientation determination for the direct geo-referencing of 3D point clouds is presented in Section 2.2.4.

The objective of uncertainty consideration in TLS is treated in Section 2.3. Basics of measurement errors and the evaluation of uncertainties in measurements are recalled in Section 2.3.1. The error budget of TLS is composed of various influencing factors during the measurement and analysis process. A classification of these influencing factors, which are related to, for instance, the sensor, the environment, the object and the data processing, is provided in Section 2.3.2. Random and systematic errors of the laser scanners (including environmental induced errors) as well as object-related errors (e.g., the incidence angle of the laser beam to the local object's surface) are denoted as positional uncertainty. This topic is outlined in Section 2.3.3. In Section 2.3.4 is discussed the error budget caused by the applied geo-referencing method which is named transformational uncertainty.

### 2.1. Terrestrial laser scanning

The TLS technique is characterised by a sequential data acquisition (called scanning) by means of an emitted laser beam. This sequential procedure builds step by step a digital copy (referred to as 3D point cloud) of an arbitrary object. This is in contrast to image-based data acquisition, which is performed simultaneously in terms of an image. The physical principles of the TLS are equivalent for the stationary and mobile usage. The 3D point cloud as the result of the laser scanner's data acquisition consists of multitude 3D points in a local sensor-defined coordinate system. The laser scanner observations are the horizontal and vertical angle, the slant range to an object's surface as well as the intensity of the reflected laser beam by the object's surface.

#### 2.1.1. Distinction of stationary and mobile terrestrial laser scanning

The TLS technique can be distinguished in stationary and mobile usage. The latter is also referred to as Mobile Laser Scanning (MLS). In the scientific community the terminology MLS as well as Kinematic Terrestrial Laser Scanning (k-TLS) are frequently used side by side. Kutterer et al. (2009) propose two distinct categories of k-TLS: those observing moving objects by stationary laser scanner and those observing static objects by moving platforms, respectively. The latter is in accord with the terminology MLS. Throughout this thesis the notation MLS is used instead of k-TLS to refer to mobile scanning applications.

Regarding the sensor-side both scenarios generally use the same physical type of instrument but in different operation modi. The fixed position of the laser scanner during the data acquisition is characteristic for the stationary TLS. This results in one unique translation and orientation (spatial reference) of the 3D point cloud in the local sensor-defined coordinate system with respect to an arbitrary national or global coordinate system. Thereby, the local sensor-defined coordinate system is defined by the position of the laser scanner reference point and the orientation of the laser scanner axes. The link to a national or global coordinate system requires a set of transformation parameters. These parameters are obtained by geo-referencing methods which will be discussed in Section 2.2. For the data acquisition a scanning mechanism for both the horizontal and the vertical direction is necessary.

MLS is characterised by variable positions of the laser scanner due to its motion during the data acquisition. This leads to an individual coordinate system for each observed point of the 3D point cloud. To provide the entire 3D point cloud in a uniform coordinate system the spatial reference has to be precisely observed using adequate sensors like Global Navigation Satellite System (GNSS) equipments and Inertial Measurement Units (IMUs). Furthermore, all sensor observations have to be synchronised with a common time reference. In contrast to the stationary TLS the mobile variant requires a scanning mechanism typically only for the vertical direction. This laser scanner operation mode is referred to as profile mode, which means repeated 2D profiles defined by the vertical beam deflection are gathered. The motion of the laser scanner induced by a mobile platform provides the third dimension. Barber et al. (2008) and more recently Puente et al. (2011) provide detailed information about land-based MLS systems in the context of mobile mapping. Barber et al. (2008) studied the performance of the Mobile Mapping System (MMS) StreetMapper<sup>1</sup> by theoretical error analysis and empirical test showing typical scenarios for mobile mapping applications. Puente et al. (2011) provide a review of existing MLS in the current market. Research work using commercial 3D laser scanners (also applicable for stationary use) as main sensor for data acquisition and their preferential combination with GNSS equipment for spatial referencing are proposed for instance by Hesse (2007) and Vennegeerts (2011). It is noteworthy that similarities in terms of the used sensors and differences regarding the required spatial reference information of the 3D point cloud for stationary and mobile scanning exist.

According to Kutterer (2010) two distinct observation modes for MMS exist: stop-and-go and on-the-fly 3D point cloud acquisition. The stop-and-go mode is similar to the introduced stationary TLS whereas the on-the-fly mode is equivalent to the MLS. Further differences in both observation modes are the spatial resolution and the geometric quality of the 3D point cloud. For the stop-and-go mode the spatial resolution is controlled by the increments of the scanning mechanism. The geometric quality is immediately consistent for the entire 3D point cloud because the transformation (geo-referencing) is performed for all points with the same set of parameters.

The spatial resolution of the on-the-fly mode depends besides the spatial and temporal resolution of the scanning mechanism on the mobile platform's velocity. Concerning the geometric quality the rectification of the 3D point cloud has the main influence due to the individual coordinate system of each observed point. As aforementioned, their individual transformation is the fundamental difference between the stationary and mobile TLS. Commonly, GNSS equipment, IMUs and further navigation sensors, like odometer, are utilised to observe the mobile platform's trajectory. For the data fusion and the determination of the transformation parameters are used state-space filtering techniques. In terms of data acquisition time, especially in case of elongated objects like roads or building façades, the on-the-fly mode or mobile scanning is preferred owing to the time-saving aspect.

Finally, it should be mentioned that various similarities exist between the on-the-fly mode in MLS (used in the geodetic community) and the autonomous navigations of robots and small-scale vehicles (frequently used in the robotic community). Although the autonomous navigation is out of the scope of this thesis, the topic is

---

<sup>1</sup>The StreetMapper is a 3D MMS by 3D Laser Mapping, Bingham, Nottingham, United Kingdom and IGI mbH, Kreuztal, Germany, further information can be found on [www.streetmapper.com](http://www.streetmapper.com)

briefly mentioned for the sake of completeness. Comprehensive information can be found, e. g., in Thrun et al. (2005). The main difference can be found in the result of the data acquisition. In the geodetic community the main interests are in the 3D point clouds. For the robotic community the 3D point clouds are often by-products which are intensively used for the navigation of the autonomous platform or robot. In general this means Simultaneous Localization And Mapping (SLAM) which covers the map building for an unknown environment and the navigation using this unfinished map (Nüchter, 2009). Research on this topic can be found for instance in Soloviev et al. (2007) or more recently in Nüchter et al. (2010).

### 2.1.2. Stationary laser scanner

In the TLS community the laser scanners are categorised by their ranging principle in two distinct groups: those utilising the Time-of-Flight (TOF) measurement and those based on the phase measurement technique. In terms of the maximum ranging distance the phase-based technique is limited to about 150 m with an accuracy in the range of millimetres. The high spatial and temporal resolution is a further characteristic of those laser scanners. On the contrary, the TOF-based laser scanners reach several hundreds of metres but with less accuracy as well as less spatial and temporal resolution compared to the phase-based laser scanners (Beraldin et al., 2010). It is noteworthy that triangulation laser scanners with an operating range of a few metres commonly used in industrial or reverse engineering applications are out of the thesis's scope. Further distinctions of laser scanner types are done according to the scanning mechanism and the corresponding Field of View (FoV).

Following Petrie and Toth (2009b) laser scanners are differentiated into three groups according to their maximum ranging distance. The laser scanners in the short range group with maximum ranges of 50 m to 100 m all fall into the category of panoramic-type scanner. Most of them utilise the phase measurement technique. Manufacturers of such laser scanners are for instance Zoller + Fröhlich (Z+F), Wangen im Allgäu, Germany and Faro Europe, Korntal-Münchingen, Germany. The medium range group covers laser scanners based on the TOF method with maximum ranges of 150 m to 350 m. Regarding the FoV there is no unique grouping. These type of laser scanners are manufactured by, e. g., Leica Geosystems, Heerbrugg, Switzerland and Trimble, Sunnyvale, CA, USA. The long range laser scanners with maximum ranges of 500 m and beyond utilise all the TOF method. A manufacturer in this segment is Riegl, Horn, Austria. For a deeper review the reader is referred for instance to Petrie and Toth (2009a) and for technical details to the manufacturer websites. The mentioned manufacturers are not an exhaustive list of all manufacturers in the market and therefore gives only an exemplary illustration of the different groups and types.

### 2.1.3. Ranging principle

The optical ranging based on light waves propagation is well-known in geodesy from the Electronic Distance Measurement (EDM) technique which is used in total stations (Joeckel et al., 2008, Rieger, 1996). In general, the ranging is based on a precise time measurement and the knowledge of the light speed in a vacuum ( $c_0 = 299792458$  m/s). The distance between the laser source and a reflective target surface and back to the laser source is obtained by the measurement of the time delay of the light travelling (Beraldin et al., 2010). Two distinct methods based on time measurement exist: those measuring the TOF of laser pulses and those comparing phase shifts of emitted Continuous Waves (CWs). For the sake of completeness, the ranging based on triangulation is only mentioned here. This method utilises a known baseline and angle measures to obtain quite precise range measures for distances of a few metre with millimetre accuracy and even less. Comprehensive background can be found for instance in Beraldin et al. (2010).

**Time-of-Flight measurement** methods make use of short discrete pulses (typical pulse width  $t_p = 5$  ns) with known propagation velocity. This leads also to the terminology timed pulse method or pulse echo method (Petrie and Toth, 2009a). The velocity  $c = \frac{c_0}{n}$  is finite and constant for light waves travelling in a given medium, characterised by its refraction index  $n$ . Measuring the time delay  $t$  resulting from the light travelling from the

laser source to a reflective target surface and back to the laser source (Beraldin et al., 2010), the range  $\rho$  is assessed by

$$\rho = \frac{1}{2} \cdot c \cdot t. \quad (2.1)$$

The determination of  $t$  in Eq. 2.1 is essential for the TOF measurement. A detection method with a suitable criterion has to be used to generate trigger pulses for controlling the time measurement. Jutzi (2007) presents seven detectors which are capable to extract features for object description by the waveform of the backscattered pulse. A transmitted pulse is characterised by its pulse width  $t_p$  and pulse rise time  $t_r$  of the laser pulse leading edge. According to Eq. 2.1 and the pulse width the pulse length is obtained. The pulse shape and the pulse repetition time are of further importance. Latter describes the time delay between subsequent emitted pulses. For multiple echoes generated by one emitted pulse, different ranges can only be discriminated if the echoes do not have an overlap, i. e., their distance must be larger than half of the pulse length.

An approximate for the range uncertainty  $\sigma_\rho$  based on a single pulse buried in additive white noise (Beraldin et al., 2010) is

$$\sigma_\rho \approx \frac{1}{2} \cdot c \cdot t_r \cdot \frac{1}{\sqrt{SNR}}, \quad (2.2)$$

where  $SNR$  denotes the signal-to-noise ratio. To gain an idea of the feasible range accuracy for a single pulse using the the TOF measurement we assume the following values:  $SNR = 100$ ,  $t_r = 1$  ns and appropriate time interval counter. At this point, the uncertainty of the time measurement is assumed to be marginal compared to the  $SNR$  and will be neglected. The evaluation of Eq. 2.2 yields  $\sigma_\rho = 15$  mm for a single pulse. An improvement can be reached by averaging of  $N$  independent pulses with the consequence of a reduced data rate. The result will be  $1/\sqrt{N}$ -times smaller  $\sigma_\rho$  (Beraldin et al., 2010).

The circumstances of multiple pulse echoes are caused by the target surface characteristic and are common at the time in case of scanning vegetation areas. Their evaluation of at least the first echo and last echo is state of the art in airborne-based systems. This multiple echo technique is also becoming available for terrestrial laser scanner (Beraldin et al., 2010). Besides the recording of multiple echoes also the recording of the entire waveform of the backscattered pulses is feasible with commercial laser scanning systems in the market. Mallet and Bretar (2009) review the literature related to these sensors called full-waveform LiDAR systems in terms of fundamentals and applications. More recently, Mallet et al. (2011) addressed the usage of full-waveform LiDAR data for the classification of urban areas.

**Phase measurement technique** utilise modulated CWs instead of short discrete pulses. The modulation can be performed by either Amplitude Modulation (AM) of the intensity of the laser beam, for instance with a sine wave, or by Frequency Modulation (FM). Due to its typical usage in laser scanners and surveying instruments such as total stations AM will be considered in the following. For further reading of FM refer to, e. g., Beraldin et al. (2010).

The ranging by means of a AM-CW is based on a precise measuring of the phase difference or the phase angle between the emitted signal and the received signal at the sensor after its reflection. Therefore, common terminology is also phase comparison or phase shift method. The former will be used throughout this thesis. Two signals with different wavelengths are involved in the AM: a high frequent carrier signal with short wavelength and a superimposed low frequent measuring signal with longer wavelength than the carrier wavelength. In order to obtain the overall range, the phase difference  $\varphi$  and the integer number  $N$  of total wavelengths  $\lambda_m$  of the modulated signal have to be measured. The determination of  $N$  is referred to as ambiguity resolution problem. This can be solved for instance by means of various modulation frequencies. Hereby, the lowest frequency and corresponding longest wavelength denote the maximal non-ambiguous range. The shortest wavelength ( $\lambda_{short}$ ) and corresponding highest frequency determine the range resolution and accuracy. The final range measure is found by the combination of the series of range measurements with the different frequencies (Petrie and Toth, 2009a, Rieger, 1996).



The measuring of  $\varphi$  can be reduced to a time measurement. The time delay  $t_\varphi = \frac{\varphi}{2\pi} \cdot \frac{\lambda_m}{c}$  results from  $\varphi$  and  $\lambda_m = c/f_m$  where  $f_m$  denotes the frequency of the modulated signal. By  $\varphi$  or  $t_\varphi$  the fractional part ( $\Delta\lambda_m = \frac{\varphi}{2\pi} \cdot \lambda_m$ ) of the overall range is represented. The overall travelling time  $t$  for the signal is composed of  $t_\varphi$  and the time delay  $t_N = N \cdot \frac{\lambda_m}{c}$  for the full wavelength's integer number. Thus, the total range  $\rho$  is found by using Eq. 2.1

$$\rho = \frac{1}{2} \cdot c \cdot (t_\varphi + t_N) = \frac{1}{2} \cdot (\Delta\lambda_m + N \cdot \lambda_m). \quad (2.3)$$

Like aforementioned,  $\lambda_{short}$  is used to evaluate the range uncertainty. Following Beraldin et al. (2010) who present some example values an approximate for  $\sigma_\rho$  is given by

$$\sigma_\rho \approx \frac{\lambda_{short}}{4 \cdot \pi} \cdot \frac{1}{\sqrt{SNR}}. \quad (2.4)$$

Comparing the AM-CW based and the pulsed TOF ranging, it can be stated that in general the former method yields higher data repetition rates for single ranging measurements than the latter one. Regarding the maximum ranges the pulsed TOF method has longer operating ranges than the AM-CW method.

**For both ranging principles error sources and models** are addressed in the following. The TOF and the AM-CW methods utilise the light speed in vacuum  $c_0$  to obtain the range. For the former the velocity of light in a medium is implicitly given in Eq. 2.1. For the latter, the modulated wavelength is a function of the corresponding frequency and the velocity of light in the transmission medium. Therefore, the transmission medium's refraction index  $n$ , which is a function of air temperature, pressure and humidity, has to be taken into account to obtain the velocity of light  $c = \frac{c_0}{n}$  for the current environmental conditions. These atmospheric influences are taken into account by the first velocity correction widely known from the EDM technique (Rüeger, 1996, Chapter 6). On account of the improvement of the laser scanner technology in terms of ranging accuracy the correction owing to atmospheric conditions is essential to obtain reliable results. This is of great importance in environments with unstable temperature conditions where the influence can reach up to 10 ppm (Rietdorf, 2005).

In addition to the propagation medium induced errors, further errors are related to drift effects in the sensor. Most of these drift effects result from thermal effects by electronic components in the laser scanner. Therefore, the internal temperature for certain components is registered to supervise and correct these effects. However, it is customary to use an internal reference distance to account for thermal effects. Further effects and their investigations in relation with the ranging of laser scanners as well as sensor calibration approaches are reported for instance by Lichti (2007), Lichti and Skaloud (2010) and Reshetyuk (2009). Dorninger et al. (2008) propose a methodology for an on-the-job detection and correction of systematic cyclic distance measurement errors of AM-CW laser scanner based on project data.

It is worth mentioning that the laser-based ranging is an active measurement technology. Thus, the interaction of the emitted laser beam with the backscattering object surface evokes further errors. These errors are mainly addicted to the natural and man-made object surface in terms of, e.g., flatness, roughness and reflection behaviour. Therefore, they are recalled in the classification of the error budget in TLS (Section 2.3.2).

#### 2.1.4. Scanning mechanism

The scanning mechanism controls the spatial and temporal resolution of the 3D point cloud. For this purpose, single laser beams are uniformly deflected in horizontal and vertical direction over the object's surface. In TLS, common scanning mechanisms utilise rotating or oscillating mirrors in combination with the rotation of the entire laser scanner device (Beraldin et al., 2010).

For stationary laser scanners a typical FoV results from the realised scanning mechanism. Staiger (2003) introduced three different categories of laser scanners with respect to their FoV. These three categories are termed the panoramic-type scanners, the camera-type scanners and the hybrid scanners.

The panoramic-type scanners are designed to scan a full circle of  $360^\circ$  in the horizontal plane. The vertical plane is only restricted by the laser scanner's base. Servo motors, which evoke the rotation of the laser scanner head about its vertical axis, are usually utilised for the horizontal beam deflection. In the vertical plane the beam deflection is performed by fast-rotating mirrors placed on the horizontal axis of the laser scanner. This mechanism is often realised for AM-CW laser scanners due to their rapid ranging.

The camera-type scanners are limited to a defined window in horizontal and vertical direction similar to digital cameras. Thereby, the laser scanner's head is stationary during the data acquisition and the beam deflection is only performed by means of moving mirrors. The hybrid scanner type is a combination of both aforementioned types. For the horizontal direction, a full circle scan is realised by servo motors. The vertical beam deflection is limited to a section, comparable with the camera-type. Hybrid and camera-type scanners are common for pulsed TOF laser scanner, which are characterised by a slower data acquisition than the AM-CW laser scanner. The reader is referred to, e.g., Petrie and Toth (2009b) for further information regarding the scanning mechanisms and examples for laser scanners in the market. Details and mathematical derivations for the angular measurements of laser scanners can be found in Joeckel et al. (2008, Chapter 10).

Besides similarities of laser scanners and total stations in terms of their ranging principle, further similarities exist in the mechanical realisation of laser scanners and total stations with respect to their instrumental axes. For this reason the instrumental errors known from total stations can be investigated in an analogous manner for laser scanners. Several other researches address the topic of laser scanner investigations and calibration, which in general can be performed component-wise or for the entire laser scanner system. A brief overview of the total error budget of TLS will be given in Section 2.3.

## 2.2. Geo-referencing of 3D point clouds

This section is dedicated to geo-referencing of 3D point clouds acquired by stationary laser scanners. To clearly state the meaning of geo-referencing the terminology used throughout this thesis is introduced. Three approaches: *indirect geo-referencing*, *direct geo-referencing* and data-driven methods, can be identified in accordance to Schuhmacher and Böhm (2005). While geo-referencing is a central topic of this thesis, the three approaches are introduced regarding their individual characteristics and the latter approach of choice (the direct geo-referencing) will be thoroughly discussed. The data-driven approaches will be briefly mentioned for sake of completeness, because typically they exploit a preceding indirect or direct geo-referencing. Thus, this leads to two major categories to obtain the transformation parameters for the geo-referencing procedure: the indirect and the direct methodology.

### 2.2.1. Terminology and the state of research

The data acquisition by laser scanners is performed in a local sensor-defined coordinate system termed  $L$ -frame (Fig. 2.1). The axes of the  $L$ -frame are defined by the principle axes of the laser scanner. Typically,  $x$ - and  $y$ -axis define a horizontal plane whereas the  $z$ -axis represents the vertical axis of the sensor and thus completes a left-handed Cartesian frame<sup>2</sup>. The laser scanner observables are (analogous to total stations) the polar elements: range  $\rho$ , horizontal direction  $\beta$  and elevation angle  $\alpha$  (Lichti and Skaloud, 2010). In the  $L$ -frame, the Cartesian coordinates  $x$ ,  $y$  and  $z$  of a single point  $\mathbf{p}_j^L = [x_j^L \ y_j^L \ z_j^L]^T$  of a 3D point cloud are expressed by

$$\mathbf{p}_j^L = \left[ \rho_j^L \cdot \sin(\alpha_j^L) \cdot \sin(\beta_j^L) \quad \rho_j^L \cdot \sin(\alpha_j^L) \cdot \cos(\beta_j^L) \quad \rho_j^L \cdot \cos(\alpha_j^L) \right]^T. \quad (2.5)$$

<sup>2</sup>It is noteworthy that the specific realisation in terms of a left-handed or a right-handed Cartesian coordinate system depends on the laser scanner type and manufacturer.

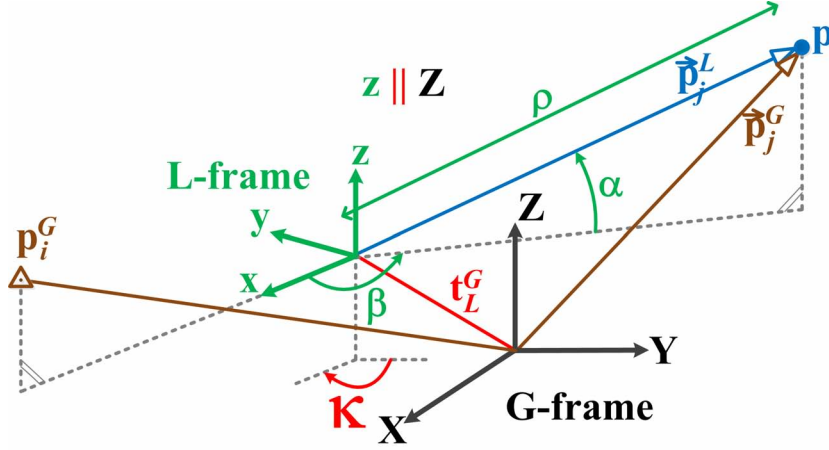


Figure 2.1: Local coordinate system  $L$ -frame, defined by the principal axes of the laser scanner. Laser scanner observables: range  $\rho$ , horizontal direction  $\beta$  and elevation angle  $\alpha$  in the  $L$ -frame. The heading  $\kappa$  denotes the azimuthal orientation of the  $L$ -frame with respect to the  $G$ -frame which indicates a global coordinate system with a known geodetic datum. Without loss of generality, parallelism is assumed for both vertical axes ( $z \parallel Z$ ). The position vector  $\mathbf{t}_L^G$  denotes the translation of the  $L$ -frame's origin with respect to the  $G$ -frame. (after Lichti and Gordon, 2004)

The Cartesian coordinates in Eq. 2.5 can be used to express the spherical coordinates of the laser scanner observables

$$\rho_j^L = \sqrt{(x_j^L)^2 + (y_j^L)^2 + (z_j^L)^2}, \quad \beta_j^L = \arctan\left(\frac{y_j^L}{x_j^L}\right) \quad \text{and} \quad \alpha_j^L = \arctan\left(\frac{z_j^L}{\sqrt{(x_j^L)^2 + (y_j^L)^2}}\right). \quad (2.6)$$

The  $L$ -frame of a 3D point cloud is unique for each separate stationary laser scanner site. In most applications of TLS a single laser scanner site is not sufficient to entirely capture an object. Thus, the relation of one 3D point cloud acquired from site 2 ( $L$ -frame-2) with respect to another 3D point cloud acquired from a site 1 ( $L$ -frame-1) requires a 3D rigid body transformation which is given by

$$\mathbf{p}_j^{L1} = \mathbf{R}_{L2}^{L1} \cdot \mathbf{p}_j^{L2} + \mathbf{t}_{L2}^{L1} \quad (2.7)$$

where  $\mathbf{R} \in \mathbb{R}^{3 \times 3}$  is the *rotation matrix* and  $\mathbf{t} \in \mathbb{R}^{3 \times 1}$  the *translation vector*, both together denote the *transformation parameters*. A matrix representation using Euler angles is introduced for the rotation representation. The rotation angles are denoted  $\omega$ ,  $\varphi$  and  $\kappa$  around the  $x$ -,  $y$ - and  $z$ -axis of the  $L$ -frame, respectively. The complete expression of  $\mathbf{R}(\cdot)$  is found in Section A.1.

In general, there is no necessity to consider a scale factor for 3D point clouds obtained with the same laser scanner. A 3D similarity transformation can be used instead of a 3D rigid body transformation if there are any reason to take a scale factor into account. For the 3D rigid body transformation exist six Degrees of Freedom (DoF) which have to be determined. It should be mentioned that the DoF can be reduced either by setting up the laser scanner over a known location (remaining number of DoF is three) or by a sufficient orientation of the laser scanner to the direction of gravity. The latter leads to  $\omega = \varphi = 0$  and therefore only four DoF are remaining. In this case, it is supposed that the remaining spatial rotations are insignificantly small after the orientation of the laser scanner to the direction of gravity.

The term *registration* denotes the provision of an unique  $L$ -frame for at least two 3D point clouds by means of the 3D rigid body transformation in Eq. 2.7. The term relative orientation (known from photogrammetry) is used as a synonym for registration. The terminology registration is putting emphasis on the role of the data itself rather than additional measurements (Brenner et al., 2008). The required transformation parameters for the registration can be obtained either by matching algorithms *without explicit point correspondences* (Section 2.2.3) or by *explicit corresponding points* in each 3D point cloud. Usually, the latter demands for a manual identification

of points in each 3D point cloud which can be used in a least-squares adjustment to obtain the transformation parameters.

The term *geo-referencing* contrary to registration is dedicated to the transformation of the  $L$ -frame into an absolute or global coordinate system ( $G$ -frame). The  $G$ -frame (cf. Fig. 2.1) is an arbitrary superior coordinate systems, mostly with a known geodetic datum such as national or global coordinate systems like, e. g., the European Terrestrial Reference System 1989 (ETRS89) combined with the Universal Transverse Mercator (UTM) projection. It is assumed that the  $Z$ -axis of the  $G$ -frame sufficiently coincides with the direction of gravity. The mathematical background in Eq. 2.7 is also valid for the geo-referencing task. It is noteworthy that the geo-referencing of a single 3D point cloud entirely includes the registration task. Although, it is possible to perform first the registration of multiple 3D point clouds of different sites into one unique 3D point cloud (interim result). Afterwards, the geo-referencing of this interim result provides the 3D point cloud in the  $G$ -frame. The usage of the two different work flows depends on various aspects which will be mentioned in the following state of research.

The above introduced terminology as well as notation for 3D points and their geo-referencing task are summarised in the following:

- $L$ -frame is a local coordinate system which is defined by the principal axes of the laser scanner.
- $G$ -frame is an absolute or global coordinate system with a generally known geodetic datum.
- $\mathbf{p}^L = [x^L \ y^L \ z^L]^T$  denotes a 3D point in the  $L$ -frame
- $\mathbf{p}^G = [X^G \ Y^G \ Z^G]^T$  denotes a 3D point in the  $G$ -frame
- $\mathbf{R}_L^G(\omega, \varphi, \kappa) \equiv \mathbf{R}_L^G \in \mathbb{R}^{3 \times 3}$  and  $\mathbf{t}_L^G \in \mathbb{R}^{3 \times 1}$  denote the rotation matrix and the translation vector, i. e., the transformation parameters.
- *Position* denotes the 3D coordinates of the laser scanner with respect to the  $G$ -frame which is determined by  $\mathbf{t}_L^G$ .
- *Orientation* denotes the spatial angular direction of the laser scanner which is obtained by  $\mathbf{R}_L^G$ . In particular, *heading* ( $\kappa$ ) denotes the spatial angular direction with respect to the  $z$ -axis.
- *Registration* denotes the transformation between the  $L$ -frames without a link to the  $G$ -frame.
- *Geo-referencing* denotes the transformation task between the  $L$ -frame and the  $G$ -frame.

## Review of the state of research in the field of geo-referencing of 3D point clouds

**Indirect** geo-referencing of 3D point clouds describes the traditional way of geo-referencing in stationary TLS applications. This procedure is identical with the analysis of observations in geodetic networks carried out by total stations. To determine the required transformation parameters in Eq. 2.7 at least three well-spread points in the scanning scene have to be utilised. From now on, these points are called *control points* and their coordinates have to be known in the  $L$ -frame and the  $G$ -frame.

To make the control point coordinates available in the  $L$ -frame typically artificial targets are used to indicate the location of the control points. These targets can either be flat markers with a specific pattern or simple 3D geometries (e. g., cylinder or spheres), respectively. The specific realisation differs for instance by the laser scanner manufacturer. For the target detection in 3D point clouds and corresponding range or intensity images well-known image processing techniques (e. g., edge detection algorithms) are applied. A brief outline of suitable methods can be found in Abmayr et al. (2008). In addition, the authors present a correlation based target finder for TLS applications. This approach is invariant to perspective projections, rotation and translation and robust to noise (Abmayr et al., 2008). This is of importance when using flat

targets and implicitly given by some 3D geometries for instance spheres. These targets can also be used for registration of 3D point clouds. This was briefly above-quoted and termed registration by explicit point correspondences.

The coordinates of these artificial targets, i.e., the control point coordinates, have to be determined in the  $G$ -frame. More precisely the characteristic point for instance the centre of a sphere has to be referred to the  $G$ -frame. This can either be solved by placing the targets on known locations (e.g., a pillar with given coordinates in the  $G$ -frame) or their coordinates have to be determined by independent surveying techniques. The choice of the adequate surveying instrument depends on whether the scene is indoor (e.g., total stations) or outdoor (e.g., GNSS equipment). This independent surveying can be a complex and time-consuming task.

Regarding the uncertainty of indirect geo-referencing approaches, it can be stated that the uncertainty mostly depends on the quality of the independent surveying of the control point coordinates. Typically, control points' coordinates can be obtained with standard deviations in a range of several millimetres by means of total stations. For GNSS-based determination this can be in the same range or rather in the range of several centimetres depending for instance on the satellite constellation.

**Direct** geo-referencing of 3D point clouds is characterised by external sensors, which are mostly attached to the laser scanner, and directly provide the required transformation parameters in Eq. 2.7. Typical sensors for the direct approach are 3D positioning sensors, inclinometers, gyroscopes and compasses. This use of external sensors is comparable to the geo-referencing in MLS applications (cf. Section 2.1.1). Besides the following outline, Section 2.2.2 is dedicated to an in-depth discussion.

In literature, two different approaches can be found for using external sensors for the direct geo-referencing procedure. First, approaches which exploit known sites for the laser scanner and demand pre-surveyed control points (backsight targets) for the heading determination (Lichti and Gordon, 2004, Lichti et al., 2005, Scaioni, 2005). A convenient methodology is proposed by Mårtensson et al. (2012), Reshetyuk (2009, 2010a) who utilise GNSS equipment on both, the laser scanner and the control point site, to determine the transformation parameters. This is reasonable since it does not demand for coordinates known in advance neither for the laser scanner site nor for the backsight target site.

Second, approaches which utilise up to two GNSS antennas eccentrically installed at the laser scanner (Paffenholz and Kutterer, 2008, Wilkinson et al., 2010) to simultaneously determine both, position and orientation information, without additional control points in the scanning scene. Thus, the work load for independent extra surveying can be significantly reduced.

The uncertainty of the direct geo-referencing approaches mainly depends on the uncertainties induced by the external sensors. In case of using control points their coordinate determination contributes to the error budget. In-depth investigations can be found in Lichti and Gordon (2004) for random error sources and investigations extended to systematic error sources are presented by Lichti et al. (2005). Furthermore, Section 2.3.4 is devoted to error sources induced by the direct geo-referencing method.

**Data-driven** approaches are based on already geo-referenced data which are used to refine coarse geo-referenced 3D point clouds by means of matching algorithms (cf. Section 2.2.3). For the coarse geo-referencing of 3D point clouds in the  $L$ -frame with respect to the  $G$ -frame two variants are feasible (Schuhmacher and Böhm, 2005): manual determination of the initial transformation parameters and adopting a direct geo-referencing approach. Both variants aim to obtain appropriate control points in the  $G$ -frame. In terms of the already geo-referenced data, the mentioned authors utilise 3D virtual city models and airborne LiDAR data for geo-referencing 3D point clouds obtained by stationary laser scanners. Böhm and Haala (2005) make use of the direct approach of Schuhmacher and Böhm (2005) and present results on the integration of airborne and terrestrial laser data to improve 3D building models. It can be noted, that the uncertainty of this data-driven approach is dominated by the uncertainty of the already geo-referenced data.

**Concluding remarks:** The indirect geo-referencing requires extra field work to establish a control point network. This control point determination is mostly performed in an independent manner by total stations or GNSS equipment and thus it is a time consuming task. Also the configuration of the network has to be planned well to obtain reliable results. Aspects of the target detection in the 3D point clouds have to be taken into account. Even though this task can be performed by a range of available automatic procedures, it was the manual target detection which again was time consuming and error-prone in the past. Nevertheless, an automatic target detection has also certain limits regarding the marker design, its size and radiometric properties.

Considering the geo-referencing of multiple 3D point clouds, on the one hand, each 3D point cloud requires a minimal number of control points. On the other hand, the multiple geo-referencing can be split in a registration by overlapping areas, which are mandatory in this case, and a subsequent geo-referencing. In most applications the indirect geo-referencing can only be completed after the post-processes have been finished, like analyses of the control points surveying. Any statements about completeness and uncertainty of the 3D point clouds can only be given by means of post-analyses. In terms of uncertainty, preference will be given to the indirect geo-referencing because it provides the most precise results compared to the direct geo-referencing. The main reason here is the precise determination of the control point network.

The major advantage of direct geo-referencing approaches lies in the time-saving determination of the geo-reference by external sensors attached to the laser scanner and therefore the waiver of control points. Hereby, it is usual to use GNSS equipment in outdoor environments and total stations for indoor applications. Also indoor positioning techniques such as Ultra Wide Band (UWB) are capable to provide the required information. There is no necessity for overlapping areas in multiple 3D point clouds for their mutual orientation. Their direct availability in the  $G$ -frame implicitly provides the interconnection. Also the direct geo-referencing can provide appropriate start values for matching algorithms (cf. Section 2.2.3). Regarding the uncertainty of the direct approaches the statement for the indirect geo-referencing is also valid. Nevertheless, the direct geo-referencing methodology offers the possibility for an on-site statement on completeness as well as on the uncertainty of the 3D point cloud.

It is worth noting that the robotics community has an advanced stage of research in geo-referencing. The reader is referred for instance to Nüchter et al. (2010) and the references therein. Primarily, focus is on the navigation in unknown areas of small and autonomous moving platforms or robots often referred to as SLAM and its variants (e. g., Montemerlo and Thrun, 2007, Nüchter, 2009). Similarities to the aforementioned methodologies can be found in the used algorithms brought up in the registration context, for further details see Section 2.2.3.

In conclusion, direct geo-referencing is valuable in terms of efficient work flows, reachable accuracy and usability. This qualifies the direct approach to reach the thesis's aim and the next section is dedicated to an in-depth discussion.

### 2.2.2. Direct geo-referencing of 3D point clouds

This section gives more details about the direct geo-referencing of 3D point clouds which has several advantages over the indirect approach as mentioned in the previous section. The main characteristic of the direct geo-referencing is the usage of additional sensors to directly obtain the transformation parameters  $\mathbf{R}_L^G(\omega, \varphi, \kappa)$  and  $\mathbf{t}_L^G$ . Recalling that the orientation of the laser scanner with respect to the direction of gravity can be obtained by means of levelling capabilities or by supporting tribrachs, the spatial rotations  $\omega$  and  $\varphi$  are controlled. Theoretically, this should yield to  $\omega = \varphi = 0$  depending on the uncertainty of the levelling process and the specifications of the used spirit level. Recent laser scanners in the market also provide electronic spirit levels or dual-axis compensators which are capable to account for any remaining residuals after rough levelling by means of bullseye levels. Assuming a sufficient orientation to the direction of gravity and parallelism for the vertical

axes of the  $L$ -frame and the  $G$ -frame ( $z \parallel Z$ ) Eq. 2.7 can be rewritten to

$$\mathbf{p}_j^G = \mathbf{R}_L^G(\kappa) \cdot \mathbf{p}_j^L + \mathbf{t}_L^G \quad (2.8)$$

where the only remaining spatial rotation  $\kappa$  (cf. Eq. A.3 for  $\mathbf{R}_L^G(\kappa)$ ) is around the vertical axis of the laser scanner. Eq. 2.8 is the mathematical background for almost all direct geo-referencing methods.

The two distinct direct geo-referencing approaches are thoroughly discussed: First, approaches which use additional backsight targets (Alba et al., 2005, Alba and Scaioni, 2007, Lichti and Gordon, 2004, Lichti et al., 2005, Reshetyuk, 2009, 2010a, Scaioni, 2005). Second, approaches which are based on external sensors (physically attached to the laser scanner) without the demand for any targets in the scanning scene (Mohamed and Wilkinson, 2009, Paffenholz and Kutterer, 2008, Schuhmacher and Böhm, 2005, Wilkinson and Mohamed, 2009, Wilkinson et al., 2010).

Lichti and Gordon (2004) and Lichti et al. (2005) report on the error propagation in directly geo-referenced 3D point clouds in cultural heritage applications. Lichti and Gordon (2004) present their analysis of the random error sources of direct geo-referencing based on using a backsight target. For the orientation determination Lichti and Gordon (2004) use a telescope attached to the laser scanner to point to a backsight target. This procedure is feasible due to optical plummets and levelling facilities to orientate the laser scanner to the direction of gravity. In particular, the authors discuss the uncertainty induced by the laser beamwidth and by the target centroid pointing. Besides this optical pointing based orientation the authors propose a variant utilising 3D resection to obtain the laser scanner orientation. The latter is also presented by Gordon and Lichti (2004). They report on centroid estimation of the backsight targets by means of the gathered 3D point clouds. This needs a target detection as well as fitting algorithm to determine the centroid position like in the indirect geo-referencing approach. Beforehand, the authors validate their error propagation and direct geo-referencing by 3D resection by simulated data. Afterwards they perform real case studies in heritage applications. Lichti et al. (2005) extend their former investigations on the random error budget to analyses of the systematic error sources which are caused by the laser scanner data independent from the geo-referencing approach.

Scaioni (2005) describes the geometric model of the direct geo-referencing approach utilising a telescope pointing to a backsight target. Again, levelling facilities of the laser scanner support this procedure. According to the proposed approach by Gordon and Lichti (2004), the author analyses the error budget for simulated and real data. The direct geo-referencing approach is tested with practical measurements. The results are contrasted with those obtained by indirect geo-referencing. Scaioni (2005) identifies architectural and road surveying as well as tunnel and indoor mine survey as fields of applications for direct geo-referencing. The latter two are thoroughly analysed by Alba et al. (2005). A report on a project which utilises direct geo-referencing in a tunnel survey can be found in Longstreet (2010). The benefits of TLS applications for the tunnel survey are reported from a practitioners perspective and, moreover, the advantages of the direct geo-referencing, in particular the time efficiency, are pointed out. Alba and Scaioni (2007) provide a comparison of indirect and direct geo-referencing as well as surface matching approaches in cultural heritage applications. The achievable performance of all mentioned approaches is evaluated under laboratory conditions. The direct geo-referencing, which is besides the surface matching approach applied to real data, is characterised by optical centring and orientation of the laser scanner to the direction of gravity over a known position. The orientation is established by either telescope or measurements to a backsight target, like in the aforementioned publications.

In contrast to the up to now cited research works, Reshetyuk (2009, 2010a) develops an integrated approach using GNSS equipment for the position determination of the laser scanner as well as for the position of a backsight target. Then, the orientation information is obtained by the scanned backsight target. For the proposed direct geo-referencing approach by means of GNSS equipment and Real-time Kinematic (RTK) measurements, Reshetyuk (2009) describes two different work flows. The first determines the laser scanner position parallel to the scanning process. This makes sense due to time-saving issues. The other work flow determines the position before or even after the scanning. Which work flow is utilised depends for instance on the laser

scanner's capabilities to attach a GNSS antenna. Reshetyuk (2009, 2010a) reports on simulations results and investigations of real data. His simulations show that the scanner position can be determined with sub-centimetre accuracy by means of RTK-Global Positioning System (GPS) measurements. In the performed tests, static GPS measurements were used for the coordinate determination of the backsight target. Reshetyuk (2010a) states a coordinate accuracy better than 1 cm at the object distance of up to 70 m. More recently, Mårtensson et al. (2012) report on in-depth investigations of the approach proposed by Reshetyuk (2010a). The authors carried out several tests by means of RTK-GPS measurements. Investigations of a rotating GNSS antenna come out with the result that the uncertainty in the position of the laser scanner is independent of both, the observation time and the radius. In addition, they confirmed the results of Reshetyuk (2010a) for the standard uncertainties of the geo-referencing procedure.

The following direct geo-referencing approaches mainly stress on the direct position and orientation determination of the laser scanner without the necessity of any artificial control points in the scanning scene. Schuhmacher and Böhm (2005) as well as Böhm and Haala (2005) consider direct geo-referencing information acquired by means of low-cost GPS equipment and digital compass readings for coarse geo-referencing with subsequent refinement by data-driven approaches. The authors tested several variants of geo-referencing such as low-cost GPS in combination with either control points or the digital compass readings. Both deliver an insufficient total accuracy in the range of metres whereas data-driven approaches reach the decimetre level and the indirect approach provides a total accuracy of millimetres. The main reason for that is seen by the authors in the used low-cost GPS equipment and the digital compass. They propose to use sophisticated equipment and optimised analyses techniques for improving the result.

A direct geo-referencing approach, which deals with the direct estimation of the position and the orientation of the laser scanner by means of kinematic GNSS observations, is introduced by Paffenholz and Kutterer (2008). This approach exploits the constant rotation of the laser scanner around its vertical axis for the position and, moreover, the orientation determination (cf. Section 5.1). An uncertainty assessment is given by the authors which states that the uncertainty of the orientation determination by means of GNSS positions (determined in post-processing) results in a metric uncertainty of 1 cm for an object at the distance of 30 m.

Mohamed and Wilkinson (2009), Wilkinson and Mohamed (2009) and Wilkinson et al. (2010) utilise two GNSS antennas mounted on top of the laser scanner to derive the position and orientation. The static GNSS data is acquired for a specific number of stops beforehand or after the laser scanner's data acquisition. In their investigations, they question the feasible number of angular stops to obtain reliable results for the orientation angle which was addressed in simulations and field measurements. For the determination of the rotation angle is proposed to use skew-symmetric rotation matrix formulation due to levelling and aligning the system with north (Wilkinson et al., 2010). The authors state a precision of the orientation angle of about  $0.05^\circ$  for their dual-antenna apparatus mounted on the scanner's head.

The determination of six DoF, i. e., the transformation parameters, is also a typical task in robot applications in industrial environments. Hennes and Richter (2008, 2009) as well as Hennes (2010) report on their instrumental solution for high-precise and near real-time determination of the six DoF. The authors see the predominant field of application in industrial applications to extend the workspace of high-precise close-range laser scanner. The solution is based on a circular rotating adapter with an attached prism. The prism is tracked by 3D positioning sensors with polar measuring principle (e. g., total station or laser tracker). The prism describes a 3D circle which is suitable to obtain the transformation parameters. The position and orientation are determined in a similar manner to the approach by Paffenholz and Kutterer (2008).

**Concluding remarks:** The direct geo-referencing enhances the efficiency of the field work flow due to a reduced number of control points or even the waiver of all control points. It is noteworthy that direct geo-referencing does not require overlapping regions for two 3D point clouds which also optimises the work flow. The use of only physically attached sensors to the laser scanner is advantageous in contrast to approaches using



additional backsight targets. It can be stated that without additional targets in the scanning scene the target detection aspects (including their error budget) are obsolete. Also the task of target placement as well as position determination is minimized. Then the geo-referencing procedure totally relies on the physically attached sensors to the laser scanner. To consider the reliability of the position and orientation of the two approaches the use of a single backsight target for the orientation determination (Reshetyuk, 2010b) is disadvantageous and less reliable compared to the use of multiple positions for the orientation calculation (Paffenholz and Kutterer, 2008, Wilkinson et al., 2010). The provided point accuracies for the used laser scanners by the aforementioned authors is comparable.

In case of real-time availability of the transformation parameters, on-site statements on completeness and uncertainties of single 3D point clouds and the entire scanning project can be given.

It can be summarised that the further development of the proposed approaches by Paffenholz and Kutterer (2008) and Wilkinson et al. (2010) are an appropriate choice for solving the direct geo-referencing of 3D point clouds as will be presented in Chapter 4.

### 2.2.3. Registration of 3D point clouds by means of matching algorithms

Matching algorithms are frequently used to obtain the transformation parameters (cf. Eq. 2.7) of partially overlapping 3D point clouds. In general, two distinct categories can be identified those utilising points and features, respectively. The Iterative Closest Point (ICP) algorithm (Besl and McKay, 1992) and its variants (Rusinkiewicz and Levoy, 2001) are prominent methods within the point-based category. Feature-based algorithms are widely applied to intensity or RGB values of digital images such as Scale-Invariant Feature Transform (SIFT) by Lowe (2004) and Speeded-Up Robust Features (SURF) descriptor by Bay et al. (2008).

Several research studies address the feature-based registration of 3D point clouds by means of the aforementioned SIFT and SURF methodology. Either reflectance images (which are characterised by the intensity return of laser beam for 3D point clouds) or co-registered digital camera images are utilised for the feature extraction. Böhm and Becker (2007) report on the application of the SIFT algorithm on a reflectance image. The extracted features are used to compute the rigid body transformation for the pair-wise registration of 3D point clouds. This methods does not demand markers in the scene and is also applicable to orient digital images with respect to the 3D point cloud. An automatic procedure for co-registration of two types of images, laser scanner's range images and images of digital cameras, is proposed by González-Aguilera et al. (2009). Shahzad and Wiggenhagen (2010) report on the co-registration of the laser scanner's intensity images and photographic images which are captured by a hand-held digital camera using scale invariant features. Barnea and Filin (2007) make use of extracted features of co-registered camera images for the 3D point cloud registration. The camera is attached to the laser scanner's body. The author's feature extraction is based on the SIFT methodology. More recently, Alba et al. (2011) introduce an automated methodology for registration of 3D point clouds based on panoramic images from intensity values or co-registered camera images. Furthermore, Weinmann and Jutzi (2011) and Weinmann et al. (2011) present approaches for automatic registration based on both the range information and the reflectance images of 3D point clouds. A résumé of range-based or image-based registration can be found in Weinmann et al. (2011) .

Moreover, methods exist which make use of geometric primitives as features for the registration of 3D point clouds. For instance, Rabbani et al. (2007) use planes, spheres, cylinders and tori for registration purposes. These geometric primitives are common in industrial scenes. Brenner et al. (2008) investigate two different methods for determination of the coarse orientation of 3D point clouds in urban areas. One approach makes use of extraction and assignment of planar patches. While the other approach utilises the normal distributions transform, known from the robotics domain. Further developments of the former approach are published by Dold (2010). Abmayr (2010) propose the registration of multiple 3D point clouds based on the 3D geometry of extracted features and additional external sensor readings of an electronic spirit level. The findings show a better performance while using the 3D geometry in the matching process in contrast to SIFT-based matching.

---

**Algorithm 2.1:** ICP algorithm (Besl and McKay, 1992, Nüchter, 2009, pp. 35 ff., modified).

---

```

1 Input:  $\mathbf{p}_j^1 \in pc^1$ ,  $\mathbf{p}_k^2 \in pc^2$ , initial transformation parameters  $\mathbf{R}_{1,0}^2$  and  $\mathbf{t}_{1,0}^2$ 
2 for  $i = 0$  to  $maxIter$  do
3   foreach  $\mathbf{p}_k^2 \in pc^2$  do
4     Utilise kd-tree to find the closest point  $\mathbf{p}_j^1 \in pc^1$  within a range  $d_{max}$  for  $\mathbf{p}_k^2 \in pc^2$ .
5     Set flag  $w_{j,k} = 1$  for corresponding point pairs within a range  $d_{max}$ , otherwise  $w_{j,k} = 0$ .
6     Calculate transformation that minimises  $Er(\mathbf{R}_{1,i+1}^2, \mathbf{t}_{1,i+1}^2) = \sum_{j=1}^{n_{pc^1}} \sum_{k=1}^{n_{pc^2}} w_{j,k} \cdot \|\mathbf{p}_j^1 - (\mathbf{R}_{1,i}^2 \cdot \mathbf{p}_k^2 + \mathbf{t}_{1,i}^2)\|^2$ ,
7     where  $Er(\cdot)$  is the error function as well as  $n_{pc^1}$  and  $n_{pc^2}$  are the number of points in  $pc^1$  and  $pc^2$ .
8     Apply transformation parameters obtained in Line 6 to entire data set  $pc^2$  by means of Eq. 2.7.
9     if  $\|Er(\mathbf{R}_{1,i+1}^2, \mathbf{t}_{1,i+1}^2) - Er(\mathbf{R}_{1,i}^2, \mathbf{t}_{1,i}^2)\| < \epsilon$  then terminate
10 Output:  $\mathbf{R}_{1,i+1}^2$ ,  $\mathbf{t}_{1,i+1}^2$ 

```

---

Recently, Schenk and Hanke (2011) illustrate a robust and automated registration approach for 3D point clouds based on genetic algorithms. The present approach does not require artificial targets and was tested in a cave environment in which traditional target-based methods reach their limits.

**An overview of matching algorithms, which utilises the ICP and its variants** (e. g., Besl and McKay, 1992, Chen and Medioni, 1992, Zhang, 1994) is given in the following due to their later usage in this thesis (Section 5.3). For the 3D point cloud registration in computer vision and in the last decade in TLS applications as well have been widely used ICP based matching algorithms, refer for instance to Rusinkiewicz and Levoy (2001), Grün and Akca (2005) and Bae and Lichti (2008) for a comprehensive review.

Alg. 2.1 presents the basic idea of the ICP algorithm, which is to use pairs of nearest-neighbourhood points in two 3D point clouds,  $pc^1$  and  $pc^2$ , and to estimate the rigid body transformation (Eq. 2.7) in order to align the 3D point clouds. The estimated transformation aims to minimise the sum of squared distances between the corresponding point pairs, also referred to as error function (Alg. 2.1, Line 6). The transformation parameters are iteratively estimated until certain convergence criteria  $\epsilon$  are satisfied. The distance between the final selected points with consideration of error sources in measurements is usually used as convergence criterion (e. g., Bae, 2006). The Singular Value Decomposition (SVD) method and least-squares adjustment with conditions, also known as Gauss-Helmert Model (GHM) (Section A.2), are frequently used for the estimation of the transformation parameters.

The search of corresponding point pairs in an automated manner is one of the most challenging tasks. By means of neighbourhood search structures, such as the k-Dimensional Binary Search Tree (kd-tree), based on either the Euclidean or the Mahalanobis distance, an efficient way of finding the closest point pairs in  $pc^1$  and  $pc^2$  is given. Besides the chosen threshold value to define the closest distance, the amount of points in the 3D point cloud influences the overall execution time of the ICP algorithm. Jost and Hügli (2003) discuss aspects of modifying the threshold value within the iteration steps. In addition, they point out further methodologies for the search of corresponding point pairs. For the identification of incorrect correspondences, several heuristic methodologies have been developed. A simple and effective approach is the analysis of the distance between corresponding points and their rejection according to an appropriate threshold (e. g., Zhang, 1994). More sophisticated approaches (e. g., Bae and Lichti, 2008, Williams and Bennamoun, 2001) analyse the geometric properties (such as the normal vector) of the 3D point clouds within the correspondence search.

An ICP variant which uses the distances from point-to-plane (in direction of the surface normal vector) instead of the nearest point-to-point distances is proposed by Chen and Medioni (1992). One drawback of this approach is the requirement for a good initial alignment of the 3D point clouds (Bae, 2006, Bae and Lichti, 2008). The variant named Geometric Primitive ICP with the Random Sample Consensus (RANSAC) for automated pair-wise registration of 3D point clouds is proposed by Bae and Lichti (2008). The authors use the change of

geometric curvature, approximate normal vectors of the surface and the variance of the estimated normal vectors for the search of corresponding point pairs. To validate the accuracy of the registration error, the positional uncertainty (cf. Section 2.3.3) is used. In order to minimise the registration error an outlier removal procedure based on the positional uncertainty with the RANSAC is implemented.

A multi-view registration algorithm named the iterative mean point as well as a pair-wise registration algorithm with consideration of an anisotropic Gaussian error model is developed by Gühring (2001). Another approach for simultaneous registration of multiple 3D point clouds using SVD to obtain optimal transformation parameters is proposed by Williams and Bennamoun (2001). In addition, the authors suggest the use of robust estimators, e.g., the M-estimator, to handle outliers in the data sets. Beinat and Crosilla (2002) use the generalised Procrustes analysis technique for a simultaneous global registration of multiple 3D point clouds. The Procrustes analysis technique is also characterised by the use of SVD for the estimation of transformation parameters. The proposed method allows for a generalised factored stochastic model with consideration of isotropic and complete anisotropic error conditions. A 3D least-squares matching based on a generalized Gauss-Markov Model (GMM) for 3D surfaces and curves is introduced by Grün and Akca (2005). More recently, Habib et al. (2010) and Al-Durgham et al. (2011) propose ICP-based approaches utilising triangular patches for simultaneous point cloud registration.

**The consideration of uncertainty measures within ICP based matching algorithm** or generally in the registration process is a beneficial way to improve the final transformation results. Pennec and Thirion (1997) investigate several methods for estimation of rigid transformation parameters and develop an assessment for verification of the accuracy of the transformation parameters. The authors use an Extended Kalman Filter (EKF) framework for the evaluation of the 3D rigid motion and their Variance Covariance Matrix (VCM) for 3D matched points or frames. The weighting of corresponding point pairs according to the uncertainty in point-to-plane distances is discussed by Rusinkiewicz and Levoy (2001). A method which takes into account the anisotropic measurement errors in the viewing direction while registering two range images is proposed by Okatani and Deguchib (2002).

The estimation of a proper uncertainty measure is essential for the consideration of positional uncertainty within the registration. Therefore, the error budget of laser scanners is thoroughly reviewed in Section 2.3.2 and the topic of positional uncertainty is pointed out in Section 2.3.3. Turning to the consideration of uncertainty measures within ICP based matching algorithms a literature review can be found for instance in Bae and Lichti (2008) and Bae et al. (2009). In most approaches (e.g., Pennec and Thirion, 1997) the laser scanner measurements are interpreted as a stochastic process with a three-dimensional, isotropic and zero-mean Gaussian probability density function (Bae and Lichti, 2008). Beinat and Crosilla (2002), Gühring (2001) and Williams (2001) also propose least-squares based approaches with anisotropic error analyses.

#### 2.2.4. Sensor candidates for a direct geo-referencing procedure

This section aims to outline the sensor candidates for direct geo-referencing of 3D point clouds which are obtained by stationary laser scanners. Fig. 2.2 categories the possible sensors with respect to the required transformation parameters. Taking the findings of Section 2.2.2 into account, the eligible sensors must be capable to continuously provide position and/or orientation information. The uncertainty of these position and orientation information mainly defines the accuracy of the later geo-referenced 3D point clouds. To fulfil the uncertainty requirements of typical applications of geo-referenced 3D point clouds (e.g., as-built and cultural heritage documentation, facility management, construction engineering, navigation applications and forensic investigations), the single position and single azimuthal orientation should be observed within an uncertainty of  $\leq 1$  cm and  $\leq 0.2^\circ$ , with an assumed significance level of 95%. Moreover, the sensors should be able to form an integrated system, called MSS, with the laser scanner as core unit. In the MSS the advantage of each sensor can be used to contribute to a superior task, i.e., the direct geo-referencing. Based on the sensors introduced

below, the specific choice of sensors (in terms of manufacturer and type) for the direct geo-referencing approach, is presented in Section 4.2.

The main field of application for the direct geo-referencing is seen by the author in outdoor environments. Therefore, the selection of sensors concentrates on those who were originally developed for outdoor usage. Nevertheless, on account of the recent developments and research activities treating the positioning and navigation in GNSS-challenged environments (e.g., Mautz et al., 2010, Moreira and Mautz, 2011), i.e., indoor positioning, the transferability to indoor applications is possible with a minimum effort. Mautz (2012) presents a broad overview of indoor positioning systems with the focus on such systems (iGPS, Locata system, Cricket ultra-sound system and a photogrammetric laser beam positioning system) with capabilities to achieve at least centimetre-level accuracy which is seen as a requirement for geodetic applications by the author. Blankenbach et al. (2009) report on their investigations of a prototype for a precise positioning and orientation by means of UWB technique. The achievable accuracy for position determination is stated with a few centimetres. A method utilising artificial generated magnetic fields for the position estimation is developed by Blankenbach and Norrdine (2010). For a first and unobstructed test scenario the authors report an accuracy of a few centimetres for ranges  $< 10$  m.

#### 2.2.4.1. 3D positioning sensors

The 3D positioning sensors: total station and GNSS equipment, with the primary task of position determination are introduced here. The latter will also be discussed in terms of their capability of orientation determination of mobile platforms by multiple antennas and receivers, respectively. Since both sensors are well-known for position determination their general properties and basic principles are only mentioned. Comprehensive background can be found in, e.g., Deumlich and Staiger (2002), Hofmann-Wellenhof et al. (2008), Joeckel et al. (2008) and Rüeiger (1996). The focus is on the errors induced by the special use in the desired 3D geo-referencing approach which exploits the rotation of the laser scanner about its vertical axis. In short, the position determination of objects, i.e., the laser scanner, in motion by 3D positioning sensors is reviewed.

**Total stations** are well-known in geodesy for the position determination by means of horizontal and vertical angle as well as slant range, i.e., polar elements. The standard usage in stationary applications for the determination of 3D positions which are signalled by prisms is state of the art since many years and therefore out of

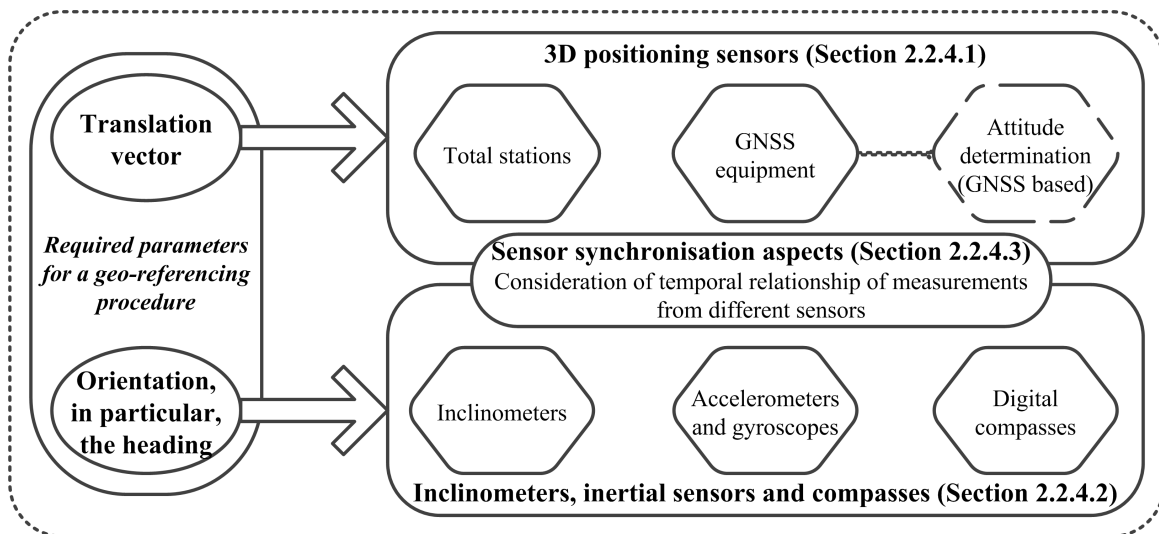


Figure 2.2: Sensor candidates for a direct geo-referencing procedure: Section 2.2.4.1 presents sensors with primary focus on position determination. Sensors, which are designed for orientation determination, are introduced in Section 2.2.4.2. Synchronisation aspects in MSSs are outlined in Section 2.2.4.3.

the scope of the subsequent discussion. The same is true for the well-known error sources of total stations for instance the axes errors as well as errors related to the EDM. The latter have been discussed in Section 2.1.3 due to the equal ranging principles of laser scanners and total stations. In fact, the robotic total stations are emphasised for an automatic and continuous data acquisition of moving objects, in this contribution a laser scanner. Main characteristics of robotic total stations are their automatic target recognition and tracking capabilities. Latest developments of total stations and discussions in terms of their accuracy and performance can be found in Zogg et al. (2009).

The kinematic mode of robotic total stations is also investigated more than one decade. Hennes (1999) discusses investigation methods of robotic total stations which are based on the well-known methods from the stationary usage but had to be extended on parameters of the kinematic usage. Stempfhuber (2004) investigates robotic total stations in terms of kinematic measurements like they are requested in machine guidance applications. One particular topic discussed by Stempfhuber (2004) is the aspect of timing of the angle and range measurements while tracking a moving object.

The standard prisms used for stationary targets are characterised by a limited aperture angle. They have to be aligned to the total station to perform the ranging. The correct mutual alignment of prism and total station is not always given in kinematic applications. Therefore, special prisms (called 360° prisms) are used. These 360° prisms overcome the limited aperture angle of standard prisms by their construction which allows the ranging from almost every direction. This special construction of the 360° prisms has an influence on the accuracy of the 3D point determination. This influence which depends on the prism's orientation is investigated by Favre and Hennes (2000). Recently, Horst and von Gösseln (2012) introduce an adaption with a standard prism which is also capable for the tracking of moving objects by total station measurements. To this end, the authors utilise a stepper motor with attached standard prism (named active prism) and wireless communication between the active prism and the total station. The consequent benefits of this active prism are seen in terms of accuracy, low costs and good efficiency in geodetic network measurements.

The evaluation of total station measurements towards a moving prism by means of a Kalman Filter (KF) is investigated by Gamse et al. (2010). The authors consider the fact of missing redundancy while observing kinematic processes by a single measurement system. To overcome the drawback of missing redundancy, the analysis is performed in a linear KF where indirect measurements (3D coordinates) and a discrete third-order kinematic model are used. The advantage of the chosen model is the capability of relating the process noise intensity to physical characteristics of the motion (Gamse et al., 2010).

**Global Satellite Navigation System equipment** is frequently used for positioning and navigation in outdoor environments. The terminology GNSS covers in general satellite-based positioning systems. Nowadays, the most important systems from a European perspective are: the Navigation Satellite Timing and Ranging GPS developed by the United States Department of Defence, the Globalnaja Nawigazionnaja Sputnikowaja Sistema (GLONASS) operated by the Russian military and Galileo which is the European system currently under configuration with two operational satellites<sup>3</sup>. For comprehensive background of the system architecture of the mentioned systems the reader is referred to the literature, e. g., Grewal et al. (2007), Hofmann-Wellenhof et al. (2008), Seeber (2003).

The satellite-based positioning is based on 3D resection utilising pseudoranges or pseudorange differences to satellites. Pseudoranges are composed of the geometric range plus a synchronisation error between the satellite clock and the receiver clock (Hofmann-Wellenhof et al., 2008). Regarding the observed pseudoranges, two different types are available per GNSS frequency: code pseudoranges  $PR$  and carrier phase measurements  $\Phi$ . Four visible satellites are required to determine the unknown 3D position of the antenna and the receiver clock bias. The position accuracy is affected by the accuracy of the pseudorange measurements and the satellite geometry

---

<sup>3</sup>Recent information regarding the Galileo system status can found on <http://www.esa.int/esaNA/galileo.html>, last accessed June 13th 2012.

(Hofmann-Wellenhof et al., 2008). The required satellite positions are calculated by their corresponding broadcast ephemerides. For high-accuracy positioning precise ephemerides and clocks are used which are provided by processing centres like, e. g., the International GNSS Service (IGS) and for combined GPS and GLONASS precise ephemerides from the Center for Orbit Determination in Europe (CODE) or European Space Agency (ESA) European Space Operations Centre (ESOC).

Three different positioning modes and therewith connected mathematical models exist (Hofmann-Wellenhof et al., 2008, Chapter 6): First, point positioning utilising a single receiver and observations to at least four satellites. Here two distinct variants have to be mentioned: those which only use pseudoranges and those using in addition carrier phase measurements as well as corrections from, e. g., the IGS (Kouba, 2009). The latter variant is termed Precise Point Positioning (PPP). Second, differential positioning by two or more receivers, one located at a known position and another one with unknown position. Between those receivers observation or position corrections are transmitted in real-time. Either to perform absolute point positioning with the corrected pseudoranges for the unknown position or to apply the transmitted position corrections. Third, relative positioning which describes the determination of an unknown position with respect to a known position. The positioning can either be performed for stationary and moving antennas. The former is referred to as static and the latter as kinematic positioning. In terms of the processing time is distinct between real-time processing and post-processing which yields the results in subsequent analyses. The former allows to obtain the positioning results without or only with slight delay.

The basic GNSS observation equation (Seeber, 2003, pp. 252 ff.) based on  $PR$  and  $\Phi$  between a satellite  $i$  and a site  $A$  is given as follows

$$PR_A^i = \rho_A^i + T_A^i + I_A^i + c \cdot (\delta t_A - \delta t^i) + d_A - d^i + \dots + \epsilon_A^i \quad (2.9)$$

$$\Phi_A^i = \rho_A^i + T_A^i - I_A^i + c \cdot (\delta t_A - \delta t^i) + \alpha_A - \alpha^i + PCC_A^i + \lambda \cdot N_A^i + \dots + \epsilon_A^{\prime i}. \quad (2.10)$$

All above given quantities are time-depended whereas for reasons of clarity the time index is not explicitly given. In both equations, the Euclidean distance between a satellite and the user site (antenna) is denoted by  $\rho_A^i = \sqrt{(X^i - X_A)^2 + (Y^i - Y_A)^2 + (Z^i - Z_A)^2}$  where the quantities are the satellite coordinates at the epoch of signal transmission and the site coordinates at the epoch of signal reception.  $T_A^i$  and  $I_A^i$  are the atmospheric propagation delays for the troposphere and ionosphere, respectively. The metric receiver clock errors are expressed by  $c \cdot \delta t_A$  and  $c \cdot \delta t^i$  for the receiver clock error of the epoch of signal reception and for the satellite clock error of the epoch of signal transmission. Hardware delays of the user site's receiver are termed  $d_A$  for  $PR$  and  $\alpha_A$  for  $\Phi$ . The satellite's hardware delays are given by  $d^i$  for  $PR$  and  $\alpha^i$  for  $\Phi$ . Observation noise is denoted by  $\epsilon_A^i$  and  $\epsilon_A^{\prime i}$ , respectively. In Eq. 2.10  $N_A^i$  is the integer number of ambiguities and  $\lambda$  represents the carrier wavelength. For the GPS, two signals, L1 and L2, are widely used which have slightly different frequencies and thus wavelengths. Phase Centre Corrections (PCC) of the receiver antenna are denoted by  $PCC_A^i$ . PCC cover a consistent set of Phase Centre Offsets (PCO) as well as their associated elevation and azimuth depending Phase Centre Variations (PCV) for each frequency and GNSS system. Eq. 2.9 and 2.10 contains the Euclidean distance and the basic systematic errors which have to be appropriately considered to avoid influences on the positioning. Depending on the analyses, network design and accuracy requirements further systematic effects have to be taken into account (cf. e. g., Hofmann-Wellenhof et al., 2008).

Uncertainties in GNSS measurements are composed of satellite specific, propagation specific and station/site specific error sources and furthermore their interaction contributes to the uncertainty. Typical numerical values of each specific error sources can be found in Seeber (2003, Chapter 7.4) or Hofmann-Wellenhof et al. (2008). To deal with satellite specific errors related to the satellite orbit and clock, products from aforementioned processing centres are used.

Propagation specific effects are mainly induced by atmospheric refraction, i. e., in the troposphere and ionosphere. They are accounted by appropriate corrections models (e. g., Klobuchar, Hopfield and Saastamoinen



(Hofmann-Wellenhof et al., 2008, p. 56). In Fig. 2.6 the cumulation of the PWU effect when an antenna is horizontally rotated about its vertical axis is depicted. The PWU effect can reach up to one full cycle due to the signal polarisation. The contribution of a horizontally rotating antenna with constant velocity to the PWU effect is linear in time and identical for all satellites visible in the topo-centre. Computing single-differences on a short baseline ( $\leq 1$  km), the net effect is constant for all satellites and thus it is absorbed in the receiver clock error. The identical remaining effect for all satellites after applying single-differencing is depicted in Fig. 2.6 for a short baseline of about 15 m.

The observation resolution (random noise) for classical geodetic receivers can be roughly assessed to 1% of the signal wavelength (Seeber, 2003, p. 323). For the GPS this leads to 300 cm and 30 cm for code measurements, which can be improved by specific receiver technology or smoothing techniques. In case of phase measurements, this results in 0.02 cm, if the integer number of ambiguities ( $N_A^i$  in Eq. 2.10) are solved.

For the adequate reduction and modelling of systematic effects (cf. Eq. 2.9 and 2.10), following approaches are suitable (Hofmann-Wellenhof et al., 2008, pp. 109 ff.): First, systematic effects can be eliminated by computation of linear combinations and differences of observations. Second, the application of deterministic correction models can reduce systematics. Third, the estimation of additional parameters in the adjustment process can be used for the modelling of systematic effects. Therefore, it is necessary to analyse the separability of parameters. Fourth, the error modelling by stochastic processes can allow for systematics. Here, the characterisation of the behaviour of errors types is necessary. The resulting uncertainty in GPS networks caused by remaining systematic errors is investigated by Schön and Kutterer (2006) within an interval approach.

Typically, for geodetic applications, phase measurements are used for static or kinematic positioning. The reason for that is the better resolution of phase measurements in terms of accuracy compared to code measurements. Mostly differential or relative positioning methods are used to benefit from range corrections provided by the known station or permanent station network in these methods. Comprehensive background on both methods and operators of permanent reference station networks can be found in Hofmann-Wellenhof et al. (2008), Seeber (2003). Typical accuracy levels for the positioning for different scenarios are also given in these references. For instance, utilising RTK-GPS (similar to differential GPS using phase measurements) for positioning, a rule of thumb for the achievable accuracy for horizontal coordinates is  $10 \text{ mm} + (1 - 2) \text{ ppm}$  and the height component results to  $15 - 20 \text{ mm} + 2 \text{ ppm}$  (Seeber, 2003, p. 338). Due to the various effects, such as baseline length, satellite constellation and analysis strategy, on the position accuracy the reader is referred to the literature for positioning accuracies in specific applications. Schön and Dilßner (2007) treat the challenges for GNSS-based positioning reaching high-accuracy level of  $< 1$  cm for the positioning. The authors present next to an overview investigations of signal multipath, signal diffraction and incompleteness of the stochastic model for GNSS observables.

**Attitude determination**, i. e., orientation determination of mobile platforms, is feasible using multiple GNSS equipments. In general, an azimuth or orientation angle in geodetic networks is calculated for a pair of 2D coordinates (forming a baseline) by means of the tangent function. This procedure is evaluated by Chang and Tsai (2006) to rapidly and precisely determine azimuth information utilising GNSS observations. The authors present results for different baselines with length of hundreds of metres to several kilometres and compare the GPS-based azimuths with astronomical azimuths.

The attitude parameters are the three rotation parameters (also referred to as roll, pitch, yaw (or heading)) of a specific body frame attached to a mobile platform with respect to a reference frame. Traditionally, these parameters are derived by measurements of IMUs (Hofmann-Wellenhof et al., 2008). The advancement of low-cost high-performance GNSS equipments foster the realisation of multiple antenna platforms consisting of at least three GNSS antennas with the aim of attitude determination. Also, multiple antenna platforms exist with high-cost geodetic equipments. The fundamental mathematical background can be found in, e. g., Hofmann-Wellenhof et al. (2008, pp. 441 ff.).



Eling et al. (2010) propose for baseline orientation calculation the use of a combination of a short ( $< \lambda_{GNSS}$ )<sup>4</sup> and a long ( $> 1$  m) baseline formed by three antennas in a row. The short baseline yields precise relative baseline parameter which are utilised to fix the ambiguities of the longer baseline. Conducted experiments by the authors delivered  $\sigma = 0.1^\circ$  for the baseline orientation, which results in a metric uncertainty of about 0.2 m in a distance of 100 m.

A sophisticated approach for precise attitude determination, i. e., GNSS compass, is presented by Teunissen (2010). The author develops a new integer least-squares theory for the GNSS compass model. His developed theory has no limitation in terms of the measurement scenario (e. g., dual-frequency GPS, multiple-frequency GNSS). Moreover, it is applicable to unaided, single-frequency, single-epoch GNSS attitude determination (Teunissen, 2010). The development and testing of a single-frequency GNSS carrier phase attitude determination method is treated by Teunissen et al. (2011). Several static and kinematic experiments were conducted. All of them show consistent results for the proposed method. In performed kinematic experiments with an aircraft, the baseline lengths are in a range of 4.9 – 7.6 m. The results for the direct GPS-derived aircraft attitude are compared against attitudes obtained from precise relative positioning of the aircraft’s antennas, where the differences are mostly within  $0.2^\circ$ . Also, the results are validated by a high-end IMU. For the GPS-IMU angular difference can be noted an empirical standard deviation for the heading of  $\sigma = 0.1^\circ$ .

#### 2.2.4.2. Inclinometers, inertial sensors and compasses

Inclinometers, inertial sensors and compasses are briefly introduced while the focus is on their provision for the orientation determination in the desired 3D geo-referencing approach. This introduction does not aim to provide in-depth fundamentals and discussion of various analyses strategies. The reader is referred to the literature, e. g., Grewal et al. (2007), Schlemmer (1996), Titterton and Weston (2004).

**Inclinometers** (also known as inclinations sensors or tilt meters) are frequently used in geodetic instruments for their orientation to the direction of gravity. Next to the integrated use in other sensors, they are used as stand-alone sensors for inclination determination of rigid bodies. Common in both cases is the measurement result what can be an inclination or inclination rate with respect to the direction of gravity. The inclination determination can be realised using liquids or pendulums. The former can be realised via levels or surfaces and the latter using horizontal or vertical pendulums. For the physical principle (resistive, optical, capacitive, inductive) of the measurement acquisition, the reader is referred to Schlemmer (1996). The used principle of inclination determination depends on the specific task and the requirements regarding robustness, resolution, measurement frequency and range. Especially in mobile applications the platform dynamics have to be carefully considered to obtain reliable results. Comprehensive investigations of static and dynamic properties of a variety of inclinometers are reported by Macheiner et al. (2009) and Woschitz (2009). About mobile platforms successfully utilising inclinometers is reported by, e. g., Neumann and Dennig (2011) and Vennegeerts (2011).

**The inertial sensors: accelerometers and gyroscopes,** represent together a typical IMU. The measurement quantities are in the former inertial accelerations and in the latter rotation rates. It is based on a measuring of attitude (expressed by roll, pitch, yaw (or heading)) rates and accelerations, starting from a known initial position, velocity and attitude. Its fundamental physical background is the fact that positions are the second integral of acceleration (Grewal et al., 2007). Small measurement errors in the attitude rates and accelerations accumulate due to the integration to obtain velocity and position. To account for drift effects, the IMU solution requires regular, external position or velocity updates by, e. g., GNSS equipment. For a comprehensive background of the sensor fusion approaches and the mandatory corrections among others due to the involved coordinate frames (e. g., inertial, body, reference and navigation frame), the reader is referred to, e. g., Grewal

<sup>4</sup> $\lambda_{GNSS}$  denotes the carrier wavelength of the GNSS signal.

et al. (2007) and Titterton and Weston (2004). IMUs are characterised by high update rates (up to 200 Hz and even more), which allows the observation of high platform dynamics typically occurring in airborne navigation or even terrestrial MMS applications. For the latter precise attitude is a requirement to obtain sufficient geo-referencing information (Barber et al., 2008). Optical gyros in form of ring lasers or fiberoptic gyroscopes are often used in high-end IMUs to obtain highest accuracy for the attitude and pendulous accelerations (Grewal et al., 2007). Thus, the assembly of those IMUs in small-scale MSS is challenging because of their overall size, weight consumption and original costs. Nevertheless, the Microelectromechanical Systems (MEMS) technology overcomes the aforementioned limitations and makes their use in small-scale and even hand-held devices possible. But it has to be considered that the MEMS based sensors provide in general considerably less accurate results compared to the aforementioned IMUs. For further reading is referred to, e.g., Grewal et al. (2007), Sternberg and Schwalm (2007) and Titterton and Weston (2004).

**Digital compasses** are sensors which provide heading information, generally the North direction is indicated. Two different types: magnetic and gyro compasses exist. The latter exploits the rotation of the Earth and aligns itself to true north (Grewal et al., 2007). The former utilises the Earth's magnetic field and aligns itself to magnetic north. Due to the saturation of the magnetic forces, magnetic compasses tend to disturbances induced by the environment. Nevertheless, both are frequently used in navigation or orientation of mobile platforms. For instance, Böhm and Haala (2005) make use of a magnetic compass for coarse alignment of a laser scanner. Also, several applications are reported in the field of personal navigation, e.g., Eglseer et al. (2010) and Grejner-Brzezinska et al. (2011).

#### 2.2.4.3. Sensor synchronisation with respect to time

Whenever multiple sensors are employed to gather data of a common phenomenon, the topic of synchronisation of the measurement quantities of the sensors arises. Thereby, the assembly of multiple (identical or different) sensors is referred as MSS and usually each sensor takes over a specific role. A MSS composed by a laser scanner and navigation sensors is assumed according to the thesis theme. In this context, spatial and temporal referencing with respect to a superior coordinate system and a common time reference, respectively, is necessary. This necessity becomes obvious, assuming MLS applications, which are characterised by a laser scanner on a platform in motion (i.e., MMS). The required synchronisation accuracy depends on the platform motion and the data acquisition rates of the involved sensors. Nevertheless, the synchronisation topic can also arise in direct geo-referencing of stationary laser scanners. The assignment of specific (geo-referencing) information to each data sequence (2D profile) of the 3D point cloud (gathered as sequence of numerous 2D profiles) is an example.

For positioning (i.e., spatial reference) in mobile and stationary scenarios, GNSS equipment is the sensor of choice. Besides the positioning capabilities, GNSS provides an adequate time reference by the GPS time (in the form of the GPS-Puls Per Second (PPS)). This time reference is implemented in several MMS (Barber et al., 2008, Puente et al., 2011). A thorough review of the time reference aspects in MSS environments is given for instance by Hesse (2007) and Toth et al. (2008).

The synchronisation can be practically realised based on either hardware or software. Three hardware-based synchronisation variants are discussed by Hesse (2007): First, the time pulse (e.g., the GPS-PPS) is incorporated in the data stream of the laser scanner. Second, a specific event pulse (e.g., rotation of the laser scanner's mirror) is recorded by the GNSS receiver event marker input and immediately assigned in the GPS time frame. Third, a separate device for synchronisation with optional A-D converter can be used, which is the most flexible solution for multiple sensor synchronisations and different signal types (analogous, digital). A software-based synchronisation approach of a laser scanner with position (GNSS equipment) and orientation (IMU) sensors is proposed by Vennegeerts et al. (2008). They exploit the constant rotation velocity of the vertical laser scanner mirror as clock. For the final synchronisation with the position and orientation information are extracted spatial information from the laser scanner data.

## 2.3. Uncertainty consideration in terrestrial laser scanning

This section aims to outline the error budget of TLS. As a reminder, the basics of measurement errors and the evaluation of uncertainties in measurements are introduced. The subsequent classification of the error budget of TLS concentrates on the errors and uncertainties related to 3D point clouds. The consideration of further post-processes like generation of arbitrary 3D models and evaluating their uncertainties is out of the thesis's scope.

### 2.3.1. Measurement errors and evaluation of uncertainties in measurements

Two classes of measurement errors can be found: those covering random errors and those covering unknown systematic errors. Random errors occur due to non predictable variations of influence factors caused by non reproducible and uncontrollable effects. Whereas systematic errors are reproducible but unknown effects which occur during measurements and are assumed to be constant at least in a specific time period. Systematic effects can be accounted by modelling of the parameters which describe the systematic behaviour or by application of suitable correction procedures. Calibration procedures of entire sensors or selected components are used for the determination of parameters to describe the systematic error component. On the contrary, random effects can be reduced by repeated measurements under same conditions and the subsequent use of averaging techniques (Grabe, 2005).

For the determination of uncertainties in measurements the Guide to the Expression of Uncertainty in Measurement (GUM) (ISO, 1995) is internationally accepted as standard. The GUM proposes two distinct categories of uncertainties according to their methods of evaluation: Type A and Type B. Traditional statistical methods are utilised for the determination of Type A. Type B is obtained by experiences with and expert knowledge about the sensor. Thereby, both types cover random and systematic effects (Koch, 2008b). For uncertainty determination, the GUM (ISO, 1995, p. 19) describes an approach which utilises the Law of Propagation of Uncertainties (LOP). In the LOP, standard uncertainties and correlation coefficients are associated with the input estimates to obtain the standard uncertainty of the measurement result. For non-linear models a linearisation using Taylor series expansion is required, what could be difficult for highly non-linear models (Hennes, 2007). Since the standard GUM framework uses only a measurement model linearised about the best available estimates of the input quantities (Alkhatib et al., 2009), results for strongly non-linear models will not be satisfied. To overcome this problem, the Extension of GUM (ISO, 2007) advises the propagation of uncertainties by means of probabilistic approaches. Monte Carlo (MC) techniques are used for this purpose. Aspects of differences between GUM (ISO, 1995) and its extension (ISO, 2007) are discussed for instance in Alkhatib et al. (2009). Hennes (2007) and Hennes and Heister (2007) discuss the usage of uncertainty measures in the engineering geodesy and explicitly recommend the usage of the GUM to provide reliable uncertainties for measurement results.

Koch (2008b) evaluates uncertainties in measurements by MC simulations. He discusses the measurement uncertainties in the context of the GUM. One outcome is that MC simulations can be utilised to obtain the variances, covariances and confidence intervals of the measurements, if measurement uncertainties are defined according to GUM. This approach is valid for various types of distributions, like trapezoidal, triangular and normal. A practical application to a TLS data set of a motorway is shown by the author to validate the theoretically developed approach. Koch (2008a) applies MC simulations to laser scanner measurements in order to determine the uncertainties of correlated measurements which are expressed by standard deviations and confidence intervals. The correlations of the laser scanner measurements are estimated from repeated observations. The author concludes that for a subset of the investigated measurements for distances, which are deduced from the coordinates, the correlations should be considered.

Alkhatib et al. (2009) report on the uncertainty modelling of random and systematic errors by means of MC and fuzzy techniques in the context of the GUM. The authors critically compare three approaches of uncertainty

modelling, namely the GUM, the probabilistic and the fuzzy-random approach, by a numerical example for a TLS application. For these approaches the distinction and specific handling of random and systematic errors is discussed in detail.

Three different approaches to compute uncertainties for large TLS data sets are investigated by Vennegeerts and Kutterer (2009). Two approaches utilise the unscented transformation and another one incrementally computes the uncertainties. The authors state the benefits of uncertainty information regarding data acquisition and interpretation.

Kutterer et al. (2010) utilise MC techniques for modelling and propagation of observation uncertainties. The authors investigate 2D profile laser scanner measurements of simulated and real scenarios. The findings are that a rather small number of input parameters for the uncertainty model are required to obtain simulation results which fit quite well to real data scenario.

Koch (2010) reports on applications of MC methods to quantify the uncertainty of results of TLS data with correlated systematic effects. Based on long time series of repetition the author determines uncertainty information caused by systematic effects in the measurements. The author's findings are that too optimistic uncertainties of the results can be avoided by the consideration of correlated measurements and correlated systematic effects.

### 2.3.2. Classification of the error budget in terrestrial laser scanning

The error budget of TLS can be distinguished in two main groups those covering internal and external sources (Lichti and Gordon, 2004). The authors denote by internal sources random errors related to the laser scanner and its measuring principles. The external sources are dedicated to random errors in both registration and instrument setup procedures. Gordon (2004) identifies six separate error sources: hardware, data, environmental, surface reflectance, target centroiding and geo-referencing errors. These six error sources can be merged following the classification proposed by Staiger (2005). This is also adopted by Reshetyuk (2009) and will be considered in the following.

**Instrumental** errors occur due to random and systematic errors in relation with the laser scanner hardware.

These are errors related to the ranging principle (Section 2.1.3) as well as the scanning mechanism and mechanical construction induced errors (Section 2.1.4) commonly referred to as axes errors (analogous to total stations). Schulz (2007) comprehensively investigates the well-known instrumental errors: eccentricities, wobble of rotation axes, error of collimation axis and error of tilting axis for one specific AM-CW laser scanner. Besides the beam divergence, the resolution of a laser scanner depends amongst others on the angular increments of the servo motors. The Boehler star is a further development of the Siemens star to investigate the resolution of laser scanners (Boehler et al., 2003). Some recent comparative investigations for different laser scanners on the market are reported by Huxhagen et al. (2011). A detailed literature review of the random and systematic errors in this group can be found in Reshetyuk (2009). To handle the systematic instrumental errors calibration approaches have been developed either for the entire laser scanner system or single components. For a review of laser scanner calibrations the reader is referred to Section A.3.

**Environmental** errors are caused by the atmospheric conditions, mainly dominated by air temperature, pressure and humidity, which influence the propagation of the laser beam. These resulting errors are tightly coupled with instrumental errors, i. e., the ranging principle. Furthermore, this group covers errors induced by the measurement environment for instance vibrations. The latter errors mentioned can be externally controlled with additional sensors.

**Object-related** errors result from the natural and man-made object surfaces which are characterised by, e. g., particular curvature, roughness, colour, reflection behaviour and incidence angle of the laser beam to the local object's surface. Several research studies address the investigations of errors in this group. For instance, Voegtle and Wakaluk (2009) report on effects on the measurements of a AM-CW laser scanner caused

by different object materials. For their investigations the authors used a variety of targets with different reflectivity common for urban environments scanned under a range of distances, incidence angles and ambient lighting and wetness conditions. Soudarissanane et al. (2009) develop a theoretical model of the incidence angle influence on the 3D point cloud quality. This model and the investigations are extended to the influence of the range on the quality of 3D point clouds by Soudarissanane et al. (2011). Their approach is validated by practical experiments and moreover it allows the optimisation of the laser scanner setup in advance to the measurements. The latter is discussed in a further publication by Soudarissanane and Lindenbergh (2011). Therein, the authors propose a method for an optimal view point determination which is based on incidence angle and range constraints as two uncorrelated factors.

**Geo-referencing** errors cover all errors associated with the mutual relative and absolute orientation of 3D point clouds. These errors depend on the used (indirect or direct) geo-referencing method. The error budget for directly geo-referenced 3D point clouds is investigated for instance by Lichti and Gordon (2004) and Reshetyuk (2009). A review in the context of the thesis's aim is given in Section 2.3.4.

The above discussed errors are merged in two groups, for ease of understanding, according to Lichti and Gordon (2004). The first group contains the instrumental, environmental as well as object-related errors and is referred to as *positional uncertainty*. The second group includes the uncertainties evoked by geo-referencing errors and is termed as *transformational uncertainty*.

### 2.3.3. Positional uncertainty

In this section the reader is familiarised with the calculation of positional uncertainty measures. The positional uncertainty of 3D point clouds from laser scanners is a function of at least the incidence angle of the laser beam to the object's surface as well as the range and angular uncertainties of the laser scanner (Lichti, 2007, Schulz, 2007).

The incidence angle is defined as angle between laser beam direction and surface normal vector. Owing to this definition, the positional uncertainty is affected by the estimation of the surface normal vector and its variance. On the one hand, this influence on the positional uncertainty can be considered by the variance of the estimated normal vector in the calculation of positional uncertainty (Bae et al., 2009). On the other hand, the calculations can be limited to planar regions because in those regions the variance of the estimated surface normal vector is small with respect to the neighbourhood size (Bae et al., 2009). For the separation of a 3D point cloud in planar and non-planar regions an appropriate threshold, like the geometric curvature as a parameter of the 3D point cloud, is required (Bae and Lichti, 2008). For environments with a lack of planar surfaces or for warped object surfaces (e. g., vegetation environments), the variance of the estimated surface normal vector has to be considered as a reliable positional uncertainty measure.

The derivation and calculation of positional uncertainty of 3D point clouds are presented by several researchers. Schaer et al. (2007) investigate the influence of the scanning geometry for airborne laser scanning data. Sur (2010) takes into account the uncertainty of 3D points in SIFT matching and 3D data fusion. Soudarissanane et al. (2009, 2011) model the influence of the incidence angle and the range on the 3D point cloud quality mathematically. In the following, the approach developed by Bae (2006) and Bae et al. (2009) will be summarised due to its use in this thesis. The fundamental equations for the positional uncertainty estimation are provided. For full and comprehensive mathematical derivation the reader is referred to the original publications.

**The covariance analysis for estimating surface normal vectors and the participating coordinate systems** are briefly introduced according to Bae and Lichti (2008) and Bae et al. (2009).

The Variance Covariance Matrix (VCM) of a subset of a 3D point cloud can be used for the estimation of the surface normal vector. This is feasible due to the equivalence of first order plane fitting and the eigenvalue problem of the VCM (Bae and Lichti, 2008). A subset of a 3D point cloud is given by a  $j$ th point  $\mathbf{p}_j$  and

its  $k$  nearest neighbour points within an appropriate neighbourhood radius  $r_{nh}$ . Typically, the value  $r_{nh}$  is heuristically chosen for the 3D point cloud. To obtain an optimal value for  $r_{nh}$ , for instance Demantké et al. (2011) propose a multi-scaled method. Based on the introduced subset, the VCM of  $\mathbf{p}_j$  results in

$$\boldsymbol{\Sigma}_{\mathbf{p}_j} = \frac{1}{k} \sum_{m=1}^k \bar{\mathbf{p}}_m \cdot \bar{\mathbf{p}}_m^T = \sum_{i=0}^2 \lambda_i \cdot \hat{\mathbf{e}}_i \cdot \hat{\mathbf{e}}_i^T. \quad (2.11)$$

In Eq. 2.11,  $\bar{\mathbf{p}}_m = \mathbf{p}_j - \mathbf{p}_{centroid}(\mathbf{p}_j)$  where  $\mathbf{p}_{centroid}(\mathbf{p}_j)$  is the centroid of  $\mathbf{p}_j$  and its  $k$  neighbour points.  $\hat{\mathbf{e}}_i$  denotes the eigenvector of the  $(i+1)$ th smallest eigenvalue  $\lambda_i$ . The desired surface normal vector  $\hat{\mathbf{n}}$  formed by the subset of  $\mathbf{p}_j$  and its neighbourhood, is the eigenvector of the smallest eigenvalue, i. e.,  $\hat{\mathbf{e}}_0$  and the tangential vectors correspond to  $\hat{\mathbf{e}}_1$  and  $\hat{\mathbf{e}}_2$ .

The main coordinate systems, which are involved with 3D point clouds in terms of positional uncertainty, are: the  $L$ -frame (Section 2.2.1) and the individual point coordinate system termed  $P$ -frame<sup>5</sup>. Based on the eigenvectors obtained by Eq. 2.11, the rotation  $\mathbf{R}_P^L \in \mathbb{R}^{3 \times 3}$  of the  $P$ -frame with respect to the  $L$ -frame is defined by

$$\mathbf{R}_P^L = [\hat{\mathbf{e}}_0 \quad \hat{\mathbf{e}}_1 \quad \hat{\mathbf{e}}_2]^T. \quad (2.12)$$

With Eq. 2.12, the transformation of points  $\mathbf{p}_j$  in the  $L$ -frame to the  $P$ -frame is performed by

$$\mathbf{p}_j^P = \mathbf{R}_P^L \cdot \mathbf{p}_j^L. \quad (2.13)$$

The transformation of the VCM  $\boldsymbol{\Sigma}_{\mathbf{p}^P}$  obtained in the  $P$ -frame (Eq. 2.15) to the  $L$ -frame is given by

$$\boldsymbol{\Sigma}_{\mathbf{p}^L} = \mathbf{R}_P^L \cdot \boldsymbol{\Sigma}_{\mathbf{p}^P} \cdot (\mathbf{R}_P^L)^T. \quad (2.14)$$

**The calculation of positional uncertainty** by means of Eq. 2.12 – 2.14 is summarised in Alg. 2.2 for a point cloud  $pc(\mathbf{p}^L)$ . The diagonal elements of the VCM of a point in a closed-form  $\boldsymbol{\Sigma}_{\mathbf{p}^P} \in \mathbb{R}^{3 \times 3}$  are given by the approximation (Bae et al., 2009)

$$\begin{aligned} \boldsymbol{\Sigma}_{\mathbf{p}^P}^{11} &\simeq (\hat{\mathbf{e}}_0, \boldsymbol{\Sigma}_{\mathbf{p}^{laser}} \hat{\mathbf{e}}_0) = \cos^2(\theta_0) \cdot \sigma_\rho^2 + \sin^2(\theta_0) \cdot \rho^2 \cdot \sigma_a^2, \\ \boldsymbol{\Sigma}_{\mathbf{p}^P}^{22} &\simeq (\hat{\mathbf{e}}_1, \boldsymbol{\Sigma}_{\mathbf{p}^{laser}} \hat{\mathbf{e}}_1) = \cos^2(\theta_1) \cdot \sigma_\rho^2 + \sin^2(\theta_1) \cdot \rho^2 \cdot \sigma_a^2, \\ \boldsymbol{\Sigma}_{\mathbf{p}^P}^{33} &\simeq (\hat{\mathbf{e}}_2, \boldsymbol{\Sigma}_{\mathbf{p}^{laser}} \hat{\mathbf{e}}_2) = \cos^2(\theta_2) \cdot \sigma_\rho^2 + \sin^2(\theta_2) \cdot \rho^2 \cdot \sigma_a^2. \end{aligned} \quad (2.15)$$

In Eq. 2.15  $\boldsymbol{\Sigma}_{\mathbf{p}^{laser}} \simeq \text{diag}(\rho^2 \cdot \sigma_a^2, \rho^2 \cdot \sigma_a^2, \sigma_\rho^2)$  denotes the positional uncertainty of a point in the local laser beam coordinate system and  $\rho$  is the range measure of the laser scanner towards the object.  $\sigma_\rho$  and  $\sigma_a$  denote the range and angular uncertainties of the laser scanner.  $\theta_{i=0..2}$  are the directional cosine angles of the laser beam relative to the local surface (Bae, 2006, Bae et al., 2009). By  $\hat{\mathbf{e}}_0$  is given the surface normal vector and  $\hat{\mathbf{e}}_{i=1,2}$  are the tangential vectors which are on the local surface of a point.

The approximate for the VCM in Eq. 2.15 neglects the effect of the variance of the estimated surface normal vector. The limitation of the calculations only for points in planar regions justifies this approximation. As aforementioned, the variance of the estimated surface normal vector is assumed to be small in planar regions. Regarding the use of a diagonal VCM is noteworthy that the Cartesian coordinates of a point calculated from the initial spherical coordinate measurements of a laser scanner may have small correlation among the  $x$ -,  $y$ - and  $z$ -components. To recover the true correlation between the spherical coordinate measurements separate investigations and calibrations of the laser scanner are required. It may be possible to empirically estimate the true correlation between the observed Cartesian coordinates from a least-squares method. A low correlation among the  $x$ -,  $y$ - and  $z$ -components of one measurement is not essential to justify the use of Eq. 2.15. Hence,

<sup>5</sup>The individual point coordinate system is termed  $\mathbf{O}_{point}$  in Bae et al. (2009, Figure 2).

---

**Algorithm 2.2:** Calculation of positional uncertainty (Paffenholtz and Bae, 2012, modified).

---

```

1 Input:  $pc(\mathbf{p}^L)$ 
2 foreach  $\mathbf{p}^L \in pc$  do
3   Calculate  $\Sigma_{\mathbf{p}^L}$  Eq. 2.11
4   Store  $\overline{pc}(\overline{\mathbf{p}}^L)$  with geometric curvature
5   Store eigenvectors of  $\Sigma_{\overline{\mathbf{p}}^L}$  Eq. 2.12
6   Obtain  $\overline{\mathbf{p}}^P$  Eq. 2.13
7   Calculate  $\theta_{i=0..2}$  for  $\overline{\mathbf{p}}^P$ 
8   Calculate  $\Sigma_{\overline{\mathbf{p}}^P}$  Eq. 2.15
9   Obtain  $\Sigma_{\overline{\mathbf{p}}^L}$  Eq. 2.14
10 Output:  $\overline{pc}(\overline{\mathbf{p}}^L)$  (with only planar regions) and corresponding positional uncertainty  $\Sigma_{\overline{pc}(\overline{\mathbf{p}}^L)}$ 

```

---

in case of dealing with registration tasks, a low correlation is necessary for selected points, which are measured from different sites of the laser scanner (Paffenholtz and Bae, 2012).

#### 2.3.4. Transformational uncertainty

This section is devoted to the errors related to the direct geo-referencing method. For sake of completeness is referred, for instance, to Gordon (2004) for the error budget of the indirect geo-referencing approach. The error budget of the direct geo-referencing of 3D point clouds using an additional backsight target is outlined according to the publications by Lichti and Gordon (2004), which is also followed by Scaioni (2005) and Reshetyuk (2009). Lichti and Gordon (2004) thoroughly investigate the error budget in direct geo-referencing of 3D point clouds. The authors focus in their analysis on the random error sources. The following error sources are identified (Lichti and Gordon, 2004): the position determination for the laser scanner as well as the backsight target by, e. g., a total station, levelling and centring of the laser scanner, centring of the backsight target, the angular and range uncertainty of the laser scanner measurements as well as the influence induced by the laser beamwidth. The authors provide the fundamental equations for each error source. The VCM for 3D points can be obtained by propagation of the random errors through the functional model. Depending on the manner of establishing the laser scanner's orientation different errors occur either by optical pointing or the target detection procedure (Gordon and Lichti, 2004, Reshetyuk, 2009). It is important to mention that the uncertainty of the laser scanner measurements (angular and range) as well as the influence caused by the laser beamwidth are considered in this thesis as instrumental errors and therefore covered by the positional uncertainty.

The remaining error sources are discussed in terms of their influence on the estimation of the transformation parameter, i. e., translation vector and rotation matrix. The translation vector (also referred to as laser scanner position) uncertainty is influenced by man-made errors due to the laser scanner levelling and the optical centring. The horizontal angle is influenced by both while the vertical angle is only influenced by the latter (Lichti and Gordon, 2004). It is worth noting that modern laser scanners even provide electronic spirit levels and compensators to minimise or mathematically correct these errors. Furthermore, the uncertainty of the known position and possible eccentricities (e. g., instrument height) or even the uncertainty induced by an independent surveying of an unknown position (by external sensors like GNSS equipment or total stations) contributes to the translation vector uncertainty. Thus, the laser scanner position determination is independently from the manner of obtaining the orientation, i. e., the use of backsight targets.

The laser scanner orientation, encapsulated in the rotation matrix, is obtained by the laser scanner position and the backsight target position. Thus, both positions contribute to the uncertainty. This contribution is twofold: First, the position determination as discussed in the preceding paragraph. Second, the uncertainty induced by the telescope pointing or by the target detection method, depending on the applied approach. Hence, the orientation uncertainty is correlated with the uncertainty of the positions, the distance between the laser

scanner and the backsight target (Reshetyuk, 2009) as well as the telescope pointing or target detection error. The variance of the azimuthal orientation can be obtained by the variance propagation of the uncertainties for the laser scanner and backsight target positions through the arctangent function (Lichti and Gordon, 2004).

The direct geo-referencing approaches without the necessity of control points in the scanning scene have error sources similar to the indirect approach in terms of unknown position determination. Though, the only position to determine is the laser scanner position itself, which is obtained by external sensors (attached to the laser scanner). This procedure dominates the uncertainty in this case. Their magnitudes depend on the used acquisition method, e. g., GNSS equipment or total station, and the post-processing steps for instance applying filtering techniques. Eccentricities are present in this approaches as well. They occur due to the mounting of the 3D positioning equipment (e. g., GNSS antenna or prism) on the scanner.

The uncertainty of the orientation is also dominated by the external sensor measurements. Depending on the used equipment (cf. Section 2.2.4.2), the uncertainty is directly related to the sensor for instance when using compasses or IMUs. Otherwise the uncertainty is a result of post-processing steps like the calculation of the azimuthal orientation when using a backsight target. In contrast to the method using backsight targets this approaches are not influenced by errors due to telescope pointing or target detection methods. Moreover, the redundancy increases since these approaches generally utilise multiple sensor measurements, i. e., 3D positions, for the orientation determination. Wilkinson et al. (2010) report a value of about  $0.05^\circ$  for the orientation angle precision in their conducted experiments.



### 3. Basics of discrete-time recursive state-space and transversal filtering

In this chapter the fundamentals of discrete-time recursive state-space filtering and transversal filtering used throughout this thesis are introduced. In Section 3.1 the basics of recursive parameter estimation are summarised. In Section 3.1.1 and Section 3.1.2, the reader is reminded of the Gauss-Markov Model (GMM) and the Gauss-Helmert Model (GHM). The recursive least-squares estimation in the GMM is outlined in Section 3.1.3. The transformation of a GHM into an equivalent GMM and the parameter elimination in GMM are briefly summarised in Section 3.1.4 and Section 3.1.5.

Recursive state-space filtering is thoroughly discussed in Section 3.2. In particular, the Kalman Filter (KF) (Kalman, 1960) is treated, one of the well-established representative of recursive state-space filters. The reader is familiarized with its mathematical fundamentals in Section 3.2.1. KF variants with regard to non-linearities in the state-space equations (like the Extended Kalman Filter (EKF)) are considered in Section 3.2.2. It is worth to note that non-linearities often occur in the motion modelling of platforms. The optimum smoothing problem in the KF framework is outlined in Section 3.2.3. Further enhancements of the KF by means of joint estimation of state and adaptive parameters as well as the use of constraints are outlined in Section 3.2.4 and Section 3.2.5.

Transversal prediction and filtering by means of Least-Squares Collocation (LSC) is outlined in Section 3.3. In Section 3.3.1, the reader is familiarised with the estimation of appropriate covariance functions which are needed to complete the stochastic model of the LSC. The solution of LSC by means of GHM is presented in Section 3.3.2.

All here introduced recursive state-space filtering approaches are used for the proposed methodology for direct geo-referencing purposes in Chapter 5. The outlined transversal filtering approach is used for data analyses purposes in Chapter 6.

#### 3.1. Recursive parameter estimation

This section introduces the recursive parameter estimation as special case of recursive state-space filtering. Based on the fundamentals of the linear GMM, the recursive least-squares estimation in GMM is presented. This recursive parameter estimation is meaningful if the same set of parameters are to be estimated from an appropriate subset of observations, rather than waiting until all observations are gathered. Also, this recursive manner is well-suited for real-time applications. In this thesis parameters are estimated in a recursive manner to make them available even before all data are processed (by running parallel algorithms) as well as to reduce the dimension of the equation systems due to large number of observations. The following situation is given: 3D GNSS positions with a data rate of 10 Hz are available for a period of 15 minutes, which results in 9000 observations for each coordinate component. Furthermore, the functional model of a circle is given, which allows the parameter estimation by means of a subset of observed positions. Then the recursive parameter estimation can be applied to reduce the equation systems and therewith the computational costs.

The circle estimation is taken up and more specified hereafter. The unknown parameters are the centre point  $\mathbf{p}^{cp} = [x^{cp} \ y^{cp}]^T$  and the radius  $r$ . The equation of a circle

$$(x_j - x^{cp})^2 + (y_j - y^{cp})^2 = r^2 \quad (3.1)$$

connects these unknown parameters and the observed  $j$ th point position  $\mathbf{p}_j = [x_j \ y_j]^T$ . This functional relation is characterised by non-separability of parameters and observations. Therefore, this adjustment problem is solved by the general case of least-squares adjustment, also known as GHM, instead of GMM. To take advantage of the benefits of recursive parameter estimation, the transformation of the GHM into an equivalent GMM is helpful. The transformed model is characterised by two groups of observations and parameters, respectively. Whereas one parameter group denotes the original parameters and the other one covers one observation group (cf. Section 3.1.4). Thus, the requirement of the same set of parameters is unfulfilled. To comply with the requirement, the group of changing parameters can be eliminated by proper algorithms. The parameter elimination in GMM (cf. Section 3.1.5) is well-known in the adjustment of geodetic networks. Here, typically orientation unknowns of angle measurements are eliminated.

### 3.1.1. Gauss-Markov model

Suppose that we have the following non-linear GMM (Koch, 1999, pp. 153 ff.)

$$E\{\mathbf{y}\} = \mathbf{y} + \mathbf{v} = \mathbf{h}(\mathbf{x}) \quad \text{and the stochastic model} \quad \boldsymbol{\Sigma}_{\mathbf{y}\mathbf{y}} = \sigma_0^2 \cdot \mathbf{Q}_{\mathbf{y}\mathbf{y}} = \sigma_0^2 \cdot \mathbf{P}^{-1}, \quad (3.2)$$

where  $E\{\cdot\}$  denotes the expectation operator and  $\mathbf{h}(\cdot)$  is a real-valued differentiable function of the unknown parameter vector  $\mathbf{x} \in \mathbb{R}^{n_x}$ , with  $n_x$  number of unknown parameters. The observation vector is  $\mathbf{y} \in \mathbb{R}^{n_y}$ , with  $n_y$  number of observations, and  $\mathbf{v} \in \mathbb{R}^{n_y}$  denotes the corresponding measurement error (residual) vector. The quantities of the stochastic model of the GMM are the regular VCM  $\boldsymbol{\Sigma}_{\mathbf{y}\mathbf{y}}$  and cofactor matrix  $\mathbf{Q}_{\mathbf{y}\mathbf{y}}$  of observations with assumed zero-mean white Gaussian measurement noise.  $\sigma_0^2$  is the (unknown) variance of the unit weight and  $\mathbf{P}$  denotes the weight matrix of observations.

The non-linear model given in Eq. 3.2 can be linearised by means of Taylor series expansion first order which leads (Gelb, 1974)

$$\Delta\mathbf{y} + \mathbf{v} = \mathbf{H} \cdot \Delta\mathbf{x} \quad \text{with} \quad \Delta\mathbf{y} = \mathbf{y} - \mathbf{y}_0 \quad \text{and} \quad \mathbf{H} = \left. \frac{\partial \mathbf{h}}{\partial \mathbf{x}} \right|_{\mathbf{x}=\mathbf{x}_0}, \quad (3.3)$$

where  $\Delta\mathbf{y}$  is the truncated observation vector, which is obtained by approximate values  $\mathbf{y}_0$ , and  $\mathbf{H}$  is the full rank  $n_y \times n_x$  design (measurement) matrix, which contains the partial derivatives of  $\mathbf{h}(\cdot)$  with respect to  $\mathbf{x}$ .  $\Delta\mathbf{x}$  denotes the truncated parameter vector, which is obtained by approximate parameters  $\mathbf{x}_0$ . The linearisation is obtained by analytical approximation of the non-linear function  $\mathbf{h}(\cdot)$  in the expansion point of  $\mathbf{x}_0$ .

The classical least-squares parameter estimation in linearised GMM minimizes the weighted sum of squared residuals

$$\mathbf{v}^T \cdot \mathbf{P} \cdot \mathbf{v} \rightarrow \min. \quad (3.4)$$

The minimisation of the cost function in Eq. 3.4 provides the optimal solution for the unknown parameters<sup>1</sup>

$$\hat{\mathbf{x}} = \mathbf{x}_0 + \Delta\hat{\mathbf{x}} \quad \text{with} \quad \Delta\hat{\mathbf{x}} = (\mathbf{H}^T \cdot \mathbf{P} \cdot \mathbf{H})^{-1} \cdot \mathbf{H}^T \cdot \mathbf{P} \cdot \Delta\mathbf{y} = \mathbf{Q}_{\hat{\mathbf{x}}\hat{\mathbf{x}}} \cdot \mathbf{H}^T \cdot \mathbf{P} \cdot \Delta\mathbf{y}. \quad (3.5)$$

In Eq. 3.5  $\mathbf{Q}_{\hat{\mathbf{x}}\hat{\mathbf{x}}}$  denotes the corresponding cofactor matrix which can be derived by applying the LOP. The inverse  $(\mathbf{H}^T \cdot \mathbf{P} \cdot \mathbf{H})^{-1} = \mathbf{Q}_{\hat{\mathbf{x}}\hat{\mathbf{x}}}$  exists due to the positive-definite matrix  $\mathbf{P}$ . Otherwise the solution can be calculated by determining the generalised inverse (Koch, 1999, pp. 48 ff.).

### 3.1.2. Gauss-Helmert model

The non-linear GHM, also known as least-squares adjustment with conditions (Mikhail, 1976, pp. 213ff.)

$$\mathbf{f}(E\{\mathbf{y}\}, \mathbf{x}) = \mathbf{h}(\mathbf{y} + \mathbf{v}, \mathbf{x}_0 + \Delta\mathbf{x}) = \mathbf{0} \quad \text{and the stochastic model} \quad \boldsymbol{\Sigma}_{\mathbf{y}\mathbf{y}} = \sigma_0^2 \cdot \mathbf{Q}_{\mathbf{y}\mathbf{y}} = \sigma_0^2 \cdot \mathbf{P}^{-1}, \quad (3.6)$$

are given.  $\mathbf{f}(\cdot)$  denotes a real-valued differentiable function of  $\mathbf{x}$  and  $\mathbf{y}$  which is characterised by non-separability of both quantities: the observations and the parameters. The further quantities are defined according to Section 3.1.1.

The linearised functional model of the GHM, known as the condition equations, is given by

$$\mathbf{U} \cdot \mathbf{v} + \mathbf{H} \cdot \Delta \mathbf{x} + \mathbf{w} = \mathbf{0} \quad \text{with} \quad \mathbf{U} = \left. \frac{\partial \mathbf{f}}{\partial \mathbf{y}} \right|_{\mathbf{y}=\mathbf{y}_0, \mathbf{x}=\mathbf{x}_0}, \quad \mathbf{H} = \left. \frac{\partial \mathbf{f}}{\partial \mathbf{x}} \right|_{\mathbf{y}=\mathbf{y}_0, \mathbf{x}=\mathbf{x}_0} \quad \text{and} \quad \mathbf{w} = \mathbf{f}(\mathbf{y}, \mathbf{x}_0), \quad (3.7)$$

where  $\mathbf{U}$  is the full rank  $n_w \times n_y$  coefficient matrix (condition matrix), which contains the partial derivatives of  $\mathbf{f}(\cdot)$  with respect to  $\mathbf{y}$ .  $\mathbf{w} \in \mathbb{R}^{n_w}$  denotes the vector of inconsistencies, with  $n_w$  number of condition equations. For the further quantities and the linearisation aspect refer to Section 3.1.1.

Optimal estimates of  $\mathbf{x}$  and  $\mathbf{v}$  in Eq. 3.7 are obtained by means of the solution of the constrained minimisation problem

$$\mathbf{v}^T \cdot \mathbf{P} \cdot \mathbf{v} + 2 \cdot \mathbf{k}^T \cdot (\mathbf{U} \cdot \mathbf{v} + \mathbf{H} \cdot \Delta \mathbf{x} + \mathbf{w}) \rightarrow \min \quad (3.8)$$

using the Lagrange multipliers method, where  $\mathbf{k}$  denotes the vector of Lagrange multipliers.

The solution of the minimisation problem in Eq. 3.8 yields the normal equation system

$$\begin{bmatrix} \mathbf{U} \cdot \mathbf{P}^{-1} \cdot \mathbf{U}^T & \mathbf{H} \\ \mathbf{H}^T & \mathbf{0} \end{bmatrix} \cdot \begin{bmatrix} \hat{\mathbf{k}} \\ \Delta \hat{\mathbf{x}} \end{bmatrix} = \begin{bmatrix} \mathbf{w} \\ \mathbf{0} \end{bmatrix}. \quad (3.9)$$

The unknown parameters and the residuals can be estimated by<sup>1</sup>

$$\hat{\mathbf{x}} = \mathbf{x}_0 + \Delta \hat{\mathbf{x}} \quad \text{and} \quad \hat{\mathbf{v}} = \mathbf{Q}_{\mathbf{y}\mathbf{y}} \cdot \mathbf{U}^T \cdot \hat{\mathbf{k}}. \quad (3.10)$$

### 3.1.3. Recursive least-squares estimation in Gauss-Markov model

For the recursive least-squares estimation in a linear GMM the observations are partitioned into two parts: observations  $\mathbf{y}_{k-1}$  until a certain epoch  $k = 1 \dots k-1$  and new available observations  $\mathbf{y}_k$  at the epoch  $k$ . The two observation vectors are assumed to be mutually uncorrelated. For an originally non-linear model (Eq. 3.2) a linearisation according to Eq. 3.3 has to be performed. For ease of representation, the following derivations are outlined for a linear model. It is mandatory that the same set of parameters are used in the two different epochs  $k-1$  and  $k$ . Thus, considering the time index  $k$  and also the partitioning into two groups of  $\mathbf{v}$ ,  $\mathbf{H}$  and  $\mathbf{P}$ , the linear GMM is rewritten to

$$\begin{bmatrix} \mathbf{v}_{k-1} \\ \mathbf{v}_k \end{bmatrix} = \begin{bmatrix} \mathbf{H}_{k-1} \\ \mathbf{H}_k \end{bmatrix} \cdot \mathbf{x} - \begin{bmatrix} \mathbf{y}_{k-1} \\ \mathbf{y}_k \end{bmatrix} \quad \text{and} \quad \mathbf{P} = \begin{bmatrix} \mathbf{P}_{k-1} & \mathbf{0} \\ \mathbf{0} & \mathbf{P}_k \end{bmatrix}. \quad (3.11)$$

The least-squares principle applied on Eq. 3.11 and following the derivations in Koch (1999, pp. 177 ff.) or Kutterer and Neumann (2011), the parameters  $\hat{\mathbf{x}}_k$  for the recent epoch  $k$  can be recursively obtained as follows

$$\hat{\mathbf{x}}_k = \hat{\mathbf{x}}_{k-1} + \mathbf{K} \cdot (\mathbf{y}_k - \mathbf{H}_k \cdot \hat{\mathbf{x}}_{k-1}) = \hat{\mathbf{x}}_{k-1} + \mathbf{K} \cdot \mathbf{i}_k. \quad (3.12)$$

In Eq. 3.12, the matrix  $\mathbf{K}$  is called the Kalman gain which is obtained by minimisation of the expectation of the estimation error given by the state  $\mathbf{x}_k$  and its estimate  $\hat{\mathbf{x}}_k$  (Simon, 2006, pp. 84 ff.)

$$E \left\{ (\mathbf{x}_k - \hat{\mathbf{x}}_k) \cdot (\mathbf{x}_k - \hat{\mathbf{x}}_k)^T \right\} \rightarrow \min, \quad \text{which is identical with} \quad \text{tr}(\mathbf{Q}_{\mathbf{x}\mathbf{x}_k}) \rightarrow \min, \quad (3.13)$$

<sup>1</sup>The optimal solution for  $\hat{\mathbf{x}}$  is obtained by means of appropriate approximate parameters  $\mathbf{x}_0$ . For insufficient  $\mathbf{x}_0$  the solution has to be iteratively calculated with an updated linearisation in each iteration step.

where  $\text{tr}(\cdot)$  denotes the trace operator. The solution of this optimisation problem leads to

$$\mathbf{K} = \mathbf{Q}_{\hat{\mathbf{x}}\hat{\mathbf{x}}_{k-1}} \cdot \mathbf{H}_k^T \cdot (\mathbf{Q}_{\mathbf{y}\mathbf{y}_k} + \mathbf{H}_k \cdot \mathbf{Q}_{\hat{\mathbf{x}}\hat{\mathbf{x}}_{k-1}} \cdot \mathbf{H}_k^T)^{-1}. \quad (3.14)$$

In addition in Eq. 3.12,  $\mathbf{i}_k$  denotes the innovations vector which expresses the discrepancy between the new observations and the observation values which can be predicted from the present parameter estimate  $\hat{\mathbf{x}}_{k-1}$  (Kutterer and Neumann, 2011). Both quantities,  $\mathbf{K}$  and  $\mathbf{i}_k$ , will appear in Section 3.2.1 with the same notation. The cofactor matrix of  $\hat{\mathbf{x}}_k$  can be obtained by using the LOP and it results

$$\mathbf{Q}_{\hat{\mathbf{x}}\hat{\mathbf{x}}_k} = \mathbf{Q}_{\hat{\mathbf{x}}\hat{\mathbf{x}}_{k-1}} - \mathbf{Q}_{\hat{\mathbf{x}}\hat{\mathbf{x}}_{k-1}} \cdot \mathbf{H}_k^T \cdot (\mathbf{Q}_{\mathbf{y}\mathbf{y}_k} + \mathbf{H}_k \cdot \mathbf{Q}_{\hat{\mathbf{x}}\hat{\mathbf{x}}_{k-1}} \cdot \mathbf{H}_k^T)^{-1} \cdot \mathbf{H}_k \cdot \mathbf{Q}_{\hat{\mathbf{x}}\hat{\mathbf{x}}_{k-1}}. \quad (3.15)$$

In Section 5.2, the above equations are used for the parameter estimation in the proposed direct geo-referencing methodology.

### 3.1.4. Transformation of Gauss-Helmert model into Gauss-Markov model

To make use of recursive least-squares estimation it is rewarding to transform the GHM into an equivalent GMM. Therefore, Jäger et al. (2005) show an algorithm based on the partitioning of the GHM observation vector  $\mathbf{y}$  into two sub vectors  $\mathbf{y}_1$  and  $\mathbf{y}_2$ , respectively. Hereby,  $\mathbf{y}_2$  is introduced in addition to  $\mathbf{x}$  as additional unknown parameter vector  $\mathbf{z}$ . This modification requires the consideration of  $\mathbf{z}$  as direct observations  $\mathbf{y}_2$ . Following the derivations in Jäger et al. (2005), the model transformation of the originated GHM (Eq. 3.7) into an equivalent linearised GMM (Eq. 3.3) is given by

$$\underbrace{\begin{bmatrix} \mathbf{v}_1 \\ \mathbf{v}_2 \end{bmatrix}}_{\mathbf{v}} = \underbrace{\begin{bmatrix} -\mathbf{U}_1^{-1} \cdot \mathbf{H}_z & -\mathbf{U}_1^{-1} \cdot \mathbf{H} \\ \mathbf{I} & \mathbf{0} \end{bmatrix}}_{\substack{:=\mathbf{H}_1 \\ :=\mathbf{H}_2}} \cdot \begin{bmatrix} \Delta \hat{\mathbf{z}} \\ \Delta \hat{\mathbf{x}} \end{bmatrix} - \underbrace{\begin{bmatrix} +\mathbf{U}_1^{-1} \cdot \mathbf{f}(\mathbf{y}_1, \mathbf{z}_0, \mathbf{x}_0) \\ \mathbf{0} \end{bmatrix}}_{\mathbf{1}} \quad \text{and} \quad (3.16)$$

$$\Sigma = \begin{bmatrix} \Sigma_{\mathbf{y}_1\mathbf{y}_1} & \Sigma_{\mathbf{y}_1\mathbf{y}_2} \\ \Sigma_{\mathbf{y}_2\mathbf{y}_1} & \Sigma_{\mathbf{y}_2\mathbf{y}_2} \end{bmatrix} = \sigma_0^2 \cdot \begin{bmatrix} \mathbf{Q}_{\mathbf{y}_1\mathbf{y}_1} & \mathbf{Q}_{\mathbf{y}_1\mathbf{y}_2} \\ \mathbf{Q}_{\mathbf{y}_2\mathbf{y}_1} & \mathbf{Q}_{\mathbf{y}_2\mathbf{y}_2} \end{bmatrix}.$$

Here  $\mathbf{U}_1$  contains the partial derivatives of the non-linear function  $\mathbf{f}(\mathbf{y}_1, \mathbf{z}_0, \mathbf{x}_0)$  for the observations  $\mathbf{y}_1$ .  $\mathbf{H}_z$  denotes the linearised measurement matrix of  $\mathbf{z}$ ,  $\Delta \hat{\mathbf{z}} = \hat{\mathbf{z}} - \mathbf{z}_0$  is the truncated parameter vector which is obtained by approximate values  $\mathbf{z}_0$ . The further quantities are defined according to Section 3.1.1 and Section 3.1.2.

### 3.1.5. Parameter elimination in Gauss-Markov model

To fulfil the requirement of the same set of parameters in the recursive least-squares estimation, a parameter elimination has to be applied to the GMM which is obtained by a transformed GHM. The parameter elimination given with its full derivation in Niemeier (2008, pp. 307 ff.) is based on a partitioning of the GMM. Thus, the already partitioned GMM in Eq. 3.16 can be utilised for this purposes. A further approach which avoids the explicit partitioning of the normal equation system is the use of a general reducing-weighting matrix (Welsch, 1975). By the reducing-weighting matrix

$$\bar{\mathbf{P}} = \mathbf{P} - \mathbf{P} \cdot \bar{\mathbf{B}} \cdot (\bar{\mathbf{B}}^T \cdot \mathbf{P} \cdot \bar{\mathbf{B}})^{-1} \cdot \bar{\mathbf{B}}^T \cdot \mathbf{P} = \mathbf{P} \cdot \left( \mathbf{I} - \bar{\mathbf{B}} \cdot (\bar{\mathbf{B}}^T \cdot \mathbf{P} \cdot \bar{\mathbf{B}})^{-1} \cdot \bar{\mathbf{B}}^T \cdot \mathbf{P} \right) = \mathbf{P} \cdot \bar{\mathbf{R}} \quad (3.17)$$

a group of parameters can be reduced off. Alternatively, the singular matrix  $\bar{\mathbf{R}}$  (Eq. 3.17) can be used to yield the reduced observation equations, i. e., the design matrix is reduced instead of modifying the weighting matrix (Niemeier, 2008, p. 310). Therefore, Eq. 3.16 has to be left-multiplied with  $\bar{\mathbf{R}}$ . In Eq. 3.16 the additionally introduced parameters  $\mathbf{z}$  are eliminated by setting  $\bar{\mathbf{B}} = \mathbf{H}_1$  in Eq. 3.17. This yields  $\bar{\mathbf{R}} \cdot \mathbf{H}_1 = \mathbf{0}$ . Finally, the

solution for the parameters  $\mathbf{x}$  is given

$$\bar{\mathbf{R}} \cdot \mathbf{v} = \bar{\mathbf{R}} \cdot \mathbf{H}_2 \cdot \Delta \hat{\mathbf{x}} - \bar{\mathbf{R}} \cdot \mathbf{l}. \quad (3.18)$$

## 3.2. Recursive state-space filtering

Recursive state-space filtering is characterised by simultaneous analyses of system states based on the system's kinematic model and external sensor measurements in a unique sequential estimation approach. In a recursive manner, the current system states are estimated using the previous estimates of the system states and new input data obtained by measurements. Thereby, errors of the system states caused by, e. g., imperfect physical modelling, as well as uncertainties of the measurements caused by, e. g., the used sensors, have to be considered. Kalman (1960) has shown that for a linear, discrete-time dynamical system the KF is an optimal filter. For a linear, continuous-time dynamical system an optimal filter is given by the Kalman-Bucy filter (Kalman and Bucy, 1961). The former discrete-time KF variant is introduced with its fundamental equations. For further readings, the full derivations and the continuous-time filter variant the reader is referred to, e. g., Bar-Shalom et al. (2001), Grewal and Andrews (2008), Haykin (2001), Simon (2006).

Based on the fundamentals of the linear discrete-time KF, approaches to handle non-linear state-space equations are pointed out. The handling of non-linearities is required in various cases owing to the fact, that linear systems exist, e. g., in engineering geodesy, only in rare cases. Many systems are considered to be non-linear. For example, Aussems (1999) and Eichhorn (2005) describe the trajectory of a vehicle with a refined model of consecutive arcs. Here, the vehicle's coordinates are non-linearly related to the other state parameters such as the angular velocity in the horizontal plane and the tangential component of the linear velocity. Eichhorn (2007) presents an adaptive extension of the KF for analyses of dynamic deformation processes. In the presented application (estimation of thermal diffusivity of an aluminium column), the incorporation of physical parameters into the state vector leads to non-linear process equations. In this thesis, the proposed direct geo-referencing approach is based on the motion modelling of a laser scanner rotating about its vertical axis (Section 4.1). From this motion modelling arises non-linearities in the state-space equations which are considered in an EKF.

Further enhancements of the KF can be obtained by the joint estimation of state and adaptive parameters. Adaptive extensions of the EKF (or in general the KF), also referred to as dual estimation (Nelson, 2000), can be used for the identification of (e. g., physical) parameters, in the process equation. Generally, the adaptive filtering assumes a priori insufficiently known functional or stochastic models which should be improved by the filtering (Gelb, 1974). Besides adaptive parameters, known functional or theoretical relationships among the unknown state parameters can exist. To take these relationships into account, equality or even inequality constraints for the state parameters can be formulated (Julier and LaViola, 2007, Simon, 2010, Simon and Chia, 2002). For instance, this can be a constant known distance between two sensors in a MSS or a constant velocity of a moving platform. The MSS introduced in Section 4.2 is characterised by certain parameters, like a specific distance between two sensors as well as a constant velocity. Therefore, in Section 5.2 the Adaptive Extended Kalman Filter (aEKF) as well as the EKF with constraints are utilised for the motion modelling of the rotating laser scanner about its vertical axis. The superior aim of both developed algorithms, the motion estimation, is core part to fulfil the thesis's aim: the direct geo-referencing of stationary laser scanners.

### 3.2.1. Discrete-time linear Kalman filter

Defining the problem of KF for the discrete-time, linear case the state vector  $\mathbf{x}_k \in \mathbb{R}^{n_x}$ , with  $n_x$  the number of state parameters, the known input vector  $\mathbf{u}_k \in \mathbb{R}^{n_u}$ , with  $n_u$  the number of known input parameters (deterministic changes of the system state, e. g., control or sensor platform motion), the process error vector  $\mathbf{w}_k \in \mathbb{R}^{n_x}$  (caused by imperfect modelling effects and other disturbances in the motion model) as well as the discrete-time

index  $k$  are given. These quantities provide the *process equation*

$$\mathbf{x}_{k+1} = \mathbf{T}_{k+1,k} \cdot \mathbf{x}_k + \mathbf{B}_{k+1,k} \cdot \mathbf{u}_k + \mathbf{S}_{k+1,k} \cdot \mathbf{w}_k, \quad (3.19)$$

where  $\mathbf{T}_{k+1,k}$  denotes the transition matrix, which takes the state from time  $k$  to time  $k+1$ , and  $\mathbf{B}_{k+1,k}$  denotes the known input gain, which takes the known input parameters from time  $k$  to time  $k+1$ .  $\mathbf{S}_{k+1,k}$  represents the coefficient matrix of disturbing variables, which takes the process error vector from time  $k$  to time  $k+1$ . Thereby,  $\mathbf{S}_{k+1,k}$  establishes the relationship of the process error vector with the states, which can demand for a problem specific realisation (cf. Eichhorn, 2005, pp. 94 ff.). The process error vector  $\mathbf{w}_k$  is assumed to be zero-mean white Gaussian process noise with VCM and cofactor matrix, respectively, defined by (Bar-Shalom et al., 2001)

$$E \{ \mathbf{w}_k \cdot \mathbf{w}_k^T \} = \Sigma_{\mathbf{w}\mathbf{w}_k} = \sigma_{0w}^2 \cdot \mathbf{Q}_{\mathbf{w}\mathbf{w}_k}, \quad (3.20)$$

where  $\sigma_{0w}^2$  is the a priori variance factor, which is typically assumed to be  $\sigma_{0w}^2 = 1.0$ .

An initial state  $\hat{\mathbf{x}}_0$  and its cofactor matrix  $\mathbf{Q}_{\hat{\mathbf{x}}\hat{\mathbf{x}}_0}$  are assumed to be known. The prediction of the state  $\hat{\mathbf{x}}_{k+1}^-$  is based on Eq. 3.19 as given as

$$\hat{\mathbf{x}}_{k+1}^- = \mathbf{T}_{k+1,k} \cdot \hat{\mathbf{x}}_k^+ + \mathbf{B}_{k+1,k} \cdot \mathbf{u}_k. \quad (3.21)$$

The corresponding cofactor matrix  $\mathbf{Q}_{\hat{\mathbf{x}}\hat{\mathbf{x}}_{k+1}^-}$  of the estimate given in Eq. 3.21 is obtained by the LOP and leads to

$$\mathbf{Q}_{\hat{\mathbf{x}}\hat{\mathbf{x}}_{k+1}^-} = \mathbf{T}_{k+1,k} \cdot \mathbf{Q}_{\hat{\mathbf{x}}\hat{\mathbf{x}}_k^+} \cdot \mathbf{T}_{k+1,k}^T + \mathbf{B}_{k+1,k} \cdot \mathbf{Q}_{\mathbf{u}\mathbf{u}_k} \cdot \mathbf{B}_{k+1,k}^T + \mathbf{S}_{k+1,k} \cdot \mathbf{Q}_{\mathbf{w}\mathbf{w}_k} \cdot \mathbf{S}_{k+1,k}^T, \quad (3.22)$$

where  $\mathbf{Q}_{\hat{\mathbf{x}}\hat{\mathbf{x}}_k^+}$  denotes cofactor matrix of the filtered estimates of the epoch  $k$  and by  $\mathbf{Q}_{\mathbf{u}\mathbf{u}_k}$  is given the cofactor matrix of the known input parameters.

The observation vector  $\mathbf{y}_{k+1}$  and the measurement matrix  $\mathbf{H}_{k+1}$  define the *measurement equation*

$$\mathbf{y}_{k+1} = \mathbf{H}_{k+1} \cdot \mathbf{x}_{k+1} - \mathbf{v}_{k+1}. \quad (3.23)$$

As in Section 3.1.1 already defined,  $\mathbf{v}_{k+1}$  is the measurement error vector, which is assumed to be zero-mean white Gaussian measurement noise with VCM and cofactor matrix, respectively, given by

$$E \{ \mathbf{v}_{k+1} \cdot \mathbf{v}_{k+1}^T \} = \Sigma_{\mathbf{y}\mathbf{y}_{k+1}} = \sigma_0^2 \cdot \mathbf{Q}_{\mathbf{y}\mathbf{y}_{k+1}}, \quad (3.24)$$

where  $\sigma_0^2$  is the (theoretical) variance factor of unit weight, which is a priori typically assumed to be  $\sigma_0^2 = 1.0$ . The two error vectors  $\mathbf{w}_k$  and  $\mathbf{v}_{k+1}$  are assumed to be mutually independent (Bar-Shalom et al., 2001). For the case that both  $\mathbf{w}_k$  and  $\mathbf{v}_{k+1}$  are stochastically dependent the reader is referred to Simon (2006, Chapter 7).

The filtering step in the KF framework is defined as recursive estimation of the state parameters after current observations  $\mathbf{y}_{k+1}$  are available

$$\hat{\mathbf{x}}_{k+1}^+ = \hat{\mathbf{x}}_{k+1}^- + \mathbf{K}_{k+1} \cdot (\mathbf{y}_{k+1} - \mathbf{H}_{k+1} \cdot \hat{\mathbf{x}}_{k+1}^-) = \hat{\mathbf{x}}_{k+1}^- + \mathbf{K}_{k+1} \cdot \mathbf{i}_{k+1}. \quad (3.25)$$

The filtering step is characterised by the update of the predicted estimate  $\hat{\mathbf{x}}_{k+1}^-$  with the second term of Eq. 3.25.  $\mathbf{i}_{k+1}$  is the innovations vector<sup>2</sup> and  $\mathbf{K}_{k+1}$  is an unknown matrix called the Kalman gain (cf. Section 3.1.3). This unknown matrix can be derived according to the theory of recursive parameter estimation given in, e. g., Koch (1999, pp. 177 ff.) and Simon (2006). The resulting estimated value is given in Eq. 3.14 and will be adapted to the context of discrete-time KF. Therefore, the state estimate and corresponding quantities from the previous epoch  $k-1$  (cf. Eq. 3.12) are substituted by the predicted state estimate and corresponding quantities from the

<sup>2</sup>The innovations vector is frequently denoted by  $\mathbf{d}$  (e. g., Niemeier, 2008, p. 464). To avoid confusions in the Kalman filtering with constraints (Section 3.2.5) the innovations vector is denoted by  $\mathbf{i}$ .

current epoch  $k + 1$ . For the Kalman gain this results in

$$\mathbf{K}_{k+1} = \mathbf{Q}_{\hat{\mathbf{x}}\hat{\mathbf{x}}_{k+1}^-} \cdot \mathbf{H}_{k+1}^T \cdot \left( \mathbf{Q}_{\mathbf{y}\mathbf{y}_{k+1}} + \mathbf{H}_{k+1} \cdot \mathbf{Q}_{\hat{\mathbf{x}}\hat{\mathbf{x}}_{k+1}^-} \cdot \mathbf{H}_{k+1}^T \right)^{-1}. \quad (3.26)$$

The cofactor matrix of the filtered estimate  $\hat{\mathbf{x}}_{k+1}^+$  is obtained by the LOP and results in

$$\mathbf{Q}_{\hat{\mathbf{x}}\hat{\mathbf{x}}_{k+1}^+} = \mathbf{Q}_{\hat{\mathbf{x}}\hat{\mathbf{x}}_{k+1}^-} - \mathbf{K}_{k+1} \cdot \mathbf{Q}_{\mathbf{i}\mathbf{i}_{k+1}} \cdot \mathbf{K}_{k+1}^T, \quad (3.27)$$

where the cofactor matrix of  $\mathbf{i}_{k+1}$  is

$$\mathbf{Q}_{\mathbf{i}\mathbf{i}_{k+1}} = \mathbf{Q}_{\mathbf{y}\mathbf{y}_{k+1}} + \mathbf{H}_{k+1} \cdot \mathbf{Q}_{\hat{\mathbf{x}}\hat{\mathbf{x}}_{k+1}^-} \cdot \mathbf{H}_{k+1}^T. \quad (3.28)$$

The main aim of KF is the jointly determination of the unknown states by means of prediction (Eq. 3.21) and filtering (Eq. 3.25) in an optimum manner according to Eq. 3.13. Considering the state estimation  $\mathbf{x}_i$  for time  $i$  with respect to the available observation data  $\mathbf{y}_1, \mathbf{y}_2, \dots, \mathbf{y}_k$  of this state, the problem is called *prediction* for  $i > k$  (Alg. 3.1, Line 4 ff.), *filtering* for  $i = k$  (Alg. 3.1, Line 9 ff.) and *smoothing* if  $1 \leq i < k$  (Alg. 3.2).

Alg. 3.1 gives an overview of the KF algorithm. The prediction step (Line 4 ff.) provides the a priori system state and its cofactor matrix for the epoch  $k + 1$  based on the dynamic model in the transition matrix ( $\mathbf{T}_{k+1,k}$ ) and the known input gain ( $\mathbf{B}_{k+1,k}$ ). The filtering step (Line 9 ff.) incorporates measurements of the system states at the epoch  $k + 1$ .

The innovations vector ( $\mathbf{i}_{k+1}$ ) (Alg. 3.1, Line 11) expresses discrepancies for the state prediction and the actual measurements. Therefore, they can be used for statistical tests of process and measurement equation within a multivariate test of the expectations (Pelzer, 1985). The null hypothesis and corresponding alternative hypothesis are

$$E\{\mathbf{i}_{k+1}\} = \mathbf{0} \quad | H_0 \quad \text{and} \quad E\{\mathbf{i}_{k+1}\} \neq \mathbf{0} \quad | H_A. \quad (3.29)$$

---

**Algorithm 3.1:** KF algorithm with its fundamental calculation steps (Simon, 2006, modified).

---

**1 Initialisation**

2 Initial system state  $\hat{\mathbf{x}}_0$  and its cofactor matrix  $\mathbf{Q}_{\hat{\mathbf{x}}\hat{\mathbf{x}}_0}$

3 **for**  $k = 1, 2, \dots, N_{epochs}$  **do**

4 **Prediction step: state estimate and cofactor matrix propagation**

5 **Input:**  $\hat{\mathbf{x}}_k^+, \mathbf{Q}_{\hat{\mathbf{x}}\hat{\mathbf{x}}_k^+}, \mathbf{u}_k, \mathbf{Q}_{\mathbf{u}\mathbf{u}_k}, \mathbf{Q}_{\mathbf{w}\mathbf{w}_k} = \frac{1}{\sigma_w^2} \cdot \Sigma_{\mathbf{w}\mathbf{w}_k}$  with  $\sigma_w^2 := 1$

6  $\hat{\mathbf{x}}_{k+1}^- = \mathbf{T}_{k+1,k} \cdot \hat{\mathbf{x}}_k^+ + \mathbf{B}_{k+1,k} \cdot \mathbf{u}_k$  Eq. 3.21

7  $\mathbf{Q}_{\hat{\mathbf{x}}\hat{\mathbf{x}}_{k+1}^-} = \mathbf{T}_{k+1,k} \cdot \mathbf{Q}_{\hat{\mathbf{x}}\hat{\mathbf{x}}_k^+} \cdot \mathbf{T}_{k+1,k}^T + \mathbf{B}_{k+1,k} \cdot \mathbf{Q}_{\mathbf{u}\mathbf{u}_k} \cdot \mathbf{B}_{k+1,k}^T + \mathbf{S}_{k+1,k} \cdot \mathbf{Q}_{\mathbf{w}\mathbf{w}_k} \cdot \mathbf{S}_{k+1,k}^T$  Eq. 3.22

8 **Output:** Predicted (a priori) state vector and its cofactor matrix:  $\hat{\mathbf{x}}_{k+1}^-, \mathbf{Q}_{\hat{\mathbf{x}}\hat{\mathbf{x}}_{k+1}^-}$

9 **Filtering step: state estimate and cofactor matrix update**

10 **Input:**  $\hat{\mathbf{x}}_{k+1}^-, \mathbf{Q}_{\hat{\mathbf{x}}\hat{\mathbf{x}}_{k+1}^-}, \mathbf{y}_{k+1}, \mathbf{Q}_{\mathbf{y}\mathbf{y}_{k+1}} = \frac{1}{\sigma_0^2} \cdot \Sigma_{\mathbf{y}\mathbf{y}_{k+1}}$  with  $\sigma_0^2 := 1$

11  $\mathbf{i}_{k+1} = \mathbf{y}_{k+1} - \mathbf{H}_{k+1} \cdot \hat{\mathbf{x}}_{k+1}^-$  Eq. 3.25

12  $\mathbf{Q}_{\mathbf{i}\mathbf{i}_{k+1}} = \mathbf{Q}_{\mathbf{y}\mathbf{y}_{k+1}} + \mathbf{H}_{k+1} \cdot \mathbf{Q}_{\hat{\mathbf{x}}\hat{\mathbf{x}}_{k+1}^-} \cdot \mathbf{H}_{k+1}^T$  Eq. 3.28

13  $\mathbf{K}_{k+1} = \mathbf{Q}_{\hat{\mathbf{x}}\hat{\mathbf{x}}_{k+1}^-} \cdot \mathbf{H}_{k+1}^T \cdot (\mathbf{Q}_{\mathbf{i}\mathbf{i}_{k+1}})^{-1}$  Eq. 3.26

14  $\hat{\mathbf{x}}_{k+1}^+ = \hat{\mathbf{x}}_{k+1}^- + \mathbf{K}_{k+1} \cdot \mathbf{i}_{k+1}$  Eq. 3.25

15  $\mathbf{Q}_{\hat{\mathbf{x}}\hat{\mathbf{x}}_{k+1}^+} = \mathbf{Q}_{\hat{\mathbf{x}}\hat{\mathbf{x}}_{k+1}^-} - \mathbf{K}_{k+1} \cdot \mathbf{Q}_{\mathbf{i}\mathbf{i}_{k+1}} \cdot \mathbf{K}_{k+1}^T$  Eq. 3.27

16 **Output:** Filtered (a posteriori) state vector  $\hat{\mathbf{x}}_{k+1}^+$  and its cofactor matrix  $\mathbf{Q}_{\hat{\mathbf{x}}\hat{\mathbf{x}}_{k+1}^+}$

---

Under the assumption of the normal distribution for  $\mathbf{i}_{k+1}$  the test statistic is

$$T = \mathbf{i}_{k+1} \cdot (\mathbf{Q}_{\mathbf{i}_{k+1}})^{-1} \cdot \mathbf{i}_{k+1} \sim \chi^2. \quad (3.30)$$

The null hypothesis  $H_0$  will be rejected if the test value  $T$  is larger than the fractile of the  $\chi^2$ -distribution with  $n_y$  DoF for a certain significance level.

The filtered state estimate and its cofactor matrix are obtained as update of the predicted states and its cofactor matrix through linear transformation of the innovations and its cofactor matrix by means of the Kalman gain (Eq. 3.26).

**The Variance Component Estimation (VCE)** is a well-known technique in the parameter estimation in linear models to obtain optimal variance factors for observations or groups of observations (e. g., Koch, 1999, pp. 225 ff.). The transfer of the VCE technique to KF is proposed by Caspary and Wang (1998), to estimate variance components for both the process noise and the measurement noise. Moreover, the authors deduce local, regional and global variance factors of unit weight. Further work on VCE in the KF framework is published by, e. g., Wang (2008) and Wang et al. (2009).

In Alg. 3.1, the variance factors  $\sigma_{0_w}^2$  (Line 5) and  $\sigma_0^2$  (Line 10) are set to 1. Their estimation according to the mentioned publications can be helpful to obtain optimal variance components.

### 3.2.2. Non-linearities in state-space equations

In Section 3.2.1, the KF is introduced with linear state-space equations, process and measurement equations, as discrete-time system with Gaussian error noise. This section is dedicated to filtering approaches which are capable to handle non-linear state-space equations and non-Gaussian state estimation. Two distinct approaches can be found to account for non-linearities in the state-space equations: First, the well-known analytical approximation of the non-linear functions utilising Taylor series expansion. Second, approaches which approximate the Probability Density Function (PDF) of measurements and states. In the latter approaches also non-Gaussian PDF can be considered. Before turning to the two distinct approaches, the equivalent state-space formulation of both is introduced.

The non-linear state-space equations can be obtained with the linear state-space equations in Eq. 3.19 and 3.23 by means of substituting the quantities  $\mathbf{T}_{k+1,k} \cdot \mathbf{x}_k$ ,  $\mathbf{B}_{k+1,k} \cdot \mathbf{u}_k$ ,  $\mathbf{S}_{k+1,k} \cdot \mathbf{w}_k$  and  $\mathbf{H}_{k+1} \cdot \mathbf{x}_{k+1}$  with the non-linear functions  $\mathbf{f}_{k+1,k}(\mathbf{x}_k, \mathbf{u}_k, \mathbf{w}_k)$  and  $\mathbf{h}_{k+1}(\mathbf{x}_{k+1}, \mathbf{v}_{k+1})$

$$\mathbf{x}_{k+1} = \mathbf{f}_{k+1,k}(\mathbf{x}_k, \mathbf{u}_k, \mathbf{w}_k) \quad \text{and} \quad \mathbf{w}_k \sim \mathcal{N}(\mathbf{0}, \mathbf{\Sigma}_{\mathbf{w}\mathbf{w}_k}), \quad (3.31)$$

$$\mathbf{y}_{k+1} = \mathbf{h}_{k+1}(\mathbf{x}_{k+1}, \mathbf{v}_{k+1}) \quad \text{and} \quad \mathbf{v}_{k+1} \sim \mathcal{N}(\mathbf{0}, \mathbf{\Sigma}_{\mathbf{y}\mathbf{y}_{k+1}}). \quad (3.32)$$

Here  $\mathbf{f}(\cdot)$  is the non-linear dynamic model. The non-linear measurement matrix is expressed by  $\mathbf{h}(\cdot)$ . Both  $\mathbf{f}(\cdot)$  and  $\mathbf{h}(\cdot)$  are (usually) known functions and are possibly time-variant. As in Section 3.2.1, the two error vectors,  $\mathbf{w}_k$  and  $\mathbf{v}_{k+1}$ , are assumed to be mutually independent and uncorrelated with (usually) known PDF, typically the Gaussian distribution (zero-mean white Gaussian noise). The consideration of coloured noise instead of white noise for process and measurement noise as well as correlations between them are realised by shaping filter approaches (Gelb, 1974, Grewal and Andrews, 2008, Li, 2011, Ramm, 2008).

#### 3.2.2.1. First-order extended Kalman filter

The EKF is widely used to deal with non-linear state-space equations. It is based on analytical approximation of the non-linear functions  $\mathbf{f}(\cdot)$  and  $\mathbf{h}(\cdot)$  utilising Taylor series expansion (Gelb, 1974). Commonly, the first and second order terms of the Taylor approximation of the non-linear functions are considered (first- and second-order EKF). In the following the first-order EKF is outlined, for further details regarding Taylor approximation



and other algorithms for polynomial approximation of non-linear functions is referred to, e. g., Gelb (1974). The linearisation of the state-space equations (Eq. 3.31 and 3.32) is performed at each time instant around the current estimate as follows

$$\begin{aligned} \mathbf{T}_{k+1,k} &= \left. \frac{\partial \mathbf{f}_{k+1,k}(\mathbf{x}_k, \mathbf{u}_k, \mathbf{w}_k)}{\partial \mathbf{x}_k} \right|_{\mathbf{x}_k = \hat{\mathbf{x}}_k^+}, \quad \mathbf{B}_{k+1,k} = \left. \frac{\partial \mathbf{f}_{k+1,k}(\mathbf{x}_k, \mathbf{u}_k, \mathbf{w}_k)}{\partial \mathbf{u}_k} \right|_{\mathbf{u}_k = \mathbf{u}_k}, \\ \mathbf{S}_{k+1,k} &= \left. \frac{\partial \mathbf{f}_{k+1,k}(\mathbf{x}_k, \mathbf{u}_k, \mathbf{w}_k)}{\partial \mathbf{w}_k} \right|_{\mathbf{w}_k = \mathbf{w}_k} \quad \text{and} \quad \mathbf{H}_{k+1} = \left. \frac{\partial \mathbf{h}_{k+1}(\mathbf{x}_{k+1}, \mathbf{v}_{k+1})}{\partial \mathbf{x}_{k+1}} \right|_{\mathbf{x}_{k+1} = \hat{\mathbf{x}}_{k+1}^-}. \end{aligned} \quad (3.33)$$

For the transition matrix  $\mathbf{T}_{k+1,k}$  the Taylor series is evaluated at the previous epoch  $\hat{\mathbf{x}}_k^+$ . The known input gain  $\mathbf{B}_{k+1,k}$  is linearised at the recent epoch around  $\mathbf{u}_k$ . The coefficient matrix of disturbing variables  $\mathbf{S}_{k+1,k}$  is linearised at the recent epoch around  $\mathbf{w}_k$ . For the measurement matrix  $\mathbf{H}_{k+1}$  the Taylor series is evaluated at the current predicted epoch  $\hat{\mathbf{x}}_{k+1}^-$ . Uncertainties induced by the limited approximation to the first-order terms have to be considered in the stochastic modelling by the process error vector and its VCM, respectively. Considering the linear approximations in Eq. 3.33, the EKF calculation scheme is similar to the fundamental calculations steps of the KF. The only differences for the EKF are in the prediction step in terms of the state estimate propagation (Alg. 3.1, Line 6) which is given for the EKF by

$$\hat{\mathbf{x}}_{k+1}^- = \mathbf{f}_{k+1,k}(\hat{\mathbf{x}}_k^+, \mathbf{u}_k) \quad (3.34)$$

and for the state estimate update (Alg. 3.1, Line 14) in the filtering step which is as follows

$$\hat{\mathbf{x}}_{k+1}^+ = \hat{\mathbf{x}}_{k+1}^- + \mathbf{K}_{k+1} \cdot (\mathbf{y}_{k+1} - \mathbf{h}_{k+1}(\hat{\mathbf{x}}_{k+1}^-)) = \hat{\mathbf{x}}_{k+1}^- + \mathbf{K}_{k+1} \cdot \mathbf{i}_{k+1}. \quad (3.35)$$

It is worth noting, that the linearisation of the state-space equations using Taylor approximations is prone to diverge in case of highly non-linear equations (Doucet et al., 2001). Therefore, higher-order derivations or iterative KF can be used (Simon, 2006, pp. 410ff.). Moreover, the derivation of the Jacobian matrices can be non-trivial in many applications and cause also implementation difficulties.

### 3.2.2.2. Further approaches dealing with non-linearities

This section outlines further approaches (besides linearisation) which are widely used to deal with non-linearities in the state-space equations. Two chosen approaches: Unscented Kalman Filter (UKF) and Sequential Monte Carlo (SMC) filter, are generally introduced with their basic idea. Both approaches are characterised by the approximation of the PDF of measurements and states. Alkhatib et al. (2008) explore and investigate both approaches and compare them with the EKF for the non-linear state estimation. Their contribution covers beside the algorithms simulations which illustrate a vehicle moving along a non-linear trajectory such as a circle arc or clothoid.

**The unscented Kalman filter,** firstly proposed by Julier and Uhlmann (1997), approximates the PDF instead of non-linear functions like the EKF does. The fundamental background of the UKF is the Unscented Transformation (UT) which utilises deterministically chosen sample points (sigma points) of probability distributions for the parametrisation of mean (first moment) and VCM (second moment). For assumed Gaussian noise for the input quantities the UKF leads the same results as the first-order EKF (Alkhatib et al., 2008). Nevertheless, the UKF can also handle noise which is not assumed to be Gaussian. The estimator yields performance equivalent to the KF for linear systems yet generalizes elegantly to non-linear systems without the linearisation steps required by the EKF (Julier and Uhlmann, 1997). For the mathematical derivations of the UKF and further readings the reader is referred to, e. g., Bar-Shalom et al. (2001) as well as Julier and Uhlmann (1997).

We can summarise that the main advantage of the UKF over the EKF is the omission of linearisation which leads for high non-linear functions to the aforementioned difficulties. In general, the utilisation of UT, and in particular the definitions of Julier and Uhlmann (1997) regarding the manner of choosing sigma points, is also feasible for efficient variance propagation of mass data which is presented by Vennegeerts and Kutterer (2009).

**The sequential Monte Carlo filter,** also known as Particle Filter (PF), is a suboptimal filter for implementing the recursive Bayesian filter by MC techniques (Doucet et al., 2001, Ristic et al., 2004). The PF utilise a set of random samples which can be generated from a known PDF for the approximation of the posteriori PDF of the state parameters. The filtering with PF can be described by three main steps: The first step is the importance sampling which covers the generation of particles for the current epoch as well as the evaluation and normalisation of the importance weights. Secondly in the resampling step particles are removed or duplicated according to their near zero or large importance weight, respectively. In the final evaluation step these particles are used to calculate the estimates of the state parameters, like mean, VCM or skewness. For the resampling schemes, the mathematical derivations of the PF and further readings is referred to, e. g., Alkhatib (2007), Doucet et al. (2001) and Ristic et al. (2004).

An equivalent representation of the posteriori PDF can be obtained by a large number of drawn particles. This can cause high computational costs due to the large number of required particles which can be critical for real-time applications.

An efficient approach to reduce the number of drawn particle by the combination of SMC filter and EKF is proposed by Alkhatib et al. (2012). The resulting filter is termed Extended Kalman Particle Filter (EKPF). The novelty of the proposed EKPF is the update of each particle at the filter epoch  $k$  using an EKF. The authors apply their filter approach to a method for the direct geo-referencing of a stationary laser scanner. The conclusions of the authors are a significant improvement of the filter effect compared to EKF results as well as a representative decrease of the number of generated particles compared to a generic PF.

**Concluding remarks:** In this section variants of filtering approaches, like EKF, UKF and PF, are introduced to deal with non-linearities in the state-space equations within recursive state-space filtering. The occurrence of non-linearities in the state-space equations is in particular motivated for trajectory modelling of moving platforms which coincides with the thesis aim. Owing to the fact of a controlled motion of the stationary laser scanner which is indeed non-linear but not highly non-linear, an EKF approach is proposed in Chapter 5 for the motion modelling. It is worth noting that the use of alternative filtering approaches or even the combination of different filtering techniques as proposed by Alkhatib et al. (2012) can strengthen the final results.

### 3.2.3. Smoothing algorithms in the Kalman filter framework

This section familiarises with the optimum smoothing problem in the KF framework. Grewal and Andrews (2008) distinguish three types of smoothers: First, fixed-interval smoothers which utilise all data in a certain interval for the state estimation. This smoother can be applied at any time after all data, i. e., measurements, are available. For this reason fixed-interval smoothers are frequently used in post-processing when all measurements are available and generally not used for real-time applications. Second, fixed-lag smoothers which run in real-time and make use of all data up to the current time. The smoothed estimate is generated with lagged time. Third, fixed-point smoothers which yield a state estimate for a fixed time based on all data up to the current time. Fixed-interval smoothers are outlined in the following, for the other two types cf. Grewal and Andrews (2008).

An available data set over the time interval  $0 < k \leq N$  is assumed with the fixed final epoch  $N$ , see Fig. 3.1. For smoothing purposes all available past and future data for the state estimation  $\mathbf{x}_k$  for  $0 < k \leq N$  are used which leads to fixed-interval smoothing. The estimation of the optimum state  $\mathbf{x}_k^f$  for  $0 < j \leq k$  based on past data  $\mathbf{y}_j$  is referred to as forward filtering (cf. Fig. 3.1 (a)). The fundamentals are given in Section 3.2.1 and the



### 3.2.4. Joint estimation of states and adaptive parameters

This section familiarises the reader with the joint estimation of states and adaptive parameters in an EKF approach. Like mentioned in Section 3.2, an enhanced description of the dynamic model is possible by adaptive parameters. These adaptive parameters are incorporated in the process equation with the aims of further filter improvements and of minimising discrepancies between dynamic model and reality (Eichhorn, 2007). The basics of the aEKF are presented in the following. For full mathematical derivations of the adaptive KF and further readings is referred to Brown and Hwang (2012), Eichhorn (2005), Heunecke (1995), Wan and Nelson (2001).

Defining the problem of the aEKF, the state vector of the EKF and its VCM are renamed by the subscript “g”:  $\mathbf{x}_{g,k}$  and  $\Sigma_{\mathbf{x}\mathbf{x}_{g,k}}$ . The adaptive parameters are termed  $\mathbf{x}_{a,k} \in \mathbb{R}^{n_{x_a}}$ , with  $n_{x_a}$  the number of adaptive parameters, and its corresponding VCM  $\Sigma_{\mathbf{x}\mathbf{x}_{a,k}}$ . Furthermore, the joint state vector and its VCM and cofactor matrix, respectively, can be written as follows

$$\mathbf{x}_k = \begin{bmatrix} \mathbf{x}_{g,k} & \mathbf{x}_{a,k} \end{bmatrix}^T \quad \text{and} \quad \Sigma_{\mathbf{x}\mathbf{x}_k} = \begin{bmatrix} \Sigma_{\mathbf{x}\mathbf{x}_{g,k}} & \mathbf{0} \\ \mathbf{0} & \Sigma_{\mathbf{x}\mathbf{x}_{a,k}} \end{bmatrix} = \sigma_0^2 \cdot \begin{bmatrix} \mathbf{Q}_{\mathbf{x}\mathbf{x}_{g,k}} & \mathbf{0} \\ \mathbf{0} & \mathbf{Q}_{\mathbf{x}\mathbf{x}_{a,k}} \end{bmatrix}. \quad (3.36)$$

The non-linear state-space equations for the aEKF can be obtained by rewriting Eq. 3.31 and 3.32 to account the general states  $\mathbf{x}_{g,k}$  and the adaptive parameters  $\mathbf{x}_{a,k}$ , as follows

$$\mathbf{x}_{k+1} = \begin{bmatrix} \mathbf{f}_{g,k+1,k}(\mathbf{x}_{g,k}, \mathbf{u}_k, \mathbf{w}_k) \\ \mathbf{f}_{a,k+1,k}(\mathbf{x}_{a,k}, \mathbf{u}_k, \mathbf{w}_k) \end{bmatrix}^T = \mathbf{f}_{k+1,k}(\mathbf{x}_k, \mathbf{u}_k, \mathbf{w}_k) \quad \text{and} \quad \mathbf{w}_k \sim \mathcal{N}(\mathbf{0}, \Sigma_{\mathbf{w}\mathbf{w}_k}), \quad (3.37)$$

$$\mathbf{y}_{k+1} = \mathbf{h}_{k+1}(\mathbf{x}_{g,k+1}, \mathbf{x}_{a,k+1}, \mathbf{v}_{k+1}) = \mathbf{h}_{k+1}(\mathbf{x}_{k+1}, \mathbf{v}_{k+1}) \quad \text{and} \quad \mathbf{v}_{k+1} \sim \mathcal{N}(\mathbf{0}, \Sigma_{\mathbf{y}\mathbf{y}_{k+1}}). \quad (3.38)$$

Here  $\mathbf{f}_g(\cdot)$  is the non-linear dynamic model of the general state vector  $\mathbf{x}_{g,k}$ .  $\mathbf{f}_a(\cdot)$  denotes a non-linear known function of the adaptive parameters  $\mathbf{x}_{a,k}$ . The further quantities are defined as in Section 3.2.2. It is worth noting that the adaptive parameters (especially in applications of engineering geodesy) are typically not observed by direct or indirect measurements (Heunecke, 1995) which is accounted by zero columns in  $\mathbf{h}_{k+1}$ . By means of Eq. 3.36 – 3.38 the solution of the aEKF can be obtained utilising the linearisation discussed in Section 3.2.2.1 (Eq. 3.33 – 3.35) and applying Alg. 3.1.

The estimation of the adaptive parameters  $\mathbf{x}_{a,k}$  (Eq. 3.36) is also known as parametric identification (Heunecke, 1995). This parametric identification is also addressed by Eichhorn (2005, 2007) for a mass-spring-damper system, a vehicle movement as well as for the estimation of thermal diffusivity of an aluminium column. An aEKF approach for purposes of direct geo-referencing of stationary laser scanners is introduced in Section 5.2.

### 3.2.5. Kalman filtering with constraints

To recall the introduction in Section 3.2, the (dynamic) system description of the KF can contain known functional or theoretical relationships among the unknown state parameters. Therefore, equality or even inequality constraints for the state parameters with the aim of further improvements of the filtering results are introduced here. An example of such constraints for multi-sensor navigation purposes in the KF framework is presented by Yang et al. (2010). The authors present a robust KF with state constraints which is evaluated in an experimental study. The authors’ findings are an accuracy improvement of the state parameters due to the robust estimation and the constraints among the state parameters compared to the standard KF. Furthermore, they show that the robust estimation is more important to control outlier in the data than to consider the constraints.

Approaches for applying linear and even non-linear constraints within the KF framework can be broadly classified into: perfect measurements, projection and re-parametrisation methods (Julier and LaViola, 2007, Simon and Chia, 2002). The perfect measurements methods are based on fictitious observations with assigned zero variance. It has to be noted that this methods leads to a singular VCM but this does not present any theoretical problems (Simon and Chia, 2002). The projection methods project the unconstrained estimates onto the

constraint surface, which is similar to the solution of the constrained parameter identification problem (Chia et al., 1991, Simon and Chia, 2002). The re-parametrisation methods reduce the system model state vector using the state constraints, afterwards the KF without constraints can be applied. Simon (2010) provides a comprehensive review of several linear and non-linear algorithms for the consideration of state constraints in the KF framework. He presents the basic equations of the different algorithms and compares the filter results for a simulated linear and a non-linear example. A “best” performing algorithm can not be pointed out. Thus, the author concludes that the appropriate algorithm generally has to be chosen with respect to the application.

The constrained state estimation in the KF framework to fulfil equality constraints is written as follows (Simon and Chia, 2002)

$$\mathbf{D} \cdot \hat{\mathbf{x}}_{k+1} = \mathbf{d}, \quad (3.39)$$

where  $\mathbf{D}$  denotes a known  $s \times n_x$  constant, full rank matrix,  $\mathbf{d}$  is a known  $s \times 1$  vector and  $s$  represents the number of constraints.  $\hat{\mathbf{x}}_{k+1}$ ,  $n_x$  and  $k$  are defined according to Section 3.2.1.

The estimate projection algorithm (Simon and Chia, 2002) is introduced with its basic equations as the algorithm of choice for the consideration of equality state constraints. For full derivations, further algorithms and inequality constraints the reader is referred to, e. g., Julier and LaViola (2007), Simon and Chia (2002) and Simon (2010). An EKF approach utilising state constraints is proposed in Section 5.2 to solve the direct geo-referencing of stationary laser scanners.

### 3.2.5.1. Estimate projection to consider linear constraints

The estimate projection algorithm projects the unconstrained state estimate  $\hat{\mathbf{x}}_{k+1}^+$  onto the constraint surface. The provided basic equations are taken from Simon and Chia (2002) as well as Simon (2010). For equality linear constraints the minimisation problem

$$\tilde{\mathbf{x}}_{k+1}^+ = \arg \min_{\mathbf{x}} (\mathbf{x} - \hat{\mathbf{x}}_{k+1}^+)^T \cdot \mathbf{W} \cdot (\mathbf{x} - \hat{\mathbf{x}}_{k+1}^+) \quad \text{such that} \quad \mathbf{D} \cdot \mathbf{x} = \mathbf{d}, \quad (3.40)$$

has to be solved, where  $\tilde{\mathbf{x}}_{k+1}^+$  denotes the constrained state estimate and  $\mathbf{W}$  is a positive-definite weighting matrix. The solution of the arg min problem in Eq. 3.40 leads to the constrained state estimate

$$\tilde{\mathbf{x}}_{k+1}^+ = \hat{\mathbf{x}}_{k+1}^+ - \mathbf{W}^{-1} \cdot \mathbf{D}^T \cdot (\mathbf{D} \cdot \mathbf{W}^{-1} \cdot \mathbf{D}^T)^{-1} \cdot (\mathbf{D} \cdot \hat{\mathbf{x}}_{k+1}^+ - \mathbf{d}). \quad (3.41)$$

The a priori constrained estimate in the prediction step is the a posteriori unconstrained state estimate  $\hat{\mathbf{x}}_k^+$  (Simon and Chia, 2002). The outcome of this is, that the standard KF calculation steps (cf. Alg. 3.1) are used and no separate prediction for the constrained filter is necessary. Hence, the constrained filter is simply given by Eq. 3.41. Under the assumption of equivalent initial values for the state parameters, the choice of  $\hat{\mathbf{x}}_k^+$  or  $\tilde{\mathbf{x}}_k^+$  as constrained a priori estimate in the prediction step yields the same constrained state estimate (Simon, 2010). In case of using  $\tilde{\mathbf{x}}_k^+$  as constrained a priori estimate, separate prediction and filtering steps for the constrained filter have to be implemented.

Depending on the choice of  $\mathbf{W}$  in Eq. 3.41 different solutions for the constrained estimates are obtained. The maximum probability estimate of the state according to state constraints is obtained if  $\mathbf{W} = \mathbf{Q}_{\tilde{\mathbf{x}}\tilde{\mathbf{x}}_{k+1}^+}^{-1}$  in case that Gaussian process and measurement noise are assumed. The least-squares estimate of the state according to state constraints is obtained for  $\mathbf{W} = \mathbf{I}$ . For comprehensive discussion and full derivation of the statistical properties is referred to Simon and Chia (2002).

The cofactor matrix of the constrained state parameters can be obtained by means of the LOP

$$\mathbf{Q}_{\tilde{\mathbf{x}}\tilde{\mathbf{x}}_{k+1}^+} = \mathbf{Q}_{\hat{\mathbf{x}}\hat{\mathbf{x}}_{k+1}^+} - \mathbf{Q}_{\hat{\mathbf{x}}\tilde{\mathbf{x}}_{k+1}^+} \cdot \mathbf{D}^T \cdot (\mathbf{D} \cdot \mathbf{Q}_{\tilde{\mathbf{x}}\tilde{\mathbf{x}}_{k+1}^+} \cdot \mathbf{D}^T)^{-1} \cdot \mathbf{D} \cdot \mathbf{Q}_{\tilde{\mathbf{x}}\tilde{\mathbf{x}}_{k+1}^+}. \quad (3.42)$$

### 3.2.5.2. Estimate projection to consider non-linear constraints

Suppose that we have the non-linear constraints

$$\mathbf{g}(\mathbf{x}_k) = \bar{\mathbf{d}} \quad (3.43)$$

where  $\mathbf{g}(\cdot)$  denotes a known non-linear function of the constraints.  $\bar{\mathbf{d}}$  is a  $s \times 1$  vector, which holds the numerical values to fulfil the constraints. The consideration of constraints given in Eq. 3.43 is handled by means of the projection approach, but firstly a linearisation of the non-linear constraints by, e.g., Taylor series expansion around  $\hat{\mathbf{x}}_{k+1}^-$  has to be done. Comparable to the handling of non-linearities in the state-space equations (Section 3.2.2), further approaches (e.g., UKF) can be utilised to deal with the non-linearities (cf. Simon, 2010).

By restricting the Taylor series expansion to the first-order term and substituting the result in Eq. 3.43 follows

$$\underbrace{\mathbf{g}'(\hat{\mathbf{x}}_{k+1}^-)}_{\mathbf{D}} \cdot \mathbf{x}_{k+1} = \bar{\mathbf{d}} - \underbrace{\mathbf{g}(\hat{\mathbf{x}}_{k+1}^-)}_{\mathbf{d}} + \underbrace{\mathbf{g}'(\hat{\mathbf{x}}_{k+1}^-)}_{\mathbf{d}} \cdot \hat{\mathbf{x}}_{k+1}^- \quad (3.44)$$

As can be seen from Eq. 3.44, the formulation of the non-linear constraints can be rewritten and, hence, it is equivalent to the linear constraints in Eq. 3.40 and 3.41.

## 3.3. Transversal prediction and filtering by means of least-squares collocation

In the field of geodesy, the approach of LSC has been introduced by Moritz (1962). This approach unifies the three main tasks: parameter estimation, filtering and prediction (Moritz, 1980, p. 133). Although, LSC was primarily used to determine the gravity field, it is meanwhile used in many other fields of geodesy, for example to determine satellite orbits (Moritz, 1980) or to predict atmospheric fields (troposphere or ionosphere) (Teunissen, 2006). In addition to it, Teunissen (2006) propose a generalised LSC approach which is capable to account for integer values for the trend parameters. This is different to the LSC with the underlying trend-signal-noise model (Moritz, 1980) which handles real-valued trend parameter.

In LSC, the vector of residuals  $\mathbf{v}$  is defined according to the GHM introduced in Eq. 3.7

$$\mathbf{v} = \mathbf{H} \cdot \mathbf{x} + \mathbf{R} \cdot \mathbf{s} - \mathbf{y}, \quad (3.45)$$

where  $\mathbf{R}$  denotes a  $n_y \times (r - n_y)$  matrix of known coefficients and  $\mathbf{s} \in \mathbb{R}^{(r-n_y)}$  is the signal vector. The further quantities are defined as in Section 3.1.2. In the model given in Eq. 3.45 the sum of  $\mathbf{y}$  and  $\mathbf{v}$  is equal to the trend, the regular systematic part  $\mathbf{H} \cdot \mathbf{x}$ , and an additional stochastic irregular systematic part  $\mathbf{R} \cdot \mathbf{s}$ , known as signal, see Koch (1999, pp. 221 ff.).

The purpose of LSC is the separation of the mentioned parts: The optimal trend parameters are estimated by means of adjustment, while the influence of the measurement noise is reduced by the filtering. Trend and signal between data points are determined by prediction. Whereas the trend is predictable by means of the estimated trend parameters, the signal's prediction requires VCMs. Stochastic relationships of adjacent signal values are utilised to build these matrices. For assumed normally distributed and mutually independent noise and signal, the stochastic model can be written as (Welsch et al., 2000, p. 182)

$$V \left( \begin{bmatrix} \mathbf{v} \\ \mathbf{s} \\ \mathbf{s}' \end{bmatrix} \right) = V(\bar{\mathbf{v}}) = \begin{bmatrix} \Sigma_{\mathbf{v}\mathbf{v}} & \mathbf{0} & \mathbf{0} \\ \mathbf{0} & \Sigma_{\mathbf{s}\mathbf{s}} & \Sigma_{\mathbf{s}\mathbf{s}'} \\ \mathbf{0} & \Sigma_{\mathbf{s}'\mathbf{s}} & \Sigma_{\mathbf{s}'\mathbf{s}'} \end{bmatrix} = \bar{\sigma}_0^2 \cdot \begin{bmatrix} \mathbf{Q}_{\mathbf{v}\mathbf{v}} & \mathbf{0} & \mathbf{0} \\ \mathbf{0} & \mathbf{Q}_{\mathbf{s}\mathbf{s}} & \mathbf{Q}_{\mathbf{s}\mathbf{s}'} \\ \mathbf{0} & \mathbf{Q}_{\mathbf{s}'\mathbf{s}} & \mathbf{Q}_{\mathbf{s}'\mathbf{s}'} \end{bmatrix}. \quad (3.46)$$

Here  $V(\cdot)$  is the variance operator and  $\mathbf{s}'$  is the predicted signal vector.  $\Sigma_{\mathbf{v}\mathbf{v}}$ ,  $\Sigma_{\mathbf{s}\mathbf{s}}$  and  $\Sigma_{\mathbf{s}'\mathbf{s}'}$  denote the VCMs of the measurement noise, the signal and the predicted signal, respectively. While  $\bar{\sigma}_0^2$  is the (theoretical)

variance factor of unit weight and  $\mathbf{Q}_{\mathbf{v}\mathbf{v}}$ ,  $\mathbf{Q}_{\mathbf{s}\mathbf{s}}$  and  $\mathbf{Q}_{\mathbf{s}'\mathbf{s}'}$  denote the corresponding cofactor matrices. The VCM of observations can be utilised to set up  $\Sigma_{\mathbf{v}\mathbf{v}}$ . The set up of the lower block dealing with the VCMs of  $\mathbf{s}$  and  $\mathbf{s}'$  is the main problem. It can be solved by covariance functions which can be derived based on observed data.

### 3.3.1. Estimation of covariance functions

Covariance functions are used in time series analysis to model stochastic relationships between one or more time series (Welsch et al., 2000). In order to estimate these functions, the underlying stochastic process has to fulfil the conditions of stationarity and ergodicity (Koch and Schmidt, 1994). As these two conditions are unfulfilled for time series containing a deterministic trend, this trend has to be removed. By means of regression analysis the corresponding trend function can be estimated.

The empirical autocovariance function  $C(d)$  can be computed by means of the values  $\xi_i$ , with  $i = 1 \dots n_\xi$ . The difference between the original measurements and the pre-estimated trend is denoted by  $\xi_i$ .  $C(d)$  can be expressed as a function of the distance  $d$ . For the simple case of homogeneous regular time series  $d$  can be the difference of multiple time steps and it follows

$$C(d) = C_\xi(d) = \frac{1}{n_\xi - d - 1} \cdot \sum_{i=1}^{n_\xi-d} (\xi_i - \bar{\xi}) \cdot (\xi_{i+d} - \bar{\xi}). \quad (3.47)$$

In Eq. 3.47,

$\bar{\xi}$  denotes the mean value of the time series  $\xi$  and  $n_\xi$  is the number of measured values. Due to the computation accuracy of the above-mentioned function,  $d$  is defined for time differences from  $0 \dots m = \frac{n}{10}$  (Welsch et al., 2000, p. 323). It is noteworthy that Eq. 3.47 yields for  $d = 0$  the empirical variance. For ease of comparison of different autocovariance functions, they are normalized by  $C(0)$ . The result of this normalization is the empirical autocorrelation function

$$K(d) = K_\xi(d) = C(d)/C(0). \quad (3.48)$$

To obtain stochastic relationships between two different time series  $\xi$  and  $\eta$ , cross-covariance functions  $C_{\xi\eta}(d)$  can be used by taking values of both different time series in Eq. 3.47. For the corresponding cross-correlation functions  $K_{\xi\eta}(d)$  follows

$$K_{\xi\eta}(d) = C_{\xi\eta}(d)/\sqrt{C_\xi(0) \cdot C_\eta(0)}. \quad (3.49)$$

Those empirical functions provide the basis for the determination of analytical correlation functions  $\hat{K}_\xi(d)$  and  $\hat{K}_{\xi\eta}(d)$ , which are estimated by means of the values of the empirical functions using regression analysis. Typical analytical covariance and correlation functions can be selected from exponential, Gaussian or damped oscillations functions. Koch et al. (2010) report on the approximation of covariance matrices estimated in multivariate models by estimated auto- and cross-covariances. By means of analytical functions the VCM  $\Sigma$  and respective cofactor matrix  $\mathbf{Q}$  can be computed as follows

$$\Sigma = C(0) \cdot \mathbf{Q} = C(0) \cdot \begin{bmatrix} 1 & \hat{K}(1) & \hat{K}(2) & \dots & \dots \\ \hat{K}(1) & 1 & \hat{K}(1) & \ddots & \vdots \\ \hat{K}(2) & \hat{K}(1) & 1 & \ddots & \hat{K}(2) \\ \vdots & \ddots & \ddots & \ddots & \hat{K}(1) \\ \vdots & \dots & \hat{K}(2) & \hat{K}(1) & 1 \end{bmatrix}. \quad (3.50)$$

The properties of the VCM restrict the choice of the functions, which can be used to build the VCMs given in Eq. 3.46. On the one hand, the functions have to be positive definite, on the other hand the correlations which are calculated by means of these functions have to take values from  $[-1, 1]$ .

### 3.3.2. Least-squares collocation

The LSC by means of GHM is given through an extension of the functional model in Eq. 3.45 with the predicted signal  $\mathbf{s}'$  due to the mutually dependency of  $\mathbf{s}'$  and  $\mathbf{s}$  according to Eq. 3.46. Thus, the functional model for the LSC is given by the following GHM

$$\mathbf{H} \cdot \mathbf{x} + \underbrace{\begin{bmatrix} -\mathbf{I} & \mathbf{R} & \mathbf{0} \end{bmatrix}}_{:=\mathbf{U}^T} \cdot \underbrace{\begin{bmatrix} \mathbf{v} & \mathbf{s} & \mathbf{s}' \end{bmatrix}^T}_{:=\hat{\mathbf{v}}^T} - \mathbf{y} = \mathbf{0}. \quad (3.51)$$

Refer to Section 3.1.2 for the definitions of the quantities in the GHM. The normal equation system of GHM (Eq. 3.9) is obtained by applying the method of least-squares on Eq. 3.51. Following the derivations in Welsch et al. (2000, pp. 178 ff.), the three main parts of LSC: the parameter estimation, the filtering of the signal and the prediction are given by

$$\begin{bmatrix} \hat{\mathbf{v}} \\ \hat{\mathbf{s}} \\ \hat{\mathbf{s}}' \end{bmatrix} = \begin{bmatrix} -\mathbf{Q}_{\mathbf{v}\mathbf{v}} \cdot \hat{\mathbf{k}} \\ \mathbf{Q}_{\mathbf{s}\mathbf{s}} \cdot \mathbf{R}^T \cdot \hat{\mathbf{k}} \\ \mathbf{Q}_{\mathbf{s}'\mathbf{s}} \cdot \mathbf{R}^T \cdot \hat{\mathbf{k}} \end{bmatrix}. \quad (3.52)$$

Here  $\hat{\mathbf{k}}$  denotes the Lagrange multipliers

$$\hat{\mathbf{k}} = \underbrace{\mathbf{M}^{-1} \cdot \left( \mathbf{M} - \mathbf{H} \cdot (\mathbf{H}^T \cdot \mathbf{M}^{-1} \cdot \mathbf{H})^{-1} \cdot \mathbf{H}^T \right)}_{:=\bar{\mathbf{K}}} \cdot \mathbf{M}^{-1} \cdot \mathbf{y} \quad \text{with} \quad \mathbf{M} = \mathbf{Q}_{\mathbf{y}\mathbf{y}} + \mathbf{R} \cdot \mathbf{Q}_{\mathbf{s}\mathbf{s}} \cdot \mathbf{R}^T. \quad (3.53)$$

The corresponding VCMs of  $\hat{\mathbf{v}}$ ,  $\hat{\mathbf{s}}$  and  $\hat{\mathbf{s}}'$  given in Eq. 3.52 can be derived using the LOP

$$\mathbf{Q}_{\hat{\mathbf{v}}\hat{\mathbf{v}}} = \mathbf{Q}_{\mathbf{v}\mathbf{v}} \cdot \mathbf{Q}_{\hat{\mathbf{k}}\hat{\mathbf{k}}} \cdot \mathbf{Q}_{\mathbf{v}\mathbf{v}}, \quad (3.54)$$

$$\mathbf{Q}_{\hat{\mathbf{s}}\hat{\mathbf{s}}} = \mathbf{Q}_{\mathbf{s}\mathbf{s}} \cdot \mathbf{R}^T \cdot \mathbf{Q}_{\hat{\mathbf{k}}\hat{\mathbf{k}}} \cdot \mathbf{R} \cdot \mathbf{Q}_{\mathbf{s}\mathbf{s}} \quad \text{and} \quad (3.55)$$

$$\mathbf{Q}_{\hat{\mathbf{s}}'\hat{\mathbf{s}}'} = \mathbf{Q}_{\mathbf{s}'\mathbf{s}} \cdot \mathbf{R}^T \cdot \mathbf{Q}_{\hat{\mathbf{k}}\hat{\mathbf{k}}} \cdot \mathbf{R} \cdot \mathbf{Q}_{\mathbf{s}'\mathbf{s}} \quad (3.56)$$

with  $\mathbf{Q}_{\hat{\mathbf{k}}\hat{\mathbf{k}}} = \bar{\mathbf{K}}^T \cdot \mathbf{Q}_{\mathbf{v}\mathbf{v}} \cdot \bar{\mathbf{K}}$ .

To complete the stochastic model of LSC, appropriate covariance functions are estimated. In Section 6.1.2 the presented LSC according to Moritz (1980) is used to investigate the prediction and filtering of high resolution 3D GNSS trajectories, which are utilised in the proposed direct geo-referencing methodology.



## 4. Conceptual design and realisation of a multi-sensor system

In this thesis, a MSS is developed in order to directly provide the transformation parameters and their uncertainty information for the purpose of direct geo-referencing of 3D point clouds. Therefore, GNSS equipment and optional inclinometers are proposed to be installed on top of a stationary laser scanner.

The proposed conceptual design and its prototype for the direct geo-referencing methodology are presented in Section 4.1 and Section 4.2, respectively. In particular, Section 4.2.1 deals with the selected sensors including the topic synchronisation for the MSS, since this topic has an importance for the implementation of the proposed design. The proposed GNSS analysis strategy is introduced in Section 4.2.2. A concept for the direct derivation of the transformation parameters and their corresponding uncertainties is proposed in Section 4.2.3.

Individual performance test results of each sensor of the MSS are presented in Section 4.3. In particular, Section 4.3.1 reports on investigations of the laser scanner in the context of its use in the MSS. A thorough review of possible errors induced by the rotation of the GNSS antennas is given in Section 4.3.2. Section 4.3.3 briefly outlines the inclinometer performance in the MSS. The subject of calibration in terms of establishing a unique spatial reference for all sensors in the MSS is discussed in Section 4.3.4. Concluding remarks and an uncertainty assessment are provided in Section 4.3.5.

### 4.1. Conceptual design of a multi-sensor system for direct geo-referencing purposes

This section presents the conceptual design of a MSS to solve the task of direct geo-referencing of a stationary laser scanner by means of physically attached sensors to the laser scanner. The general demand and the procedure for geo-referencing in TLS applications are introduced in Section 2.2.1. As a reminder, to solve the geo-referencing task six DoF (namely the translation and rotation between the two involved 3D coordinate systems) have to be determined. Referring to the concluding remarks of the reviewed state of research and to Section 2.2.2, we can conclude that the direct geo-referencing by means of external sensors (e.g., Reshetyuk, 2009) is an appropriate choice to determine the six DoF. The use of physically attached sensors to the laser scanner (e.g., Paffenholz and Kutterer, 2008, Wilkinson et al., 2010) shows great promise in terms of efficiency. The conceptual design for a MSS proposed here is based on the MSS suggested by Paffenholz and Kutterer (2008) and will be introduced in the following. Tab. 4.1 summarises the details of the proposed MSS.

The usage of panoramic-type or hybrid scanners is advantageous due to their horizontal rotation about  $360^\circ$  during its data acquisition. Therefore, the circular and constant rotation of the laser scanner about its vertical axis can be exploited as a function of time and orientation reference (Hesse and Kutterer, 2007). For a simultaneous data acquisition, these sensors must be capable for kinematic measurements. Furthermore, a proper synchronisation has to be established for the association of the horizontal rotation steps of the laser scanner and the external sensor measurements.

In order to maintain the compactness of the MSS and prevent any unnecessary systematic errors by an inclined rotation axis of the laser scanner, the number of additional sensors must be kept as small as possible. For that reason high-end and costly IMUs are not considered to be implemented. Instead, standard surveying equipment is proposed to use, e.g., GNSS equipment, total stations and inclinometers. The pros and cons of the utilisation of low-cost sensors will be discussed in Section 4.3.

The first developmental step for the MSS is to design a support structure on top of the laser scanner to mount either GNSS antennas or prism, which provide time series of 3D coordinates to determine the translation parameters and relevant uncertainty information. The orientation parameters can be indirectly derived by the

Table 4.1.: Requirements for a MSS for direct geo-referencing purposes and proposals to fulfil them.

Requirement	Proposal to meet the requirement
<i>Exploit the 360° rotation</i> of the laser scanner about its vertical axis as a function of time and orientation reference.	<ul style="list-style-type: none"> <li>– Use of panoramic-type or hybrid scanner.</li> <li>– Continuous data acquisition of additional sensors with synchronisation capabilities.</li> </ul>
Use a <i>minimal number of additional sensors</i> to keep the MSS compact and simple regarding complexity and operability.	<ul style="list-style-type: none"> <li>– Study the pros and cons of low-cost sensors and standard surveying equipment regarding the uncertainty requirements.</li> </ul>
Obtain translation and orientation parameters by means of <i>only physically attached sensors</i> and provide an universal concept for the additional sensors.	<ul style="list-style-type: none"> <li>– Design an adequate support structure to mount the additional sensors.</li> <li>– Allow an exchange of the additional sensors while using the same support structure.</li> <li>– Develop a flexible algorithm which is not predefined to a specific sensor.</li> </ul>
Obtain an <i>uncertainty</i> with an assumed significance level of 95% for a single point of the geo-referenced 3D point clouds of $\leq 5$ cm (Helmert's point error) in a distance of 30 m, which is suitable for scenarios like, e. g., as-built documentation.	<ul style="list-style-type: none"> <li>– The position must be determined with a discrepancy of a few centimetres or even a couple of millimetres to the expectation value.</li> <li>– The orientation must be determined with a discrepancy of <math>\leq 0.08^\circ</math> to the expectation value to fulfil the requirement.</li> </ul>
Provide <i>uncertainty measures of the transformation parameters</i> for subsequent analyses.	<ul style="list-style-type: none"> <li>– Use an algorithm based on, e. g., least-squares adjustment or state-space filtering (e. g., KF).</li> </ul>
<i>Increase the efficiency</i> of the field work flow by waiver/reduction of control points to a minimum.	<ul style="list-style-type: none"> <li>– Rely only on physically attached sensors to the laser scanner.</li> </ul>

3D positions. It is important to remember that, by orientating the laser scanner to the direction of gravity, i. e., levelling, the only remaining spatial orientation around the vertical axis (heading) needs to be determined. This procedure is feasible for all recent laser scanners by means of integrated inclinometers, which leads us to only determine four DoF, i. e., three translational parameters and the heading.

The transformation parameters for stationary laser scanners are constant during the data acquisition at each site. The position can be determined by total stations or GNSS equipment with a discrepancy of a few centimetres or even a couple millimetres to the expectation value based on kinematic measurements. In order to fulfil the required uncertainty with an assumed 95%-significance level of  $\leq 5$  cm (Helmert's point error) for a single point in a geo-referenced 3D point cloud within a range of 30 m (typical scanning distance), the most challenging task is the determination of the heading. The primary focus is on the heading determination by means of the available time series of 3D positions. Furthermore, a recursive state-space filter, e. g., KF, is also proposed to be utilised to the time series of the 3D positions, which provides filter and smoothing capabilities. Due to the involvement of several 3D positions in the determination of the transformation parameters the redundancy is higher compared to the use of single measurements.

## 4.2. Prototypic realisation of the conceptual design

This section presents the prototypic realisation of a MSS which is based on the conceptual design. The core sensor is a panoramic-type laser scanner which comes along with physically attached 3D positioning sensors as

well as levelling capabilities. Primary, the MSS is designed for outdoor applications. Thus, from the group of 3D positioning sensors both types introduced in Section 2.2.4.1 are applicable. Total stations need extra sites to track the attached prism whereas the entire GNSS equipment can be directly attached to the laser scanner. It is worth noting that in order to obtain 3D positions by means of GNSS equipment with a few  $10^{th}$  millimetres uncertainty at least one reference station is required (Section 4.2.2). In the following, GNSS equipment has been selected for the 3D positioning. Nevertheless, the interchangeability of the 3D positioning sensor is taken into consideration for the construction of a proper support structure as well as for the algorithm (to obtain the desired transformation parameters). According to the conceptual design, a minimum number of additional sensors is integrated in the MSS on the one hand. On the other hand, 3D positions instead of extra sensors are proposed to use for the determination of the orientation. In the following, inclinometers are used for the laser scanner setup as well as for investigations of the MSS. At this developmental stage, IMUs and compasses are not considered due to the slightly increasing orientation change of the laser scanner. To obtain reliable measurements the usage of high-end and costly equipment would be necessary. Their weights and physical dimensions are not suitable to meet the requirement of compactness for the MSS. The corresponding low-cost sensors are characterised with higher measurement noises. Especially digital compasses are subject to magnetic disturbances (e.g., Grejner-Brzezinska et al., 2011). Thus, the integration of low-cost sensors in the MSS demands separate investigations.

#### 4.2.1. Sensors in the multi-sensor system

The operation of the laser scanner should neither be restricted nor disturbed by the additional sensors. Hence, the advantage of the individual characteristics of any sensor in the MSS should be taken into account. Fig. 4.1 shows a sketch of the MSS. The indicated components are explained in the following. Tab. 4.2 summarises the used sensors with their specifications<sup>1</sup> and their task in the MSS.

**Laser scanner and wing support structure to mount additional sensors:** According to the requirements listed in Tab. 4.1, the laser scanner of choice is a panoramic-type laser scanner. The requirement of exploitation the  $360^\circ$  rotation as a function of time and orientation reference can be fulfilled by this laser scanner type.

In this thesis the phase-measuring laser scanner Z+F IMAGER 5006, manufacturer Zoller + Fröhlich GmbH, is used. This laser scanner is designed for stationary 3D point cloud acquisitions for distances up to  $\approx 80$  m. This is realised with a high spatial resolution (a few millimetres for mean distances of about 25 m) as well as with a very high frequency (up to 50 profiles per second) in a local sensor-defined coordinate system termed *L*-frame. The *x*-axis points to the scan direction and the *y*-axis is perpendicular to the scan direction counting positive in direction of  $\mathbf{p}^\circ$ . The *z*-axis which corresponds to the rotation axis completes the left-handed coordinate system. This *L*-frame is predefined by the manufacturer. A typical set of parameters for a 3D point cloud obtained by the Z+F IMAGER 5006 is a scanning resolution of about 10000 2D vertical profiles per horizontal rotation of  $360^\circ$ . With a frequency of 12.5 profiles per second this leads to an acquisition time of about 13 min. The manufacturer's specifications of the Z+F IMAGER 5006 can be found in Section B.1.

The Z+F IMAGER 5006 is also equipped with a built-in dual-axis inclinometer<sup>1</sup> with a resolution of  $0.001^\circ$  and a measurement range of  $\pm 1.5^\circ$  (Section B.1). The inclinometer is designated (by the manufacturer of the laser scanner) for the orientation of the laser scanner to the direction of gravity. Moreover, the inclinometer measurements before and after the scanning procedure are compared with each other. This comparison allows a statement regarding to abnormal movements of the laser scanner and subsequent changes in the orientation to

<sup>1</sup>For the full specifications of the used sensors (given in Tab. 4.2) the reader is referred to Appendix B.

<sup>1</sup>According to the hardware query of the used Z+F IMAGER 5006 at the Geodetic Institute, Leibniz Universität Hannover, Germany, the built-in inclinometer is of type NS/AAL2-UDD, manufacturer Measurement Specialties. The measurement principle of this inclinometer is based on changes of a electrolytic fluid level over electrodes.

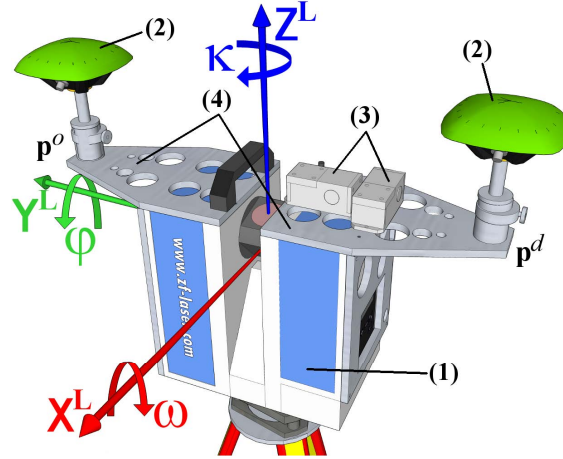


Figure 4.1: Prototypic realisation of the MSS: (1) Phase measuring laser scanner Z+F IMAGER 5006 with its manufacturer defined left-handed coordinate system (L-frame), (2) Javad GrAnt G3T GNSS antenna, (3) Schaevitz LSOC-1° inclinometer, (4) Wing support structure with positions  $\mathbf{p}^d$  and  $\mathbf{p}^o$  (eccentrically arranged with respect to the laser scanner's reference point).

Table 4.2.: Sensors with their specifications and tasks in the MSS.

Type / Name	Specifications <sup>1</sup>	Task / measured quantity
(1) Phase measuring laser scanner Z+F IMAGER 5006	Range noise of 4 mm rms @50 m (20% reflectivity); $\approx 10000$ 2D profiles per horizontal rotation of $360^\circ$	3D point cloud (composed of several 2D vertical profiles)
(2) Javad GrAnt G3T GNSS antenna connected to a Javad TRE G3T Delta receiver	GPS and GLONASS observations; 10 20 Hz data rate; synchronisation capabilities by PPS signal and event marker input	3D positions describing the motion of the MSS
(3) Schaevitz LSOC-1° inclinometer	Single-axis inclinometers; resolution of $0.1''$ ; measurement range of $\pm 1^\circ$	Supporting the orientation to the direction of gravity; residual spatial rotations
(4) Wing support structure	Symmetric support structure made from aluminium with two pre-defined positions $\mathbf{p}^d$ and $\mathbf{p}^o$ with a maximum distance of about 0.6 m	Provide space for mounting sensors

the direction of gravity during the laser scanner's data acquisition. The preset configuration does not take inclinometer measurements during the scanning procedure. Nevertheless, the acquisition of measurements and their storage for each profile can be forced by an additional scanning parameter. A synchronisation is immediately given due to the storage of measurements for each profile.

To physically attach the additional sensors to the laser scanner body an adequate support structure is developed (Brieden, 2009). For the prototypic MSS the support structure is made from aluminium. Thereby, a compromise is achieved, which considers a minimal weight as well as maximum stability regarding additional sensor weights and temperature. The developed wing support structure and its influence on the laser scanner are treated in Section 4.3.1. The wing support structure consists of two parts ("wings") which are attached on each of the symmetric body sides of the laser scanner (cf. Fig. 4.1). Each "wing" is capable to carry one 3D positioning sensor (e. g., GNSS antenna or prism) and further navigation sensors like inclinometers. The wing support structure allows the realisation of a maximum distance of about 0.6 m for two 3D positioning sensors in

$\mathbf{p}^d$  and  $\mathbf{p}^o$ . This results in a diametrical constellation. During the laser scanner's rotation about its vertical axis the sensors in  $\mathbf{p}^d$  and  $\mathbf{p}^o$  describe 3D circles. The centre points of the 3D circles correspond to the laser scanner's reference point besides an offset in each coordinate component. The relative positions of the additional sensors on the wing support structure with respect to the laser scanner's reference point are discussed in Section 4.3.4.

**GNSS equipment:** The 3D positioning sensor of choice is GNSS equipment, i.e., a pair of antenna and receiver. At least one GNSS equipment is required to perform the direct geo-referencing of the MSS and to fulfil most of the requirements in Tab. 4.1. The fulfilment of the uncertainty requirement is a challenging task because of the kinematic data acquisition for the short period of a  $360^\circ$  rotation of the laser scanner. The usage of one or two GNSS equipments offers different approaches within the GNSS analysis which are discussed in the next section.

In the conducted experiments different types of GNSS equipments are used. However, in all cases the receiver Javad TRE G3T Delta is used. This receiver is capable for GPS and GLONASS observations with data rates up to 100 Hz. The typically used data rate is 10 – 20 Hz. Furthermore, the receiver provides synchronisation capabilities by the PPS signal and the event marker input.

In case of only one involved GNSS equipment, the Javad GrAnt G3T antenna is connected to the receiver. For experiments with two involved antennas, two identical Leica LEIAX1202GG antennas are connected to two similar Javad TRE G3T Delta receivers.<sup>2</sup> All GNSS antennas are individually and absolutely calibrated based on the Hannover concept at the Institut für Erdmessung (IfE), Leibniz Universität Hannover, Germany (Section 2.2.4.1). For further specifications of the GNSS equipment the reader is referred to Section B.3. Detailed information of the used receiver and antenna as well as the acquisition parameters are mentioned separately in each experimental study.

The GNSS antennas are mounted in  $\mathbf{p}^d$  and  $\mathbf{p}^o$  on the wing support structure (Fig. 4.1). Following the conceptual design, the 3D circles described by the GNSS ARPs are utilised for the estimation of the transformation parameters. Since precise 3D GNSS positions are required, especially to obtain reliable orientation parameters, the GNSS equipment is separately treated in Section 4.3.2. In particular, the special usage in terms of  $360^\circ$  rotations of the GNSS equipment is thoroughly investigated.

**Inclinometers:** Two kind of inclinometers are available in the prototypic MSS: on the one hand the already introduced built-in dual-axis inclinometer of the Z+F IMAGER 5006 and externally adapted inclinometers on the other hand. Latter ones are two single-axis Schaevitz LSOC-1° inclinometers with a resolution of 0.1" and a measurement range of  $\pm 1^\circ$  (Section B.2). They are installed each corresponding with a axis of the  $x$ - $y$ -plane (Fig. 4.1). The Schaevitz inclinometer is a gravity referenced servo inclinometer. The measurement principle is based on a pendulous mass attached to a torque motor. A tilt of the inclinometer will induce a movement of the pendulous mass. This position change is detected by a position sensor which produces an error signal. This error signal controls the torque motor to move the pendulous mass to its former position. The demanded electricity is the measure for the tilt, which is provided as analogous data. An external computer with Real-Time Operating System (RTOS) and integrated A-D converter is used to digitise the analogous data and to provide the data with time stamps. Further information regarding the external computer for synchronisation purposes are presented in the subsequent paragraph.

Since the MSS is designed for stationary data acquisition, a rough orientation of the laser scanner to the direction of gravity in a range of  $5'$  can be performed by a bullseye level. Thus, only residual spatial rotations about the  $x$ - and  $y$ -axis of the MSS are remaining. Aforementioned, built-in inclinometer of the Z+F IMAGER 5006 is used to improve the rough levelling of the bullseye level. It is noteworthy that owing to the orientation to the direction of gravity the use of inclinometers is non-compulsory. Assuming a sufficient orientation to the

<sup>2</sup>The author acknowledges the support with parts of the GNSS equipment which was provided by Prof. S. Schön, who is with the Institut für Erdmessung, Leibniz Universität Hannover, Germany

direction of gravity, remaining variations for the  $z$ -axis, which occur during the rotation of the laser scanner about its vertical axis, are expressed by the trunnion axis error or wobble of vertical axis (Schulz, 2007). Due to the slow-going horizontal rotation of the laser scanner about its vertical axis, no significant influences are expected on the inclinometer measurements caused by their rotation with the laser scanner (Section 4.3.3).

**Synchronisation aspects:** The general task of synchronisation of sensor measurements is outlined in Section 2.2.4.3. In the particular case of the prototypic MSS, the synchronisation of the laser scanner, the 3D positioning sensors as well as the optional inclinometers has to be realised. These synchronised data are used in recursive state-space filters, like KF, to solve the direct geo-referencing.

Due to the usage of GNSS equipment it is straightforward to make use of the GPS time as unique time reference in the MSS. The data of the laser scanner, optional inclinometers and (if available) total stations are not immediately provided with GPS time stamps. A proper way to incorporate this information for the acquired data has to be chosen.

The Z+F IMAGER 5006 has synchronisation capabilities with the line synchronisation pulse, which is emitted for each rotation of the mirror (i. e., for each 2D vertical profile). In the MSS, this pulse is registered by the GNSS receiver event marker input. Thus, a specific entry is added to the GNSS observation file for each pulse. Analogous and serial data streams, as provided for the inclinometer and total station measurements, can not be registered by the GNSS receiver event marker input. Instead an external computer with RTOS, integrated A-D converter, I/O interfaces and serial interfaces is used. The used external computer in the MSS is the decentralized, intelligent I/O systems MAX5*dip*<sup>3</sup> by Sorcus GmbH, Heidelberg, Germany. For comprehensive information about the MAX5*dip* in a similar synchronisation scenario, in terms of the involved sensors, the reader is referred to Hesse (2007). Next to the analogous data of the optional (Schaevitz) inclinometers, (optional) serial data of total stations, the PPS signal and a National Marine Electronics Association (NMEA) sentence are inputs to the MAX5*dip*. A suitable NMEA sentence to provide GPS time information is the NMEA sentence ZDA<sup>4</sup>. In addition, the line synchronisation pulse of the laser scanner can be registered a second time. The PPS signal and the NMEA sentence ZDA are used to introduce the GPS time to the internal time scale of the MAX5*dip*.

#### 4.2.2. GNSS analysis strategy

This section deals with the kinematic GNSS analysis strategy, which provides time series of 3D positions and their corresponding VCMs. These 3D positions and VCMs are used to estimate position and orientation information of the MSS by means of recursive state-space filtering. Consequently, the quality of the estimated transformation parameters of the MSS are depending on the GNSS analysis. Therefore, in this section the following aspects are discussed: First, some general remarks are given concerning the processing of the GNSS observations. This also covers the mathematical approach (epoch-wise versus filter-based point estimation) within the GNSS analysis, which itself affects the quality of the 3D position estimation. Second, the topic of the number of GNSS equipments (whether one or two) in the MSS is revisited.

**Processing of the GNSS observations:** The GNSS data processing can be performed either in post-processing or in real-time, depending on the used equipment and available infrastructure. The different positioning modes are introduced in Section 2.2.4.1. Here, relative positioning in post-processing is utilised to obtain the 3D positions of the ARP during the 360° rotation of the laser scanner about its vertical axis. At this developmental stage, real-time processing is not required but is possible in general. As a result, higher variances for the 3D positions of the ARP trajectory are expected for real-time processing (cf. e. g., Hofmann-Wellenhof et al., 2008). Meanwhile, the short observation time of about 13 min makes the GNSS analysis a challenging

<sup>3</sup>For detailed information regarding the specifications the reader is referred to the company website [www.sorcus.com](http://www.sorcus.com).

<sup>4</sup>For information regarding the NMEA sentences the reader is referred to, e. g., the GNSS equipment's documentation.

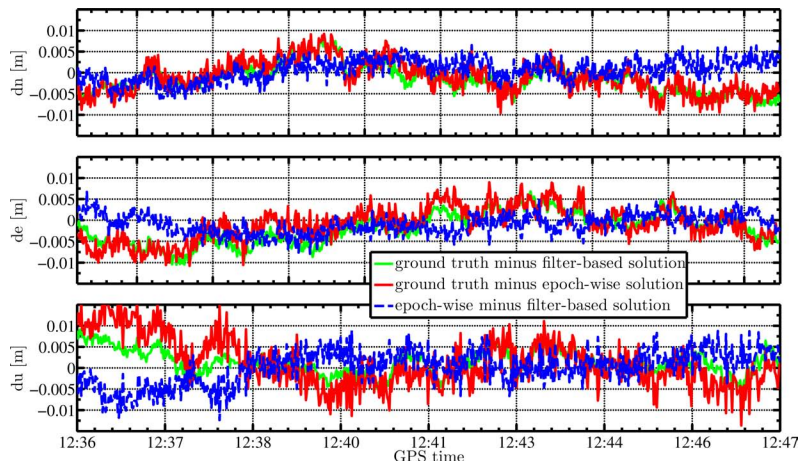


Figure 4.2: Difference of NEU coordinates of epoch-wise solution (Wa1) and filter-based solution (GNSMART). The shown differences are calculated between the ground truth and the epoch-wise solution (red) as well as the filter-based solution (green). Furthermore, the direct difference of both solutions is calculated (blue).

Table 4.3.: Numerical values for comparison of epoch-wise and filter-based solution for 3D position estimation in Fig. 4.2.

	$dn$ [m]		$de$ [m]		$du$ [m]	
	min	max	min	max	min	max
ground truth minus filter-based solution	-0.008	0.008	-0.011	0.007	-0.006	0.011
ground truth minus epoch-wise solution	-0.010	0.009	-0.011	0.009	-0.014	0.019
difference of epoch-wise and filter-based solution	-0.007	0.007	-0.008	0.007	-0.012	0.009

problem which has to be overcome.

For the relative positioning in post-processing, different options are available regarding the GNSS reference station: On the one hand, we can use a service, e.g., the satellite positioning service of the German state survey SAPOS or the satellite positioning services ascos operated by AXIO-NET GmbH, Hannover, Germany. If necessary, both services can provide a virtual reference station. On the other hand, we can utilise an own reference station with known coordinates close to the scanning scene. The coordinates can be determined (if needed) with an aforementioned service.

In addition, two mathematical approaches can be distinguished in the GNSS analysis: First, epoch-wise, independent solutions and, second, the use of filter algorithms, e.g., KF, within the GNSS analysis with a-priori known motion models.

The influence of the two approaches on the 3D position estimation is assessed for the particular MSS with the horizontally rotating GNSS antenna. Therefore, two GNSS analyses with identical parameters for the same time series were performed. The GNSS data was acquired on 2011, Day of Year (DOY)025 (Fig. 4.6(a) shows the GPS satellite configuration). Also, a ground truth trajectory for the circular motion was obtained by simultaneous measurements with a total station, which tracks a  $360^\circ$  prism. The prism was directly attached below the GNSS antenna (cf. Fig. 4.4(d)). The analysis was done with the software Wa1 (Wanninger, 2009b) which provides an independent solution for each epoch. The other analysis was performed with the software GNSMART (Wübbena et al., 2001), which estimates the coordinates within a KF by means of forward and backward filtering. In Fig. 4.2 are depicted the results for the trajectory of the ARP. The result is shown per coordinate component in the North-, East- and Up-axes (NEU) coordinate system with origin in the used nearby reference station (baseline length  $\approx 14$  m). Both solutions correspond in a range of 10 mm with the ground truth (Tab. 4.3). As anticipated, the epoch-wise solution (red) is more noisy compared with the filter-based solution (green). Their direct comparison (blue) fits in a range of 5 mm. Here the noise level of the epoch-wise solution dominates. The noise level of the up-component is slightly larger compared to the north- and east-components.

Especially, the larger noise level of the epoch-wise solution between 12 : 36 GPS time and 12 : 37 GPS time results in larger differences for the direct comparison (blue).

**The number of GNSS equipments:** As a minimum, one GNSS antenna and the knowledge of the centre point of the circular motion are sufficient to determine the transformation parameters. The usage of two GNSS antennas with a specific, in general well-known, distance can also be exploited to obtain orientation information (Section 2.2.4.1). Depending on the used number of GNSS equipments different approaches within the GNSS analysis are possible:

**Single baselines** can be calculated for each involved GNSS antenna with respect to a reference station. As a result, for each ARP a separate 3D circle is obtained. Consequently, this approach is applicable to one or two GNSS equipments. In case of two equipments, for the further analyses are feasible a separate treatment of both 3D circles or their combination in a proper mathematical model.

**A relative baseline** for the two horizontally rotating GNSS antennas can be established. Obviously, this approach can only be applied in case of two GNSS equipments. The results of the GNSS analysis are the 3D baseline components, which can be utilised to obtain at least two spatial rotation parameters. In particular, for the prototypic MSS these are pitch ( $\varphi$ ) and heading ( $\kappa$ ) (cf. Fig. 4.1). Whereas, for a sufficient orientation to the direction of gravity the horizontal rotation of the two GNSS antennas is performed in the  $x - y$ -plane, which yields zero for the pitch. This sketched approach is known in literature as GNSS compass (e.g., Teunissen et al., 2011). The limited baseline length of  $\approx 0.6$  m in the MSS pose a challenge, to obtain heading information with an accuracy level of sub degrees. Typically, the baseline length in GNSS compass approaches is larger than 1 m (cf. Section 2.2.4.2).

**Concluding remarks:** The GNSS analysis is performed in post-processing since real-time availability of the 3D GNSS positions is non-compulsory at this developmental stage of the MSS. It is worth to note that real-time processing is possible in general. Especially, the estimation of the transformation parameters by means of recursive state-space filtering is capable to deal with real-time processed GNSS data.

Regarding the question of epoch-wise and filter-based point estimation, the epoch-wise point estimation is preferred for the following reasons. First, there is only a slight difference of both estimation approaches. Second, the reduction of the noise level of the epoch-wise solution is accounted by the recursive state-space filter approach to obtain the transformation parameters.

In terms of the number of GNSS equipments, the usage of two equipments and the calculation of single baselines are proposed. The algorithm to obtain the transformation parameters will be designed to be flexible in terms of the used equipments and the different baseline information.

#### 4.2.3. Conception of an algorithm to derive the transformation parameters

This section is dedicated to the conception of an algorithm to estimate the transformation parameters. Here, only the basic idea how to solve the direct geo-referencing by means of recursive state-space filtering as well as recursive least-squares adjustment in GMM is introduced. The specific mathematical realisation is formulated in Section 5.2. Revisiting the requirements proposed in Tab. 4.1, the algorithm should be independent in terms of a specific 3D positioning sensor (e.g., either GNSS equipment or total station measurements towards a prism) and should be ready for an optional incorporation of other sensor types and corresponding measurements like inclinometers and compasses. In addition to the transformation parameters corresponding uncertainty measures for subsequent analyses should be provided. First, the preconditions and assumptions for the algorithm are pointed out. Second, the qualification of recursive state-space filtering as the basis for the algorithm is clearly stated. Third, the state parameters for the MSS and their connection to the required transformation parameters are introduced. Finally, Alg. 4.1 summarises the discussion.



**Preconditions and assumptions:** Following the explanations in Section 4.1, the algorithm to obtain the transformation parameters primary relies on 3D positions. This leads to an independence of the used 3D positioning sensor. To exploit the laser scanner’s horizontal rotation of  $360^\circ$  as a function of time and orientation reference, the MSS’s measurements have to be synchronised, i. e., all measurements have to be provided with a proper time stamp. Both, the position vector and the orientation (heading) are constant values for a 3D point cloud obtained by the MSS. Due to the constant position vector a sufficient orientation to the direction of gravity can be established. At a first developmental stage, this allows for the waiver of additional inclinometers. Nevertheless, their later consideration can be meaningful. Thus, the main input quantities for the algorithm are the measurements of the 3D positioning sensors (GNSS equipment) mounted eccentrically on top of the laser scanner (Fig. 4.1).

To establish a unique spatial reference for all sensors in the MSS two offsets have to be determined (Section 4.3.4 and Fig. 4.10): First, an offset  $\Delta$  for the translation vector  $t_L^G$  has to be defined, which describes the metric offset to the laser scanner’s reference point. Second, an offset  $\Theta$  for the heading  $\kappa$  has to be determined, which represents an angular offset due to the installation of the wing support structure with respect to the scan direction.

**Qualification of recursive state-space filtering:** The availability of the 3D point positions in form of time series for the  $360^\circ$  rotation of the laser scanners predestines the usage of recursive state-space filters like the KF. In Section 3.2 the KF and its variants, which can handle non-linearities, are introduced for purposes of trajectory modelling. The benefit of KF over least-squares adjustment in recursive manner (Section 3.1) is the consideration of a motion model. Furthermore, the KF requires less computational costs due to smaller equation systems than least-squares adjustment. Moreover, the KF is capable for real-time processing. The modelling of the motion of the MSS, i. e., the laser scanner, is straightforwardly realised by means of a sine oscillation or a circle in 3D space in an EKF. In addition, information about specific MSS parameters is considered which can be the horizontal rotation frequency or the aforementioned offsets  $\Delta$  and  $\Theta$  (adaptive parameters). Furthermore, constraints among the state parameters are taken into account, which can be the distance of the two pre-defined positions on the wing support structure and the constant velocity of the MSS. The application of a smoothing algorithm (Section 3.2.3), like the Rauch-Tung-Striebel smoother makes sense for further enhancements of the overall filter performance. Alg. 4.1 summarises the procedure to obtain the transformation parameters.

**State parameters and their connection to the required transformation parameters:** The state parameters of the MSS are: the two positions of the 3D positioning sensors ( $\mathbf{p}_k^d$  and  $\mathbf{p}_k^o$ ) on the wing support structure as well as the velocity ( $v_k$ ) of the MSS. Neither the heading ( $\kappa$ ) nor the centre point ( $\mathbf{p}^{cp}$ ), i. e., the translation vector ( $\mathbf{t}_L^G$ ), will be directly observed. Therefore, both have to be estimated by the state parameters. As an option, the heading can be considered as state parameter (which is not mandatory). This keeps the number of unobserved state parameters minimal and avoids filter divergences. Such divergences can result from a lack of controllability by other observations and the recursive nature of the filter which negatively affects the variance propagation. Nevertheless, the heading can be directly observed by means of compasses or even GNSS compass approaches. Since the required heading is proposed to be calculated by means of coordinates (using the tangent function), two ways are feasible: First, the usage of the centre point which has to be determined beforehand (single antenna scenario, cf. Section 5.2.1.1) and second, the usage of both positions  $\mathbf{p}_k^d$  as well as  $\mathbf{p}_k^o$  (dual antenna scenario, cf. Section 5.2.1.2). The sequential calculation of the heading by means of the filtered or smoothed positions linearly increase due to the assumed constant rotation of the laser scanner about its vertical axis. Thus, the linearly increasing heading has to be adequately reduced to the start of the scanning procedure. The centre point is proposed to be recursively estimated in each filter or smoothing step by means of least-squares adjustment. Due to the mechanical construction of the laser scanner (laser emission in the middle) a direct observation can hardly be realised during the scanning process.

---

**Algorithm 4.1:** Conception of an algorithm to derive the transformation parameters.

---

```

1 Initialisation for  $k = 0$ 
2   | Initial guess for the state parameters as well as for the heading and the translation vector
3 Input: Time series of 3D positions for  $\mathbf{p}_k^d$  and  $\mathbf{p}_k^o$  (in the following named trajectories)
4 for  $k = 1 \dots, N$  do
5   | EKF
6     | Prediction of trajectories based on the motion model                               Section 5.2.1
7     | Optional consideration of adaptive parameters                               Section 5.2.1.1
8     | Filtering of trajectories by means of available measurements                 Section 5.2.2
9     | Calculation of heading by means of filtered trajectories                   Section 5.2.3
10    | Optional application of state constraints                                   Section 5.2.1.2
11    |   | Estimation of constrained trajectories
12    |   | Calculation of heading by means of constrained trajectories             Section 5.2.3
13    | Recursive least-squares estimation in GMM                               Section 5.2.3
14    |   | Estimation of translation vector by means of constrained trajectories
15 for  $k = N - 1 \dots, 1$  do
16   | Application of Rauch-Tung-Striebel smoother                               Section 5.2.3
17   |   | Estimation of smoothed trajectories
18   |   | Calculation of heading by means of smoothed trajectories                 Section 5.2.3
19   |   | Recursive least-squares estimation in GMM                               Section 5.2.3
20   |   |   | Estimation of translation vector by means of smoothed trajectories
21 Result: Transformation parameters (translation vector and heading) with uncertainty measures

```

---

### 4.3. Investigations of the multi-sensor system's components

This section summarises investigations of the used sensors in the MSS, which are introduced in Section 4.2.1. These investigations focus on the specific use of the sensors in the assembled MSS. It is noteworthy that comprehensive sensor investigations are out of the thesis's scope.

#### 4.3.1. Laser scanner and wing support structure to mount additional sensors

The usage of the laser scanner is mostly equivalent to the well-investigated standard scenario of 3D point cloud acquisition by means of a stationary laser scanner. Therefore, it is referred to Section 2.3.2 for instrumental errors in TLS. The reported investigations focus on the influence of the wing support structure firmly mounted on top of the laser scanner.

The analysis of the behaviour of the vertical axis ( $z$ -axis), i. e., wobble of the vertical axis or trunnion axis error, allows to draw conclusions for the influence of the wing support structure. Therefore, the inclinometer measurements of several conducted experiments are analysed analogous to the proposed investigations for wobble of the vertical axis by Schulz (2007).

The inclinometer measurements were gathered with the introduced Schaevitz LSOC-1° inclinometers, which are firmly mounted on the wing support structure close by the laser scanner's vertical axis (Fig. 4.1). The data were parallel acquired to the scanning process for a duration of five subsequent 360° rotations. The laser scanner was set up on a massive pillar in a tribrach and was operated with a frequency of 12.5 profiles per second. The reader is referred to Section 4.3.3 for separate investigations of the used inclinometers in the above-mentioned scenario.

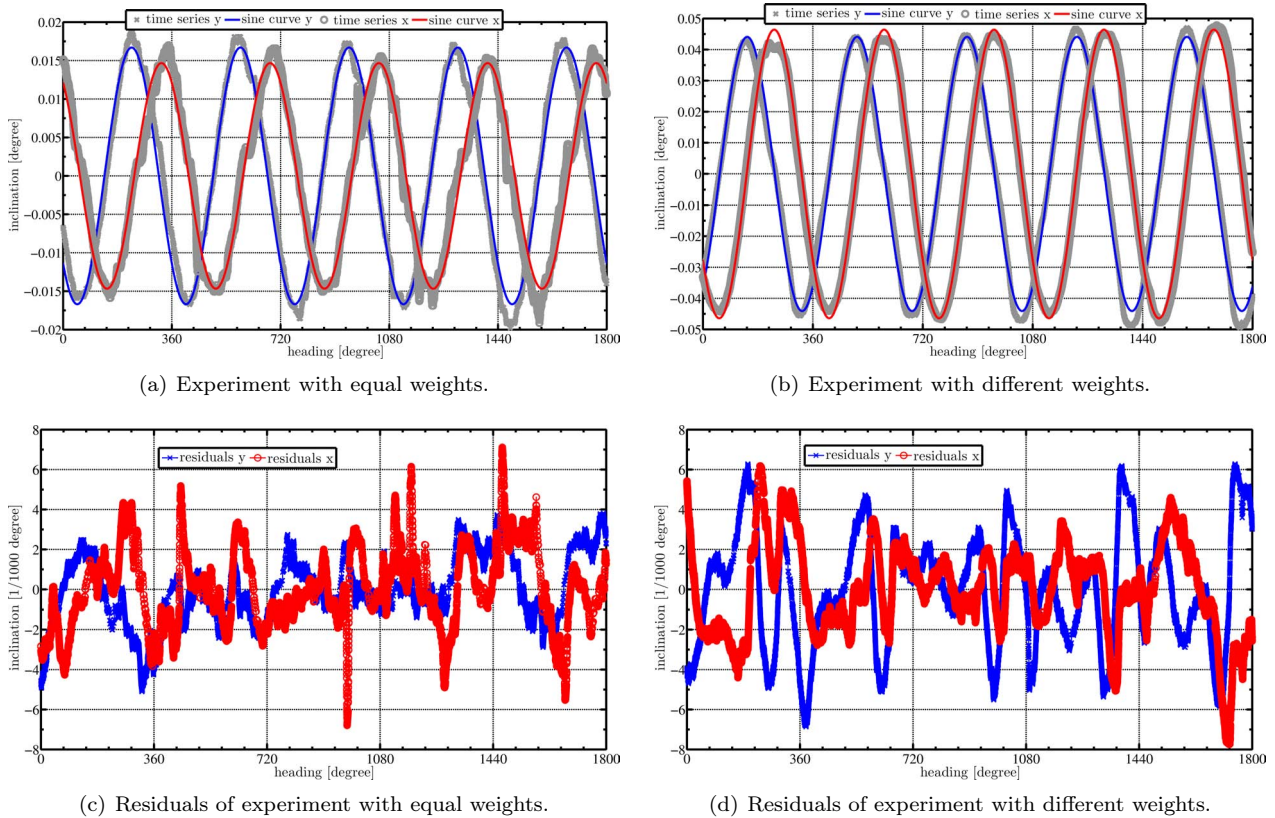


Figure 4.3: Analyses of the influence of the wing support structure on the rotation of the laser scanner: (a) Acquired inclinations and estimated sine curves for the experiment with two identical antennas, which were mounted on top of the laser scanner. (c) Remaining residuals between the measurements and the sine curves. (b) Acquired inclinations and estimated sine curves for the experiment with only one antenna and without any weight for compensation purposes. (d) Remaining residuals between the measurements and the sine curves.

Two different experimental arrangements were considered in the analyses. In the first experiment two identical GNSS antennas were mounted on the laser scanner, which results in equal weights for both sides of the laser scanner. The second experiment was conducted with only one GNSS antenna and without any weight for compensation purposes.

The analyses are carried out by the following steps: First, the acquired inclinations are corrected by the levelling error. The levelling error is estimated by a sine curve separately for  $x$ - and  $y$ -direction. To illustrate this point, Fig. 4.3(a) and Fig. 4.3(b) show the inclinations and the sine curves defining the levelling error. For both experiments, the amplitudes of the  $x$ - and  $y$ -direction differ by only a few  $1/1000$  degree. The dominant frequency corresponds to the laser scanner's rotation frequency of 12.5 profiles per second. According to Schulz (2007), the wobble of the vertical axis is expressed by the residuals between the acquired inclinometer data and the sine curves. Fig. 4.3(c) depicts the remaining residuals for the first experiment, which show no obvious systematic trends. They are in a range of  $\pm 4/1000$  degree. For the second experiment the remaining residuals show a similar behaviour regarding the systematic trend. Fig. 4.3(d) depicts the residuals which are in a slight larger range of  $\pm 6/1000$  degree compared to the first experiment. Thus, it can be concluded that the wing support structure on top of the laser scanner does not induce significant effects on the laser scanner's rotation about its vertical axis. Furthermore, the unbalanced experiment (with a weight difference of  $\approx 1$  kg due to the use of only one antenna) indicates no significant influence on the laser scanner's rotation.

At this point, it should be noted that the manufacturer's interval inspections of the Z+F IMAGER 5006 do not show any irregularities or even problems with the servo motor due to the extra weight of the wing support structure with the additional sensors.

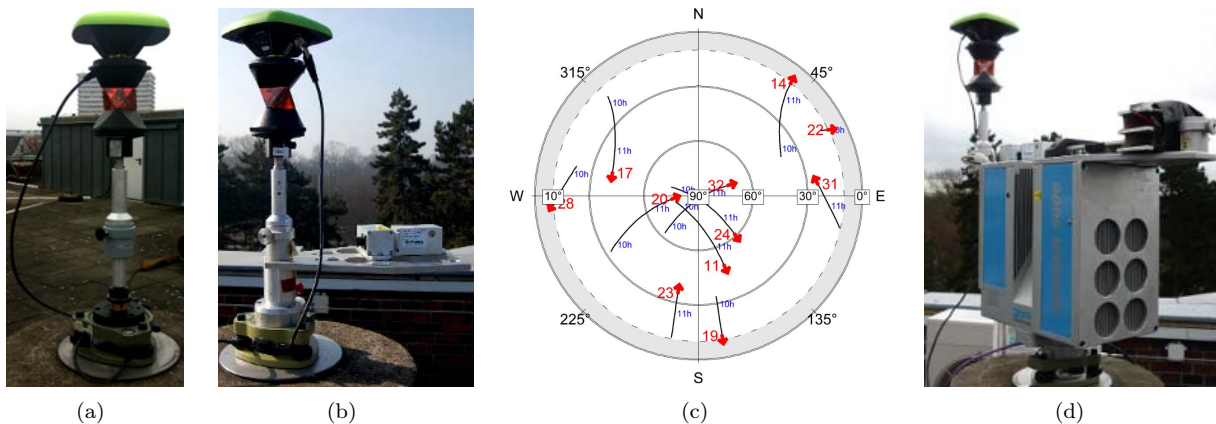


Figure 4.4: Parameters of static and kinematic experiments with the GNSS equipment on P6: (a) Setup of 2011, DOY049: antenna with standard tribrach. (b) Setup of 2011, DOY041 with wing support structure. (c) Sky plot of GPS satellites for DOY049 09:51–11:25 GPS time. The arrows show the flight direction of visible satellites (indicated by PRN numbers) in the topo-centric system. The grey area indicates the elevation cut-off angle of  $10^\circ$ . (d) Laser scanner with wing support structure for kinematic experiments.

#### 4.3.2. GNSS equipment

The investigations of the error budget of the GNSS equipment concentrate on error sources induced by the specific utilisation of the GNSS antennas in the MSS, i. e., the alternating antenna orientation with respect to a coordinate system (e. g., ETRS89). This rotation of  $360^\circ$  will contribute to the error budget due to the right-hand circular polarisation of the GNSS signals and the azimuthally varying PCC. In addition, near-field multipath effects possibly caused by the aluminium wing support structure on the laser scanner, or possibly far-field multipath from the surrounding area may contribute to the error budget (cf. Dilkner, 2007). An overview of the entire error budget of GNSS measurements as well as the fundamentals for the following investigations are given in Section 2.2.4.1. In the following, the explanations summarises the most important findings of Paffenholtz et al. (2011). Two kind of experiments and analyses were performed: A static experiment with a non-rotating GNSS antenna and a kinematic experiment with an eccentrically rotating antenna. First, data analyses are reported with respect to systematic effects in the observation domain. Second, data analyses are conducted in the coordinate domain, which is of major interest because of the position and orientation estimation from coordinates.

The experiments were performed at the roof of the building of the Geodetic Institute (Messdach), Leibniz Universität Hannover, Germany. On this roof a geodetic network with nine pillars<sup>5</sup> is located (Fig. 6.1(b)), which allows investigations under semi-controlled conditions. The GNSS antenna under test was the Javad GrAnt G3T antenna<sup>6</sup> which was connected to a Javad TRE G3T Delta receiver. The GNSS antenna was mounted in  $\mathbf{p}^d$  on the wing support structure and an additional balance weight was placed on the opposite side (Fig. 4.4(d)).

The reference station<sup>7</sup> was equipped with an individually and absolutely calibrated Leica AR25 (Rev. 3) antenna, which was connected to a Javad TRE G3T Delta receiver. The relative baseline between the reference station and the MSS equipped with the GNSS antenna under test is about 14 m. The GNSS analysis was carried out in post-processing with the Wa1 software (Wanninger, 2009b) using single-differences between receivers to eliminate orbit errors, satellite clock errors as well as errors due to propagation delays in the atmosphere. Due to the fact of the short baseline all atmospheric effects can be neglected.

For a ground truth of the ARP trajectory simultaneous and synchronised measurements with a total station

<sup>5</sup>The pillar's coordinates are available in the International Terrestrial Reference Frame 2005 (ITRF05).

<sup>6</sup>For detailed information regarding the PCC of the Javad GrAnt G3T antenna the reader is referred to Section B.3.

<sup>7</sup>The reference station is operated by the Institut für Erdmessung, Leibniz Universität Hannover, Germany.

(Leica TS30) to a  $360^\circ$  prism were obtained. The prism was directly attached below the GNSS antenna (Fig. 4.4(d)). The total station was placed in a distance of about 27 m and has tracked the prism with a data rate of 2 Hz. In addition, a theoretic trajectory was computed based on the known geometry of the GNSS antenna installation on top of the laser scanner. For the further investigations, both trajectories were used as reference. They independently describe the circular motion of the laser scanner.

**Static experiments:** Special attention is given to assess the performance of the used GNSS equipment for estimating coordinates with a non-rotating antenna. Within these experiments two different setups were used at P6. The combination of antenna and directly attached  $360^\circ$  prism (Fig. 4.4(a) and (b)) was identical in both experimental setups. Also the height above P6 was chosen to identical values. The difference was the additional use of the wing support structure for the antenna on top of the laser scanner in the measurements on 2011, DOY041 (Fig. 4.4(b)). The observation time (with 1 Hz data rate) was for DOY041 10:23–11:57 GPS time and 2011, DOY049 09:51–11:25 GPS time, respectively. The sky plot in Fig. 4.4(c) depicts the GPS constellation of DOY049 with four satellites with high elevations (above  $45^\circ$ ) and a good signal strength (45 – 53 dBHz). Additionally, six other GPS satellites had an elevation above  $10^\circ$ . Furthermore, there were five GLONASS satellites visible for the whole observation time. The time difference of DOY041 and DOY049 corresponds to the difference between sidereal and solar day length over eight days. By this observation timing the same satellite constellation for GPS and GLONASS as well as nearly identical repeat tracks for the satellite vehicles can be assumed. Hence, it is possible to evaluate the influence of the wing support structure on the GNSS measurements. This is feasible due to identical ground tracks which generate a similar far-field multipath signal on the observations but different near-field multipath. The latter is caused by the different near-field environments of the antenna (cf. Fig. 4.4(a) and (b)).

**Kinematic experiments:** To analyse the impact of the rotating GNSS antenna, the MSS (Fig. 4.4(d)) was used to acquire GNSS measurements of several independent  $360^\circ$  rotations each with about 13 min duration. The experiments were conducted on 2011, DOY025 11:28–12:48 GPS time. The time difference of these measurements corresponds again to the difference between sidereal and solar day length over 16 and 24 days, respectively. This allows the comparison of all static and kinematic measurements within the entire conducted experiments.

**Analyses and interpretation of the results in the observation domain:** To detect systematic effects the Double-Differences (DD) of phase measurements for DOY041 and DOY049 are analysed. The identification of systematics in the observation domain can facilitate the interpretation of the data in the coordinate domain. Furthermore, identified systematics in the observation domain (e. g., Signal Strength (CN/0) variations) can be considered by appropriate estimation models for the coordinate determination (Wieser, 2002).

In Fig. 4.5 the CN/0 versus elevation of the satellite under investigation (PRN 11 and PRN 19) and the reference satellite (PRN 32) in the antenna topo-centric system as well as the DD are exemplarily plotted for DOY049 and DOY041. The time shift of about 30 min between the time series for DOY041 and for DOY049 results from the sidereal repeatability which was considered in the observation planning. The two antenna sites in the investigation are P6 and P8 with a baseline of 13.6 m. The reference PRN 32 is characterised by a very high and homogeneous CN/0 in a range of 53 dBHz to 55 dBHz for elevations near zenith as expected for such a satellite and receiver geometry. The DD PRN 11-32 (Fig. 4.5(a)) are in a range of  $\pm 5$  mm with small amplitude within the time span 9.8–11.5 GPS time on DOY049. After 11.5 GPS time the amplitude of the DD increase slightly what is related to the descending CN/0 and its increasing variations. For DOY041 the same amplitude and pattern as for DOY049 can be seen for the whole analysed time span (Fig. 4.5(c)). In comparison to PRN 11, the PRN 19 has a low elevation (below  $35^\circ$ ) with higher DD residuals (Fig. 4.5(b) and (d)) what is possibly caused by diffraction effects in the antenna's far-field. For both DOYs, the residuals also show systematic variations with a magnitude of up to 2 cm. These variations increase for decreasing elevations. To sum up the DD analyses for time series of DOY049 and DOY041 can be concluded that there is no significant

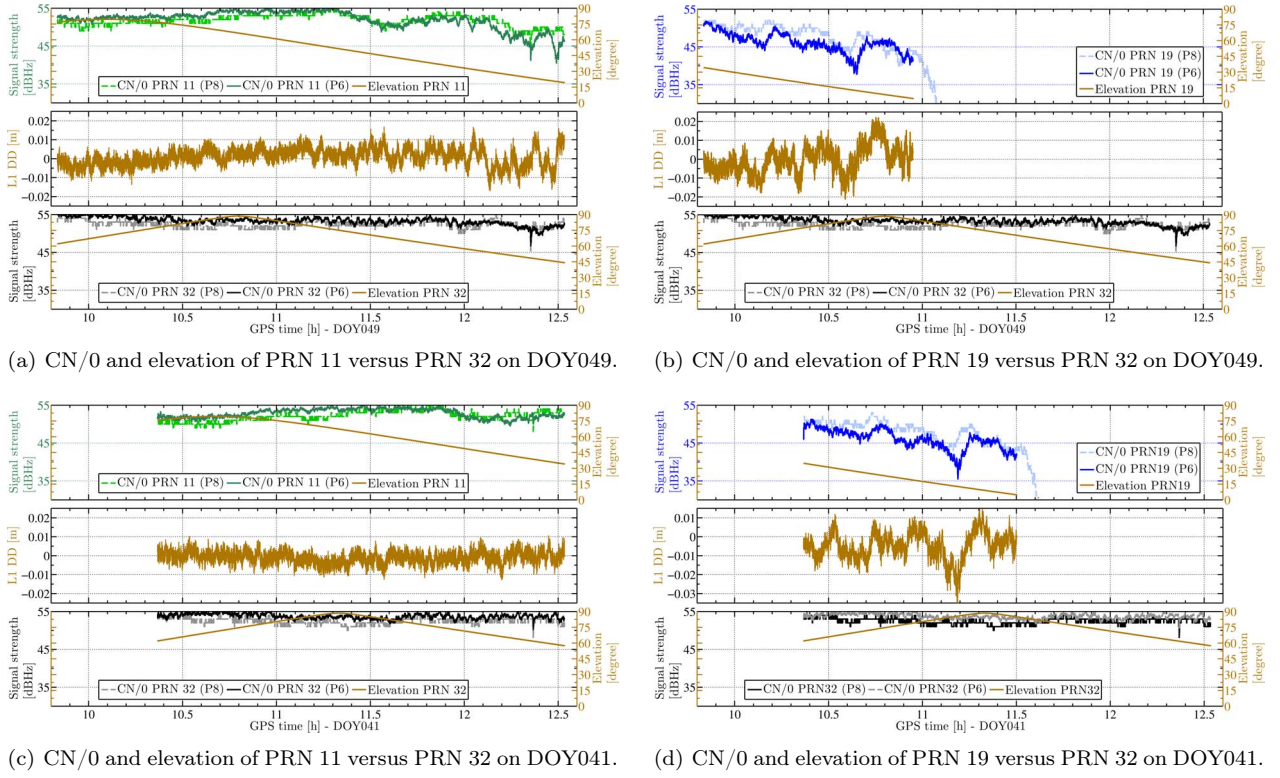


Figure 4.5: DD analyses for two specific satellites: (a) and (c) L1 DD and CN/0 for PRN 11 with visibility in zenith. (b) and (d) L1 DD and CN/0 for the descending PRN 19. The CN/0 for the used reference satellite PRN 32 is given in the lower part of all figures. For all satellites the specific elevation is drawn in brown beside the corresponding CN/0. The colour code for the CN/0 is: P8 light colour and P6 corresponding dark colour.

influence due to the wing support structure (used on DOY041) because same variations could be detected on both DOYs for the same satellites.

To analyse the impact of the PCC, corrections in different combinations are applied to the measurements. Furthermore, the question of the necessity to take a rotated PCC correction for the GNSS antenna in the MSS into account should be answered. Thus, for every epoch a new set of PCC for an eccentrically rotated antenna is calculated and projected into the line of sight to individual satellites.

$$PCO_c = f(PCO, \alpha_0, r, \Delta\alpha) \quad \text{and} \quad PCV_c = f(PCV, \alpha_0, r, \Delta\alpha) \quad (4.1)$$

$$\Phi_{c_i}^j = \Phi_i^j - PWU_{c_i}^j + PCO_{c_i}^j - PCV_{c_i}^j \quad (4.2)$$

The corrected PCOs and PCVs (Eq. 4.1) are functions of the original PCO and PCV, the initial azimuth of the

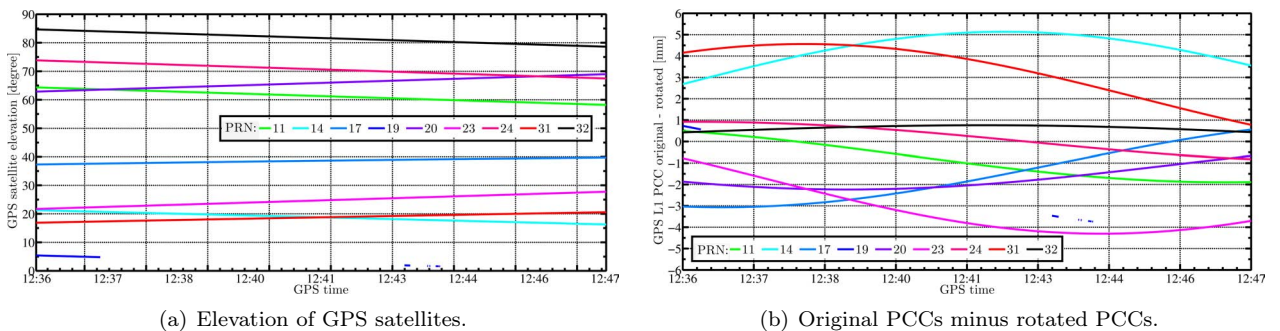


Figure 4.6: GPS satellites constellation 2011, DOY025 12:36-12:47 and PCC analyses of GPS L1 signals.

antenna orientation  $\alpha_0$  (at the beginning of the scan), the radius  $r$  and  $\Delta\alpha$ , which denotes the angle increment between two rotation steps. The corrected carrier phase measurements  $\Phi_{c_i}^j$  are given by Eq. 4.2, where the index  $i$  denotes the individual frequency and  $j$  stands for the satellite number. The PWU effect is constant and thus absorbed in the receiver clock offset in the adjustment (Section 2.2.4.1). In Fig. 4.6(b) the original PCCs are subtracted from the rotated PCCs. For GPS L1, magnitudes of up to 5 mm occur at low elevations. These values are in the range of the azimuthal variations of the PCV in a small elevation band (cf. Fig. 2.4 and Fig. B.1(a)). Within the time span of 13 min, where the laser scanner performs one full circle, the satellite only moves a small amount (Fig. 4.6(a)). It is noteworthy that the influence of an omitted rotation of the PCC on the data acquired in the laser scanner scenario disappears in the azimuthal variations of the PCV.

**Analyses and interpretation of the results in the coordinate domain:** As already stated in the previous paragraph, in the DD analyses no significant influence due to the different antenna environment on DOY041 and DOY049 can be reported. By implication, this is the same in the coordinate domain. Fig. 4.7(a) depicts the NEU coordinate differences of the static experiments with respect to the well known coordinate of P6 in different scenarios. Two different GNSS analyses are performed: A static estimation of the coordinate (blue for DOY041 and red for DOY049) and a kinematic estimation of the coordinates (cyan for DOY041 and light magenta for DOY049). We can assess the kinematic coordinate estimation potential of the used GNSS antenna within a maximum range of 1 cm for the north- and east-components and up to 2 cm for the up-component.

For the investigation of the kinematic measurements with the eccentrically rotating antenna two GNSS trajectories are estimated (GPS only solution). The difference between these two estimations is the set of applied PCCs. One estimation is done with the original PCCs, a non-rotating antenna is assumed. The other one is performed with the modified observations by rotating the PCCs (cf. Eq. 4.1 and 4.2) as explained in the previous paragraph. Hereby, the GNSS range observations are modified using WaRINEX (Wanninger, 2009a). The rotated PCCs are applied within the Receiver Independent Exchange Format (RINEX) observation files. Afterwards, a re-processing of the modified GNSS observations is done. To indicate the influence of the rotated PCC in the coordinate domain these two trajectories are compared on basis of their NEU coordinates in Fig. 4.7(b). The displayed time series are results of the difference of each GNSS trajectory and the ground truth. Furthermore, the differences between both GNSS trajectories with the different PCCs applied to GPS frequencies L1 and L2 are calculated (blue line in Fig. 4.7(b)). For the north-component a magnitude of 0 mm to  $-4$  mm can be seen and the other way round for the east-component. As expected, the up-component is not affect by any rotation. This is indicated by discrepancies almost equal to zero.

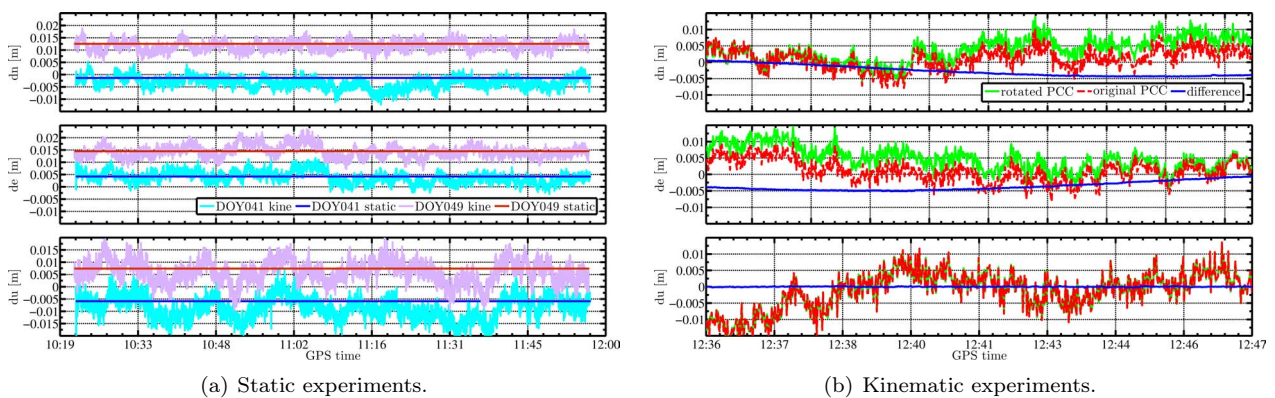


Figure 4.7: Analyses in the coordinate domain: (a) NEU coordinate differences of the static experiments: DOY041 with wing support structure: kinematic and static analysis; DOY049 with standard tribrach: kinematic and static analysis (time series of DOY049 are shifted 1 cm up for visualisation purposes). (b) NEU coordinate differences for computed differences between ground truth trajectory and rotated (green) as well as original (red) PCC pattern. Furthermore, the difference between GNSS trajectories with original PCCs and rotated PCCs is indicated (blue line).

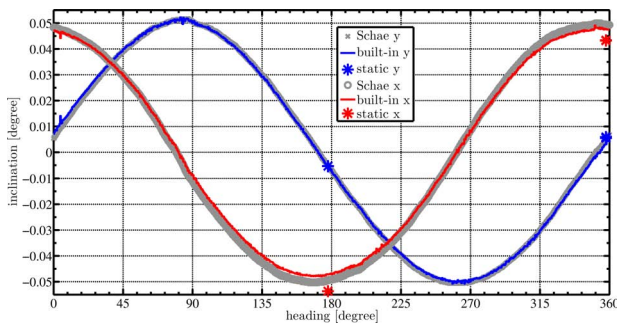
**Concluding remarks:** The reported investigations of the GNSS related errors, which are potentially caused by the specific use in the MSS, yield not to a significant impact on the used antenna wing support structure within a DD analysis in the observation domain. The PWU effect is constant and, therefore, treated as receiver clock offset in the adjustment (Section 2.2.4.1). As expected, the rotated PCC against the original PCC has an effect of up to 5 mm in the observation domain. This corresponds to the horizontal offset component of the used GNSS antenna. The analyses in the coordinate domain also indicate an effect of up to 5 mm. They show that the PCC effect is dominated by the PCO components. We can conclude that within an epoch-wise GNSS analysis (Section 4.2.2) the effect of rotated PCC has no significant impact on the transformation parameters in the geo-referencing procedure.

### 4.3.3. Inclinometers

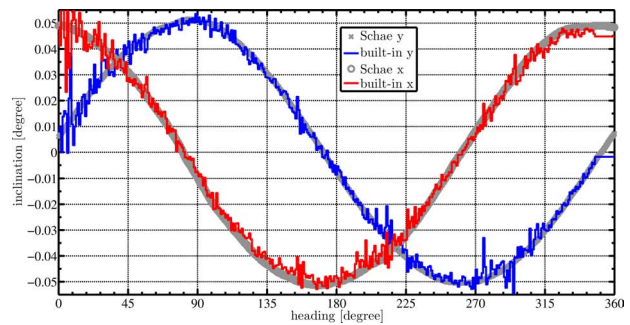
According to Section 4.2, in the prototypic MSS, inclinometers are not primarily used for the direct geo-referencing. Instead they are used for the laser scanner setup and for investigations of the MSS (Section 4.3.1). The inclinometers usage in the MSS investigations is identical to their optional usage in the direct geo-referencing procedure. Therefore, the inclinometer characteristics will be briefly treated especially regarding the laser scanner’s horizontal rotation. The aim is to show the potential and performance of both types of inclinometers: the built-in dual-axis sensor and the two standalone single-axis Schaevitz inclinometers in the specific MSS; not comprehensive investigations or calibration of these inclinometers.

The use of inclinometers with mobile platforms requires a consideration of the individual platform motion to obtain reliable results. In the prototypic MSS, the built-in sensor is situated nearby the vertical axis at the bottom of the laser scanner. The two Schaevitz sensors are installed as close as possible to the vertical axis (to minimise the influence of centripetal acceleration). This can be sufficiently realised for the  $y$ -direction while the position of the sensor for the  $x$ -direction is not optimal (cf. Fig. 4.1). Since the MSS will be oriented to the direction of gravity, the remaining residuals are small values also during the slow-going rotation about the laser scanner’s vertical axis. Thus, the introduced sensors provide sufficient measurement ranges (Section 4.2.1).

To characterise the laser scanner’s rotation about its vertical axis, separate synchronised measurements with a laser tracker (Leica LTD640) were performed. Therefore, a Corner Cube Reflector (CCR) (a precise reflector to use with laser trackers) was placed at the wing support structure in  $\mathbf{p}^d$  with a distance of about 0.3 m to the rotation axis. During the laser scanner’s operation with its typically rotation of 12.5 profiles per second, the laser tracker measures the polar elements to the CCR. The laser tracker’s measurements were triggered by the line synchronisation pulse of the laser scanner, i. e., for each profile a precise coordinate is available. These coordinates are used to calculate a velocity for the progress between two subsequent profiles. A mean velocity



(a) Rotation speed of 12.5 profiles per second.



(b) Rotation speed of 25 profiles per second.

Figure 4.8: Inclinometer measurements for different rotation speeds of the laser scanner: (a) Inclinations of the Schaevitz sensors (grey dots) and built-in inclinometer measurements (coloured lines). In addition, static measurements of the built-in inclinometer are shown (stars). (b) Inclinations of the Schaevitz sensors (grey dots) and built-in inclinometer measurements (coloured lines).



of  $v = 0.0024 \frac{\text{m}}{\text{s}}$  was obtained for the laser scanner's rotation about its vertical axis. Thus, the rotation can be stated as slow-going motion and no significant influences are expected on the inclinometer measurements.

The performance of both types of inclinometers is shown in Fig. 4.8. For the experiment the laser scanner was mounted on a massive pillar in the laboratory. Several independent  $360^\circ$  rotations were performed. The results for a rotation speed of 12.5 profiles per second (Fig. 4.8(a)) show a good correspondence with low noise for the Schaevitz data (grey dots) and the built-in inclinometer data (coloured lines). In addition, the built-in inclinometer measurements (stars) before and after the scanning procedure are depicted. Here, the values are adequate for both inclinations in  $y$ -direction whereas for the  $x$ -direction for both inclinations maximal differences of  $5/1000$  degree are reported. This maximal differences would result in a metric error of 3 mm in an object distance of 30 m. These slightly larger discrepancies for the  $x$ -direction are present in all experiments. To finally judge them further investigations are necessary which are beyond the scope of this thesis. In Fig. 4.8(b), inclinometer measurements for a rotation speed of 25 profiles per second are illustrated. The larger noise level of the built-in inclinometer with a maximal amplitude of  $0.01^\circ$  is clearly visible. Especially at the start of the scanning procedure the noise level is high and decreases over time. It is noteworthy that for the typically used rotation speed (12.5 profiles per second) the inclinometers provide sufficient results (Fig. 4.8(a)). Nevertheless, kinematic inclinometer measurements are not considered in the geo-referencing procedure at this developmental stage. The inclinometers are only used for the orientation of the MSS to the direction of gravity before the scanning procedure. Their later integration is conceivable but requires thorough investigations of the inclinometer characteristics in the MSS.

#### 4.3.4. Multi-sensor system calibration

This section treats the establishment of an unique spatial reference for all sensors in the MSS, i. e., calibration of the MSS. In particular, the relative position of the pre-defined positions ( $\mathbf{p}^d$  and  $\mathbf{p}^o$ ) on the wing support structure with respect to the laser scanner's reference point has to be defined (cf. Fig. 4.10). This task is twofold: First, an offset  $\Delta$  for the translation vector, and second, an offset  $\Theta$  for the heading have to be determined.  $\Delta$  describes the metric offset of  $\mathbf{p}^d$  and  $\mathbf{p}^o$  with respect to the laser scanner's reference point.  $\Theta$  represents the angular offset between the scan direction and the wing support structure. In addition, the distance  $d^{do} = |\mathbf{p}^d \mathbf{p}^o|$  between the pre-defined positions has to be determined. The quantity  $d^{do}$  will be considered as additional information in the motion modelling (Section 5.2.1.2). Uncertainties of  $\Delta$  constantly affect all parts of a 3D point cloud within the direct geo-referencing procedure. The impact of uncertainties of  $\Theta$  increase with the object distance. The aim is to keep the contribution of the calibration's uncertainties with an assumed significance level of 95 % to the entire uncertainty budget below 1 cm in an object distance of 30 m.

The calibration concept of the MSS is proposed by Brieden (2009). In general, a photogrammetric determination or an object space based determination is possible for the calibration task. In the former approach, the points of interest have to be indicated with suitable markers and measurements of the laser scanner are not required. In the latter approach, well-distributed targets in the object space are measured by the laser scanner on the one hand and by additional sensors (e. g., a precise total station or a laser tracker) on the other hand. In addition,  $\mathbf{p}^d$  and  $\mathbf{p}^o$  have to be equipped with suitable targets and to be measured by the additional sensors. Suitable targets, which can be measured by laser scanners and precise total stations or a laser trackers, are spheres. The unknown  $\Delta$  can be calculated by means of a 3D Helmert transformation (Section A.2) of the laser scanner's and the additional sensor's data set. The unknown  $\Theta$  can be calculated either by synchronised kinematic or static measurements of, e. g., a laser tracker. The former is similar to the procedure described in Section 4.3.3 to characterise the laser scanner's rotation about its vertical axis, i. e., to estimate a mean velocity for the progress between two subsequent profiles. In the latter approach, the laser scanner is not moving during the data acquisition. Instead, the laser scanner is manually moved with a fixed known angular step pattern (cf. Brieden, 2009). Common for both approaches is the final calculation of  $\Theta$  by reducing the measurements with the angular values given by the profile progress or the angular step pattern. This calculation is equivalent

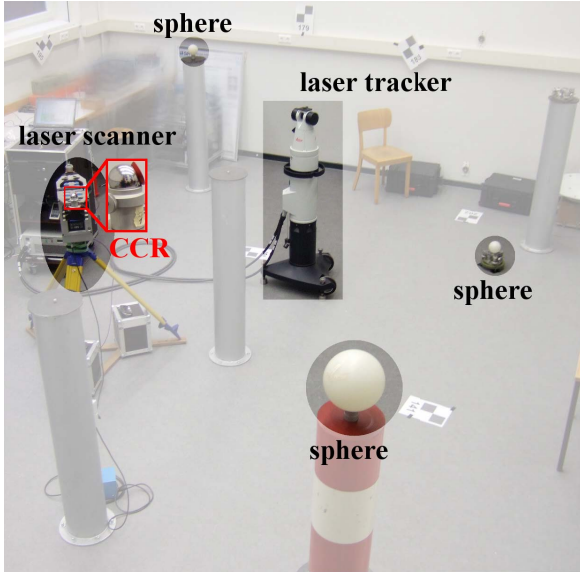


Figure 4.9: Sketch of the MSS calibration in the laboratory. Depicted are the laser scanner, the laser tracker, the spheres for transformation purposes as well as a zoom of the CCR in  $\mathbf{p}^d$ . (Brieden, 2009).

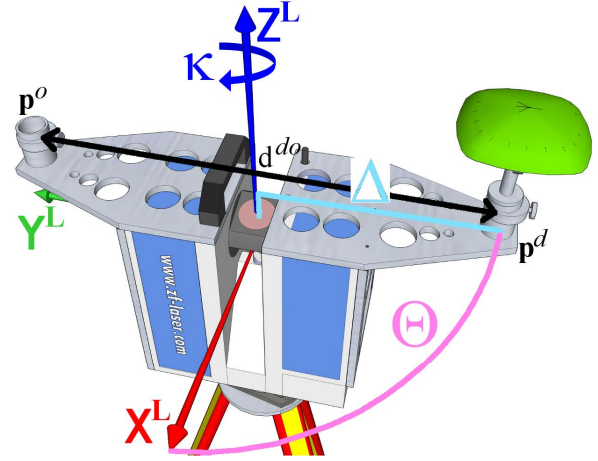


Figure 4.10: Unique spatial reference for sensors of the MSS:  $\mathbf{p}^d$  and  $\mathbf{p}^o$  indicate the pre-defined positions on the wing support structure. The distance between  $\mathbf{p}^d$  and  $\mathbf{p}^o$  is denoted by  $d^{do}$ .  $\Delta$  stands for the metric offset of the translation vector with respect to the laser scanner's reference point.  $\Theta$  describes the angular offset of the heading due to the installation of the wing support structure on the laser scanner.

to the determination of the orientation unknown of angular measurements by total stations. The distance  $d^{do}$  can be obtained by the coordinate difference  $\mathbf{p}^d$  and  $\mathbf{p}^o$ .

The calibration measurements were performed under laboratory conditions with a laser tracker (Leica LTD640) and well-distributed spheres for the connection of the coordinate systems of the laser scanner and the laser tracker (Fig. 4.9). The laser scanner was manually moved with a fixed, known angular step pattern (e. g.,  $20^\circ$ ). For each step the position of the CCR in  $\mathbf{p}^d$  and  $\mathbf{p}^o$  was measured. A 3D Helmert transformation yields  $\Delta$  with standard deviations in a range of 1–2 mm. The calculation of  $\Theta$  by means of the CCR positions results in standard deviations of  $< 0.01^\circ$ . A metric uncertainty of the calibration procedure of  $< 1$  cm in an object distance of 30 m can be stated.  $d^{do}$  was calculated by means of several CCR coordinate pairs of  $\mathbf{p}^d$  and  $\mathbf{p}^o$  with standard deviations  $< 3$  mm. It is noteworthy that due to a precise orientation of the laser scanner to the direction of gravity (during the calibration measurements)  $d^{do}$  is a horizontal distance.

#### 4.3.5. Concluding remarks and uncertainty assessment

The prototypic MSS is introduced with its individual sensor components, algorithmic concept for the estimation of the transformation parameters and aspects of the MSS's calibration. In the following the major findings regarding the contribution to the entire uncertainty budget of the direct geo-referencing by means of the MSS (*transformational uncertainty*) are summarised within an uncertainty assessment. It is noteworthy that the positional uncertainty (Section 2.3.3) is not explicitly included in the given uncertainty assessment. Nevertheless, rule of thumb values for the used laser scanner Z+F IMAGER 5006 in terms of the instrumental errors are a range noise of 4 mm rms at a distance of 50 m for 20% reflectivity and an accuracy of the deflection unit of  $0.007^\circ$  rms (cf. manufacturer specifications in Section B.1).

The *transformational uncertainty* budget is composed of the following individual error sources:

1. A MSS setup error caused by imperfect orientation to the direction of gravity. An orientation to the direction of gravity by means of the built-in inclinometer can drastically correct this problem. Thus, it has no significant contribution.
2. The investigations of a wobble of the vertical axis due to the wing support structure yield that no significant effect can be reported (Section 4.3.1).

3. For the used GNSS equipment the performance of the kinematic coordinate estimation is reported within a range of 1 cm for the north- and east-components by means of epoch-wise point estimation (Section 4.3.2). Since the desired transformation parameters are estimated in a KF approach by prediction, filtering and smoothing an improvement for the translation vector uncertainty is assumed in a range of 0.5 – 1 cm. For the heading, which is estimated based on the filtered and smoothed trajectory, an uncertainty in a range of  $0.05 - 0.08^\circ$  is assumed. For an object distance of 30 m this results in a metric uncertainty of about 4 cm. The heading uncertainty is dominated by the trajectory uncertainties and the short baseline  $d^{do} = |\mathbf{p}^d \mathbf{p}^o| \approx 0.6$  m.
4. The uncertainties caused by the MSS calibration are assumed to a metric uncertainty of  $< 1$  cm in an object distance of 30 m (Section 4.3.4).

Finally, the *transformational uncertainty* budget can be assumed as the sum of the aforementioned individual errors. Thus, an approximate value of 4 – 5 cm with an assumed 95%-significance level in a typical object distance of 30 m can be noted. This approximate value covers the uncertainty induced by the translation vector, the heading as well as the MSS calibration.



## 5. Novel methodology for geo-referencing of 3D point clouds

This chapter introduces a novel methodology for the direct and simultaneous geo-referencing of 3D point clouds from stationary laser scanners using the information from physically attached sensors to the laser scanner as explained in Chapter 4. This method also has an imbedded algorithm for utilising the uncertainty information from relevant sensors and their mechanical properties, i. e., laser scanner, GNSS equipment and the additional uncertainties caused from their temporal synchronisation.

As an introduction, the estimation of transformation parameters by means of 3D circle adjustment is to be discussed in Section 5.1. Hereby, the difficulties of the geo-referencing problem of the stationary laser scanner in a MSS are shown. To overcome these difficulties, the novel algorithm for direct geo-referencing of 3D point clouds considering uncertainties is fundamentally based on the motion modelling of the MSS in a recursive state-space filter, i. e., EKF. The algorithm is developed in Section 5.2. In Section 5.2.1, two different variants of modelling the system are presented: one which considers adaptive parameters and the other which makes use of state constraints. Section 5.2.2 deals with the measurement equation. The entire state-space equations come along with their stochastic model. Finally, the proposed algorithm is summarised in Section 5.2.3.

The optimisation of the transformation parameters by means of ICP based matching algorithms considering uncertainties is presented in Section 5.3. The adaption of the threshold for the closest distance based on positional uncertainties and the adjustment model for estimation of the transformation parameters are outlined as well. Finally, an ICP based matching algorithm for 3D point clouds considering uncertainties is summarised in Alg. 5.2.

### 5.1. Transformation parameters from 3D circle estimation

One of the simplest approaches to estimate the transformation parameters of the laser scanner is to utilise the 3D circle described by the GNSS equipment installed on top of the stationary laser scanner (Paffenholz and Kutterer, 2008). As presented in Fig. 4.1, suppose that for  $\mathbf{p}^d$  and  $\mathbf{p}^o$  on the wing support structure time series of 3D positions are available. These time series can be used to obtain the transformation parameters of the laser scanner, which are parametrised by their centre points and the distance between  $\mathbf{p}^d$  and  $\mathbf{p}^o$  (diameter). The same principle can be applied to the case of a single GNSS equipment installed on the wing support structure. The estimation procedure of the 3D circular trajectory, which provides the adjusted positions, is spilt into two parts as follows:

1. The 3D positions are orthogonally projected onto a best-fitting plane by means of a principal axis transformation.
2. A best-fitting circle through the projected positions is estimated.

Both independent least-squares parameter estimations (for the plane and the circle) minimise the cost functions in Eq. 3.4. For the detection and elimination of outliers a statistical test based on the standardised residuals (Baarda, 1968) is applied. This test is also known as Baarda's data snooping. However, this two-step procedure allows to obtain the additional spatial rotations either by insufficient orientation to the direction of gravity or coordinate transformations.

The best-fitting plane for 3D positions  $\mathbf{p}_j^{d/o} = [x_j \ y_j \ z_j]^T$  with  $j > 3$  is characterised by minimal perpendicular distances  $\nu_j$  of each point to the best-fitting plane. A 3D plane is defined as

$$n_x \cdot x_j + n_y \cdot y_j + n_z \cdot z_j + d = 0, \quad (5.1)$$

where  $\mathbf{n} = [n_x \ n_y \ n_z]^T$  denotes the normal unit vector and  $d$  is the distance parameter.

The unknown surface normal vector,  $\mathbf{n}$ , can be simply estimated by utilising the SVD of the matrix as explained in Eq. 2.11. The normal unit vector  $\hat{\mathbf{n}}$  (of the best-fitting plane) is the eigenvector  $\hat{\mathbf{e}}_0$  of the smallest eigenvalue  $\lambda_0 = \nu^T \cdot \nu$  and the tangential vectors correspond to the other eigenvectors. For the derivation of the VCM of  $\hat{\mathbf{n}}$  by means of the eigenvectors  $\hat{\mathbf{e}}_1$  and  $\hat{\mathbf{e}}_2$  as well as their corresponding eigenvalues the reader is referred to Drixler (1993). In order to detect and eliminate outliers, the perpendicular distances  $\nu_j$  are analysed by a statistical test and the parameter estimation is iteratively conducted within the scope of SVD (Paffenzholz and Kutterer, 2008). Afterwards, the 3D positions are orthogonally projected onto the best-fitting plane by means of principal axis transformation utilising the estimated  $\hat{\mathbf{n}}$ .

The estimation of a best-fitting circle through the projected positions provides next to the circle parameters the adjusted positions. In Section 3.1, the circle from Eq. 3.1 illustrates the transformation of the primary formulation in a GHM into an equivalent GMM (Section 3.1.4). This model transformation is seized upon in Paffenzholz and Kutterer (2008) to apply Baarda's data snooping for the detection and elimination of outliers. In contrast to the plane estimation, the circle estimation allows for the VCMs of the orthogonally projected 3D positions. To increase the robustness of the adjustment, the circle estimation is iteratively done whereas in each step the positions are analysed by a statistical test.

The translation vector is available using the centre point of the above adjustments. The heading for each 2D profile is derived by the tangent function (Eq. 5.15) utilising the centre point and the (adjusted) 3D positions of each 2D profile. The introduced fundamentals of the estimation of the transformation parameters by means of explicit 3D circle estimation show certain drawbacks:

1. The separation into *two independent adjustments* as well as the *omission of the 3D positions' VCMs* in the plane estimation.
2. The *computational efforts* owing to large equation systems in the adjustment which result from assumed high frequent trajectories<sup>1</sup>. The computational costs grow due to the iterative calculation in case of identified outliers.
3. *No consideration of the known and determinable motion* of the laser scanner which would allow spanning data gaps better than simple interpolation, i. e., prediction.
4. *No real-time capability* because the data acquisition must be completed before the adjustments can be performed.


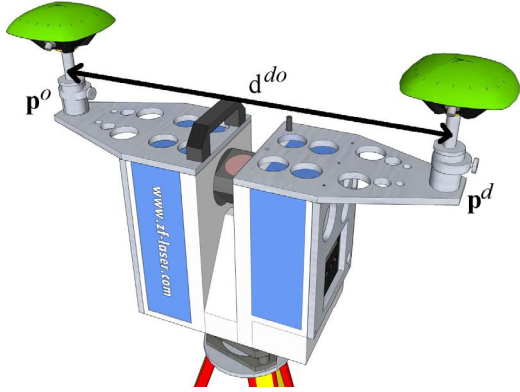
To overcome these drawbacks the following points are proposed. With the use of bullseye levels and the subsequent use of inclinometers a sufficient orientation to the direction of gravity as well as the acquisition of residual spatial rotations are feasible. In addition, these measurements would enable a mathematical consideration of the residual spatial rotations. The manner of data acquisition is generally suitable for recursive parameter estimation. Thus, it is reasonable to apply recursive least-squares estimation (Section 3.1) and moreover to make use of recursive state-space filtering (Section 3.2). The latter is beneficial due to the explicit modelling of the circular motion of the laser scanner. The application of KF and its variants is well-known for prediction based on the motion model as well as for filtering (to reduce the measurement noise). All these mentioned points are in accordance with the conceptual design (Section 4.1) and its realisation (Section 4.2).

## 5.2. Motion modelling of the multi-sensor system in recursive state-space filters

Based on the Alg. 4.1 to derive the transformation parameters, the mathematical derivations of the novel approach are presented in detail here. The core of the algorithm is the motion modelling of the MSS in state-space filters. The motion modelling accesses the prototypic MSS with its sensors introduced in Section 4.2.1. As

<sup>1</sup>For instance, 9000 3D positions will result from 15 minutes GNSS data acquisition with a data rate of 10 Hz.

Table 5.1.: Aim, states, observations and output of different system modelling approaches.

	 <p><b>Single antenna motion modelling</b> (Section 5.2.1.1)</p>	 <p><b>Dual antennas motion modelling</b> (Section 5.2.1.2)</p>
Aim:	means of the trajectory of $\mathbf{p}^o$ . In addition, MSS specific quantities (adaptive parameters) are estimated.	means of the trajectory of $\mathbf{p}^d$ and $\mathbf{p}^o$ . Furthermore, constraints are used to take functional relationship among the state parameters into account.
Description of the MSS motion by		
States	Position of $\mathbf{p}^o$ , local heading orientation $\kappa^L$ and the adaptive parameters $r$ , $\theta$ and $s_{ltd}$ .	Positions of $\mathbf{p}^d$ and $\mathbf{p}^o$ as well as the MSS's velocity $v$
Observations acquired by	one GNSS equipment and the horizontal motor steps of the laser scanner.	two GNSS equipments.
Output	State estimates for subsequent determination of the transformation parameters. Estimates of $r$ , $\theta$ , $s_{ltd}$ which can be used to check the MSS's calibration values.	

already mentioned, the trajectories of  $\mathbf{p}^d$  and  $\mathbf{p}^o$  geometrically describe 3D circles due to the circular motion of the laser scanner about its vertical axis. The motion modelling is based on 3D coordinates in a local topo-centric NEU system or the ETRS89 combined with the UTM projection for the trajectories of  $\mathbf{p}^d$  and  $\mathbf{p}^o$ .

The parametrisation of these trajectories as circles by means of polar elements or time series of sine oscillations yield to non-linearities in the process equation. Thus, for the modelling of the motion of the MSS the usage of an EKF is proposed, which handles non-linearities by means of Taylor series expansion.

### 5.2.1. Process equation

This section is dedicated to the process equation (Eq. 3.31) of the proposed EKF. Two different variants of modelling the system are developed; an overview is given in Tab. 5.1. Both approaches utilise parts of the obtained quantities  $\Delta$ ,  $\theta$  and  $d^{do}$  during the MSS calibration (Section 4.3.4). The joint estimation of states as well as adaptive parameters ( $\Delta$  and  $\theta$ ) (also known as aEKF) is developed for a single antenna scenario. This can lead to a minimisation of discrepancies between the dynamic model and reality (Eichhorn, 2007).

The other approach proposes to use two antennas and takes into account functional relationships among the unknown state parameters. This is realised by the introduction of state constraints. In particular, the distance  $d^{do}$  and the constant velocity  $v$  of the MSS will be considered as constraints. Owing to the data acquisition principle of the laser scanner its horizontal and vertical rotations are assumed to be sufficiently constant which leads to a non-accelerated motion with constant  $v$ .

The laser scanner motion during its data acquisition is assumed to be free of disturbances caused by acceleration,

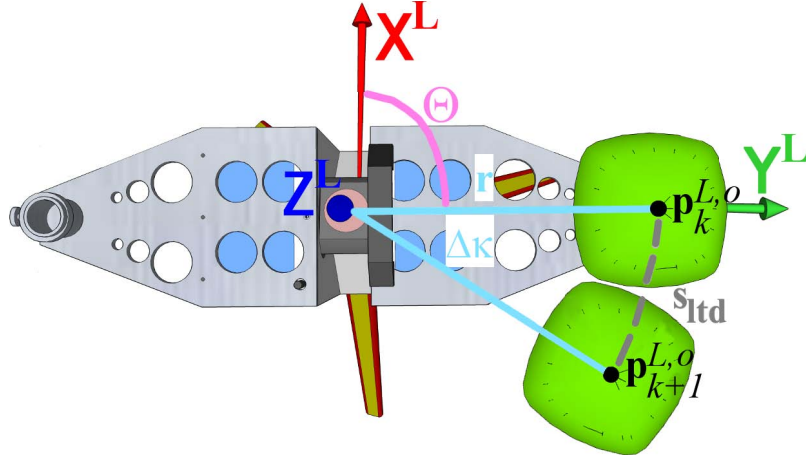


Figure 5.1: States and adaptive parameters for motion modelling: Circular in-plane motion of  $\mathbf{p}_k^{L,o}$  in the  $L$ -frame.

braking and steering movements. This leads to a controlled and straightforward prediction of the undisturbed circular motion of the laser scanner about its vertical axis. For this reason both process equations are introduced as undisturbed process equations. Thus, the coefficient matrix of disturbing variables  $\mathbf{S}$  (Eq. 3.19 and 3.33) is the identity matrix  $\mathbf{I}$  and for the process error vector follows  $E\{\mathbf{w}\} = 0$ . The VCM  $\Sigma_{\mathbf{w}\mathbf{w}}$  is assumed to be a random constant process (Gelb, 1974, p. 79). This undisturbed motion modelling is contrary to the typical motion modelling of vehicles treated in Eichhorn (2005), which allows for tangential accelerations due to discrepancies to the homogeneous circular motion. These discrepancies can be caused by acceleration, braking and steering movements of the vehicle.

### 5.2.1.1. Single GNSS antenna motion modelling by states and adaptive parameters

The modelling of the MSS's motion by states and adaptive parameters in an aEKF is introduced in this section (Paffenzholz et al., 2010a). As aforementioned, the trajectory of the MSS is parametrised by a circle in 3D space. In contrast to the general trajectory modelling in engineering geodesy (e.g., Aussems, 1999), this parametrisation is feasible due to the defined circular motion of the MSS, i.e., the trajectory of  $\mathbf{p}^o$  for a single GNSS antenna scenario. In the subsequent modelling the state vector includes four states: These are the 3D position  $\mathbf{p}_k^o$  of the positioning sensor (GNSS equipment) and the local heading  $\kappa_k^L$  (cf. Fig. 4.1). The adaptive parameters are the radius  $r_k$  (2<sup>nd</sup> component of  $\Delta$ ) and the angular offset  $\theta_k$  (cf. Fig. 4.10). In addition, the circular arc segment  $s_{ltd,k}$  (Fig. 5.1) is introduced as an adaptive parameter. These three adaptive parameters are time invariant and system-specific with well-known initial values which are determined within the MSS's calibration procedure (Section 4.3.4).

The circular in-plane motion of  $\mathbf{p}_k^o = [x_k^o \ y_k^o \ z_k^o]^T$  for two subsequent epochs  $k$  and  $k+1$  is depicted in Fig. 5.1. An epoch  $k$  is defined by the line synchronisation pulse of the laser scanner (available for each 2D vertical profile, cf. Section 4.2.1). The time span  $\Delta t$  between  $k$  and  $k+1$  is given by the typical rotation frequency of 12.5 Hz.

The motion parametrisation starts in the  $L$ -frame (Fig. 5.1). In general, there will be a residual divergence of the orientation to the direction of gravity which affects the  $x$  and  $y$  axis. This effect can be considered by the residual spatial rotations about the  $x$  axis  $\omega_k$  and about the  $y$  axis  $\varphi_k$  (cf. Paffenzholz et al., 2010a). It is noteworthy that the consideration of these residual spatial rotations is optional, since  $\omega_k$  and  $\varphi_k$  become small<sup>2</sup> if a proper orientation to the direction of gravity is assumed. Their impact on the motion model as well as on the final result is expected to be smaller than the uncertainties induced by the GNSS positions (cf. Fig. 4.7(b))

<sup>2</sup>Typical discrepancies for  $\omega_k$  and  $\varphi_k$  are  $< 0.05^\circ$  after a thorough orientation to the direction of gravity (cf. Section 4.3.1 and 4.3.3). The maximal metric uncertainty induced by this residuals in the distance of about 0.3 m is  $< 1.0$  mm.



and the laser scanner itself.

The orientation change  $\Delta\kappa_k$  of  $\mathbf{p}_k^{L,o}$  between  $k$  and  $k+1$  is expressed by  $\Delta\kappa_k = s_{ltd,k}/r_k$ . On the contrary, Paffenholtz et al. (2009) substitute the quantity  $s_{ltd,k}$  by  $v \cdot \Delta t$ , where  $v$  is the MSS's velocity and  $\Delta t$  the time span between  $k$  and  $k+1$ . The vector  $\mathbf{p}_{k+1}^{L,o}$  with respect to the centre point of the circle in the  $L$ -frame is given by

$$\mathbf{p}_{k+1}^{L,o} = \begin{bmatrix} x_k^{L,o} & y_k^{L,o} & z_k^{L,o} \end{bmatrix}^T = \begin{bmatrix} r_k \cdot \sin(\Delta\kappa_k) & r_k \cdot \cos(\Delta\kappa_k) & 0.0 \end{bmatrix}^T. \quad (5.2)$$

The circle's centre point has to be taken into account to reveal  $\mathbf{p}_{k+1}^{L,o}$  with respect to the previous epoch quantity  $\mathbf{p}_k^{L,o}$ . Therefore, the offsets  $\mathbf{\Delta}$  and  $\theta$  obtained within the MSS calibration are used to describe the translation  $\mathbf{\Delta}_{cp}^o$  between the actual  $\mathbf{p}_{k+1}^{L,o}$  and the circle's centre point

$$\mathbf{\Delta}_{cp,k}^o = \begin{bmatrix} -r_k \cdot \cos(\theta_k) & r_k \cdot \sin(\theta_k) & h^z \end{bmatrix}^T. \quad (5.3)$$

The value for  $\theta_k$  depends on the GNSS antenna position on the wing support structure. For the GNSS antenna in  $\mathbf{p}^o$  (positive  $y$ -axis) is  $\theta_k \approx 90^\circ$  (Fig. 5.1). For an antenna in  $\mathbf{p}^d$  (negative  $y$ -axis) is  $\theta_k \approx 270^\circ$ . Like the translations in  $y$ -direction, the translation in  $x$ -direction can be expressed by means of the radius (2<sup>nd</sup> component of  $\mathbf{\Delta}$ ) and  $\theta$ . The translation in  $z$ -direction  $h^z$  optionally allows for the antenna height which can already be considered in the GNSS analysis and has then to be set to zero.

The motion description of  $\mathbf{p}_{k+1}^{L,o}$  is completed by consideration of the local orientation  $\kappa_k^L$  in the  $L$ -frame by means of the rotation matrix  $\mathbf{R}_{\kappa^L}^L$  (Eq. A.3). Thereby,  $\kappa^L$  describes the angular progress during the rotation of the laser scanner about its vertical axis. This local orientation is updated by  $\kappa_{k+1}^L = \kappa_k^L + \Delta\kappa_k$  and the motion description is written as follows

$$\Delta\mathbf{p}_{k+1}^{L,o} = \left( \mathbf{R}_{\kappa^L}^L(\kappa_{k+1}^L) \right)^T \cdot \left[ \mathbf{p}_{k+1}^{L,o} - \mathbf{\Delta}_{cp,k}^o \right]. \quad (5.4)$$

Eq. 5.4 is the last step of the motion modelling of  $\mathbf{p}_{k+1}^{L,o}$  in the  $L$ -frame. The transformation to the  $G$ -frame and the consideration of  $\mathbf{p}_k^{G,o} = [X_k^{G,o} \ Y_k^{G,o} \ Z_k^{G,o}]^T$  at the previous epoch  $k$  completes the motion modelling and yields the non-linear function  $\mathbf{f}_{k+1,k}(\mathbf{x}_k, \mathbf{u}_k)$  of the undisturbed motion model

$$\mathbf{f}_{k+1,k}(\mathbf{x}_k, \mathbf{u}_k) = \mathbf{p}_k^{G,o} + \left( \mathbf{R}_{\kappa^G}^G(\kappa^G) \right)^T \cdot \Delta\mathbf{p}_{k+1}^{L,o} \quad (5.5)$$

In Eq. 5.5  $\mathbf{R}_{\kappa^G}^G(\kappa^G)$  (Eq. A.3) defines the global azimuthal orientation with respect to the  $G$ -frame. The value for the initial global azimuthal orientation  $\kappa^G$  can be calculated by the observed trajectory points.

The state vector  $\mathbf{x}_{k+1}$  is composed of seven quantities: the four general states in  $\mathbf{x}_{g,k+1}$  and the three adaptive parameters in  $\mathbf{x}_{a,k+1}$ , and is written as

$$\mathbf{x}_{k+1} = \left[ \mathbf{x}_{g,k+1} \mid \mathbf{x}_{a,k+1} \right]^T = \left[ \mathbf{p}_{k+1}^{G,o} \ \kappa_{k+1}^L \mid r_k \ \theta_k \ s_{ltd,k} \right]^T. \quad (5.6)$$

The transition matrix  $\mathbf{T}_{k+1,k}$  to predict the state vector is given as follows

$$\mathbf{T}_{k+1,k} = \left[ \begin{array}{ccc|ccc} 1 & 0 & 0 & \left. \frac{\partial X_{k+1}^{G,o}}{\partial \kappa_k^L} \right|_{\hat{\mathbf{x}}_k^+} & \left. \frac{\partial X_{k+1}^{G,o}}{\partial r_k} \right|_{\hat{\mathbf{x}}_k^+} & \left. \frac{\partial X_{k+1}^{G,o}}{\partial \theta_k} \right|_{\hat{\mathbf{x}}_k^+} & \left. \frac{\partial X_{k+1}^{G,o}}{\partial s_{ltd,k}} \right|_{\hat{\mathbf{x}}_k^+} \\ 0 & 1 & 0 & \left. \frac{\partial Y_{k+1}^{G,o}}{\partial \kappa_k^L} \right|_{\hat{\mathbf{x}}_k^+} & \left. \frac{\partial Y_{k+1}^{G,o}}{\partial r_k} \right|_{\hat{\mathbf{x}}_k^+} & \left. \frac{\partial Y_{k+1}^{G,o}}{\partial \theta_k} \right|_{\hat{\mathbf{x}}_k^+} & \left. \frac{\partial Y_{k+1}^{G,o}}{\partial s_{ltd,k}} \right|_{\hat{\mathbf{x}}_k^+} \\ 0 & 0 & 1 & 0 & 0 & 0 & 0 \\ 0 & 0 & 0 & 1 & -\hat{s}_{ltd,k}^+ / (\hat{r}_k^+)^2 & 0 & 1 / \hat{r}_k^+ \\ \hline \mathbf{0} & & & & & & \mathbf{I} \\ 3,4 & & & & & & 3,3 \end{array} \right]. \quad (5.7)$$

The explicit partial derivatives of Eq. 5.7 are given in Section A.4. No known input parameters are considered which leads to  $\mathbf{u}_k = \mathbf{0}$ . Thus, the prediction of the state (Eq. 5.6) is performed according to Eq. 3.34 and the corresponding cofactor matrix is calculated by means of Eq. 5.7 and Eq. 3.22. To illustrate the point, results are discussed in Section 6.1.1.1.

For the description of the progress in  $\Delta t$  the presented motion model relies on the circular arc segment  $s_{ltd,k}$  which is a sensor specific parameter. Thus, this manner of modelling can be entitled as *sensor-orientated modelling*. It is a necessity in this parametrisation that the observations of  $\mathbf{p}_k^o$  are available with the same  $\Delta t$ . Since the GNSS (and inclinometer) observations are acquired with different data rates (typically used GNSS data rate is 10 Hz), the observations have to be interpolated with respect to the line synchronisation pulses of the laser scanner because these values define the epochs of the introduced motion model. Due to the high data rate of the GNSS observations, it is expected that the error induced by linear interpolation is not significant in this application. An alternative approach for prediction and filtering is LSC (Section 3.3), which uses the whole stochastic information of the GNSS time series. Separate investigations of the trajectories by means of LSC are outlined in Section 6.1.2.

### 5.2.1.2. Dual GNSS antennas motion modelling by states with constraints

Besides the circle parametrisation in 3D space, the parametrisation by means of sine oscillations for the  $x$ - and  $y$ -components of  $\mathbf{p}^d$  and  $\mathbf{p}^o$  is feasible. In the subsequent modelling, the states are the 3D position  $\mathbf{p}_k^d$  and  $\mathbf{p}_k^o$  of the positioning sensors (GNSS equipments) and the velocity of the MSS  $v_k$ . The distance  $d^{do} = |\mathbf{p}^d \mathbf{p}^o|$ , which is an output quantity of the MSS calibration (Section 4.3.4), and the constance of the velocity  $v$ , which results from the non-accelerated motion, are introduced as state constraints  $\mathbf{D}$ . In addition, the significant frequency of the sine oscillation is introduced as known input  $u_k$  (e.g.,  $u_k = 0.001265$  for the  $360^\circ$  rotation). This value is empirically obtained by the analyses of several independent data acquisitions during the MSS's calibration. Furthermore, it can be obtained from the manufacturer specifications. The consideration of the significant frequency as known input  $u$  is comparable to the causative modification of the kinematic motion model published by Eichhorn (2005, pp. 90 ff.).

The sine oscillation for the north- and east-components of  $\mathbf{p}_k^{d/o} = [x_k^{d/o} \ y_k^{d/o} \ z_k^{d/o}]^T$  is depicted in Fig. 5.2. The values of the up-component vary around the height of the laser scanner in the given coordinate system with a magnitude of a 1 cm. This is in accordance with the achievable coordinate uncertainty in kinematic GNSS analyses and furthermore in compliance with the performance tests of the used GNSS antennas

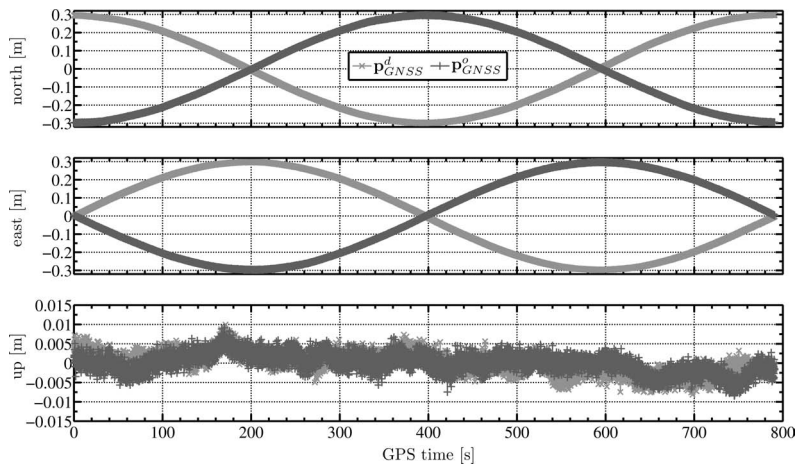


Figure 5.2: States with constraints and control input for motion modelling: The north- and east-components are characterised by a sinusoidal oscillation which results from the  $360^\circ$  rotation of the laser scanner. The up-component varies around the height of the laser scanner in the given coordinate system. The depicted time series for  $\mathbf{p}^d$  (light grey) and  $\mathbf{p}^o$  (dark grey) are real observations which are centred by their mean values for visualisation purposes.

(cf. Section 4.3.2 and Fig. 4.7(a)). Therefore, the non-linear function  $\mathbf{f}_{k+1,k}(\mathbf{x}_k, u_k)$  of the undisturbed motion model is given

$$\mathbf{f}_{k+1,k}(\mathbf{x}_k, u_k) = \begin{bmatrix} X_k^{G,d} + v_k \cdot \Delta t \cdot \sin(2 \cdot \pi \cdot u_k \cdot t_k) \\ Y_k^{G,d} - v_k \cdot \Delta t \cdot \cos(2 \cdot \pi \cdot u_k \cdot t_k) \\ Z_k^{G,d} \\ X_k^{G,o} - v_k \cdot \Delta t \cdot \sin(2 \cdot \pi \cdot u_k \cdot t_k) \\ Y_k^{G,o} + v_k \cdot \Delta t \cdot \cos(2 \cdot \pi \cdot u_k \cdot t_k) \\ Z_k^{G,o} \\ v_k \end{bmatrix} \quad (5.8)$$

where  $\Delta t$  denotes the time span between epoch  $k$  and  $k+1$  and  $t_k = t_{k-1} + \Delta t$  is the passed time counting from the model initialisation which is equivalent to the start of the motion. The state vector  $\mathbf{x}_{k+1}$  is written as

$$\mathbf{x}_{k+1} = \begin{bmatrix} \mathbf{p}_{k+1}^{G,d} & \mathbf{p}_{k+1}^{G,o} & v_k \end{bmatrix}^T. \quad (5.9)$$

The transition matrix  $\mathbf{T}_{k+1,k}$  and the known input gain  $\mathbf{B}_{k+1,k}$  to predict the state are given as follows

$$\mathbf{T}_{k+1,k} = \left[ \begin{array}{c|c} \mathbf{I}_{6,6} & \mathbf{T}_{12} \\ \hline \mathbf{0}_{1,6} & \mathbf{I}_{1,1} \end{array} \right] \quad \text{and} \quad \mathbf{B}_{k+1,k} = \begin{bmatrix} v_k \cdot \Delta t \cdot 2 \cdot \pi \cdot t \cdot \cos(2 \cdot \pi \cdot u_k \cdot t) \\ v_k \cdot \Delta t \cdot 2 \cdot \pi \cdot t \cdot \sin(2 \cdot \pi \cdot u_k \cdot t) \\ 0 \\ -v_k \cdot \Delta t \cdot 2 \cdot \pi \cdot t \cdot \cos(2 \cdot \pi \cdot u_k \cdot t) \\ -v_k \cdot \Delta t \cdot 2 \cdot \pi \cdot t \cdot \sin(2 \cdot \pi \cdot u_k \cdot t) \\ 0 \\ 0 \end{bmatrix}, \quad (5.10)$$

$$\text{where } \mathbf{T}_{12} = \begin{bmatrix} \Delta t \cdot \sin(2 \cdot \pi \cdot u_k \cdot t) & -\Delta t \cdot \cos(2 \cdot \pi \cdot u_k \cdot t) & 0 \\ -\Delta t \cdot \sin(2 \cdot \pi \cdot u_k \cdot t) & \Delta t \cdot \cos(2 \cdot \pi \cdot u_k \cdot t) & 0 \end{bmatrix}^T.$$

The prediction of the state (Eq. 5.9) is performed according to Eq. 3.34 and the corresponding cofactor matrix is calculated by means of Eq. 5.10 and Eq. 3.22.

In the modelling of the sine oscillation in Eq. 5.8 constraints for the distance are allowed, which involves all seven states: the two positions and the velocity. The fundamentals and sample applications for states with constraints are introduced in Section 3.2.5. It is noteworthy that state constraints are applied to the filtered estimates.

We know that the distance  $d^{do} = |\mathbf{p}^d \mathbf{p}^o|$  is a fixed value due to their diametrical positioning on the wing support structure (cf. Fig. 4.10). Furthermore, owing to the fact of the non-accelerated motion of the laser scanner, the velocity is constant for the time period of data acquisition. Utilising Eq. 3.43, this leads to the following non-linear constraint for  $d^{do}$  and linear constraint for  $v$

$$\mathbf{g}_1(\mathbf{x}_{k+1}) = \begin{bmatrix} \sqrt{\left(X_{k+1}^{G,d} - X_{k+1}^{G,o}\right)^2 + \left(Y_{k+1}^{G,d} - Y_{k+1}^{G,o}\right)^2 + \left(Z_{k+1}^{G,d} - Z_{k+1}^{G,o}\right)^2} \\ v_{k+1} - (\pi \cdot u_k \cdot d^{do}) \end{bmatrix} = \begin{bmatrix} d^{do} \\ 0 \end{bmatrix}. \quad (5.11)$$

Alternatively, the constraint regarding  $d^{do}$  can be supplemented by the current heading of the distance. By means of Eq. 3.40 the following set of linear constraints is obtained

$$\mathbf{g}_2(\mathbf{x}_{k+1}) = \begin{bmatrix} \cos(\kappa_{k+1}) \cdot d^{do} - \left(X_{k+1}^{G,d} - X_{k+1}^{G,o}\right) \\ \sin(\kappa_{k+1}) \cdot d^{do} - \left(Y_{k+1}^{G,d} - Y_{k+1}^{G,o}\right) \\ \sin(\omega_{k+1}) \cdot d^{do} - \left(Z_{k+1}^{G,d} - Z_{k+1}^{G,o}\right) \\ v_{k+1} - (\pi \cdot u_k \cdot d^{do}) \end{bmatrix} = \begin{bmatrix} 0 \\ 0 \\ 0 \\ 0 \end{bmatrix}, \quad (5.12)$$

where the current heading  $\kappa_{k+1}$  can be calculated with the tangent function (cf. Eq. 5.15) utilising the filtered state estimates. The rotation  $\omega_{k+1}$  is assumed to be zero owing to the fact of the orientation of the laser scanner to the direction of gravity. The constraint given in Eq. 5.11 considers only the distance itself without the orientation of the distance which is allowed by the constraints in Eq. 5.12. Results for both sets of constraints are shown as an example in Section 6.1.1.2.

In the above introduced motion model an appropriate  $\Delta t$  is adopted for the prediction step. In particular  $\Delta t = 0.1$  s, which corresponds to the typically used GNSS acquisition rate, is chosen following the laser scanner's vertical rotation frequency of 12.5 Hz. Thus, this manner of modelling can be entitled as *data-orientated modelling* which can handle also different acquisition rates for both GNSS equipments. This is in contrast to the motion model in Section 5.2.1.1 where the observations have to be pre-processed to compile with the set  $\Delta t$ . After the measurements are available, the predicted states are filtered and the constraints given in Eq. 5.11 and 5.12 are applied. A comprehensive discussion regarding the benefit of using the state constraints is given in Section 6.1.1.2.

### 5.2.2. Measurement equation

As a reminder of Section 3.2, the general measurement equation (Eq. 3.23) is given by the vector of observations  $\mathbf{y}_{k+1}$ , the corresponding measurement error vector  $\mathbf{v}_{k+1}$ , the measurement matrix  $\mathbf{H}_{k+1}$  and  $\mathbf{x}_{k+1}$ . The observation vector is defined by the used sensors in the MSS. For both approaches: the single and the dual antennas scenario, 3D GNSS positions<sup>3</sup> in a local topo-centric NEU system or in the ETRS89 combined with the UTM projection with 10 Hz data rate are assumed. At the current developmental stage of the MSS, the GNSS analysis is performed in post-processing with respect to a reference station; for further details the reader is referred to Section 4.2.2. The stochastic model of observations is given by the VCMs of the 3D positions which are obtained by the GNSS analysis. In accordance to the two distinct approaches for the motion modelling, the corresponding observation vectors in the linearised measurement equations are given in the following.

**In the single GNSS antenna scenario,** the observation vector is composed of the 3D positions  $\mathbf{p}_{GNSS, k+1}^o = [X_{GNSS, k+1}^o \ Y_{GNSS, k+1}^o \ Z_{GNSS, k+1}^o]^T$  and the horizontal motor steps of the laser scanner  $\kappa_{Scan, k+1}$ . The horizontal motor steps of the laser scanner are available during the data acquisition or can be extracted in post-processing from the 3D point cloud (Zoller+Fröhlich GmbH, 2009). This observation vector fits to the motion modelling by states and adaptive parameters with the state vector in Eq. 5.6. The linearised measurement equation is given as

$$\begin{aligned} \frac{\mathbf{y}_{k+1}}{6,1} &= \left[ \mathbf{p}_{GNSS, k+1}^o \quad \kappa_{Scan, k+1} \right]^T \\ &= \begin{bmatrix} \mathbf{I} & \mathbf{0} \\ 4,4 & 4,3 \end{bmatrix} \cdot \frac{\mathbf{x}_{k+1}}{7,1} + \frac{\mathbf{v}_{k+1}}{4,1} = \frac{\mathbf{H}_{k+1}}{4,7} \cdot \frac{\mathbf{x}_{k+1}}{7,1} + \frac{\mathbf{v}_{k+1}}{4,1} \quad \text{with} \quad \mathbf{v}_{k+1} \sim \mathcal{N}(\mathbf{0}, \Sigma_{\mathbf{y}\mathbf{y}_{k+1}}). \end{aligned} \quad (5.13)$$

**In the dual GNSS antennas scenario,** the observation vector is composed of the 3D positions  $\mathbf{p}_{GNSS, k+1}^{d/o} = [X_{GNSS, k+1}^{d/o} \ Y_{GNSS, k+1}^{d/o} \ Z_{GNSS, k+1}^{d/o}]^T$ . This vector of observations fits to the motion modelling by states with constraints with the state vector in Eq. 5.9. For the linearised measurement equation follows

$$\begin{aligned} \frac{\mathbf{y}_{k+1}}{6,1} &= \left[ \mathbf{p}_{GNSS, k+1}^d \quad \mathbf{p}_{GNSS, k+1}^o \right]^T \\ &= \begin{bmatrix} \mathbf{I} & \mathbf{0} \\ 6,6 & 6,1 \end{bmatrix} \cdot \frac{\mathbf{x}_{k+1}}{7,1} + \frac{\mathbf{v}_{k+1}}{6,1} = \frac{\mathbf{H}_{k+1}}{6,7} \cdot \frac{\mathbf{x}_{k+1}}{7,1} + \frac{\mathbf{v}_{k+1}}{6,1} \quad \text{with} \quad \mathbf{v}_{k+1} \sim \mathcal{N}(\mathbf{0}, \Sigma_{\mathbf{y}\mathbf{y}_{k+1}}). \end{aligned} \quad (5.14)$$

<sup>3</sup>The coordinate components of a 3D position  $\mathbf{p}^G = [X^G \ Y^G \ Z^G]^T$  in the local topo-centric NEU system or the ETRS89 with the UTM projection are denoted as follows:  $X$  corresponds to the north-,  $Y$  to the east- and  $Z$  to the up-component.

### 5.2.3. Proposed algorithm for direct geo-referencing of 3D point clouds

This section seizes upon the comprehensive explanations of the novel algorithm's concept (Alg. 4.1) for direct geo-referencing (Section 4.2.3). Tab. 5.2 summarises the novel algorithm's calculation steps for the single antenna and the dual antennas scenario. The tasks beyond the EKF (to obtain the transformation parameters), the *calculation of the heading* and the *estimation of the translation vector* by means of recursive least-squares estimation in GMM, are introduced. Furthermore, the final *direct geo-referencing by means of 3D rigid body transformation* considering uncertainty measures is addressed.

**The calculation of the heading**  $\kappa$  is performed by the tangent function utilising the  $X$ - and  $Y$ -coordinates of two 3D positions  $\mathbf{p}^a$  and  $\mathbf{p}^b$

$$\kappa_k = \arctan\left(\frac{Y^a - Y^b}{X^a - X^b}\right) \quad \text{with the VCM } \Sigma_{\kappa\kappa}, \quad (5.15)$$

where  $\Sigma_{\kappa\kappa}$  is obtained by applying the LOP.

For the single antenna scenario, the heading is obtained by Eq. 5.15 for each  $\mathbf{p}^a := \mathbf{p}_k^{G,d}$  with respect to the centre point  $\mathbf{p}^b := \mathbf{p}^{G,cp}$ . This sequential calculation of  $\kappa$  yields linearly increasing values due to the assumed constant rotation of the laser scanner about its vertical axis. The state parameter  $\kappa_{Scan,k}$  (Eq. 5.6) is used to reduce the heading with respect to the first epoch which is equivalent to the motion start. Thus, this value represents the desired heading for the transformation.

In the dual antennas scenario, the heading is calculated utilising Eq. 5.15 with both positions  $\mathbf{p}^a := \mathbf{p}_k^{G,d}$  and  $\mathbf{p}^b := \mathbf{p}_k^{G,o}$ . Again,  $\kappa$  yields linearly increasing values for the  $360^\circ$  of the laser scanner. By application of the Rauch-Tung-Striebel smoother optimal state estimates for the first epoch  $k$  are obtained, i. e., this provides the desired heading in the dual antennas scenario.

**The estimation of the translation vector**  $\mathbf{t}_L^G = \mathbf{p}^{G,cp} = [X^{G,cp} \ Y^{G,cp} \ Z^{G,cp}]^T$  is realised by means of recursive least-squares estimation in GMM which allows the calculation for each epoch parallel to the prediction and filtering in the EKF. Since the translation vector is equivalent to the centre point of the 3D circle (given through the trajectories of  $\mathbf{p}^{G,d}$  and  $\mathbf{p}^{G,o}$ ), this circumstance can be used for the estimation. For the single antenna scenario, the centre point estimation is outlined in Section 5.1 and the condition equation

Table 5.2.: Calculation steps of the novel algorithm for the single and the dual antennas scenario.

Task	Single GNSS antenna scenario	Dual GNSS antennas scenario
Prediction of	a priori estimate of $\hat{\mathbf{x}}_{k+1}^-$ (Eq. 5.6).	a priori estimate of $\hat{\mathbf{x}}_{k+1}^-$ (Eq. 5.9).
Filtering of	a posteriori estimate of $\hat{\mathbf{x}}_{k+1}^+$ (Eq. 5.13).	a posteriori estimate of $\hat{\mathbf{x}}_{k+1}^+$ (Eq. 5.14).
<i>Calculation of heading by means of filtered trajectories.</i>		
Application of state constraints	–	given in Eq. 5.11 or Eq. 5.12; afterwards the heading is calculated by means of the obtained constrained trajectories.
<i>Estimation of translation vector by means of recursive least-squares estimation in GMM.</i>		
Smoothing of	–	trajectories by means of Rauch-Tung-Striebel smoother (Section 3.2.3) and repetition of 3 <sup>rd</sup> and 5 <sup>th</sup> task with the smoothed trajectories.

of the GHM is given by the equation of a circle (Eq. 3.1). To perform the estimation in a recursive manner, a GMM formulation is required (Section 3.1.3). Paffenholz and Kutterer (2008) show the transformation of the primary GHM into an equivalent GMM for outlier detection purposes in the single antenna scenario. The utilisation of the transformed model for the recursive estimation is qualified for the estimation of the translation vector and its VCM.

In the dual antennas scenario, both diametrical positions and their known distance  $d^{do}$  are utilised for the estimation of  $\mathbf{t}_L^G$ . Thus, the functional model is given in a GHM by the non-linear function

$$\mathbf{f}(E\{\mathbf{y}\}, \mathbf{x}) = \begin{bmatrix} X^{G, cp} - \left( X_{k+1}^{G, d} + \frac{d^{do}}{2} \cdot \cos(\arctan(\frac{\Delta Y}{\Delta X})) \right) \\ Y^{G, cp} - \left( Y_{k+1}^{G, d} + \frac{d^{do}}{2} \cdot \sin(\arctan(\frac{\Delta Y}{\Delta X})) \right) \\ Z^{G, cp} - \left( 0.5 \cdot (Z_{k+1}^{G, d} + Z_{k+1}^{G, o}) \right) \end{bmatrix} = \begin{bmatrix} 0 \\ 0 \\ 0 \end{bmatrix}, \quad (5.16)$$

where  $\Delta X = X_{k+1}^{G, d} - X_{k+1}^{G, o}$  and  $\Delta Y = Y_{k+1}^{G, d} - Y_{k+1}^{G, o}$ . The vector of observations is  $\mathbf{y} = [\mathbf{p}_{k+1}^{G, d} \ \mathbf{p}_{k+1}^{G, o}]^T$  and the vector of parameters is  $\mathbf{x} = [\mathbf{p}^{G, cp}]^T$ . Thus, for the recursive estimation the functional model in Eq. 5.16 has to be transformed according to Section 3.1.4. The required partitioning of  $\mathbf{y}$  is given by  $\mathbf{y}_1 = [Y_{k+1}^{G, d} \ Z_{k+1}^{G, d} \ Y_{k+1}^{G, o}]^T$  and  $\mathbf{y}_2 = [X_{k+1}^{G, d} \ X_{k+1}^{G, o} \ Z_{k+1}^{G, o}]^T$ . The resulting linearised GMM (Eq. 3.16) allows the recursive estimation of the vector of parameters (Eq. 3.12) and its VCM (Eq. 3.15).

**The final direct geo-referencing** is performed by the 3D rigid body transformation given in Eq. 2.8 with the previously estimated transformation parameters (Eq. 5.15 and 5.16). The uncertainty aspect in the proposed algorithm for direct geo-referencing is illustrated in Fig. 5.3. Two main components of the uncertainty in the determination of global positions of objects in 3D point clouds exist: First, the positional uncertainty (Section 2.3.3), which is caused by the laser scanner's systematic and random error budget. For registration tasks of 3D point clouds in iterative matching algorithms these uncertainties are used (cf. Section 2.2.3). Second, the transformational uncertainty (Section 2.3.4), which is related to the applied geo-referencing method, i. e., for direct geo-referencing the main contribution is given by the VCMs of the transformation parameters. This uncertainties have not been widely considered in the geo-referencing of 3D point clouds acquired by stationary laser scanners.

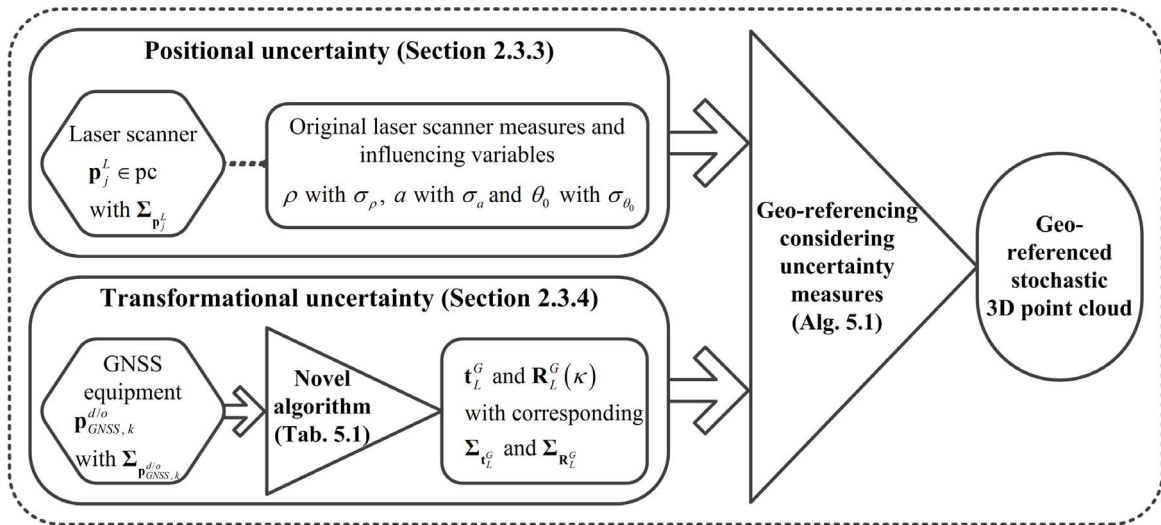


Figure 5.3: Uncertainty aspects in the direct geo-referencing of 3D point clouds with their functional relation and influencing variables.  $pc$  denotes a 3D point cloud with its  $\mathbf{p}_j^L$  points.  $\rho$  denotes the range measurement,  $a = [\beta \ \alpha]$  represents the angular measurements and  $\theta_0$  is the incidence angle.  $\mathbf{P}_{GNSS,k}^{d/o}$  denote the trajectory obtained by the GNSS equipment and  $\kappa$  is the heading.

The entire (positional and transformational) uncertainty information for each  $\mathbf{p}^G$  of a 3D point cloud in the  $G$ -frame can be obtained by applying the LOP to Eq. 2.8 which yields the corresponding VCM

$$\Sigma_{\mathbf{p}^G} = \mathbf{F} \cdot \begin{bmatrix} \Sigma_{\mathbf{t}_L^G} & \mathbf{0} & \mathbf{0} \\ \mathbf{0} & \Sigma_{\mathbf{R}_L^G} & \mathbf{0} \\ \mathbf{0} & \mathbf{0} & \Sigma_{\mathbf{p}^L} \end{bmatrix} \cdot \mathbf{F}^T, \quad (5.17)$$

where  $\mathbf{F} = \left[ \frac{\partial \mathbf{p}^G}{\partial t_x} \quad \frac{\partial \mathbf{p}^G}{\partial t_y} \quad \frac{\partial \mathbf{p}^G}{\partial t_z} \quad \frac{\partial \mathbf{p}^G}{\partial \kappa} \quad \frac{\partial \mathbf{p}^G}{\partial x^L} \quad \frac{\partial \mathbf{p}^G}{\partial y^L} \quad \frac{\partial \mathbf{p}^G}{\partial z^L} \right]$  expresses the Jacobi matrix of Eq. 2.8. The submatrices in Eq. 5.17 are the VCMs of the translation vector  $\Sigma_{\mathbf{t}_L^G}$  and the heading (rotation matrix)  $\Sigma_{\mathbf{R}_L^G} := \Sigma_{\kappa\kappa}$ . The positional uncertainty is covered by  $\Sigma_{\mathbf{p}^L} := \Sigma_{\bar{\mathbf{p}}^L}$  and their calculation is summarised in Alg. 2.2.

The direct geo-referencing considering the above-mentioned uncertainty measures are subsumed in Alg. 5.1. As can be seen in Alg. 5.1, depending on the available VCMs, separate investigations regarding positional or transformational uncertainty are feasible. If  $\Sigma_{\mathbf{t}_L^G}$  and  $\Sigma_{\mathbf{R}_L^G}$  are set to zero in Eq. 5.17, only positional uncertainty is considered. Thus, the results will be identical with those of Pennec and Thirion (1997) and Bae et al. (2009). In case of  $\Sigma_{\mathbf{p}^L}$  has been set to zero, the sole impact of transformational uncertainty can be analysed. As aforementioned, transformational uncertainty has not been widely taken into account for stationary laser scanner scenarios. This is owed to the fact that usually additional position equipment, such as GNSS equipment and its proper analyses, are required in order to obtain the transformational uncertainty. The novel algorithm (introduced in this section) is capable to deliver next to the transformation parameters their corresponding VCMs. It is noteworthy that the major benefit of propagating the transformational uncertainty to 3D point clouds is seen for subsequent analyses. This can be the application of iterative matching algorithms to improve the geo-referencing or other post-processes such as classification and segmentation. The 3D point clouds supplemented with positional and transformational uncertainties (Line 9 in Alg. 5.1) are called *geo-referenced stochastic 3D point clouds* (Paffenholtz and Bae, 2012, Vennegeerts, 2011). For the visualisation of the geo-referenced stochastic 3D point cloud the mean coordinate uncertainty (Vennegeerts, 2011, Eq. 4.17)

$$\bar{\sigma}_{\mathbf{p}^G} = \sqrt{\frac{1}{3} \cdot \text{tr}(\Sigma_{\mathbf{p}^G})} \quad (5.18)$$

where  $\mathbf{p}^G \in pc$  with  $\Sigma_{\mathbf{p}^G}$  (Eq. 5.17) is used.

---

**Algorithm 5.1:** Direct geo-referencing considering uncertainty measures (Paffenholtz and Bae, 2012, modified).

---

```

1 Input:  $\bar{pc}(\bar{\mathbf{p}}^L)$ ,  $\Sigma_{\bar{pc}(\bar{\mathbf{p}}^L)}$ ,  $\mathbf{t}_L^G$ ,  $\Sigma_{\mathbf{t}_L^G}$ ,  $\mathbf{R}_L^G$ ,  $\Sigma_{\mathbf{R}_L^G}$ 
2 foreach  $\bar{\mathbf{p}}^L \in \bar{pc}$  do
3     3D rigid body transformation of  $\bar{\mathbf{p}}^L$  with estimated transformation parameters Eq. 2.8
4     Propagation of variances Eq. 5.17
5         if  $\Sigma_{\mathbf{t}_L^G} \equiv \Sigma_{\mathbf{R}_L^G} \equiv \mathbf{0}$  then
6              $\left[ \text{Only positional uncertainty} \right]$ 
7         else if  $\Sigma_{\bar{\mathbf{p}}^L} \equiv \mathbf{0}$  then
8              $\left[ \text{Only transformational uncertainty} \right]$ 
9         else if  $\Sigma_{\mathbf{t}_L^G} \neq \Sigma_{\mathbf{R}_L^G} \neq \Sigma_{\bar{\mathbf{p}}^L} \neq \mathbf{0}$  then
10             $\left[ \text{Positional and transformational uncertainty} \right]$ 
11 Output:  $\bar{pc}(\bar{\mathbf{p}}^G) = \bar{pc}^G$  and  $\Sigma_{\bar{pc}(\bar{\mathbf{p}}^G)} = \Sigma_{\bar{pc}^G}$ 

```

---

### 5.3. Optimisation of transformation parameters considering uncertainties

This section proposes a matching algorithm named the *Geo-referencing ICP with Helmert 3D transformation (Gref-ICPHe3)* (Paffenzholz and Bae, 2012) which improves the relative orientation between two laser scanner sites. The rough work flow is illustrated in Fig. 5.4. The Gref-ICPHe3 requires as input values at least two geo-referenced stochastic 3D point clouds. The novel algorithm introduced in Section 5.2.3 is dedicated to provide this type of stochastic 3D point cloud. Recalling Fig. 5.3, the novel algorithm is intended to provide a 3D point cloud with two kinds of stochastic information positional and transformational uncertainty in an optimal manner. An “optimal” point cloud is defined as a stochastic 3D point cloud with minimal variances for each 3D point in an absolute coordinate system (Paffenzholz and Bae, 2012).

First, this section presents an adaptive modification of the threshold for the closest distance search which aims to reduce and refine the search space. Second, the chosen adjustment model for the estimation of the transformation parameters within the matching algorithm is outlined. Third, the Gref-ICPHe3 proposed by Paffenzholz and Bae (2012) is summarised in Alg. 5.2. The algorithm’s aim is the optimisation of the relative orientation between two 3D point clouds. To achieve this aim, an ICP based matching (Section 2.2.3) is utilised which rigorously allows for the uncertainty measures given by the participating stochastic 3D point clouds.

The topics of searching corresponding point pairs as well as the definition of an appropriate threshold to indicate the closest distance are introduced in Section 2.2.3. For the modification of the threshold for the closest distance search within each iteration, two approaches (Alg. 5.2, Line 14 ff.) are utilised in the Gref-ICPHe3: First, the closest distance statistics (mean value and standard deviation) are used (Zhang, 1994). Second, the positional uncertainty of the two corresponding points is used to modify the threshold value (Paffenzholz and Bae, 2012). For the latter approach, an approximate for the joint standard deviation of the positional uncertainty of the possible corresponding points  $\mathbf{cpp}^{G,12} = [\mathbf{p}^{G,1} \quad \mathbf{p}^{G,2}]$  is calculated as follows

$$\bar{\sigma}_{\mathbf{cpp}^{G,12}}^L = \sqrt{\frac{1}{3} \cdot \text{tr} \left( \Sigma_{\mathbf{p}^{L,1}} + \mathbf{R}_2^1 \cdot \Sigma_{\mathbf{p}^{L,2}} \cdot (\mathbf{R}_2^1)^T \right)} \quad (5.19)$$

In Eq. 5.19,  $\Sigma_{\mathbf{p}^{L,1}}$  and  $\Sigma_{\mathbf{p}^{L,2}}$  denote the positional uncertainty of the participating points  $\mathbf{p}^{G,1} \in pc^{G,1}$  and  $\mathbf{p}^{G,2} \in pc^{G,2}$ . The rotation matrix  $R_2^1$  accounts for the relative orientation between the point clouds  $pc^{G,1}$  and  $pc^{G,2}$ .

For the estimation of the relative transformation parameters (Alg. 5.2, Line 25 ff.) a least-squares adjustment by means of GHM is used. In particular, the closed-form solution proposed by Bleich and Illner (1989) is

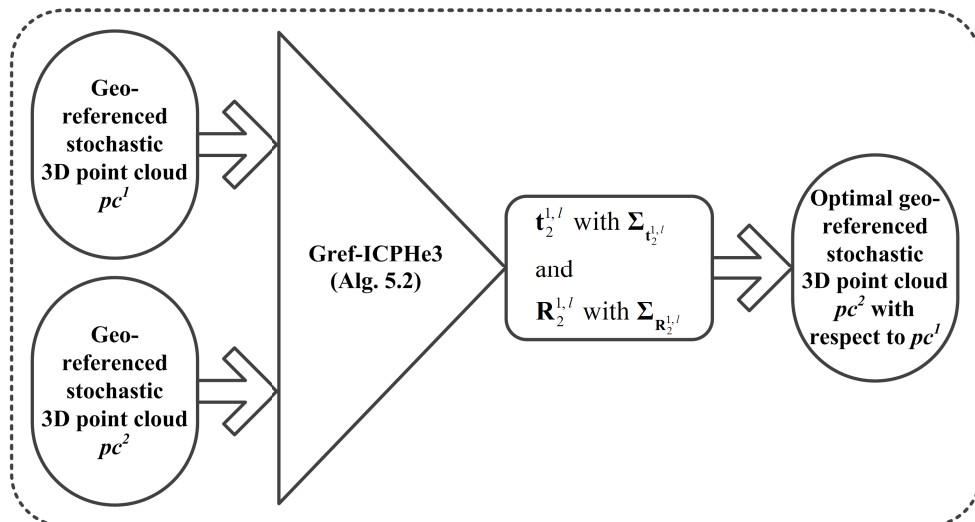


Figure 5.4: Optimisation of transformation parameters by means of Gref-ICPHe3.



---

**Algorithm 5.2:** Iterative matching by means of Gref-ICPHe3 (Paffenholz and Bae, 2012, modified).

---

```

1 Input:  $\overline{pc}^{G, s=1,2}$ ,  $\Sigma_{\overline{pc}^{G, s=1,2}}$ ,  $\tau_D$ ,  $\epsilon_m$ , and  $\overline{rg}^L$ 
2 Gref-ICPHe3
3   Initialisation and setting of thresholds and epsilons
4      $\tau_D$ ,  $\epsilon_m$ ,  $\epsilon_{rg_{rms}}$ ,  $\epsilon_{CRLB}$ 
5     Initial values:  $\tau_{D_{query}} = 2 \cdot \tau_D$ ,  $\tau_{rg_{rms}} = 1$ ,  $\tau_{CRLB} = 1$ ,  $no_C = 0$ ,  $l = 0$  (iteration counter)
6     Set up kd-tree  $kdt_{\overline{pc}^{G,1}}$  for  $\overline{pc}^{G,1}$ 
7   while ( $|\Delta t| > \epsilon_m$ ) & ( $|\Delta R| > \epsilon_{rad}$ ) & ( $no_C \neq 3$ ) do
8      $l = l + 1$ 
9     Uncertainty consideration after proper corresponding points are found
10    if  $l > 1$  &  $\tau_{rg_{rms}} < \epsilon_{rg_{rms}}$  then
11      [ Rigorous consideration of uncertainties
12    Searching closest distance in  $kdt_{\overline{pc}^{G,1}}$  for all points in  $\overline{pc}^{G,2,l}$  according to  $\tau_{D_{query}}$ 
13    Store  $n_{cpp}$  corresponding point pairs  $\mathbf{cpp}_i^{G,12} = [\overline{p}^{G,pc^1} \ \overline{p}^{G,pc^2}]$  and closest distances  $d_{min,i}^{12}$ 
14    Adaptation of  $\tau_{D_{query}}$ 
15    if  $\tau_{CRLB} > \epsilon_{CRLB}$  then Calculate distance statistics  $\mu_{d_{min,i}^{12}}$ ,  $\sigma_{d_{min,i}^{12}}$  for all  $d_{min,i}^{12}$ 
16      if  $\mu_{d_{min,i}^{12}} < \tau_D$  then
17         $\tau_{D_{query}} = \mu_{d_{min,i}^{12}} + 2 \cdot \sigma_{d_{min,i}^{12}}$ 
18      else if  $\mu_{d_{min,i}^{12}} < 2 \cdot \tau_D$  then
19         $\tau_{D_{query}} = \mu_{d_{min,i}^{12}} + \sigma_{d_{min,i}^{12}}$ 
20      Reject  $d_{min,i}^{12} > \tau_{D_{query}}$ 
21    else Calculate  $\overline{\sigma}_{\mathbf{cpp}_i^{G,12}}^L$  according to Eq. 5.19
22      if  $d_{min,i}^{12} > 2 \cdot \overline{\sigma}_{\mathbf{cpp}_i^{G,12}}^L$  then
23        Reject  $d_{min,i}^{12}$ 
24       $\tau_{D_{query}} = \text{mean}(\overline{\sigma}_{\mathbf{cpp}_i^{G,12}}^L)$ 
25    Helmert 3D transformation loop
26    Input:  $\overline{pc}^{G,1}$ ,  $\Sigma_{\overline{pc}^{G,1}}$ ,  $\overline{pc}^{G,2,l}$ ,  $\Sigma_{\overline{pc}^{G,2,l}}$ ,  $\epsilon_m$ 
27    while no convergence do
28      [ Least-squares adjustment according to Bleich and Illner (1989)
29    Output:  $\mathbf{t}_2^{1,l}$ ,  $\Sigma_{\mathbf{t}_2^{1,l}}$ ,  $\mathbf{R}_2^{1,l}$ , and  $\Sigma_{\mathbf{R}_2^{1,l}}$ 
30    Transformation of  $\overline{pc}^{G,2,l}$  with  $\Sigma_{\overline{pc}^{G,2,l}}$  (cf. Alg. 5.1)
31    Overall transformation parameters and their corresponding variances
32     $\mathbf{R}_2^1 = \mathbf{R}_2^{1,l} \cdot \mathbf{R}_2^1$  and  $\Sigma_{\mathbf{R}_2^1}$ 
33     $\mathbf{t}_2^1 = \mathbf{R}_2^{1,l} \cdot \mathbf{t}_2^{1,l}$  and  $\Sigma_{\mathbf{t}_2^1}$ 
34    if ( $|\Delta t| < \epsilon_m$ ) & ( $|\Delta R| < \epsilon_{rad}$ ) then  $no_C = +1$  else  $no_C = 0$ 
35 Output:  $\widehat{\overline{pc}}^{G,2}$ ,  $\Sigma_{\widehat{\overline{pc}}^{G,2}}$ ,  $\widehat{\mathbf{t}}_2^1$ ,  $\Sigma_{\widehat{\mathbf{t}}_2^1}$ ,  $\widehat{\mathbf{R}}_2^1$ ,  $\Sigma_{\widehat{\mathbf{R}}_2^1}$ 

```

---

implemented. Within each iteration step of the matching algorithm, the VCMs of the relative transformation parameters are considered in the stochastic model of the GHM. General aspects of the functional model for the transformation problem (Eq. 2.8), such as linearisation aspects in the GHM are outlined in Section 3.1.2. It is noteworthy that owing to the already geo-referenced 3D point clouds (Alg. 5.1), good initial transformation parameters are assumed to be available. This yields small values for the remaining rotational parameters and thus justifies the linearisation of the rotation matrix in the functional model of the GHM.

The Gref-ICPHe3 for the optimisation of transformation parameters while considering the two kinds of

stochastic information, the positional and the transformational uncertainty, is given in Alg. 5.2. The input data used in the Gref-ICPHe3 are two stochastic 3D point clouds in a common  $G$ -frame with their corresponding VCM obtained by Eq. 5.17. The positional uncertainty calculation according to Alg. 2.2 also provides a separation of the 3D point cloud in planar and non-planar regions. It is noteworthy that in the matching only points in planar regions of each 3D point cloud  $\overline{pc}^{G,1}$  and  $\overline{pc}^{G,2}$  are involved. It is straightforward to use the novel algorithm summarised in Tab. 5.2 for the estimation of the transformation parameters and their VCMs. The subsequent direct geo-referencing is proposed to be performed according to Alg. 5.1.

The final result of the Gref-ICPHe3 is an optimal aligned stochastic 3D point cloud  $\hat{pc}^{G,2}$  (first limited to planar regions) with respect to  $\overline{pc}^{G,1}$ . The obtained relative transformation parameters  $\hat{\mathbf{t}}_2^1$  with  $\Sigma_{\hat{\mathbf{t}}_2^1}$  and  $\hat{\mathbf{R}}_2^1$  with  $\Sigma_{\hat{\mathbf{R}}_2^1}$  are used for the transformation of the non-planar regions which leads to the entire stochastic 3D point cloud  $\hat{pc}^{G,2}$ .

For the Gref-ICPHe3 (common for iterative matching algorithms) the definition of several threshold ( $\tau$ ) and termination ( $\epsilon$ ) criteria is required. The threshold values are explained and moreover a priori information to define them and how they are updated during each iteration is provided in the following listing (taken from Paffenholz and Bae, 2012):

- $\tau_D$  indicates whether the match between two point clouds is good or not. The value should be chosen with respect to the scanning resolution (Zhang, 1994, p. 125) and a priori knowledge about the uncertainties.
- $\tau_{D_{query}}$  is the threshold for the closest distance search within the kd-tree. For the first iteration this threshold is initialised by  $\tau_{D_{query}} = 2 \cdot \tau_D$ . In all subsequent iterations an adaptive update is performed according to Alg. 5.2, Lines 14 – 24.
- $\epsilon_m$  is the metric criterion for the translational parameters, which is used to terminate the iterative calculations. Whenever an arbitrary metric parameter improvement descends below  $\epsilon_m$  during the iteration steps, it is assumed that no further significant parameter improvement can be reached. In contrast to other threshold values for the Gref-ICPHe3, it is needed to be set in an empirical manner, which typically is in a range of 0.01 – 1 mm.
- $\epsilon_{rad}$  is the angular criterion which is used to terminate the iterative calculations. Whenever an arbitrary angular parameter improvement descends below  $\epsilon_{rad}$  during the iteration steps, it is assumed that no further significant parameter improvement can be reached. This value can be defined according to the previous explanations for  $\epsilon_m$  or as a function of  $\epsilon_m$ . This is proposed to be  $\epsilon_{rad} = \epsilon_m / \overline{rg}^L$ , where  $\overline{rg}^L$  denotes an average of the measured ranges by the laser scanner, which is deduced from a simple orthogonal relationship between the translation and rotation components in the Cartesian coordinate systems.
- $no_C$  is a counting variable to guarantee the convergence of the iterative calculations. It counts the number of times when a parameter improvement descends below the termination criteria ( $\epsilon_m$  and  $\epsilon_{rad}$ ) during an iteration step.
- $\tau_{rms}$  describes the root mean square error of the ranges. It is calculated in each iteration step by the closest distances before and after the transformation. This provides information for the level of correspondence of the two point clouds. Once this criterion is satisfied, the rigorous consideration of the total uncertainties is conducted in all subsequent iteration.
- $\tau_{CRLB}$  denotes the Cramer-Rao lower bound (for details see, e.g., Bae, 2006). It is calculated in each iteration step by the corresponding point variances in each point cloud after the transformation. When it descends below  $\epsilon_{CRLB}$  (rule of thumb), the calculation method for  $\tau_{D_{query}}$  is changed to the proposed method (Eq. 5.19) taking uncertainty measures into account.

## 6. Results of practical investigations

The results of the developed MSS (Chapter 4) and the proposed novel methodology (Chapter 5) for the direct geo-referencing of 3D point clouds from the MSS are presented in this chapter. Two real data sets: *Saxon Steed* and *Geodetic Institute* shown in Fig. 6.1 and Tab. 6.1, are utilised for the rigorous tests of the proposed methodology.

The 3D trajectories for the estimation of the translation vector and heading of the laser scanner are analysed in depth in Section 6.1. The details of the proposed modelling of the MSS's motion which is realised in an EKF approach for two scenarios, i. e., the single and the dual GNSS antennas scenario, are presented in Section 6.1.1. Further analyses by means of LSC are treated in Section 6.1.2. Both previously presented analyses are discussed in Section 6.1.3.

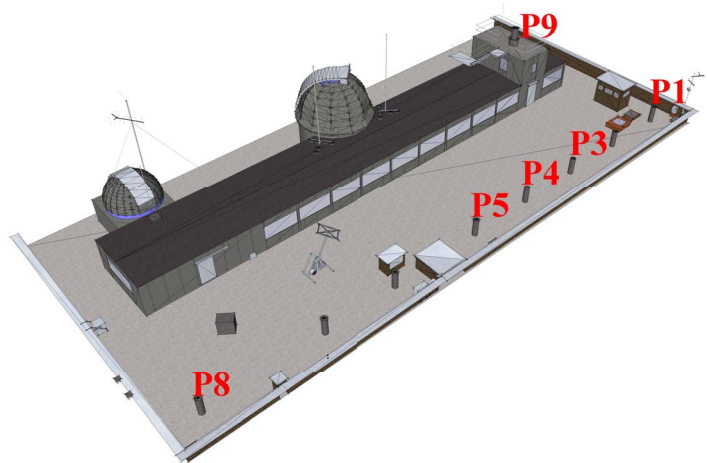
The topic of positional uncertainty is discussed in Section 6.2 with the Geodetic Institute data set. Positional uncertainty will be included in the direct geo-referencing (Section 6.3) to obtain geo-referenced stochastic 3D point clouds. In addition, the optimisation of the relative orientation of two 3D point clouds (Section 6.4) utilises these positional uncertainty.

In Section 6.3.1, the single GNSS antenna scenario is used for the Saxon Steed data set which consists of three MSS sites around the Saxon Steed in front of the main building of the Leibniz Universität Hannover, Germany. Subsequently, results of the dual GNSS antennas scenario are presented for the Geodetic Institute data set in Section 6.3.2. This data set is composed of two MSS sites on the roof of the building of the Geodetic Institute (Messdach), Leibniz Universität Hannover, Germany.

The optimisation of the relative orientation of two 3D point clouds by means of iterative matching with the Gref-ICPHe3 is shown for the Saxon Steed data in Section 6.4. The benefits of the propagation of positional and transformational uncertainties within the iterative matching are pointed out, especially with respect to subsequent 3D point cloud analyses.



(a) Situation Saxon Steed data set.



(b) Situation Geodetic Institute (Messdach) data set.

Figure 6.1: Data sets used in the experimental studies: (a) Saxon Steed in front of the main building of the Leibniz Universität Hannover, Germany with MSS in the foreground. (b) Roof of the building of the Geodetic Institute (Messdach), Leibniz Universität Hannover, Germany (Zaddach, 2010).

Table 6.1.: Data sets with their main characteristics used throughout the experimental studies.

Data set	Saxon Steed (Fig. 6.1(a))	Geodetic Institute (Fig. 6.1(b))
Sites	Three around the Saxon Steed on tripods.	Two on massive pillars.
Object distance	About 16 m.	About 20 m.
MSS	Prototypic realisation introduced in Fig. 4.1 with specifications in Tab. 4.2.	
Scan parameters	Z+F IMAGER 5006 operating with scanning resolution high, low noise (12.5 profiles per second) for horizontal positions from $0^\circ$ to $364^\circ$ ; this leads to about 13 min acquisition time.	
GNSS equipment <sup>1</sup>	One Javad GrAnt G3T antenna in $\mathbf{p}^o$ connected to a Javad TRE G3T Delta receiver.	Two Leica LEIAX1202GG antennas each connected to a Javad TRE G3T Delta receiver.
GNSS acquisition parameters	GPS and GLONASS observations (dual frequency) with 10 Hz data rate; relative baseline to reference station <sup>2</sup> $\approx 625$ m.	GPS and GLONASS observations (dual frequency) with 20 Hz data rate; relative baseline to reference station <sup>2</sup> $\approx 20$ m.
GNSS satellites visibility	At least seven GPS and four GLONASS satellites.	At least seven GPS and seven GLONASS satellites.
GNSS analysis	Relative kinematic positioning (Section 2.2.4.1) with respect to known reference station <sup>2</sup> ; GNSS analysis in post-processing with the Wa1 software (Wanninger, 2009b); $10^\circ$ cut-off angle, broadcast ephemerides, PCC applied.	

## 6.1. Analyses of high resolution 3D trajectories for direct geo-referencing purposes

This section treats the analyses of the high resolution 3D trajectories obtained with the GNSS component of the MSS for the purpose of direct geo-referencing. The focus is on the motion modelling of the MSS which is thoroughly investigated for the single antenna scenario and the dual antennas scenario. Furthermore, the trajectory of a single antenna is analysed with transversal prediction and filtering by means of LSC to gain a better understanding of the stochastic properties of the trajectory. Therefore, methods of time series analysis like covariance functions are used.

### 6.1.1. Modelling of the multi-sensor system's motion in recursive state-space filters

The following section deals with investigations carried out for the two introduced system modelling approaches in Section 5.2.1. The presented results concentrate on the modelled motion since the trajectories are the basis to estimate the transformation parameters (Section 6.3). Both scenarios, which are distinguished by the number of GNSS equipments used, are treated separately.

<sup>1</sup>The reader is referred to Section 4.2.1 for comprehensive information regarding the GNSS equipment.

<sup>2</sup>The reference station is operated by the Institut für Erdmessung and its location is on the roof of the building of the Geodetic Institute (Messdach), both of them are institutes of the Leibniz Universität Hannover, Germany.

### 6.1.1.1. Single GNSS antenna scenario in aEKF approach

For the investigations of the MSS's motion modelling in the aEKF approach (Section 5.2.1.1), the Saxon Steed data set is utilised. The main characteristics regarding the acquisition parameters and especially the GNSS analysis are summarised in Tab. 6.1. To illustrate the point, the results of the obtained trajectory for the site S3 (cf. Fig. 6.1(a)) are analysed. Next to the filter performance depicted in Fig. 6.2, the estimates for the adaptive parameters (Fig. 6.3(b)) are discussed.

The stochastic model of observations is given by the VCM for each 3D position obtained by the relative kinematic positioning and a theoretical value ( $\sigma_{\kappa^L} = 4/1000$  degree) for the horizontal motor steps of the laser scanner. The latter value is taken from the manufacturer specifications Section B.1. The magnitude of the standard deviations of the 3D positions is in a range of 2 – 6 mm for the in-plane (north- and east-) components and in a range of 4 – 11 mm for the up-component. These values are in accordance with the separate investigations of the used GNSS equipment in Section 4.3.2. The VCM of the process noise  $\Sigma_{\mathbf{w}\mathbf{w}}$  is set up by empirical values. These values are derived by analysis of experiments with the MSS and priori knowledge of the motion of the MSS.

As already mentioned in Section 5.2.1.1, the sensor-orientated modelling in this aEKF approach requires as pre-processing step the interpolation of the 10 Hz position data with respect to the line synchronisation pulses of the laser scanner (12.5 Hz). At this developmental stage, this step is realised by a simple linear interpolation.

The state parameter  $\mathbf{p}^{G,\circ}$  is shown in 3D space in Fig. 6.2(a), which clearly visualises the filter effect. The trajectory described by  $\mathbf{p}^{G,\circ}$  is given in the ETRS89 combined with the UTM projection whereas the coordinates are centred by the mean value of observations which is done only for visualisation purposes. Especially, for up-component the filter effect can be clearly seen in Fig. 6.2(b). The north- and east-components are dominated by a sinusoidal oscillation which results from the  $360^\circ$  rotation of the laser scanner. The standard deviations for the three components of this state parameter are in a range of 1 – 2 mm.

The state parameter  $\kappa^L$ , which denotes the local orientation and corresponds to the observables of the horizontal motor of the laser scanner, is depicted in Fig. 6.3(a). The upper part shows the linearly increasing values for a full  $360^\circ$  rotation of the laser scanner. Since the divergence of the linearity can be seen as indicator for the quality of observations and estimates, the lower part shows the residuals of  $\kappa_{Scan}$  and  $\hat{\kappa}^L$  with respect to a linear regression. The residuals are in a range of  $\pm 4/1000$  degree and correspond to the theoretical value. The filtered state  $\hat{\kappa}^L$  is used for the calculation of the final heading (cf. Section 6.3.1).

The estimates of the adaptive parameters  $r_k$ ,  $\theta_k$  and  $s_{ltd,k}$  are shown in Fig. 6.3(b). The process noise for these parameters is set up in accordance with their estimation in the MSS calibration procedure outlined in Section 4.3.4. All three estimated adaptive parameters confirm their a-priori known values. The divergences for the radius  $\hat{r}$  increase slightly over time with a magnitude of  $\pm 0.005$  mm with respect to the known value.

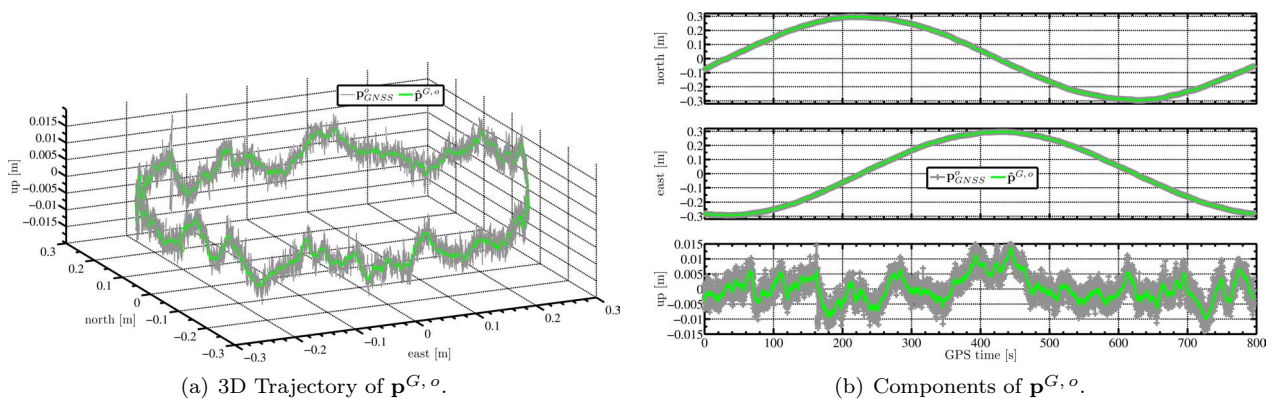


Figure 6.2: Single antenna scenario – Saxon Steed data set: Trajectory in mean centred ETRS89 combined with the UTM projection of the observations  $\mathbf{p}_{GNSS}^{G,\circ}$  (grey) and the filtered state  $\hat{\mathbf{p}}^{G,\circ}$  (green).

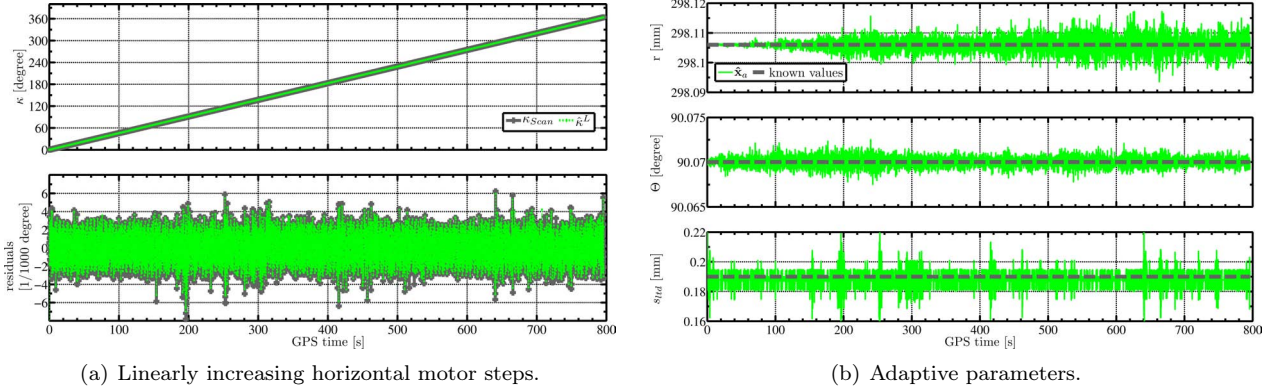


Figure 6.3: Single antenna scenario – Saxon Steed data set: (a) Upper part: Observations of the horizontal motor of the laser scanner  $\kappa_{Scan}$  (grey) and the estimated state  $\hat{\kappa}^L$  (green). Lower part: Residuals of  $\kappa_{Scan}$  and  $\hat{\kappa}^L$  with respect to a linear regression. (b) Known values of  $r$ ,  $\theta$  and  $s_{tld}$  (grey) and their estimates (adaptive parameters)  $\hat{\mathbf{x}}_a = [\hat{r} \ \hat{\theta} \ \hat{s}_{tld}]^T$ .

For the angular offset  $\hat{\theta}$  the divergences have a magnitude of  $\pm 5/1000$  degree. This results in an uncertainty of 3 mm for objects in a distance of 30 m and thus can be neglected. For the circular arc segment  $\hat{s}_{tld}$  occur divergences with a magnitude of  $\pm 0.01$  mm with respect to the known value. The visible systematic behaviour for all adaptive parameters, in particular for  $\hat{r}$  and  $\hat{s}_{tld}$ , is presumed due to neglected dependencies among the parameters. In addition, the systematics for  $\hat{s}_{tld}$  are presumed due to numerical reason if their magnitude of sub-millimetre range is considered.

The findings regarding the adaptive parameters can be summarised as follows: The apparent systematics have to be separately investigated. The known values are confirmed and no significant divergences occur. This information is important in case of attaching/detaching of the wing support structure and the validity of the MSS calibration values.

#### 6.1.1.2. Dual GNSS antennas scenario in EKF with state constraints

For the investigations of the modelled motion of the MSS in the EKF with state constraints (Section 5.2.1.2), the Geodetic Institute data set is used. The main characteristics regarding the acquisition parameters and especially the GNSS analysis are summarised in Tab. 6.1. The results, which are obtained for the measurements on P1 (cf. Fig. 6.1(b)), are taken to illustrate the filter performance in Fig. 6.4. The two different sets of constraints are thoroughly discussed according to Fig. 6.5.

The stochastic model of observations is given by the VCM for each 3D position obtained by the relative kinematic positioning. The magnitude of standard deviations of the 3D positions for both trajectories is in a range of 4 – 6 mm for the in-plane (north- and east-) components and in a range of 8 – 16 mm for the up-component. These values are in a typical order for the used GNSS equipment. Empirical values are assigned to the VCM of the process noise  $\Sigma_{ww}$ . The analysis of experiments with the MSS and priori knowledge of the MSS motion model provide these values.

The state parameters  $\mathbf{p}^{G,d}$  and  $\mathbf{p}^{G,o}$  are shown in 3D space in Fig. 6.4(a) and (c), which clearly visualise the filter effect (green) as well as the impact of the state constraint (magenta) for both trajectories. The trajectories described by  $\mathbf{p}^{G,d}$  and  $\mathbf{p}^{G,o}$  are given in the ETRS89 combined with the UTM projection whereas the coordinates are centred by the mean value of observations which is done only for visualisation purposes. In Fig. 6.4(b) and (d) the single components of the trajectories are depicted. In particular, for the up-component the filter effect and moreover the applied state constraint is clearly visible. The north- and east-components follow the expected sinusoidal oscillation. The standard deviations for the three components of the state parameters  $\mathbf{p}^{G,d}$  and  $\mathbf{p}^{G,o}$  are in a range of 1 – 3 mm.

The state parameter  $v$  varies with a magnitude of  $\pm 0.4 \frac{\text{mm}}{\text{s}}$  around the expected value of  $v = 0.0024 \frac{\text{m}}{\text{s}}$  which

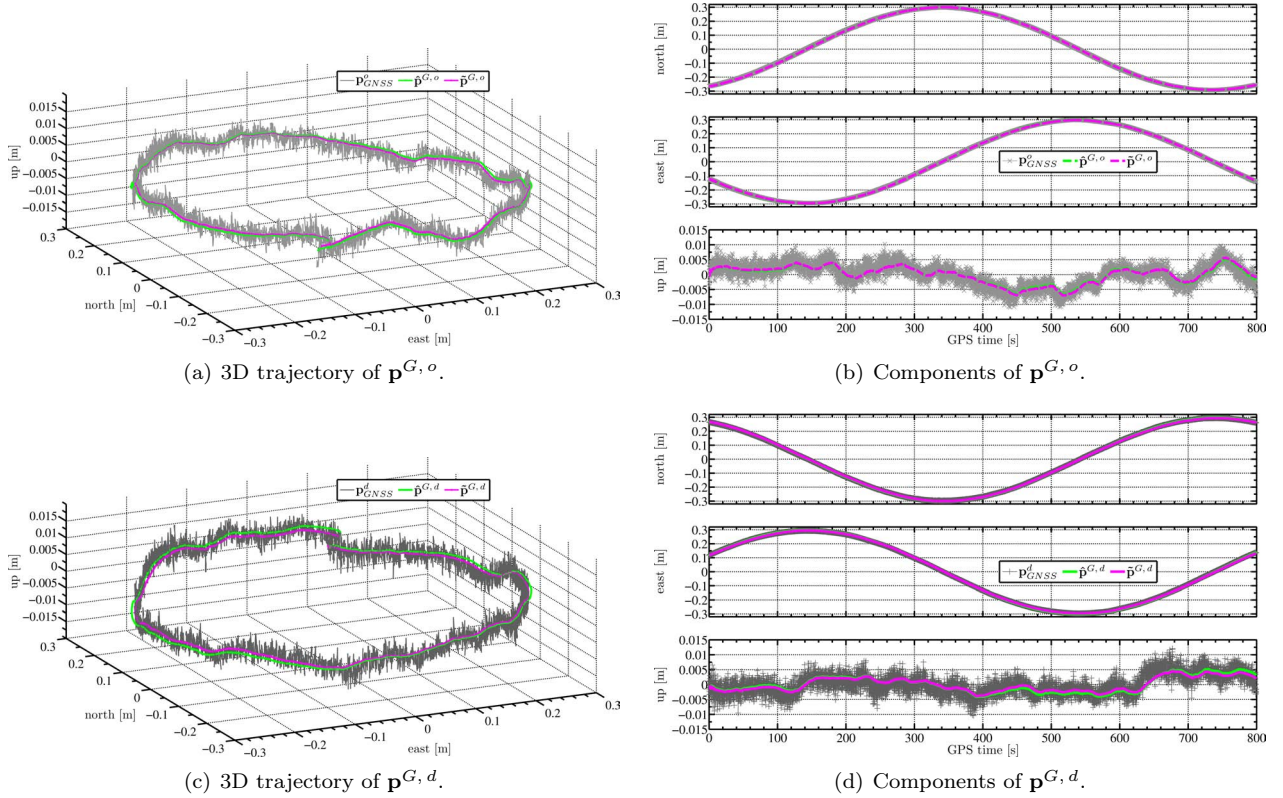


Figure 6.4: Dual antennas scenario – Geodetic Institute data set: Trajectory in mean centred ETRS89 combined with the UTM projection of the observations  $\mathbf{p}_{GNSS}^{d/o}$  (grey), the filtered state  $\hat{\mathbf{p}}^{G,d/o}$  (green) and the constrained filtered state  $\tilde{\mathbf{p}}_{GNSS}^{G,d/o}$  (magenta).

was also obtained in the investigation of the MSS's components (Section 4.3.3).

It is worth to note that also smoothed trajectories by means of the Rauch-Tung-Striebel smoother (Section 3.2.3) are obtained. This is done to determine optimal estimates for the first epoch since these estimates are used to calculate the final heading parameter. The smoothing effect on the heading calculation (Eq. 5.15) is seized upon in Section 6.3.2.

Fig. 6.5 illustrates the impact of the state constraints on the trajectory. To show the impact more clearly, the following scenario is simulated: The observations  $\mathbf{p}_{GNSS}^d$  are modified in a way that the sampling rate is reduced from 10 Hz to 1 Hz. In addition, the first 25 s of observations are deleted, i. e., the observations of  $\mathbf{p}^{G,d}$  are available with a delay of 25 s with respect to the observations of  $\mathbf{p}^{G,o}$ . Also, only an approximate start value for  $\mathbf{p}^{G,d}$  is given which differs in a range of decimetres from the true observations. The observations  $\mathbf{p}_{GNSS}^o$  are not modified and used with the original data rate of 10 Hz.

In Fig. 6.5(a) are visualised the results for the constraint given in Eq. 5.11. This constraint utilises only the distance  $d^{do}$  independent from the current orientation of  $\mathbf{p}^{G,o}$  and  $\mathbf{p}^{G,d}$ . As can be seen, the constrained trajectory (magenta) is correct in terms of the behaviour but it starts with an offset compared to the expected sinusoidal oscillation. The offset is obvious in the north- and east-components and results in a jump to the expected sinusoidal oscillation with the first available observation of  $\mathbf{p}^{G,d}$  after 25 s. The reason is seen in the manner of constraint which considers only the distance but not the direction of the distance. The filtered trajectory (green) for  $\mathbf{p}^{G,d}$  is non-satisfying in case of missing observations and depends strongly on the approximate start values.

The results of the constraint given Eq. 5.12 are depicted in Fig. 6.5(b). The constraint is characterised by the addition of the current heading (of  $\mathbf{p}^{G,o}$  with respect to  $\mathbf{p}^{G,d}$ ) to the distance  $d^{do}$ . In contrast to the previous discussed results, the constrained trajectory corresponds here to the expected sinusoidal oscillation. This is

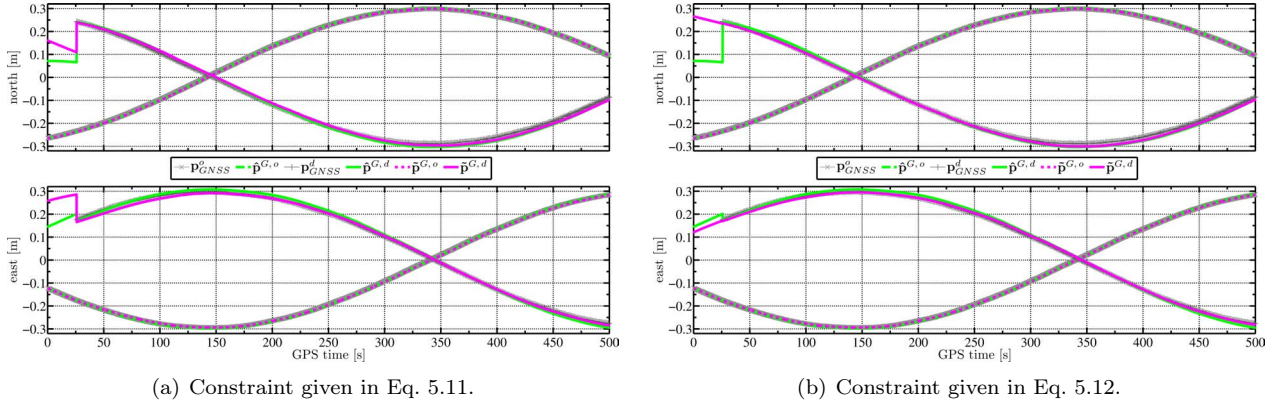


Figure 6.5: Dual antennas scenario – Geodetic Institute data set: Demonstration of the impact of state constraints. Constraint based on (a) the distance  $d^{do}$  and on (b) the distance  $d^{do}$  supplemented with the current heading.

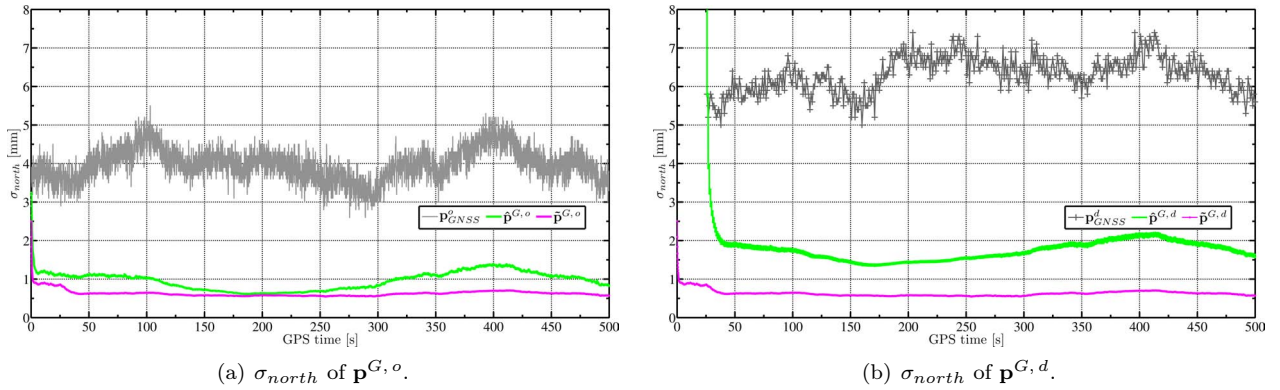


Figure 6.6: Dual antennas scenario – Geodetic Institute data set: Standard deviations of observations ( $\hat{\mathbf{p}}_{GNSS}^{d/o}$ , grey), filtered ( $\hat{\mathbf{p}}^{G,d/o}$ , green) and constrained ( $\tilde{\mathbf{p}}_{GNSS}^{G,d/o}$ , magenta) estimates for the north-component. The constraint given in Eq. 5.12 is applied.

obvious since no jump occurs after the first available observations of  $\mathbf{p}^{G,d}$ . The reason is the consideration of the orientation of  $d^{do}$  and not only the consideration of the fixed distance between  $\mathbf{p}^{G,o}$  and  $\mathbf{p}^{G,d}$ , like in Fig. 6.5(a). The effect of the constraint is also noticeable in the standard deviations. This is exemplarily shown for the north-component in Fig. 6.6. In Fig. 6.6(a) the values for  $\sigma_{north}$  are depicted for  $\mathbf{p}^{G,o}$  which clearly show a reduced noise level. Furthermore, a decrease of the systematic oscillation owing to the constraint can be noted. In Fig. 6.6(b) the standard deviations in case of data gaps for  $\mathbf{p}^{G,d}$  are drawn.  $\sigma_{north}$  of the filtered trajectory  $\hat{\mathbf{p}}^{G,d}$  (green) has magnitudes of 60 mm in case of data gaps. Whereas,  $\sigma_{north}$  of the constrained trajectory  $\tilde{\mathbf{p}}^{G,d}$  (magenta) provide sufficient results in comparison to  $\sigma_{north}$  of  $\hat{\mathbf{p}}^{G,d}$  even for the period of data gaps. When observations are available the findings are the same as for the trajectory of  $\mathbf{p}^{G,o}$ .

It can be summarised that the application of state constraints makes sense to improve and strengthen the results of the EKF. Especially, if observations of one GNSS antenna are not available. Furthermore, the constrained trajectories have a smaller noise level compared to the filtered trajectory. Finally, this results in smaller standard deviations for the constrained estimates.

### 6.1.2. Transversal prediction and filtering by means of least-squares collocation

The fundamentals of prediction and filtering by means of LSC are introduced in Section 3.3. This section is dedicated to analyses of the high resolution 3D GNSS trajectories of  $\mathbf{p}^{G,d/o}$  with prediction and filtering by means of LSC to gain a better understanding of the stochastic properties of the used GNSS time series. The explanations summaries the major findings of Harmening et al. (2012). The main topics outlined are: the



required covariance functions to solve the LSC and the solution of LSC by means of GHM. In the subsequent analyses, the Geodetic Institute data set (characteristics are summarised in Tab. 6.1) is used. In particular, the results are shown for the trajectory of  $\mathbf{p}^{G,d}$  which covers in total five subsequent  $360^\circ$  rotations of the MSS, acquired on P5. The three coordinate components of  $\mathbf{p}^{G,d}$  are termed north-, east- and up-time series in the following.

Appropriate covariance functions are determined according to Section 3.3.1: First, empirical auto- and cross-covariance functions are computed by means of Eq. 3.47. Second, empirical auto- and cross-correlation functions (Eq. 3.48 and 3.49) are obtained by normalisation of the estimated empirical auto- and cross-covariance functions. Fig. 6.7(a) depicts the autocorrelation functions for the north-, east- and up-time series. In Fig. 6.7(b) the cross-correlation functions are shown. No obvious systematic behaviour can be detected and their values are in the small range of about  $-0.1$  to  $0.2$ . Thus, it is assumed that the cross-correlations can be neglected in the stochastic model.

The autocorrelation functions of all three coordinate components (Fig. 6.7(a)) show a similar behaviour: They are characterised by a jump between the first and the second time step. Afterwards, the autocorrelation functions of the east- (red) and up-time series (green) descend distinctly slower to the function value  $\widehat{K}(\Delta t) = 0$ . The autocorrelation function of the north-time series (blue) shows a slightly different behaviour and descends to  $\widehat{K}(\Delta t) = -0.3$  for  $\Delta t = 230$ s. For all three functions can be seen small variations around  $\widehat{K}(\Delta t) = 0$  for  $\Delta t > 250$ s. Based on these findings and the major period of interest for  $\Delta t < 100$ s, an exponential function is supposed to be the analytical autocorrelation function.

The analytical autocorrelation functions are estimated by means of regressions analysis (Harmening et al., 2012). It is noteworthy that for the estimation of these functions the used time series have to fulfil the conditions of stationarity and ergodicity (Section 3.3.1). A problem to face while estimating the analytical functions is the jump from the first to the second time step. The autocorrelation function has to take the value  $\widehat{K}(\Delta t) = 1$  (time series divided by empirical variance for  $\Delta t = 0$ , cf. Eq. 3.48). This constraint provides a good approximation of the estimated correlation function based on the empirical values. Unfortunately, the piecewise estimation of more than one theoretical correlation function yields non-positive definite covariance matrices because of the violation of the isotropy condition (Sansò and Schuh, 1987).

Fig. 6.7(c) exemplarily shows the empirical and analytical correlation function for the east-time series of  $\mathbf{p}^{G,d}$ . As aforementioned, the analytical correlation function has been chosen from the family of exponential functions.

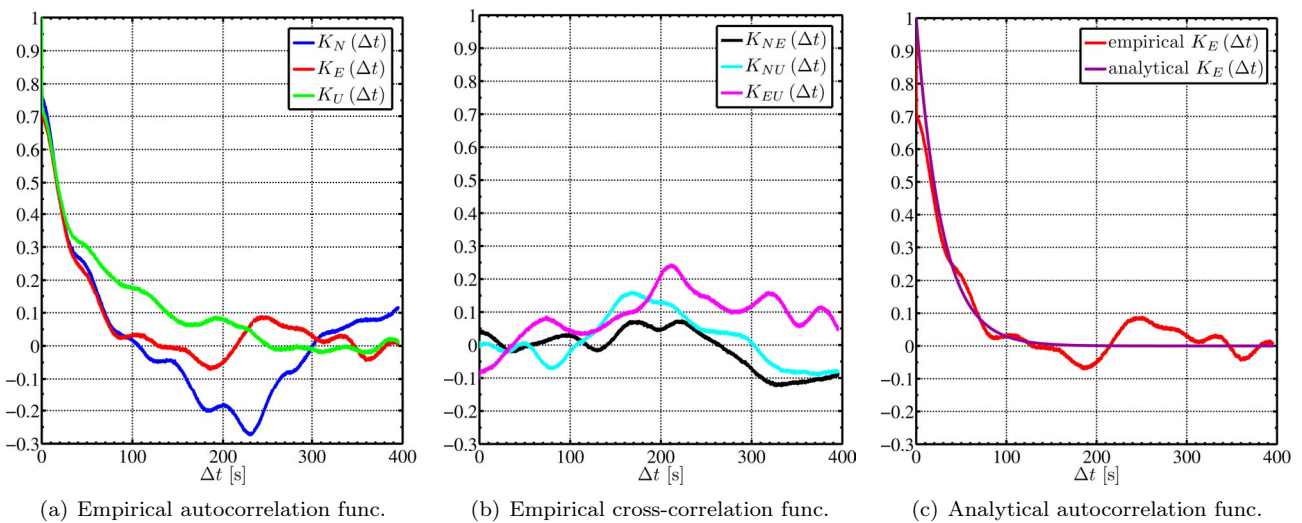


Figure 6.7: Determination of covariance functions exemplary for the trajectory of  $\mathbf{p}^{G,d}$  acquired on P5 (Geodetic Institute data set): (a) Empirical autocorrelation functions for the north- (blue), east- (red) and up-time series (green). (b) Empirical cross-correlation functions for north-east- (black), north-up- (cyan) and east-up-time series (magenta). (c) Empirical (red) and analytical (purple) autocorrelation function of the east-times series.

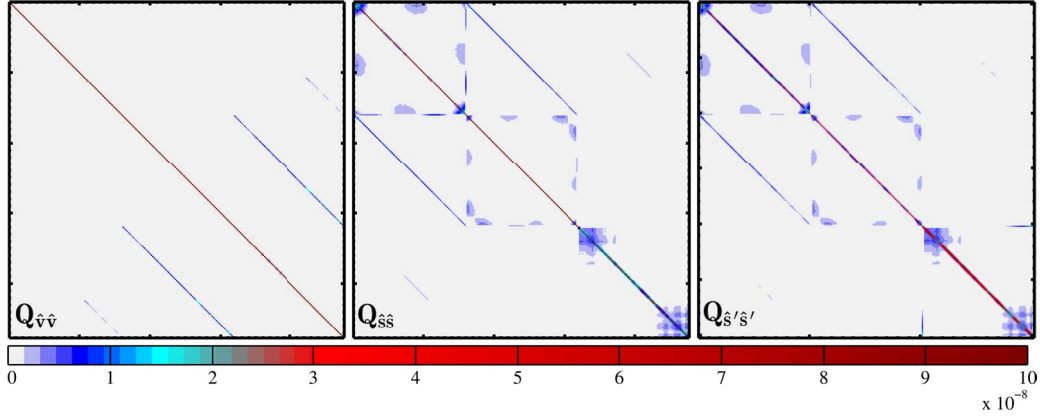


Figure 6.8: Cofactor matrices of the estimated residuals  $\mathbf{Q}_{\hat{\mathbf{v}}\hat{\mathbf{v}}}$ , the estimated signal  $\mathbf{Q}_{\hat{\mathbf{s}}\hat{\mathbf{s}}}$  and the estimated predicted signal  $\mathbf{Q}_{\hat{\mathbf{s}}'\hat{\mathbf{s}}'}$ . The estimated predicted signal's  $\mathbf{Q}_{\hat{\mathbf{s}}'\hat{\mathbf{s}}'}$  corresponds to the predicted 3D positions, which are illustrated in Fig. 6.9. The quantities in the VCMs are given first for the north-component of all 3D positions followed up by the east- and up-components.

It is noteworthy that the results confirm the determination and investigations of covariance functions carried out by Harmening (2011) for the same MSS but different data sets.

The solution of LSC by means of GHM is theoretically introduced in Section 3.3.2. The matrix of known coefficients  $\mathbf{R}$  (Eq. 3.45) is equal to the identity matrix  $\mathbf{I}$ , which express the functional relationship between observations and signal. The circular motion is modelled as non-linear trend, which requires a linearisation of the functional relationship (Harmening et al., 2012). The parameter estimation, the filtering of the signal and the prediction are performed according to Eq. 3.52. The predicted 3D positions ( $\mathbf{p}_{LSC}^{G,d}$ ) with respect to the specific 2D profiles (defined by the line synchronisation pulses) out of the trajectory of  $\mathbf{p}^{G,d}$  are illustrated in Fig. 6.9. Their common discussion with the obtained trajectory by means of the EKF can be found in the subsequent concluding remarks.

The required VCM  $\mathbf{\Sigma}_{\mathbf{s}'\mathbf{s}}$  is obtained by means of analytical correlation functions (Fig. 6.7(c)). The VCMs of the estimated quantities (Fig. 6.8) are obtained by means of Eq. 3.54 – 3.56. Owing to the large scale of the VCMs (in some cases up to  $25000 \times 25000$  elements) the computation of the LSC becomes computationally expensive<sup>3</sup>. From Fig. 6.8 can be seen that the VCMs have a strong block diagonal structure with low correlations ( $< 0.2$ , see also Fig. 6.7(b)) for the north- and east-components in  $\mathbf{Q}_{\hat{\mathbf{s}}\hat{\mathbf{s}}}$  and  $\mathbf{Q}_{\hat{\mathbf{s}}'\hat{\mathbf{s}}'}$ . For  $\mathbf{Q}_{\hat{\mathbf{v}}\hat{\mathbf{v}}}$  a low correlation ( $< 0.15$ ) is present for the east- and up-components.

### 6.1.3. Concluding remarks

Both variants of modelling the MSS's motion in EKF approaches show the expected results which are a reduced noise level of the trajectories of  $\mathbf{p}^{G,d/o}$  compared to the original observations. The aEKF approach is also capable to deliver estimates for the MSS specific quantities  $r$ ,  $\theta$  and  $s_{ltd}$  which are known from the MSS calibration. This allows a statement regarding the calibration values for the current measurements. This can be important if the wing support structure was detached from the laser scanner. One drawback of this approach is the necessity of the observation's pre-processing in terms of the adaption of the data acquisition rates. The dual antennas motion modelling by states with constraints shows the benefit of considering known functional relations among the state parameters. Especially, in case of missing observations for one antenna. Also, the acquisition rate of both antennas must not be identical and no pre-processing of observations like in the aforementioned approach is required. To summarise the findings related to the EKF approaches, it can be noted that the performance is comparable for both approaches. Their particular use depends on the available number of GNSS equipments.

<sup>3</sup>The LSC results presented here were partially carried out on the Regionales Rechenzentrum für Niedersachsen (RRZN) cluster system at the Leibniz Universität Hannover, Germany.

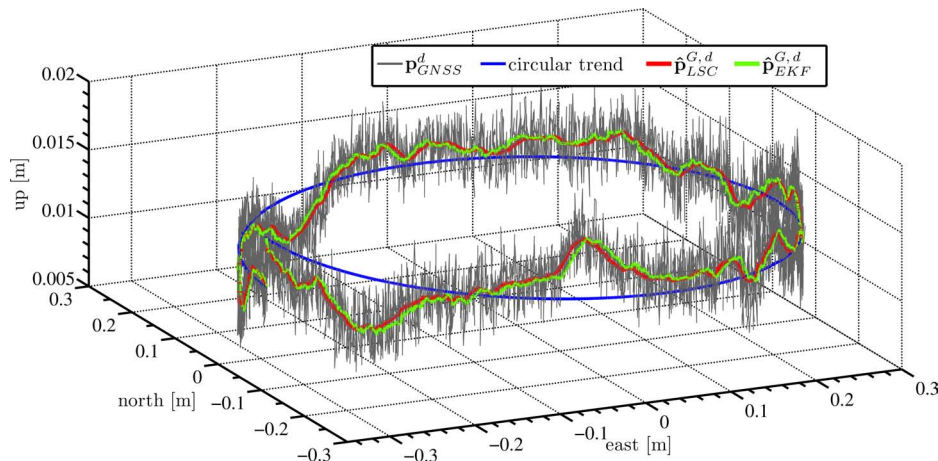


Figure 6.9: Filtering and prediction of the 3D trajectory of  $\mathbf{p}^{G,d}$  (grey) by means of LSC ( $\hat{\mathbf{p}}_{LSC}^{G,d}$ , red) and EKF ( $\hat{\mathbf{p}}_{EKF}^{G,d}$ , dual antennas scenario without constraints, green).

In Fig. 6.9, the comparison is illustrated for the filtering and prediction of  $\mathbf{p}^{G,d}$  by means of the LSC approach and the EKF approach (dual antennas scenario without constraints). The trajectories are centred by the mean value of observations which is done only for visualisation purposes. The observations  $\mathbf{p}^{G,d}$  are depicted in grey and the estimated circular trend in the LSC approach is demonstrated in blue. The estimates  $\hat{\mathbf{p}}_{LSC}^{G,d}$  of the LSC are shown in red and the filtered estimates  $\hat{\mathbf{p}}_{EKF}^{G,d}$  of the EKF are drawn in green. It can be seen that the filter effect is fulfilled in both approaches and that the results are comparable. Thus, no significant influence in the calculation procedure of the transformation parameters is expected by the two trajectories. The LSC trajectory differs from the trend by the predicted signal. In comparison to  $\mathbf{p}^{G,d}$  the predicted one  $\hat{\mathbf{p}}_{LSC}^{G,d}$  is much smoother, which means, that the influence of the measurement noise has been reduced by the filtering. Irregular-systematic oscillations can be seen in the whole observed trajectory  $\mathbf{p}^{G,d}$ . They still remain in the estimates  $\hat{\mathbf{p}}_{LSC}^{G,d}$  and  $\hat{\mathbf{p}}_{EKF}^{G,d}$ . For their explanation further investigations are required. The following advantages can be noted for the EKF approach: It requires less computational effort and it is capable for real-time applications due to the recursive estimation approach.

## 6.2. Positional uncertainty

This section deals with the topic of positional uncertainty (Section 2.3.3), in particular with the calculation scheme summarised in Alg. 2.2 to obtain the positional uncertainty of a 3D point cloud. The similar calculation scheme is used by Paffenholz and Bae (2012). The authors show a benchmarking of the calculation scheme for the free-available and widely used data set of the Agia Sanmarina Church<sup>4</sup>. Thereby, the obtained results are in agreement with the published results by Bae (2009), who proposed the used method for positional uncertainty calculation.

The positional uncertainty is considered during the geo-referencing in Section 6.3 to obtain the stochastic 3D point clouds and in the optimisation of relative transformation parameters by means of Gref-ICPHe3 in Section 6.4. In the subsequent sections only the final results will be shown. Therefore, the results for calculated positional uncertainty measures by means of Alg. 2.2 are exemplarily shown for a subset of the Geodetic Institute data set in the following. Thus, this section treats the laser scanner component of the MSS for purposes of direct geo-referencing. Since, a laser scanner calibration is out of the thesis's scope, manufacturer values are assumed for radial and angular standard deviations. For the used Z+F IMAGER 5006, the following values are taken from the specifications (Section B.1): radial standard deviation  $\sigma_r = 0.0005 \text{ m} + 20 \text{ ppm}$  and angular (horizontal

<sup>4</sup>The data set of the Agia Sanmarina church, Greece, is currently available through ISPRS Working Group V/3 Terrestrial Laser Scanning, [www.commission5.isprs.org/wg3](http://www.commission5.isprs.org/wg3)

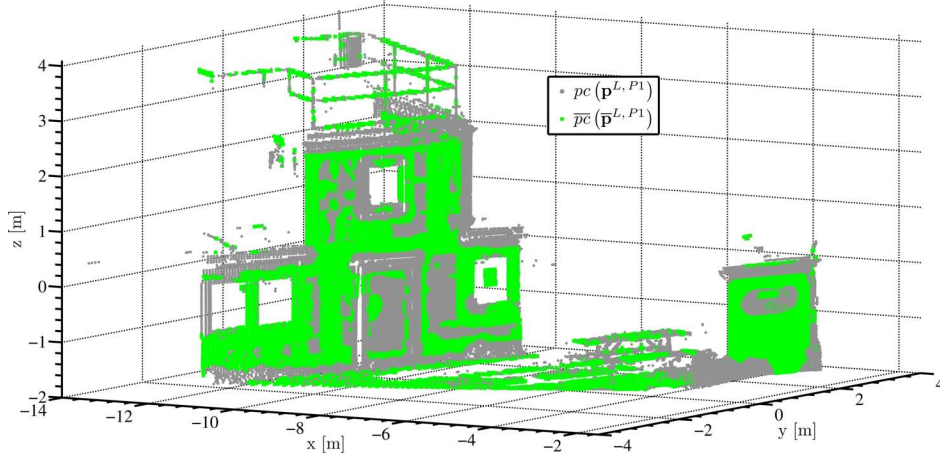
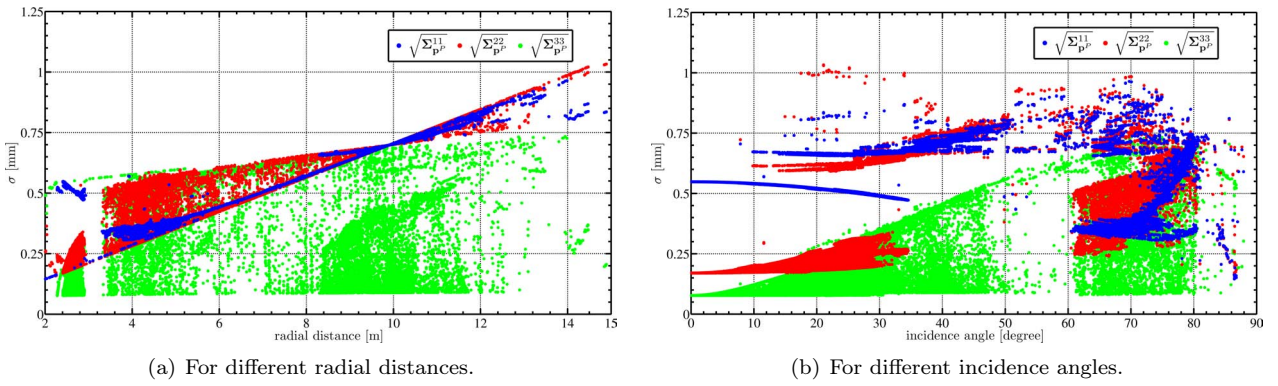


Figure 6.10: Positional uncertainty – Geodetic Institute data set: Separation of the 3D point cloud  $pc(\mathbf{p}^{L, P1})$  (grey) acquired from  $P1$  into planar regions  $\overline{pc}(\overline{\mathbf{p}}^{L, P1})$  (green).



(a) For different radial distances.

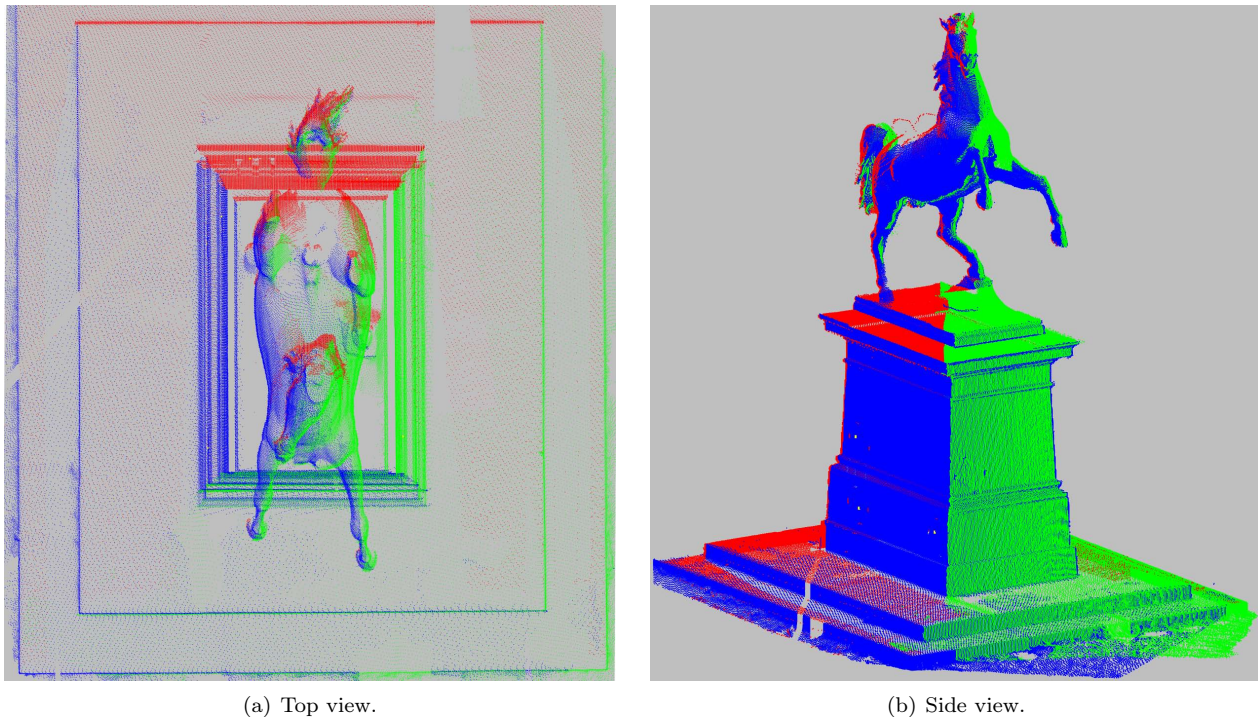
(b) For different incidence angles.

Figure 6.11: Positional uncertainty – Geodetic Institute data set: Positional uncertainty in the  $P$ -frame (Eq. 2.15) for 3D point cloud acquired from  $P1$  with radial distances up to 15 m and with incidence angles from  $0^\circ$  to  $90^\circ$ . The colour code for the component-wise standard deviation in the  $P$ -frame is:  $\sqrt{\Sigma_{\mathbf{p}^P}^{11}}$  blue,  $\sqrt{\Sigma_{\mathbf{p}^P}^{22}}$  red and  $\sqrt{\Sigma_{\mathbf{p}^P}^{33}}$  green.

and vertical) standard deviation  $\sigma_a = 0.007^\circ$ . Nevertheless, these quantities can be easily substituted by results of a separate laser scanner calibration (cf. Section A.3).

The area under investigation of the Geodetic Institute data set is illustrated in Fig. 6.10. It corresponds to the right hand area in Fig. 6.1(b) with the small tower building with  $P9$  on top. This area is characterised by the full spectrum of incidence angles from  $0^\circ$  to  $90^\circ$  and a maximum radial distance of 15 m. Fig. 6.10 depicts the 3D point cloud  $pc(\mathbf{p}^{L, P1})$  (grey) as well as the planar regions  $\overline{pc}(\overline{\mathbf{p}}^{L, P1})$  (green) in the  $L$ -frame. To separate the 3D point cloud in planar and non-planar regions the geometric curvature (as a parameter of the 3D point cloud) is compared to an empirically defined threshold (Section 2.3.3). This separation is a necessity to use the approximation of the positional uncertainty in Eq. 2.15. It is noteworthy that this approximation neglects the effect of the variance of the estimated surface normal vector, for further details the reader is referred to Section 2.3.3.

The diagonal elements of the calculated positional uncertainty ( $\sqrt{\text{diag}(\Sigma_{\mathbf{p}^P})}$  in the  $P$ -frame) are graphically summarised in Fig. 6.11. Despite the limited radial distance of 15 m, the range dependency of the positional uncertainty is clearly visible in Fig. 6.11(a). Especially, for the  $x$ - and  $y$ -direction the linearly increasing positional uncertainty ( $\sqrt{\Sigma_{\mathbf{p}^P}^{11}}$  and  $\sqrt{\Sigma_{\mathbf{p}^P}^{22}}$ ) dominates. The dominant pattern in  $\sqrt{\Sigma_{\mathbf{p}^P}^{33}}$ , which is also visible for  $\sqrt{\Sigma_{\mathbf{p}^P}^{22}}$ , is induced by the variation of the tangential vectors on the local surface of each point (cf. Eq. 2.15). Whereas,  $\sqrt{\Sigma_{\mathbf{p}^P}^{11}}$  is influenced by the variation of the surface normal vector. Fig. 6.11(b) depicts the positional



(a) Top view.

(b) Side view.

Figure 6.12: Single antenna scenario – Saxon Steed data set: For the data acquisition three MSS sites around the sculpture of the Saxon Steed were used. The colour code for the geo-referenced 3D point clouds is: S1 red, S2 green and S3 blue.

uncertainty for the different incidence angles of the 3D point cloud's area. Values smaller than 0.25 mm for incidence angles in a range from  $0^\circ$  to  $10^\circ$  for the  $y$ - and  $z$ -components can be identified. To summarise the findings, the positional uncertainty of the investigated area of the Geodetic Institute data set shows the assumed behaviour with standard deviations in a range of 0.25 – 1.0 mm for radial distances up to 15 m.

### 6.3. Direct geo-referencing by means of the novel algorithm

The novel algorithm (Section 5.2.3) is based on the motion modelling of the MSS to obtain the required translation vector (Eq. 5.16) and heading (Eq. 5.15). This section illustrates the results for the direct geo-referencing of 3D point clouds acquired by the MSS, i. e., stationary laser scanner equipped with 3D positioning sensors such as GNSS equipment. First, the results obtained by the single GNSS antenna scenario are discussed according to the Saxon Steed data set. Second, the Geodetic Institute data set is discussed whereas the results are determined by the dual GNSS antennas scenario. The focus is on the direct geo-referencing and the 3D point clouds. The 3D trajectories as input quantities to estimate the transformation parameters are separately discussed in Section 6.1.

#### 6.3.1. Saxon Steed data set – single GNSS antenna scenario

The Saxon Steed data set is introduced in Tab. 6.1 with its main characteristics. Fig. 6.1(a) gives an overview of the location in front of the main building of the Leibniz Universität Hannover, Germany. Three MSS sites (S1, S2 and S3) were used for the data acquisition. In addition, several artificial targets (control points) were placed in the scanning scene. The coordinates of these control points were obtained by independent total station (Leica TS30) measurements. The connection to the ETRS89 combined with the UTM projection was available through local tie points which were determined by independent GNSS measurements.

The translation vectors of S1, S2 and S3 are estimated each as the centre point of the circular trajectory of  $\hat{\mathbf{p}}^{G,o}$  (Eq. 3.1). The headings of S1, S2 and S3 are calculated according to Eq. 5.15. For details regarding both

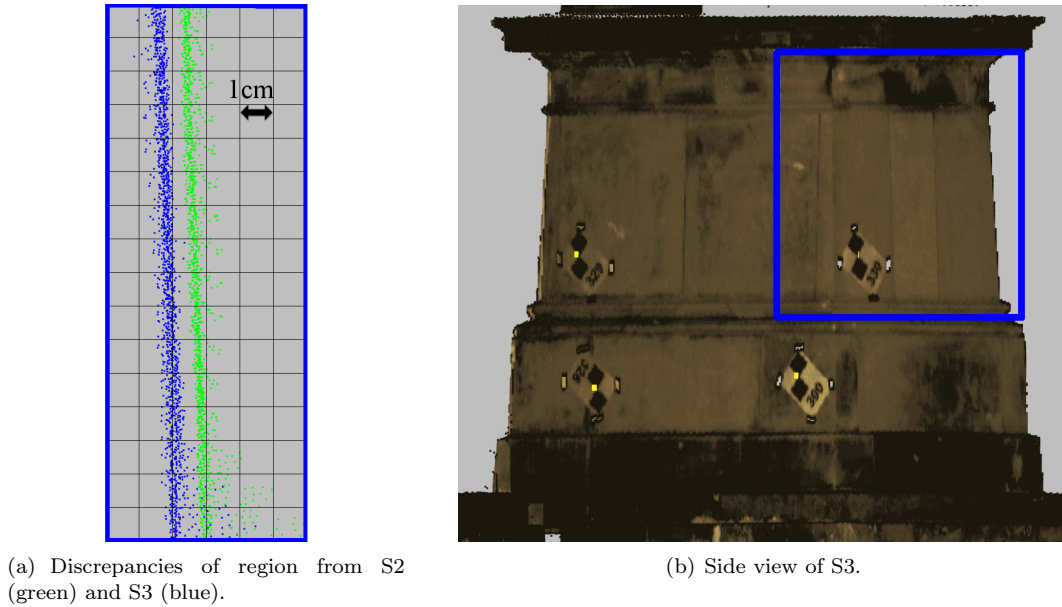


Figure 6.13: Single antenna scenario – Saxon Steed data set: (a) Discrepancies of a planar region of the sculpture’s foundation. (b) Side view of the 3D point cloud of S3 with indicated control points (yellow). In addition, the planar region under investigation in (a) is indicated (blue rectangle).

calculations, the reader is referred to Section 5.2.3. The desired heading is obtained by the reduction of the output of Eq. 5.15 by means of the estimated state parameter  $\hat{\kappa}_L$  (Fig. 6.3(a)) (this procedure is comparable to the determination of the orientation unknown of angle measurements by total stations). Thus, the transformation parameters and their corresponding variances are available. The standard deviations for the translation vectors of the three sites are in a range of 1–3 mm for all three coordinate components. The heading’s standard deviation is  $\sigma_{\kappa}^{S1} = 0.22^\circ$  for S1,  $\sigma_{\kappa}^{S2} = 0.21^\circ$  for S2 and  $\sigma_{\kappa}^{S3} = 0.31^\circ$  for S3. The geo-referencing of the 3D point clouds is performed according to Alg. 5.1.

The geo-referencing results of the three MSS sites are visualised in Fig. 6.12. Each MSS site is drawn in a different colour to visualize the good agreement of the geo-referenced 3D point clouds, whereas numerical values will be discussed below. The colour code for the geo-referenced 3D point cloud is: S1 red, S2 green and S3 blue. The top view (in orthographic projection) in Fig. 6.12(a) indicates the good coincidence of the 3D point clouds for the connection points of the horizontal and vertical lines. These lines correspond to the base and the foundation of the sculpture. The same conclusion can be drawn from the side view of the Saxon Steed in Fig. 6.12(b). In particular, the coincidences of the foundation (lower part) and the sculpture (upper part) of the Saxon Steed are visible.

The stochastic information of the 3D point clouds are calculated by means of Eq. 5.17 which results in stochastic 3D point clouds. These 3D point clouds provide information about the positional and the transformational uncertainties. The main part of the Saxon Steed is in a distance of about 16 m and the mean coordinate uncertainties (Eq. 5.18) are in a range of 3–5 cm for S1 and S2 as well as 5–8 cm for S3 (cf. Fig. 6.19). The main contribution of these uncertainties is induced by the aforementioned standard deviations of the heading.

Although, there exist minor discrepancies for the geo-referenced 3D point cloud from two sites. These discrepancies are demonstrated for a planar region of the foundation of the sculpture (blue rectangle in Fig. 6.13(b)) which was captured from S2 and S3. The maximal discrepancy of the same part of the sculpture’s foundation has a magnitude of 1 cm which is visualised in Fig. 6.13(a) (side view). To improve the geo-referencing result, i. e., to minimise the aforementioned discrepancies, the application of matching algorithms is meaningful. This will be illustrated by the use of the Gref-ICPHe3 in Section 6.4.

Table 6.2.: Single antenna scenario – Saxon Steed data set: Control point differences.

Site	Point no <sup>5</sup>	$\rho$ [m]	$\Delta x$ [m]	$\Delta y$ [m]	$\Delta z$ [m]	$\Delta s$ [m]
S1	<b>325</b>	14.3	-0.009	-0.001	-0.015	0.017
	<b>335</b>	14.1	0.002	-0.006	-0.011	0.013
	218	9.8	-0.001	0.003	-0.022	0.022
	312	28.7	0.003	0.015	-0.011	0.019
	327	29.0	-0.014	0.017	0.010	0.024
S2	<b>328</b>	15.2	-0.027	-0.018	0.006	0.033
	<b>348</b>	16.2	-0.032	-0.019	0.004	0.037
	<b>318</b>	16.3	-0.032	-0.020	-0.001	0.038
	<b><i>330</i></b>	16.2	<i>-0.022</i>	<i>-0.023</i>	<i>-0.002</i>	<i>0.032</i>
S3	<b><i>330</i></b>	15.8	<i>-0.004</i>	<i>-0.013</i>	<i>-0.011</i>	<i>0.018</i>
	<b>300</b>	15.6	0.002	-0.016	-0.006	0.017
	<b>326</b>	17.0	0.002	-0.022	-0.014	0.026
	<b>329</b>	17.3	0.003	-0.015	-0.008	0.017
	128	8.9	-0.015	-0.002	-0.019	0.024
	107	8.8	-0.012	-0.006	-0.017	0.022
	103	9.0	-0.009	-0.021	-0.002	0.023

For the further assessment of the reached accuracy of the geo-referencing, the control points on the Saxon Steed (Fig. 6.13(b)) and the control points in the surrounding area were compared with the coordinates determined by the total station measurements. Tab. 6.2 summarises the numerical values of the coordinate differences and their resulting spatial difference  $\Delta s$  for the control points. It can be seen that the discrepancies of the control point coordinates are in a range of 1 – 3 cm. The distances  $\rho$  of the sites to the sculpture were about 16 m whereas the control points in the surrounding area were in distances up to 29 m.

The artificial target 330 was available in the 3D point cloud acquired from S2 and S3. It is located left in the planar region (blue rectangle) depicted in Fig. 6.13(b). The coordinate differences of the target 330 are smaller for S3 than for S2 (cf. Tab. 6.2). Thus, a better correspondence of data of S3 with respect to the reference values of the control points is assumed. The same behaviour can be seen for the other control points of S2 and S3 on the sculpture. For all control points of S2 the spatial difference is about 1 cm larger than for S3. The reason is presumed to be in the heading of both sites. The aforementioned standard deviations of both headings will result in metric uncertainties of maximal 5 – 6 cm in the given control point distances which is also in the range of the spatial differences to the control points. Nevertheless, the reached coincidence among the 3D point clouds of S2 and S3 is acceptable if one considers the uncertainty of each geo-referenced 3D point cloud (cf. Fig. 6.19). It is noteworthy that in addition to the GNSS equipment a 360° prism (Leica GRZ4) was mounted on the wing support structure in  $\mathbf{p}^d$ . The prism was tracked by a total station (Leica TS30). Investigations and comparisons of both tracking approaches are discussed in Paffenholz et al. (2010b). The authors show differences of several centimetres for the control points on the Saxon Steed for both tracking approaches. The comparison to the reference measurements with the total station were stated with even larger differences in the decimetre range. The re-processing of the entire data of the experiment and the estimation of the transformation parameters according to Section 5.2.3 remedied these discrepancies which were found in the calculated heading (as assumed by Paffenholz et al. (2010b)).

It can be summarised that the above presented results achieved for the Saxon Steed data set with its three

<sup>5</sup>Bold numbers represent targets on the sculpture and bold italic numbers are available in more than one point cloud.

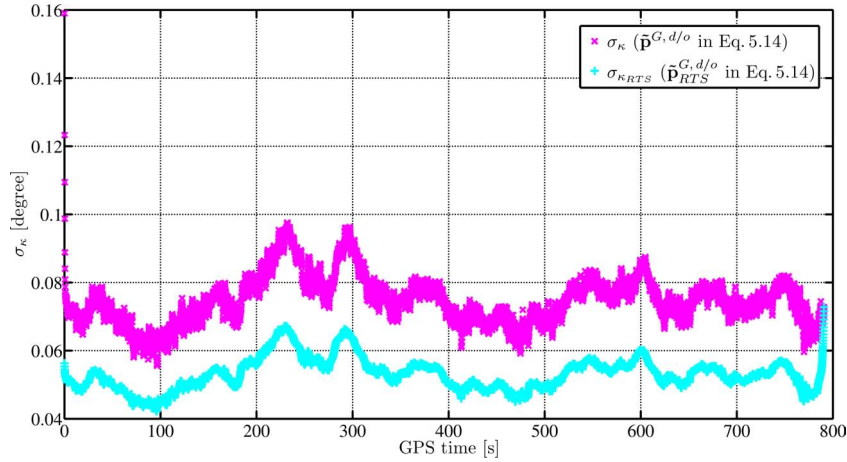


Figure 6.14: Dual antennas scenario – Geodetic Institute data set: Standard deviation of the heading  $\sigma_{\kappa}^{P5}$  obtained by the constrained positions  $\tilde{\mathbf{p}}^{G, d/o}$  (magenta) and the smoothed, constrained positions  $\tilde{\mathbf{p}}_{RTS}^{G, d/o}$  (cyan).

MSS sites are satisfying and meet the accuracy assessment of the MSS (Section 4.3.5). In particular, a good coincidence among the three MSS sites as well as discrepancies smaller than 5 cm with respect to control points can be noted. As expected, the main contribution to the uncertainty of the stochastic 3D point clouds is induced by the standard deviation of the heading. Nonetheless, the geo-referencing result is suitable for the desired fields of application for the developed methodology, like the as-built documentation.

### 6.3.2. Geodetic Institute data set – dual GNSS antennas scenario

The Geodetic Institute data set is introduced in Tab. 6.1 with its main characteristics. Fig. 6.1(b) gives an overview of the situation on the roof of the building of the Geodetic Institute (Messdach), Hannover, Germany. On this roof a geodetic network with nine pillars<sup>6</sup> is located. Two MSS sites (P1 and P5) were used for the data acquisition. Thus, for the evaluation of the geo-referencing results the known coordinates of these two pillars as well as further pillars (P3, P4 and P9) can be used. For ease of interpretation, the coordinate comparisons are carried out in the local topo-centric NEU coordinate system with origin in the nearby reference station (P8).

The translation vectors of P1 and P5 are estimated by means of the corresponding smoothed, constrained trajectories of  $\tilde{\mathbf{p}}_{RTS}^{G, o}$  and  $\tilde{\mathbf{p}}_{RTS}^{G, d}$  according to Eq. 5.16. The headings of P1 and P5 are calculated by the same trajectories as the translation vectors according to Eq. 5.15. For details regarding both calculations, the reader is referred to Section 5.2.3. By means of the transformation parameters and their corresponding variances the geo-referencing is performed as stated in Alg. 5.1.

The estimated translation vectors and the priori known coordinates of P1 and P5 differ in a range of 1–3 mm for the in-plane coordinate components and in a range of 2–5 mm for the up-component. The standard deviations of both translation vectors can be noted in sub-millimetre range (0.1–0.3 mm) owing to the large number ( $\approx 10000$ ) of participating points in the recursive estimation of the translation vector. The standard deviation of the heading is  $\sigma_{\kappa}^{P1} = 0.099^\circ$  for P1 and  $\sigma_{\kappa}^{P5} = 0.056^\circ$  for P5.

To illustrate the smoothing effect for the trajectories, the heading and its standard deviation is calculated twice: One calculation uses the constrained positions  $\tilde{\mathbf{p}}^{G, d/o}$  and the other calculation is performed by means of the smoothed, constrained positions  $\tilde{\mathbf{p}}_{RTS}^{G, d/o}$ . The expected smaller standard deviations  $\sigma_{\kappa_{RTS}}$  (cyan) in comparison to  $\sigma_{\kappa}$  (magenta) are visualised in Fig. 6.14.

The geo-referencing results of the two MSS sites are visualised in Fig. 6.15. Each MSS site is drawn in a different colour to clearly show the good agreement of the geo-referenced 3D point clouds. Thereby, the colour code of the geo-referenced 3D point cloud is: P1 red and P5 blue. To evaluate the coincidence of the 3D

<sup>6</sup>The pillar's coordinates are available in the ITRF05.



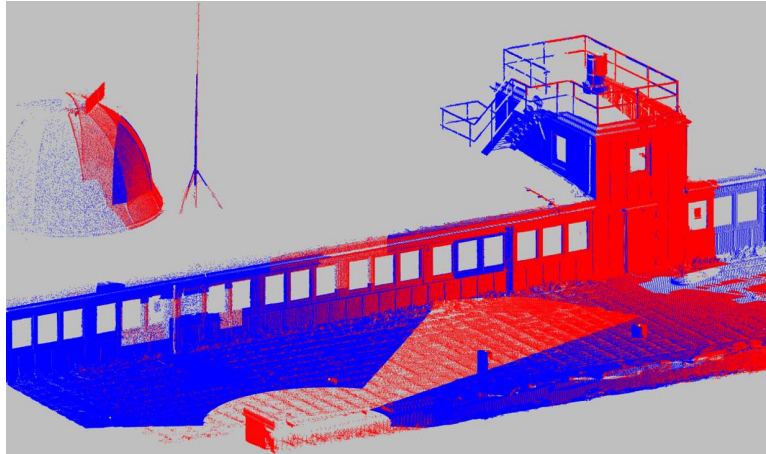


Figure 6.15: Dual antennas scenario – Geodetic Institute data set: Overview of the geo-referenced 3D point clouds of the two sites. The colour code for the geo-referenced 3D point clouds is: P1 red and P5 blue.

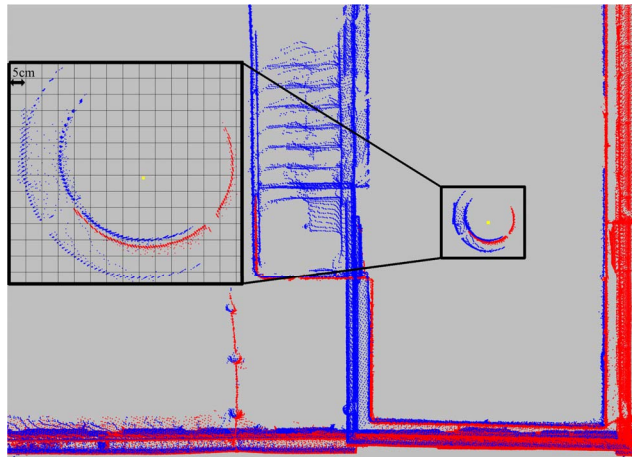


Figure 6.16: Dual antennas scenario – Geodetic Institute data set: Top view of the tower building and zoom of the cylindrical shape of P9 which indicate the coincidence of the two geo-referenced 3D point clouds (grid spacing 5cm; colour code: P1 red and P5 blue). In addition, the known coordinate of P9 is drawn in yellow.

point clouds, the area of the tower building with P9 on top is enlarged in Fig. 6.16. The discrepancies for the horizontal and vertical lines which represent the walls of the tower building are smaller than 2 cm. The zoom of the area of P9 shows a cylindrical shape with an underlying grid with 5 cm spacing. It can be noted that the discrepancies between the two cylindrical shapes are maximal 2 cm at a distance of 12.3 m for P1 and 18.4 m for P5. It is noteworthy that this shape does not represent the pillar itself. Instead it is a mantle which includes the pillar. Unfortunately, the pillar is not located in the centre of the mantle. Thus, the centre point of the cylindrical shapes can not be identical with the known coordinate of P9 (indicated by a yellow square); see also the numerical values of the coordinates comparison in Tab. 6.3.

To further illustrate the agreement of the geo-referencing result, geometric primitives in the 3D point clouds are analysed. In particular, P3 and P4 (this pillars do not have a separate mantle, the cylindrical shape corresponds to the pillar itself) as well as a building corner are considered in the analyses. An overview of the specific parts under investigation is given in Fig. 6.17; the underlying grid has a spacing of 5 cm. As it can be seen in Fig. 6.17(a) and (b), each 3D point cloud covers only half of the pillar which results from the location of the MSS sites with respect to the pillars. Thus, there does not exist overlapping parts in the 3D point cloud of P1 and P5. The connection points of both data shows only minor differences of maximal 2 cm for P3 and even smaller for P4. The corner of a building's wall is depicted in Fig. 6.17(c). The differences for the horizontal line in Fig. 6.17(c) are about 1 cm. It is worth to note that the object distance is only 2.5 m for P1 (red) with

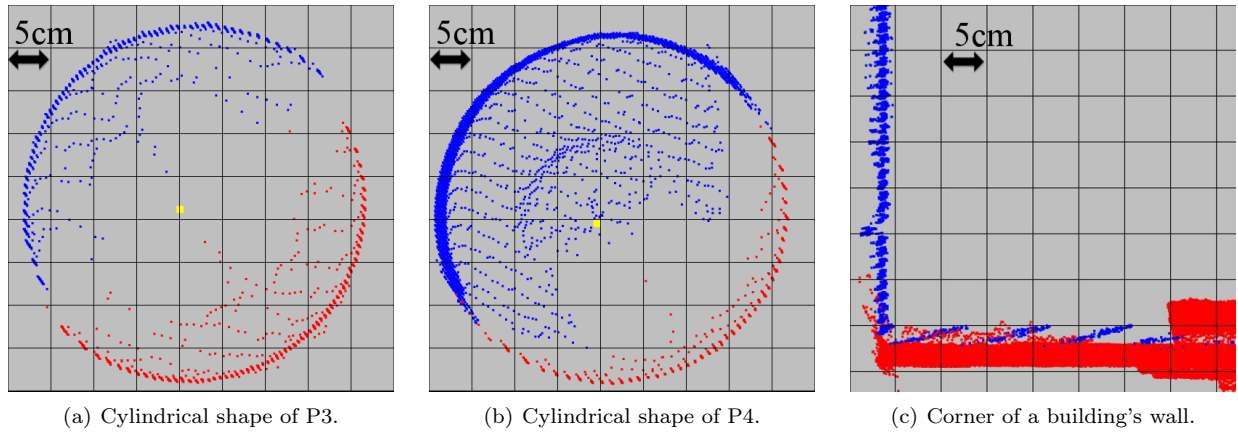


Figure 6.17: Dual antennas scenario – Geodetic Institute data set: Geometric primitives in the geo-referenced 3D point clouds which indicate the coincidence of the two 3D point clouds (grid spacing 5cm; colour code: P1 red and P5 blue). In addition, the known coordinates of P3 and P4 are drawn in yellow.

Table 6.3.: Dual antennas scenario – Geodetic Institute data set: Coordinate differences calculated by known pillar coordinates and estimated cylinder centre points.

	$\rho$ [m]	$\Delta x$ [m]	$\Delta y$ [m]		$\Delta x$ [m]	$\Delta y$ [m]	$\rho$ [m]
	10.0	-0.002	-0.013	P3	-0.014	-0.020	10.0
P1	14.9	-0.018	-0.017	P4	-0.019	-0.017	5.0
	12.3	-0.015	-0.041	P9	-0.033	-0.050	18.4

incidence angle near to  $90^\circ$ . In contrast, the object distance is about 19.2 m for P5 (blue) with incidence angles smaller than  $25^\circ$  which results in a significant difference of the number of 3D points on each wall. Despite this differences, the reconstruction of the walls's corner is possible.

To evaluate the geo-referencing with respect to the known coordinates of P3 and P4 (indicated by a yellow square in Fig. 6.17(a) and 6.17(b)), the centre points of the cylindrical shapes are utilised. Therefore, a best-fitting cylinder is estimated through the corresponding parts of the 3D point clouds. The estimated cylinder centre points are compared with the known coordinates of P3 and P4. This comparison assumes that the known coordinates of P3 and P4 represent the pillars centre point. The numerical values of the in-plane coordinate components are summarised in Tab. 6.3. The differences for P3 and P4 are in a range of 1–2 cm which is a good result with respect to the aforementioned assumption. The larger differences of about 5 cm for P9 result from the violation of the assumption that the cylinder centre point is identical with the known coordinate, as already stated above.

The information of the stochastic 3D point clouds are calculated by means of Eq. 5.17. Thus, in addition to the traditional geometric information, the positional and the transformational uncertainty of each 3D point in the cloud is available. The resulting standard deviations for the geo-referenced 3D point clouds of P1 and P5 (for the same area as shown in Fig. 6.15) are depicted in Fig. 6.18 with respect to the object distance. The standard deviations are in a range of 0.5–2.3 cm for P1 and in a range of 0.5–1.8 cm for P5. The main contribution of these uncertainties is induced by the heading's standard deviation.

It can be summarised that the obtained geo-referencing results for the Geodetic Institute data set provide good coincidence among the two MSS sites as well as small discrepancies of about 2 cm to known coordinates. Thus, the results met the accuracy assessment of the MSS (Section 4.3.5) and are suitable for typical laser scanning applications. In particular, the task of as-built documentation. In addition to the standard product in TLS applications, the results also provide uncertainty information of the transformation parameters. It is

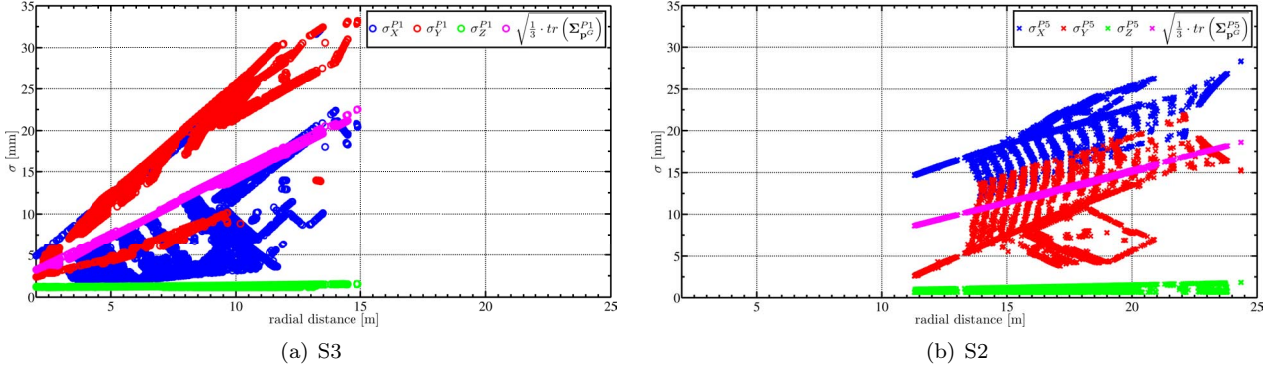


Figure 6.18: Dual antennas scenario – Geodetic Institute data set: Positional and transformational uncertainty of 3D point clouds of (a) P1 and (b) P5 with respect to the object distance. The mean coordinate uncertainty calculated by means of Eq. 5.18 is drawn in magenta. The colour code for the component-wise standard deviation is: X blue, Y red and Z green.

noteworthy that further improvements of remaining misalignments of the two sites can be obtained by means of matching algorithms, like the Gref-ICPHe3.

#### 6.4. Optimisation of transformation parameters by means of Gref-ICPHe3

The optimisation of transformation parameters by means of Gref-ICPHe3 (Section 5.3) is reasonable to reduce remaining misalignments of two partially overlapping 3D point clouds obtained by different MSS sites. This topic is illustrated for the Saxon Steed data set in the following. As input data the geo-referenced stochastic 3D point clouds of S2 and S3 are used which share the planar region under investigation in Fig. 6.13. It is noteworthy that these stochastic 3D point clouds consider both uncertainty measures, the positional and the transformational uncertainty. This yields the block diagonal structured VCM  $\Sigma_{\mathbf{p}^G}$  given in Eq. 5.17 where all diagonal elements are different from the zero matrix and all off-diagonal elements are the zero matrix. This structured VCM is kept within all calculations of Gref-ICPHe3. The topic of correlations is discussed for the positional uncertainty in Section 2.3.3. It is worth to note that the use of block diagonal structured VCMs provides more stable results for the iterative search of proper corresponding point pairs within Gref-ICPHe3. Comparative investigations of Gref-ICPHe3 considering only positional and combined (positional and transformational) uncertainty measures are discussed in Paffenholz and Bae (2012).

Before going into the discussion of the obtained results for the Saxon Steed data set, the used threshold ( $\tau$ ) and termination ( $\epsilon$ ) criteria in Alg. 5.2 for this particular data set are outlined. The quantity  $\tau_D = 0.051$  m indicates whether the coincidence of the two point clouds is satisfying or not. It is set up with respect to the scanning resolution in the object distance and the known positional and transformational uncertainties (cf. Fig. 6.19). The termination criteria are set to  $\epsilon_m = 0.001$  m and  $\epsilon_{rad} = f(\epsilon_m, \overline{rg}_L)$ . These quantities indicate that no further significant improvement of the transformation parameters during the iteration steps is expected. The remaining termination criteria are defined as follows:  $\epsilon_{rg_{rms}} = 0.05$  m and  $\epsilon_{CRLB} = 0.005$  m. In the Helmert 3D transformation loop (Alg. 5.2, Line 25) convergence is reached when the condition ( $|\Delta \mathbf{t}| < 0.1 \cdot \epsilon_m$ ) & ( $|\Delta \mathbf{R}| < 0.1 \cdot \epsilon_{rad}$ ) is fulfilled. The Helmert transformation provides the relative transformation parameters and their corresponding VCMs. It is worth mentioning that the VCM of the relative transformation parameters is considered in the subsequent loop runs. The overall transformation parameters and their corresponding variances (these are obtained by using the LOP) represent the final output of the Gref-ICPHe3. These overall transformation parameters are capable for the transformation of arbitrary points even in non-planar regions of the 3D point clouds. It is noteworthy that the subsequent results for the Saxon Steed data set are produced by the final overall transformation parameters.

Fig. 6.19 depicts the positional and transformational uncertainty measures of the 3D point clouds of S3 and

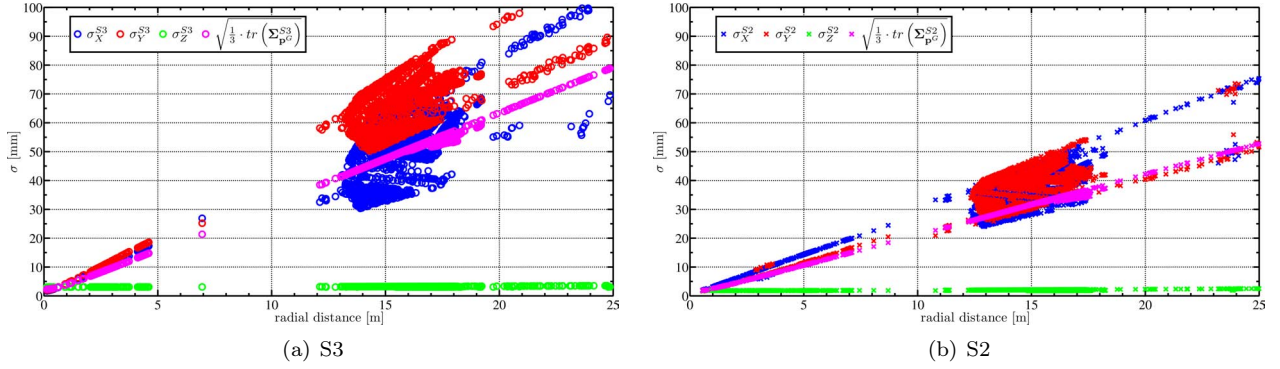


Figure 6.19: Single antenna scenario – Saxon Steed data set: Positional and transformational uncertainty of 3D point clouds of (a) S3 and (b) S2 with respect to the object distance. The mean coordinate uncertainty calculated by means of Eq. 5.18 is drawn in magenta. The colour code for the component-wise standard deviation is: X blue, Y red and Z green.

S2 with respect to the distance to the Saxon Steed sculpture. The main contribution to the uncertainty budget is induced by the heading's standard deviations ( $\sigma_{\kappa}^{S2} = 0.21^\circ$  and  $\sigma_{\kappa}^{S3} = 0.31^\circ$ ). The translation vector's standard deviations for both sites are 1 – 3 mm for all three coordinate components. The difference of about 15 mm for the mean coordinate uncertainty (Eq. 5.18) of both sites corresponds to the difference in the headings standard deviations in the object distance.

The application of the Gref-ICPHe3 with the above introduced input quantities provides the relative transformation parameters and their corresponding VCM to reduce the misalignment of S2 with respect to S3. The iterative matching by Gref-ICPHe3 ends after 11 iterations with 1070 corresponding points out of about 7000 points (in planar regions) with a final  $rg_{rms} = 0.003$  m. Fig. 6.20(a) visualises the change in the closest distances for the first and last (11<sup>th</sup>) iteration step. The closest distances decrease from centimetre to sub-millimetre range. The convergence of the estimated relative transformation parameters is depicted in Fig. 6.20(b). The convergence for the translation vector is reached with sub-millimetre range after seven iterations. For the rotation angles it takes nine iterations to reach 1/1000 degree range. The iterative calculations are terminated if three times in a row no parameter improvements are larger than the aforementioned defined thresholds ( $\epsilon_m$  and  $\epsilon_{rad}$ ). The final overall transformation parameters for S2 with respect to S3 are as follows

$$\mathbf{R}_{S2}^{S3}(\omega, \varphi, \kappa) = \text{diag} \left( [ -0.040 \quad 0.101 \quad 0.341 ]_{[^\circ]} \right) \quad \text{with} \quad \sigma_\omega = 0.020^\circ, \sigma_\varphi = 0.032^\circ, \sigma_\kappa = 0.254^\circ,$$

$$\mathbf{t}_{S2}^{S3} = [ 0.008 \quad 0.012 \quad -0.004 ]_{[\text{m}]}^T \quad \text{with} \quad \sigma_X = 6 \text{ mm}, \sigma_Y = 7 \text{ mm}, \sigma_Z = 1 \text{ mm}.$$

The a priori orientation of the MSS to the direction of gravity can be seen in the elements of  $\mathbf{R}_{S2}^{S3}$ . The dominant element is the heading  $\kappa_{S2}^{S3}$ . As expected, the standard deviation of the heading is in the same magnitude with respect to the values of the direct geo-referencing procedure. It is noteworthy that the misalignment of S2 was reduced with respect to S3 owing to the smaller differences of S3 with regard to the control points (cf. Tab. 6.2). It follows a slight increase of  $\kappa_{S2}^{S3}$  in comparison to  $\sigma_{\kappa}^{S2}$ .

The stochastic 3D point cloud of S2 obtained by means of the estimated transformation parameters as well as the stochastic 3D point cloud of S3 are visualised in Fig. 6.21. Fig. 6.21(a) depicts the planar region (available in the 3D point cloud of S2 (green) and S3 (blue)) which was already under investigation in Section 6.3.1. This zoomed area of the stochastic 3D point cloud clearly shows the minimised misalignment which was obviously seen in Fig. 6.13(a). Fig. 6.21(b) shows the resulting stochastic 3D point cloud of S2 after the use of the Gref-ICPHe3 as well as the stochastic 3D point cloud of S3. The depicted mean coordinate uncertainty (Eq. 5.18) for the stochastic 3D point cloud of S2 varies in a range of 3.3 – 3.6 cm in the distance of about 17 m to the sculpture of the Saxon Steed. The mean coordinate uncertainty of S3 is slightly higher which is indicated by the darker green colour (left part of the sculpture).

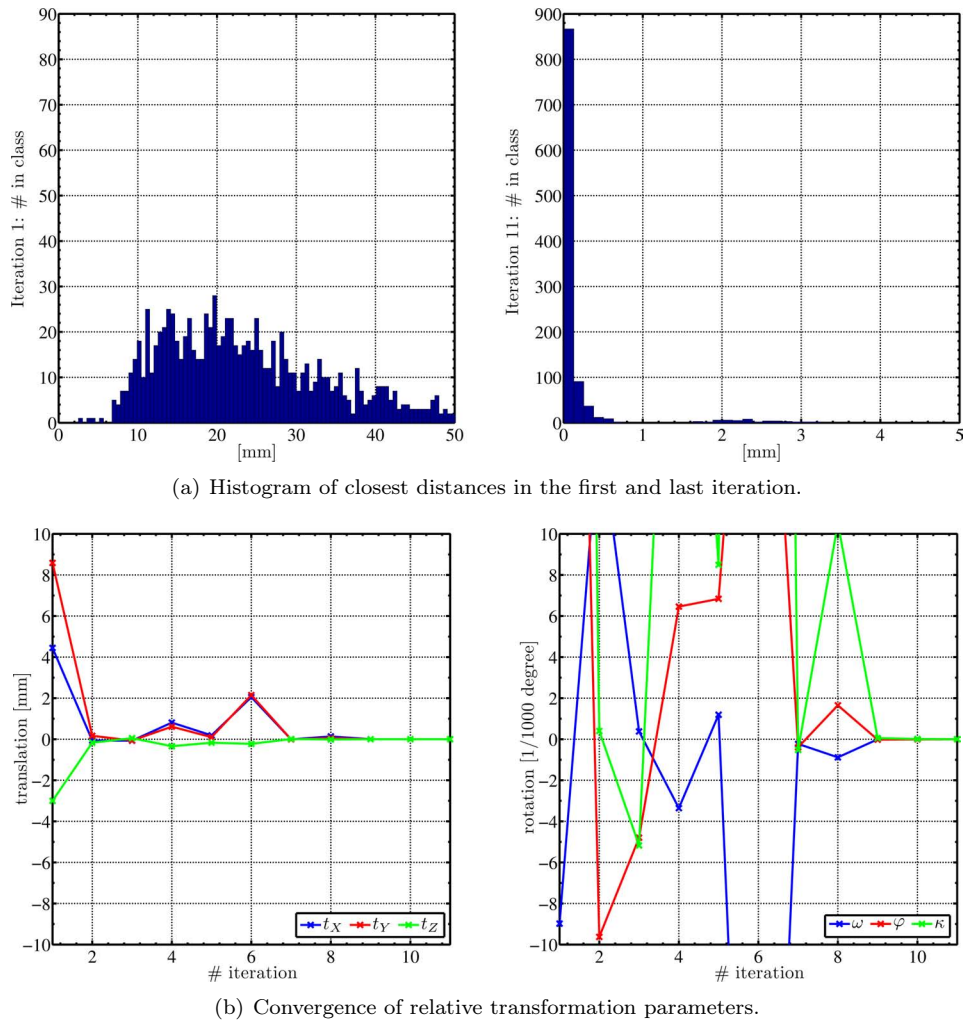
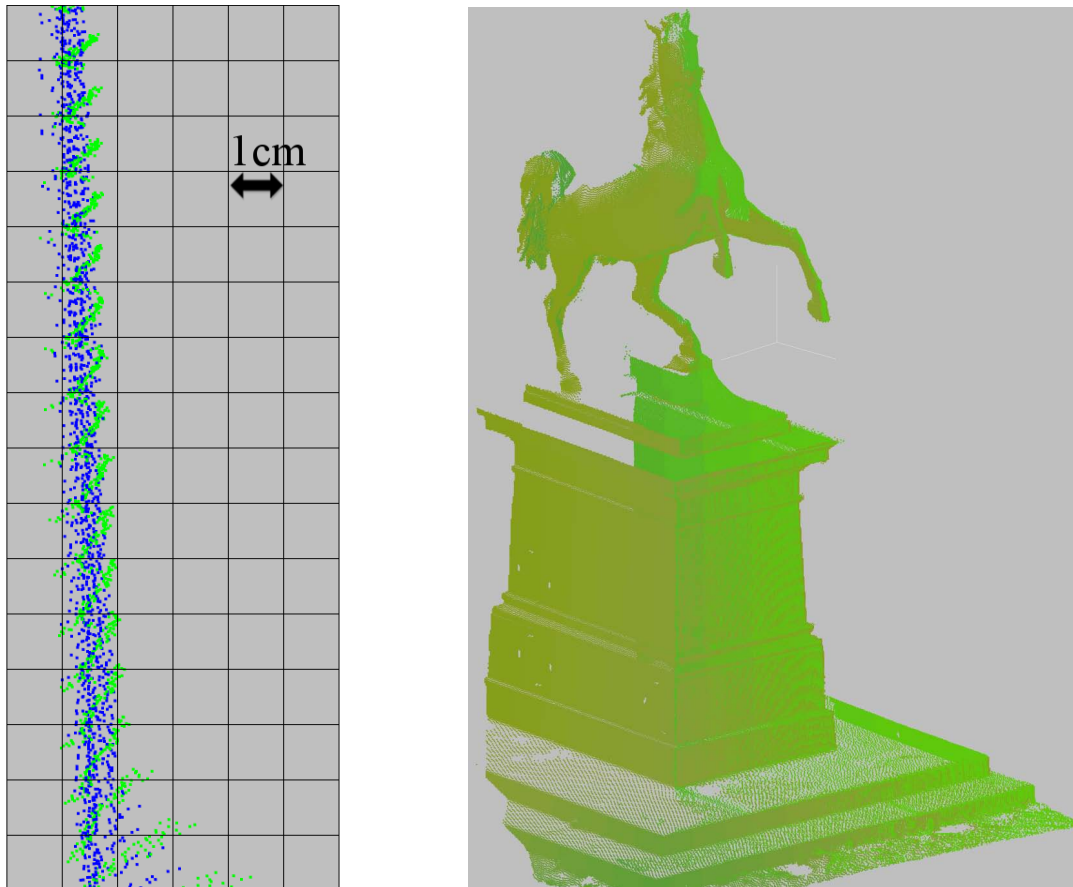


Figure 6.20: Single antenna scenario – Saxon Steed data set: Results of the Gref-ICPHe3 applied to the geo-referenced stochastic 3D point clouds of S2 and S3.

It can be summarised that fulfilling results are obtained by means of the Gref-ICPHe3 applied to S2 and S3 for the Saxon Steed data set. On the one hand, the remaining misalignments of the 3D point clouds of S2 and S3 could be minimised. On the other hand, the available stochastic information of the input data was considered during the matching process. Thus, the final outcome of the Gref-ICPHe3, the geo-referenced stochastic 3D point cloud, provides spatial and statistical information of the 3D point clouds. This stochastic information is composed of the uncertainties of the laser scanner (positional), the a priori geo-referencing (transformational) uncertainties and the uncertainties of the relative transformation parameters obtained by Gref-ICPHe3. Thus, valuable information of the 3D point cloud is available for post-process analyses. This can be the estimation of geometric primitives such as planes, cubes or cylinders.



(a) Zoom of planar region from S2 (green) and S3 (blue).

(b) Stochastic 3D point clouds of S2 and S3.

Figure 6.21: Single antenna scenario – Saxon Steed data set: Geo-referenced stochastic 3D point cloud of S2 with respect to S3 after the use of Gref-ICPHe3. (a) Minimised misalignment of planar region under investigation in Fig. 6.13(a). (b) Geo-referenced stochastic 3D point cloud with a mean coordinate uncertainty (Eq. 5.18) in a range of 3.3 – 3.6 cm for object distances up to 17 m.

## 7. Conclusions and outlook

This thesis presents a prototypic MSS and a novel algorithm to perform the geo-referencing of 3D point clouds considering uncertainty measures. The MSS is composed of two main sensors: a stationary laser scanner for the 3D point cloud acquisition and up to two GNSS equipments to obtain the required transformation parameters. The novel algorithm uses extensively the rotation of the laser scanner about its vertical axis. An EKF is used for the prediction and filtering of the circular motion of the laser scanner. The algorithm's outcome are the transformation parameters and their corresponding VCMs. The uncertainties induced by the transformation parameters and, in addition, by the laser scanner are jointly propagated to the geo-referenced 3D point clouds. As final result, geo-referenced spatial and stochastic information of the 3D point clouds is available.

### 7.1. Conclusions

The first objective was the *development of an innovative approach to obtain the required parameters for the transformation of the local sensor-defined 3D point cloud of a stationary laser scanner to an absolute coordinate system without the use of auxiliary control points*. This objective was achieved by the development of a prototypic MSS established by the fusion of a laser scanner and GNSS equipment. Furthermore, the modelling of the circular motion of the laser scanner during its data acquisition and their prediction and filtering by means of a filter in state-space, as EKF, provides the transformation parameters.

The fusion of the laser scanner with 3D positioning sensors, in particular GNSS equipment, and their mutual temporal synchronisation is reasonable to obtain the transformation parameters. The eccentric installation of the GNSS equipment with respect to the laser scanner's rotation axis permits the determination of both, translation vector and heading, only by means of physically attached sensors to the laser scanner. This sensor fusion provides synchronised 3D trajectories which are circles owing to the circular motion of the laser scanner about its vertical axis. They correspond to the horizontal angle progress of the laser scanner's data acquisition. Thanks to an assumed sufficient orientation of the laser scanner to the direction of gravity any remaining spatial rotations besides the heading can be neglected. The prototypic MSS allows a time-saving, simultaneous acquisition of 3D point clouds and their geo-reference information. No further external or auxiliary control points are required.

The available data enable a redundant estimation of the transformation parameters which increases the fidelity and reliability of the proposed geo-referencing approach. The prediction and filtering of the high resolution (up to 10 Hz) 3D trajectories, which are resulting from the circular motion of the laser scanner, are realised in an EKF approach. In particular, two variants of the system's modelling are developed by means of

- states and adaptive parameters in a single antenna scenario on the one hand and
- states with constraints in a dual antennas scenario on the other hand.

Both approaches show good performance in terms of prediction and filtering of the 3D trajectories which indicates the sufficient reduction of the measurement noise.

The translation vector, which is equivalent to the circle's centre point, is obtained by recursive estimation in a least-squares adjustment based on the 3D trajectories. This adjustment is running simultaneously to the EKF when a sufficient number of observations is available.

The benefit of the estimation of adaptive parameters is the possibility to verify MSS specific parameters which are usually obtained by separate calibration procedures. This topic is important if the wing support structure

was detached and thus the specific parameters might be out of date. One minor drawback of this approach is the sensor-orientated modelling of the motion which requires observations' pre-processing in terms of the adaption of data acquisition rates. Sensor-orientated modelling means that the motion modelling is strongly connected with the horizontal progress steps of the laser scanner. Heading parameters are calculated for each horizontal progress step and finally reduced to the first epoch which is comparable to the determination of the orientation unknown of angle measurements by total stations.

The consideration of MSS specific parameters by means of state constraints is beneficial, especially if two GNSS equipments in known diametrical positions are used. This approach is free of any pre-processing of observations since the motion modelling is more data-orientated. The constant velocity of the circular motion of the laser scanner and the fixed baseline of the two GNSS equipments are considered as constraints. Owing to this state constraints, the filter performance can be enhanced. Moreover, the constrained trajectories are more sufficient compared to the filtered trajectories in terms of data gaps of one antenna. It is noteworthy that no adaption of different acquisition rates is necessary. In fact, this approach is capable for different acquisition rates of both used GNSS equipments. The desired heading in the dual antennas scenario is equivalent to the motion start. Thus, an optimal estimate is obtained by backward filtering, i. e., smoothing.

An alternative prediction and filtering approach is LSC which also considers the stochastic properties of the 3D trajectories. Furthermore, by the required covariance functions to set up the VCMs in the LSC, more detailed information of the stochastic behaviour of the 3D trajectories was gained. The comparison of the LSC and the EKF results has shown no significant difference between both filtered trajectories. The main disadvantage of the LSC is the high computational effort for the covariance function estimation and the missing real-time capability in comparison to the recursive estimation by means of EKF.

Reconsidering the second objective, *the supplementation of the geo-referenced 3D point clouds with both, laser scanner and geo-reference uncertainties*, recursive state-space filtering by means of EKF and least-squares adjustment with conditions (GHM) provides uncertainty measures for the transformation parameters. Their common propagation with uncertainties induced by the laser scanner (positional uncertainty) provides geo-referenced stochastic 3D point clouds.

It is remarkable that the consideration of positional uncertainty is frequently used in the scope of matching algorithms. In contrast, transformational uncertainty is rarely used in stationary laser scanner applications. The reason for this is the fact that the uncertainties of the transformation parameters (in the traditional way of geo-referencing) are typically not available. Thus, the geo-referenced stochastic 3D point clouds pave the way for rigorous consideration of the entire uncertainty budget of a 3D point cloud for subsequent analysis like, e. g., estimation of geometric primitives. The proposed optimisation of transformation parameters by means of Gref-ICPHe3 uses both kinds of uncertainties and also incorporates those of the relative transformation parameters within the iterative matching. For the consideration of positional uncertainty the approach of Bae et al. (2009) was utilised.

Both objectives of this thesis have been met successfully. The potential of the MSS and the novel algorithm were shown for both modelling approaches (single and dual antennas scenario). It can be summarised that the results show good coincidence of overlapping regions from different sites in a range of 1–3 cm for object distances up to 20 m. The comparison to known control point coordinates are in the same range of centimetres. Owing to the use of one set of transformation parameters for the geo-referencing of the entire 3D point cloud, each 3D point cloud is consistent. It can be stated that the main influencing factor of the proposed geo-referencing approach is the heading and its uncertainty. As expected, the heading and its uncertainty is strongly related to the baseline length used for the heading determination. The baseline length in the MSS is about 0.6 m. The obtained heading uncertainties are in a range of 0.06 – 0.3°.

In conclusion, the proposed methodology with the introduced MSS and developed algorithm is suitable to meet the requirements of several laser scanning applications, like as-built documentation, densification of MLS point clouds and provision of proper initial values with uncertainty information for matching algorithms.



## 7.2. Outlook

Even if the objectives of the thesis were met successfully, there are open questions and recommendations for future work.

Considering the prototypic MSS, the enlargement of the baseline length for the two GNSS antennas would be beneficial. It is suggested to increase the distance to the laser scanner's rotation axis for one side of the wing support structure. The use of a light-weight antenna (typically this is true for low-cost equipment) is proposed. Consequently, the stability of the wing enlargement during the rotation has to be investigated and adjusted in length. In addition, balanced weights for both sides of the wing support structure have to be considered. Differences, which can be present in terms of acquisition rate and noise level for the suggested constellation of GNSS equipments, are accounted in the motion modelling by states with constraints.

Furthermore, the consideration of inclinometers not only for the orientation to the direction of gravity but also for the system modelling can be meaningful. In this case, the occurring dynamics during the rotation have to be investigated.

Regarding the algorithmic part of the proposed geo-referencing methodology, the following topics are recommended for future work: For filter improvements, especially when dealing with different types of sensors (in terms of accuracy range), the VCE is a technique (well-known from parameter estimation in linear models) to obtain optimal variance factors. In particular, the estimation of variance components for the process and measurement noise (Casparly and Wang, 1998) as well as for groups of observations (different GNSS equipments, inclinometer observations) is recommended.

Currently, for the VCM of the process noise a random constant process is assumed. More sophisticated stochastic processes (random walk) which take into account the sinusoidal oscillation have to be studied with respect to their influence on the filter performance.

A sensitivity analysis according to Schwieger (2005) is a suggestion for future work to gain in-depth information of the modelled motion of the MSS. The situation of sensor outages and their impact on the results can also be analysed in this manner.

The recent implementation of the Gref-ICPHe3 is capable for mutual registration of two 3D point clouds. The extension of the algorithm to both, multiple 3D point clouds registration and the introduction of conditions for specific regions of the point clouds based on uncertainty measures are plans for further developments.

At the current developmental stage the MSS is prepared for outdoor use. Nonetheless, the replacement of the GNSS antennas with indoor positioning sensors paves the way to GNSS-denied environments. The derivation of the transformation parameters is carried out in post-processing but the algorithm is capable for real-time analysis. This allows on-site information regarding the reached uncertainty range after the geo-referencing and thus can strengthen the work flow in terms of station optimisation.

In short, the proposed methodology with the developed MSS and the novel algorithm for the direct geo-referencing of 3D point clouds contributes to an efficient acquisition of 3D spatial data for various TLS applications. Next to the spatial data supplemental stochastic information is provided by means of geo-referenced stochastic 3D point clouds.



## References

- Abmayr, T., 2010. Calibration and registration framework for multisensor panoramic color scanning: PhD thesis. Shaker, Aachen.
- Abmayr, T., Dalton, G., Härtl, F., Hines, D., Liu, R., Hirzinger, G., Fröhlich, C., 2005. Standardization and visualization of 2.5D scanning data and color information by inverse mapping. In: Grün, A., Kahmen, H. (Eds.), *Optical 3-D Measurement Techniques VII*. Vol. I. pp. 164–173.
- Abmayr, T., Härtl, F., Hirzinger, G., Burschka, D., Fröhlich, C., 2008. A correlation based target finder for terrestrial laser scanning. *Journal of Applied Geodesy* 2 (3), 131–137.
- Abmayr, T., Härtl, F., Wagner, A., Burschka, D., Hirzinger, G., Fröhlich, C., 2009. Calibration and registration framework for 3D reconstruction of the Kirche Seefeld. In: Remondino, F., El-Hakim, S., Gonzo, L. (Eds.), *3D-ARCH 2009*. Vol. XXXVIII-5/W1 of ISPRS Archives. p. 8.
- Al-Durgham, M., Datchev, I., Habib, A. F., 2011. Analysis of two triangle-based multi-surface registration algorithms of irregular point clouds. In: Lichti, D. D., Habib, A. F. (Eds.), *ISPRS Workshop Laser Scanning 2011*. Vol. XXXVIII-5/W12 of ISPRS Archives. pp. 61–66.
- Alba, M., Barazzetti, L., Scaioni, M., Remondino, F., 2011. Automatic registration of multiple laser scans using panoramic RGB and intensity images. In: Lichti, D. D., Habib, A. F. (Eds.), *ISPRS Workshop Laser Scanning 2011*. Vol. XXXVIII-5/W12 of ISPRS Archives. pp. 49–54.
- Alba, M., Giussani, A., Roncoroni, F., Scaioni, M., 2005. Strategies for direct georeferencing of Riegl LMS-Z420i data. In: Grün, A., Kahmen, H. (Eds.), *Optical 3-D Measurement Techniques VII*. Vol. II. pp. 395–400.
- Alba, M., Scaioni, M., 2007. Comparison of techniques for terrestrial laser scanner data georeferencing applied to 3-D modeling of cultural heritage. In: Remondino, F., El-Hakim, S. (Eds.), *3D-ARCH 2007*. Vol. XXXVI-5/W47 of ISPRS Archives. p. 8.
- Alkhatib, H., 2007. On Monte Carlo methods with applications to the current satellite gravity missions. PhD thesis, Universität Bonn, Bonn.  
URL <http://nbn-resolving.de/urn:nbn:de:hbz:5N-10783>
- Alkhatib, H., Neumann, I., Kutterer, H., 2009. Uncertainty modeling of random and systematic errors by means of Monte Carlo and fuzzy techniques. *Journal of Applied Geodesy* 3 (2), 67–79.
- Alkhatib, H., Neumann, I., Neuner, H., Kutterer, H., 2008. Comparison of sequential Monte Carlo filtering with Kalman filtering for nonlinear state estimation. In: Ingensand, H., Stempfhuber, W. (Eds.), *1st International Conference on Machine Control & Guidance - Proceedings*. pp. 132–142.
- Alkhatib, H., Paffenholz, J.-A., Kutterer, H., 2012. Sequential Monte Carlo filtering for nonlinear GNSS trajectories. In: Sneeuw, N., Novák, P., Crespi, M., Sansò, F. (Eds.), *VII Hotine-Marussi Symposium on Mathematical Geodesy: Proceedings of the Symposium in Rome*. Vol. 137 of *International Association of Geodesy Symposia*. Springer, pp. 81–86.
- Althen GmbH, 2010. *Aliso\_en*: Version 1.02: Data sheet.
- Aussems, T., 1999. Positionsschätzung von Landfahrzeugen mittels Kalman-Filterung aus Satelliten- und Koppelnavigationsbeobachtungen. PhD thesis, Veröffentlichungen des Geodätischen Institutes der Rheinisch-Westfälischen Technischen Hochschule Aachen, Aachen.
- Baarda, W., 1968. A testing procedure for use in geodetic networks. Vol. 2:5 of *Publications on geodesy*. Netherlands Geodetic Commission, Delft.
- Bae, K.-H., 2006. Automated registration of unorganised point clouds from terrestrial laser scanners. PhD thesis, Curtin University of Technology, Perth, WA.
- Bae, K.-H., 2009. Evaluation of the convergence region of an automated registration method for 3D laser scanner point clouds. *Sensors* 9 (1), 355–375.
- Bae, K.-H., Belton, D., Lichti, D. D., 2009. A closed-form expression of the positional uncertainty for 3D point clouds. *IEEE Transactions on Pattern Analysis and Machine Intelligence* 31 (4), 577–590.
- Bae, K.-H., Lichti, D. D., 2007. On-site self-calibration using planar features for terrestrial laser scanners. In: Rönnholm, P., Hyypä, H., Hyypä, J. (Eds.), *Proceedings of the ISPRS Workshop*. Vol. XXXVI-3/W52 of ISPRS Archives. pp. 14–19.
- Bae, K.-H., Lichti, D. D., 2008. A method for automated registration of unorganised point clouds. *ISPRS Journal of Photogrammetry and Remote Sensing* 63 (1), 36–54.
- Bar-Shalom, Y., Li, X. R., Kirubarajan, T., 2001. *Estimation with applications to tracking and navigation: Theory algorithms and software*. John Wiley & Sons, Inc, New York, NY.
- Barber, D., Mills, J., Smith-Voysey, S., 2008. Geometric validation of a ground-based mobile laser scanning system. *ISPRS Journal of Photogrammetry and Remote Sensing* 63 (1), 128–141.
- Barnea, S., Filin, S., 2007. Registration of terrestrial laser scans via image based features. In: Rönnholm, P., Hyypä, H., Hyypä, J. (Eds.), *Proceedings of the ISPRS Workshop*. Vol. XXXVI-3/W52 of ISPRS Archives. pp. 32–37.
- Bay, H., Ess, A., Tuytelaars, T., Van Gool, L., 2008. SURF: Speeded up robust features. *Computer Vision and Image Understanding* 110 (3), 346–359.
- Beinat, A., Crosilla, F., 2002. A generalized factored stochastic model for optimal registration of LIDAR range images. In: Kallianay, R., Leberl, F., Frauendorfer, F. (Eds.), *Photogrammetric Computer Vision*. Vol. B of ISPRS Archives. pp. 36–39.
- Beraldin, J.-A., Blais, F., Lohr, U., 2010. Laser scanning technology. In: Vosselman, G., Maas, H.-G. (Eds.), *Airborne and terrestrial laser scanning*. Whittles Publishing, Dunbeath, pp. 1–42.
- Besl, P. J., McKay, N. D., 1992. A method for registration of 3-D shapes. *IEEE Transactions on Pattern Analysis and Machine Intelligence* 14 (2), 239–256.
- Blankenbach, J., Norrdine, A., 2010. Position estimation using artificial generated magnetic fields. In: Mautz, R., Kun, M., Ingensand, H. (Eds.), *Proceedings of the 2010 International Conference on Indoor Positioning and Indoor Navigation*. IEEE Xplore Digital Library, pp. 1–5.

- Blankenbach, J., Norrdine, A., Willert, V., 2009. Ultra wideband based indoor positioning: A localization prototype for precise 3D positioning and orientation. In: Grün, A., Kahmen, H. (Eds.), *Optical 3-D Measurement Techniques IX*. Vol. II. pp. 179–188.
- Bleich, P., Illner, M., 1989. Strenge Lösung der räumlichen Koordinatentransformation durch iterative Berechnung. *Allgemeine Vermessungs-Nachrichten* 96 (4), 133–144.
- Boehler, W., Bordas Vicent, M., Marbs, A., 2003. Investigating laser scanner accuracy. In: *Proceedings of the CIPA 2003 XVIII International Symposium: The International Archives of the Photogrammetry, Remote Sensing and Spatial Information Science*. Vol. XXXIV-5/C15. pp. 696–701.
- Böhm, J., Becker, S., 2007. Automatic marker-free registration of terrestrial laser scans using reflectance features. In: Grün, A., Kahmen, H. (Eds.), *Optical 3-D Measurement Techniques VIII*. pp. 338–344.
- Böhm, J., Haala, N., 2005. Efficient integration of aerial and terrestrial laser data for virtual city modeling using LASERMAPS. In: Vosselman, G., Brenner, C. (Eds.), *Proceedings of the ISPRS Workshop Laser scanning 2005*. Vol. XXXVI-3/W19 of ISPRS Archives. pp. 192–197.
- Brenner, C., Dold, C., Ripperda, N., 2008. Coarse orientation of terrestrial laser scans in urban environments. *ISPRS Journal of Photogrammetry and Remote Sensing* 63 (1), 4–18.
- Brieden, P., 2009. Untersuchung eines Multi-Sensorsystems zur direkten Georeferenzierung basierend auf einem terrestrischen Laserscanner. Diploma thesis (unpublished), Leibniz Universität Hannover, Hannover.
- Brown, R. G., Hwang, P. Y. C., 2012. Introduction to random signals and applied Kalman filtering: With MATLAB exercises, 4th Edition. John Wiley & Sons, Inc, Hoboken, NJ.
- Casparly, W., Wang, J.-G., 1998. Redundanzanteile und Varianzkomponenten im Kalman Filter. *Zeitschrift für Geodäsie, Geoinformation und Landmanagement* 123 (4), 121–128.
- Chang, C. C., Tsai, W. Y., 2006. Evaluation of a GPS-based approach for rapid and precise determination of geodetic/astronomical azimuth. *Journal of Surveying Engineering* 132 (4), 149–154.
- Chen, Y., Medioni, G., 1992. Object modelling by registration of multiple range images. *Image and Vision Computing* 10 (3), 145–155.
- Chia, T. L., Chow, P.-C., Chizeck, H. J., 1991. Recursive parameter identification of constrained systems: An application to electrically stimulated muscle. *IEEE Transactions on Biomedical Engineering* 38 (5), 429–442.
- Chow, J., Lichti, D. D., Glennie, C., 2011. Point-based versus plane-based self-calibration of static terrestrial laser scanners. In: Lichti, D. D., Habib, A. F. (Eds.), *ISPRS Workshop Laser Scanning 2011*. Vol. XXXVIII-5/W12 of ISPRS Archives. pp. 121–126.
- Demantké, J., Mallet, C., David, N., Vallet, B., 2011. Dimensionality based scale selection in 3D lidar point clouds. In: Lichti, D. D., Habib, A. F. (Eds.), *ISPRS Workshop Laser Scanning 2011*. Vol. XXXVIII-5/W12 of ISPRS Archives. pp. 97–102.
- Deumlich, F., Staiger, R., 2002. *Instrumentenkunde der Vermessungstechnik*, 9th Edition. Wichmann, Heidelberg.
- Dilßner, F., 2007. Zum Einfluss des Antennenumfeldes auf die hochpräzise GNSS-Positionsbestimmung: Nr. 271. Phd thesis, Leibniz Universität Hannover, Hannover.
- Dold, C., 2010. Ebenenbasierte Verfahren für die automatische Registrierung terrestrischer Laserscans: PhD thesis. Vol. 646 of Reihe C. DGK, München.
- Dorninger, P., Nothegger, C., Pfeifer, N., Molnár, G., 2008. On-the-job detection and correction of systematic cyclic distance measurement errors of terrestrial laser scanners. *Journal of Applied Geodesy* 2 (4), 191–204.
- Doucet, A., Freitas, N. d., Gordon, N., 2001. *Sequential Monte Carlo methods in practice*. Springer, New York, NY.
- Drixler, E., 1993. Analyse der Form und Lage von Objekten im Raum: PhD thesis. Vol. 409 of Reihe C. DGK, München.
- Eggert, D. W., Lorusso, A., Fisher, R. B., 1997. Estimating 3-D rigid body transformations: a comparison of four major algorithms. *Machine Vision and Applications* 9 (5-6), 272–290.
- Eglseer, A., Reiterer, A., Eichhorn, A., 2010. Fußgängerortung im Out- und Indoorbereich mit einem autonomen Ortungssystem. *Allgemeine Vermessungs-Nachrichten* 117 (7), 243–249.
- Eichhorn, A., 2005. Ein Beitrag zur Identifikation von dynamischen Strukturmodellen mit Methoden der adaptiven KALMAN-Filterung: PhD thesis. Vol. 585 of Reihe C. DGK, München.
- Eichhorn, A., 2007. Analysis of dynamic deformation processes with adaptive KALMAN-filtering. *Journal of Applied Geodesy* 1 (1), 9–15.
- Eling, C., Zeimetz, P., Kuhlmann, H., 2010. Determination of a GPS-single-epoch orientation based on double differences. In: Schulze Lammers, P., Kuhlmann, H. (Eds.), *2nd International Conference on Machine Control & Guidance - Proceedings*. pp. 151–159.
- Favre, C., Hennes, M., 2000. Zum Einfluss der geometrischen Ausrichtung von 360°-Reflektoren bei Messungen mit automatischer Zielerfassung. *Vermessung Photogrammetrie Kulturtechnik* 98 (2), 72–78.
- Gamse, S., Wunderlich, T. A., Wasmeier, P., Kogoj, D., 2010. The use of Kalman filtering in combination with an electronic tachometer. In: Mautz, R., Kun, M., Ingensand, H. (Eds.), *Proceedings of the 2010 International Conference on Indoor Positioning and Indoor Navigation*. IEEE Xplore Digital Library, pp. 1–9.
- Gelb, A. (Ed.), 1974. *Applied optimal estimation*. MIT Press, Cambridge, Mass.
- González-Aguilera, D., Rodríguez-González, P., Gómez-Lahoz, J., 2009. An automatic procedure for co-registration of terrestrial laser scanners and digital cameras. *ISPRS Journal of Photogrammetry and Remote Sensing* 64 (3), 308–316.
- Gordon, S. J., 2004. Structural deformation measurement using terrestrial laser scanners. Phd thesis, Curtin University of Technology, Perth, WA.
- Gordon, S. J., Lichti, D. D., 2004. Terrestrial laser scanners with a narrow field of view: The effect on 3D resection solutions. *Survey Review* 37 (292), 448–468.
- Gottwald, R., 2008. Field procedures for testing terrestrial laser scanners (TLS): A contribution to a future ISO standard. In: *Proceedings of the FIG Working Week 2008*. p. 14.
- Gottwald, R., Heister, H., Staiger, R., 2009. Zur Prüfung und Kalibrierung von terrestrischen Laserscannern - eine Standortbestimmung. *Zeitschrift für Geodäsie, Geoinformation und Landmanagement* 134 (2), 88–96.

- Grabe, M., 2005. Measurement uncertainties in science and technology. Springer, Berlin, Heidelberg.
- Grafarend, E. W., Awange, J. L., 2003. Nonlinear analysis of the three-dimensional datum transformation [conformal group  $C_7(3)$ ]. *Journal of Geodesy* 77 (1-2), 66–76.
- Grejner-Brzezinska, D. A., Toth, C. K., Lee, J.-K., Wang, X., 2011. Positioning and navigation in GPS-challenged environments: cooperative navigation concept: Presentation. In: *Proceedings of the FIG Working Week 2011*. p. 19.
- Grewal, M. S., Andrews, A. P., 2008. Kalman filtering: Theory and practice using MATLAB, 3rd Edition. John Wiley & Sons, Inc, Hoboken, NJ.
- Grewal, M. S., Weill, L. R., Andrews, A. P., 2007. Global positioning systems, inertial navigation, and integration, 2nd Edition. John Wiley & Sons, Inc, Hoboken, NJ.
- Grün, A., Akca, D., 2005. Least squares 3D surface and curve matching. *ISPRS Journal of Photogrammetry and Remote Sensing* 59 (3), 151–174.
- Gühring, J., 2001. Reliable 3D surface acquisition, registration and validation using statistical error models. IEEE Computer Society Press: Third International Conference on 3-D Digital Imaging and Modeling, 224–231.
- Gühring, J., 2002. 3D-Erfassung und Objektrekonstruktion mittels Streifenprojektion: PhD thesis. Vol. 560 of Reihe C. DGK, München.
- Habib, A. F., Datchev, I., Bang, K., 2010. A comparative analysis of two approaches for multiple-surface registration of irregular point clouds. *International Archives of the Photogrammetry, Remote Sensing and Spatial Information Science XXXVIII-Part 1*.
- Harmening, C., 2011. Bestimmung von hochaufgelösten 3D-Trajektorien mittels Kollokation nach kleinsten Quadraten. Bachelor thesis (unpublished), Leibniz Universität Hannover, Hannover.
- Harmening, C., Paffenholz, J.-A., Alkhatib, H., 2012. Analysis of high resolution 3D trajectories for geo-referencing purposes. In: *Proceedings of the FIG Working Week 2012*. p. 12.
- Haykin, S., 2001. Kalman filters. In: Haykin, S. (Ed.), *Kalman Filtering and Neural Networks*. John Wiley & Sons, Inc, New York, NY, pp. 1–21.
- Hennes, M., 1999. Grundlegende Aspekte zur Bestimmung der Leistungsfähigkeit von Robottachymetern. *Allgemeine Vermessungs-Nachrichten* 106 (11-12), 374–385.
- Hennes, M., 2007. Konkurrierende Genauigkeitsmaße - Potential und Schwächen aus der Sicht des Anwenders. *Allgemeine Vermessungs-Nachrichten* 114 (4), 136–146.
- Hennes, M., 2010. Determining 6DOF: A-TOM - a low-cost module for range enlargement of measuring systems.
- Hennes, M., Heister, H., 2007. Neuere Aspekte zur Definition und zum Gebrauch von Genauigkeitsmaßen in der Ingenieurgeodäsie. *Allgemeine Vermessungs-Nachrichten* 114 (11-12), 375–383.
- Hennes, M., Richter, E., 2008. A-TOM - eine neuartige instrumentelle Lösung für die hochpräzise und echtzeitnahe 6DOF-Bestimmung. *Allgemeine Vermessungs-Nachrichten* 115 (8-9), 301–310.
- Hennes, M., Richter, E., 2009. Ein neuartiges Verfahren zur 6DOF-Bestimmung. In: Luhmann, T., Müller, C. (Eds.), *Photogrammetrie, Laserscanning, optische 3D-Messtechnik*. Wichmann, pp. 254–261.
- Hesse, C., 2007. Hochauflösende kinematische Objekterfassung mit terrestrischen Laserscannern: PhD thesis. Vol. 608 of Reihe C. DGK, München.
- Hesse, C., Kutterer, H., 2007. A mobile mapping system using kinematic terrestrial laser scanning (ktls) for image acquisition. In: Grün, A., Kahmen, H. (Eds.), *Optical 3-D Measurement Techniques VIII*. Vol. II. pp. 134–141.
- Heunecke, O., 1995. Zur Identifikation und Verifikation von Deformationsprozessen mittels adaptiver Kalman-Filterung (Hannoversches Filter): Nr. 208. Phd thesis, Universität Hannover, Hannover.
- Hofmann-Wellenhof, B., Lichtenegger, H., Wasle, E., 2008. GNSS - Global Navigation Satellite Systems: GPS, GLONASS, Galileo and more. Springer, Wien. URL <http://www.springerlink.com/content/978-3-211-73012-6#section=931378&page=1&locus=0>
- Horst, S., von Gösseln, I., 2012. Active prism for total station measurements. In: Schwieger, V., Böttinger, S., Zheng, B. (Eds.), *3rd International Conference on Machine Control & Guidance*. pp. 211–220.
- Huxhagen, U., Kern, F., Siegrist, B., 2011. Untersuchung zum Auflösungsvermögen terrestrischer Laserscanner mittels BÖHLER-Stern. In: Seyfert, E. (Ed.), *Tagungsband der 31. Wissenschaftlich-Technischen Jahrestagungen der DGPF*. Vol. 20. pp. 409–418.
- ISO, 1995. Guide to the expression of uncertainty in measurement (gum).
- ISO, 2007. Evaluation of measurement data - supplement 1 to the guide to the expression of uncertainty in measurement - propagation of distributions using a Monte Carlo method.
- Jäger, R. R., Müller, T., Saler, H., Schwäble, R., 2005. Klassische und robuste Ausgleichungsverfahren: Ein Leitfaden für Ausbildung und Praxis von Geodäten und Geoinformatikern. Wichmann, Heidelberg.
- Joekel, R., Stober, M., Huep, W., 2008. Elektronische Entfernung- und Richtungsmessung und ihre Integration in aktuelle Positionierungsverfahren, 5th Edition. Wichmann, Heidelberg.
- Jost, T., Hügli, H., 2003. A multi-resolution ICP with heuristic closest point search for fast and robust 3D registration of range images. In: *Proceedings of the Fourth International Conference on 3-D Digital Imaging and Modeling*. IEEE Computer Society, pp. 427–433.
- Julier, S. J., LaViola, J. J. J., 2007. On Kalman filtering with nonlinear equality constraints. *IEEE Transactions on Signal Processing* 55 (6), 2774–2784.
- Julier, S. J., Uhlmann, J. K., 1997. A new extension of the Kalman filter to nonlinear systems. In: *SPIE Proceedings of AeroSense: The 11th International Symposium on Aerospace/Defense Sensing, Simulation and Controls*. p. 12.
- Jutzi, B., 2007. Analyse der zeitlichen Signalform von rückgestreuten Laserpulsen: PhD thesis. Vol. 611 of Reihe C. DGK, München.
- Kalman, R. E., 1960. A new approach to linear filtering and prediction problems. *Journal of Basic Engineering* 82 (1), 35–45.
- Kalman, R. E., Bucy, R. S., 1961. New results in linear filtering and prediction theory. *Journal of Basic Engineering* 83 (1), 95–108.
- Koch, K.-R., 1999. Parameter estimation and hypothesis testing in linear models, 2nd Edition. Springer, Berlin.

- Koch, K.-R., 2008a. Determining uncertainties of correlated measurements by Monte Carlo simulations applied to laserscanning. *Journal of Applied Geodesy* 2 (3), 139–147.
- Koch, K.-R., 2008b. Evaluation of uncertainties in measurements by Monte Carlo simulations with an application for laserscanning. *Journal of Applied Geodesy* 2 (2), 67–77.
- Koch, K.-R., 2010. Uncertainty of results of laser scanning data with correlated systematic effects by Monte Carlo methods. *Zeitschrift für Geodäsie, Geoinformation und Landmanagement* 135 (6), 376–385.
- Koch, K.-R., Kuhlmann, H., Schuh, W.-D., 2010. Approximating covariance matrices estimated in multivariate models by estimated auto- and cross-covariances. *Journal of Geodesy* 84 (6), 383–397.
- Koch, K.-R., Schmidt, M., 1994. Deterministische und stochastische Signale: Mit Anwendungen in der digitalen Bildverarbeitung. Ferd. Dümmler Verlag, Bonn.
- Kouba, J., 2009. A guide to using International GNSS Service (IGS) products. URL <http://acc.igs.org/UsingIGSProductsVer21.pdf>
- Kutterer, H., 2010. Mobile mapping. In: Vosselman, G., Maas, H.-G. (Eds.), *Airborne and terrestrial laser scanning*. Whittles Publishing, Dunbeath, pp. 293–311.
- Kutterer, H., Alkhatib, H., Paffenholz, J.-A., Vennegeerts, H., 2010. Monte-carlo simulation of profile scans from kinematic TLS. In: *Proceedings of the FIG Congress 2010*. p. 12.
- Kutterer, H., Neumann, I., 2011. Recursive least-squares estimation in case of interval observation data. *International Journal of Reliability and Safety* 5 (3/4), 229–249.
- Kutterer, H., Paffenholz, J.-A., Vennegeerts, H., 2009. Kinematisches terrestrisches Laserscanning. *Zeitschrift für Geodäsie, Geoinformation und Landmanagement* 134 (2), 79–87.
- Li, L., 2011. Separability of deformations and measurement noises of GPS time series with modified Kalman filter for landslide monitoring in real-time. Phd thesis, Universität Bonn, Bonn. URL <http://nbn-resolving.de/urn:nbn:de:hbz:5N-26054>
- Lichti, D. D., 2007. Error modelling, calibration and analysis of an AM-CW terrestrial laser scanner system. *ISPRS Journal of Photogrammetry and Remote Sensing* 61 (5), 307–324.
- Lichti, D. D., 2009. The impact of angle parameterisation on terrestrial laser scanner self-calibration. In: Bretar, F., Pierrot-Deseilligny, M., Vosselman, G. (Eds.), *Laserscanning '09*. Vol. XXXVIII-3/W8 of ISPRS Archives. pp. 171–176.
- Lichti, D. D., 2010. Terrestrial laser scanner self-calibration: Correlation sources and their mitigation. *ISPRS Journal of Photogrammetry and Remote Sensing* 65 (1), 93–102.
- Lichti, D. D., Gordon, S. J., 2004. Error propagation in directly georeferenced terrestrial laser scanner point clouds for cultural heritage recording. In: *Proceedings of the FIG Working Week 2004*. p. 16.
- Lichti, D. D., Gordon, S. J., Tipdecho, T., 2005. Error models and propagation in directly georeferenced terrestrial laser scanner networks. *Journal of Surveying Engineering* 131 (4), 135–142.
- Lichti, D. D., Skaloud, J., 2010. Registration and calibration. In: Vosselman, G., Maas, H.-G. (Eds.), *Airborne and terrestrial laser scanning*. Whittles Publishing, Dunbeath, pp. 83–133.
- Longstreet, B., 2010. New tech for old task: Tunnel surveyors use the latest technology on New York's No. 7 subway extension. *Tunnel Business Magazine* (August), 24–26.
- Lowe, D. G., 2004. Distinctive image features from scale-invariant keypoints. *International Journal of Computer Vision* 60 (2), 91–110.
- Luhmann, T., Robson, S., Kyle, S., 2006. *Close range photogrammetry: Principles, methods and applications*. Whittles, Dunbeath.
- Macheiner, K., Woschitz, H., Brunner, F. K., 2009. Test dynamischer Eigenschaften ausgewählter Neigungssensoren. *tm - Technisches Messen* 76 (11), 509–516.
- Mader, G. L., 1999. GPS antenna calibration at the National Geodetic Survey. *GPS Solutions* 3 (1), 50–58.
- Mallet, C., Bretar, F., 2009. Full-waveform topographic lidar: State-of-the-art. *ISPRS Journal of Photogrammetry and Remote Sensing* 64 (1), 1–16.
- Mallet, C., Bretar, F., Roux, M., Soergel, U., Heipke, C., 2011. Relevance assessment of full-waveform lidar data for urban area classification. *ISPRS Journal of Photogrammetry and Remote Sensing* 66 (6), S71–S84.
- Mårtensson, S.-G., Reshetyuk, Y., Jivall, L., 2012. Measurement uncertainty in network RTK GNSS-based positioning of a terrestrial laser scanner. *Journal of Applied Geodesy* 6, 25–32.
- Mautz, R., 2012. *Indoor positioning technologies*. Habilitation thesis, ETH Zurich, Zurich.
- Mautz, R., Kun, M., Ingensand, H. (Eds.), 2010. *Proceedings of the 2010 International Conference on Indoor Positioning and Indoor Navigation*. IEEE Xplore Digital Library.
- Mikhail, E. M., 1976. *Observations and least squares*. IEP, New York.
- Mikhail, E. M., Bethel, J. S., McGlone, J. C., 2001. *Introduction to modern photogrammetry*. Wiley, New York.
- Mohamed, A. H., Wilkinson, B. E., 2009. Direct georeferencing of stationary LiDAR. *Remote Sensing* 1 (4), 1321–1337.
- Montemerlo, M., Thrun, S., 2007. *FastSLAM: A Scalable Method for the Simultaneous Localization and Mapping Problem in Robotics*. Vol. 27 of Springer tracts in advanced robotics. Springer, Berlin, Heidelberg, New York.
- Moreira, A., Mautz, R. (Eds.), 2011. *Proceedings of the 2011 International Conference on Indoor Positioning and Indoor Navigation*. IEEE Xplore Digital Library.
- Moritz, H., 1962. *Interpolation and prediction of gravity and their accuracy*.
- Moritz, H., 1980. *Advanced physical geodesy*. Wichmann and Abacus Press, Karlsruhe, Tunbridge, Eng.
- Nelson, A. T., 2000. *Nonlinear estimation and modeling of noisy time-series by dual Kalman filtering methods*. Phd thesis, Oregon Graduate Institute of Science and Technology, Portland, Oregon.
- Neumann, I., Dennig, D., 2011. Development of the kinematic crane-track-surveying-system „railcontrol“: Reducing operational interruption of crane tracks. *Allgemeine Vermessungs-Nachrichten* 118 (5), 162–169.
- Niemeier, W., 2008. *Ausgleichsrechnung: Statistische Auswertemethoden*, 2nd Edition. de Gruyter, Berlin.

- Nüchter, A., 2009. 3D robotic mapping: The simultaneous localization and mapping problem with six degrees of freedom. Vol. 52 of Springer tracts in advanced robotics. Springer, Berlin, Heidelberg.
- Nüchter, A., Elseberg, J., Schneider, P., Paulus, D., 2010. Study of parameterizations for the rigid body transformations of the scan registration problem. *Computer Vision and Image Understanding* 114 (8), 963–980.
- Okatani, I. S., Deguchib, K., 2002. A method for fine registration of multiple view range images considering the measurement error properties. *Computer Vision and Image Understanding* 87 (1-3), 66–77.
- Paffenzholz, J.-A., Alkhatib, H., Brieden, P., Kutterer, H., 2009. Optimized direct geo-referencing strategy for a TLS-based multi-sensor-system. In: Grün, A., Kahmen, H. (Eds.), *Optical 3-D Measurement Techniques IX*. Vol. I. pp. 287–292.
- Paffenzholz, J.-A., Alkhatib, H., Kutterer, H., 2010a. Direct geo-referencing of a static terrestrial laser scanner. *Journal of Applied Geodesy* 4 (3), 115–126.
- Paffenzholz, J.-A., Bae, K.-H., 2012. Geo-referencing point clouds with transformational and positional uncertainties. *Journal of Applied Geodesy* 6 (1), 33–46.
- Paffenzholz, J.-A., Horst, S., Alkhatib, H., Kutterer, H., 2010b. On the tracking of a laser scanner for geo-referencing tasks by means of geodetic sensors. In: Schulze Lammers, P., Kuhlmann, H. (Eds.), *2nd International Conference on Machine Control & Guidance - Proceedings*. pp. 85–94.
- Paffenzholz, J.-A., Kersten, T., Schön, S., Kutterer, H., 2011. Analysis of the impact of rotating GNSS antennae in kinematic terrestrial applications. In: *Proceedings of the FIG Working Week 2011*. p. 16.
- Paffenzholz, J.-A., Kutterer, H., 2008. Direct georeferencing of static terrestrial laser scans. In: *Proceedings of the FIG Working Week 2008*. p. 15.
- Pelzer, H., 1985. Statische, kinematische und dynamische Punktfelder. In: Pelzer, H. (Ed.), *Geodätische Netze in Landes- und Ingenieurvermessung II: Kontaktstudium 1985*. Konrad Wittwer, Stuttgart, pp. 225–262.
- Pennec, X., Thirion, J.-P., 1997. A framework for uncertainty and validation of 3-D registration methods based on points and frames. *International Journal of Computer Vision* 25 (3), 203–229.
- Petrie, G., Toth, C. K., 2009a. Introduction to laser ranging, profiling, and scanning. In: Shan, J., Toth, C. K. (Eds.), *Topographic laser ranging and scanning*. CRC Press and Taylor & Francis [distributor], Boca Raton, Fla, London, pp. 1–27.
- Petrie, G., Toth, C. K., 2009b. Terrestrial laser scanners. In: Shan, J., Toth, C. K. (Eds.), *Topographic laser ranging and scanning*. CRC Press and Taylor & Francis [distributor], Boca Raton, Fla, London, pp. 87–126.
- Puente, I., González-Jorge, H., Arias, P., Armesto, J., 2011. Land-based mobile laser scanning systems: A review. In: Lichti, D. D., Habib, A. F. (Eds.), *ISPRS Workshop Laser Scanning 2011*. Vol. XXXVIII-5/W12 of ISPRS Archives. pp. 163–168.
- Rabbani, T., Dijkman, S., van den Heuvel, F., Vosselman, G., 2007. An integrated approach for modelling and global registration of point clouds. *ISPRS Journal of Photogrammetry and Remote Sensing* 61 (6), 355–370.
- Ramm, K., 2008. Evaluation von Filter-Ansätzen für die Positionsschätzung von Fahrzeugen mit den Werkzeugen der Sensitivitätsanalyse: PhD thesis. Vol. 619 of Reihe C. DGK, München.
- Rauch, H. E., Tung, F., Striebel, C. T., 1965. Maximum likelihood estimates of linear dynamic systems. *AIAA Journal* 3 (8), 1445–1450.
- Reshetyuk, Y., 2009. Self-calibration and direct georeferencing in terrestrial laser scanning. Phd thesis, Royal Institute of Technology (KTH), Stockholm.
- Reshetyuk, Y., 2010a. Direct georeferencing with GPS in terrestrial laser scanning. *Zeitschrift für Geodäsie, Geoinformation und Landmanagement* 135 (3), 151–159.
- Reshetyuk, Y., 2010b. A unified approach to self-calibration of terrestrial laser scanners. *ISPRS Journal of Photogrammetry and Remote Sensing* 65 (5), 445–456.
- Rietdorf, A., 2005. Automatisierte Auswertung und Kalibrierung von scannenden Messsystemen mit tachymetrischem Messprinzip: PhD thesis. Vol. 582 of Reihe C. DGK, München.
- Ristic, B., Arulampalam, S., Gordon, N., 2004. Beyond the Kalman filter: Particle filters for tracking applications. Artech House, Boston, Mass.
- Rüeger, J. M., 1996. Electronic distance measurement: An introduction, 4th Edition. Springer, Berlin, Heidelberg.
- Rusinkiewicz, S., Levoy, M., 2001. Efficient variants of the ICP algorithm. *IEEE Computer Society Press: Third International Conference on 3-D Digital Imaging and Modeling*, 145–152.
- Sansò, F., Schuh, W.-D., 1987. Finite covariance functions. *Bulletin Géodésique* 61, 331–347.
- Scaioni, M., 2005. Direct georeferencing of TLS in surveying of complex sites. In: El-Hakim, S., Remondino, F., Gonzo, L. (Eds.), *3D-ARCH 2005*. Vol. XXXVI-5/W17 of ISPRS Archives. p. 8.
- Schaer, P., Skaloud, J., Landtwing, S., Legat, K., 2007. Accuracy estimation for laser point cloud including scanning geometry. In: Vettore, A., El-Sheimy, N. (Eds.), *MMT'07*. Vol. XXVI-5/C55 of ISPRS Archives. p. 8.
- Schenk, S., Hanke, K., 2011. Automatic registration of laser scanner point clouds with genetic algorithms. *Österreichische Zeitschrift für Vermessung und Geoinformation* 99 (2), 162–170.
- Schlemmer, H., 1996. Grundlagen der Sensorik: Eine Instrumentenkunde für Vermessungsingenieure. Wichmann, Heidelberg.
- Schön, S., Dillkner, F., 2007. Challenges for GNSS-based high precision positioning - some geodetic aspects. In: Kaiser, T., Jobmann, K., Kyamakya, K. (Eds.), *Proceedings of the 4th Workshop on Positioning, Navigation and Communication*. IEEE Xplore Digital Library, pp. 229–237.
- Schön, S., Kutterer, H., 2006. Uncertainty in GPS networks due to remaining systematic errors: The interval approach. *Journal of Geodesy* 80 (3), 150–162.
- Schuhmacher, S., Böhm, J., 2005. Georeferencing of terrestrial laserscanner data for applications in architectural modeling. In: El-Hakim, S., Remondino, F., Gonzo, L. (Eds.), *3D-ARCH 2005*. Vol. XXXVI-5/W17 of ISPRS Archives. p. 7.
- Schulz, T., 2007. Calibration of a terrestrial laser scanner for engineering geodesy. Phd thesis, ETH Zurich, Zurich.

- Schwieger, V., 2005. Nicht-lineare Sensitivitätsanalyse gezeigt an Beispielen zu bewegten Objekten: Habilitationsschrift. Vol. 581 of Reihe C. DGK, München.
- Seeber, G., 2003. Satellite geodesy: foundations, methods, and applications, 2nd Edition. de Gruyter, Berlin.
- Shahzad, S., Wiggenhagen, M., 2010. Co-registration of terrestrial laser scans and close range digital images using scale invariant features. *Allgemeine Vermessungs-Nachrichten* 117 (6), 208–212.
- Simon, D., 2006. Optimal state estimation: Kalman, H infinity, and nonlinear approaches // Kalman, H [infinity] and nonlinear approaches. John Wiley & Sons, Inc, Hoboken, NJ.
- Simon, D., 2010. Kalman filtering with state constraints: a survey of linear and nonlinear algorithms. *IET Control Theory & Applications* 4 (8), 1303–1318.
- Simon, D., Chia, T. L., 2002. Kalman filtering with state equality constraints. *IEEE Transactions on Aerospace and Electronic Systems* 38 (1), 128–136.
- Soloviev, A., Bates, D., van Grass, F., 2007. Tight coupling of laser scanner and inertial measurements for a fully autonomous relative navigation solution. *NAVIGATION: Journal of the Institute of Navigation* 54 (3), 189–205.
- Soudarissanane, S., Lindenbergh, R., 2011. Optimizing terrestrial laser scanning measurement set-up. In: Lichti, D. D., Habib, A. F. (Eds.), *ISPRS Workshop Laser Scanning 2011*. Vol. XXXVIII-5/W12 of ISPRS Archives. pp. 127–132.
- Soudarissanane, S., Lindenbergh, R., Menenti, M., Teunissen, P. J. G., 2009. Incidence angle influence on the quality of terrestrial laser scanning points. In: Bretar, F., Pierrot-Deseilligny, M., Vosselman, G. (Eds.), *Laserscanning '09*. Vol. XXXVIII-3/W8 of ISPRS Archives. pp. 183–188.
- Soudarissanane, S., Lindenbergh, R., Menenti, M., Teunissen, P. J. G., 2011. Scanning geometry: Influencing factor on the quality of terrestrial laser scanning points. *ISPRS Journal of Photogrammetry and Remote Sensing* 66 (4), 389–399.
- Staiger, R., 2003. Terrestrial laser scanning technology, systems and applications. In: *Proceedings of the 2nd FIG Regional Conference*. p. 10.
- Staiger, R., 2005. The geometrical quality of terrestrial laser scanner (TLS). In: *Proceedings of the FIG Working Week 2005 and GSDI-8*. p. 11.
- Stempfhuber, W., 2004. Ein integritätswahrendes Messsystem für kinematische Anwendungen: PhD thesis. Vol. 576 of Reihe C. DGK, München.
- Sternberg, H., Schwalm, C., 2007. Qualification process for MEMS gyroscopes for the use in navigation systems. In: Vettore, A., El-Sheimy, N. (Eds.), *MMT'07*. Vol. XXVI-5/C55 of ISPRS Archives. p. 8.
- Sur, F., 2010. Robust matching in an uncertain world. In: *20th International Conference on Pattern Recognition*. IEEE Computer Society, pp. 2350–2353.
- Teunissen, P. J. G., 2006. Least-squares collocation with integer parameters. *Artificial Satellites* 41 (2), 59–66.
- Teunissen, P. J. G., 2010. Integer least-squares theory for the GNSS compass. *Journal of Geodesy* 84 (7), 433–447.
- Teunissen, P. J. G., Giorgi, G., Buist, P. J., 2011. Testing of a new single-frequency GNSS carrier phase attitude determination method: Land, ship and aircraft experiments. *GPS Solutions* 15 (1), 15–28.
- Thrun, S., Burgard, W., Fox, D., 2005. Probabilistic robotics. MIT Press, Cambridge, Mass.
- Titterton, D. H., Weston, J. L., 2004. Strapdown inertial navigation technology, 2nd Edition. American Institute of Aeronautics and Astronautics and Institution of Electrical Engineers, Reston, VA, Stevenage.
- Toth, C. K., Shin, S. W., Grejner-Brzezinska, D. A., Kwon, J. H., 2008. On accurate time synchronization of multi-sensor mobile mapping systems. *Journal of Applied Geodesy* 2 (3), 159–166.
- Umeyama, S., 1991. Least-squares estimation of transformation parameters between tow point patterns. *IEEE Transactions on Pattern Analysis and Machine Intelligence* 13 (4), 376–380.
- Vennegeerts, H., 2011. Objektraumgestützte kinematische Georeferenzierung für Mobile-Mapping-Systeme: PhD thesis. Vol. 657 of Reihe C. DGK, München.
- Vennegeerts, H., Kutterer, H., 2009. Variants to compute variance information for mass data. In: Bretar, F., Pierrot-Deseilligny, M., Vosselman, G. (Eds.), *Laserscanning '09*. Vol. XXXVIII-3/W8 of ISPRS Archives. pp. 277–282.
- Vennegeerts, H., Martin, J., Kutterer, H., Becker, M., 2008. Validation of a kinematic laserscanning system. *Journal of Applied Geodesy* 2 (2), 79–84.
- Voegtle, T., Wakaluk, S., 2009. Effects on the measurements of the terrestrial laser scanner HDS 6000 (Leica) caused by different object materials. In: Bretar, F., Pierrot-Deseilligny, M., Vosselman, G. (Eds.), *Laserscanning '09*. Vol. XXXVIII-3/W8 of ISPRS Archives. pp. 68–74.
- Vosselman, G., Maas, H.-G. (Eds.), 2010. Airborne and terrestrial laser scanning. Whittles Publishing, Dunbeath.
- Wan, E. A., Nelson, A. T., 2001. Dual extended Kalman filter methods. In: Haykin, S. (Ed.), *Kalman Filtering and Neural Networks*. John Wiley & Sons, Inc, New York, NY, pp. 123–173.
- Wang, J.-G., 2008. Test statistics in Kalman filtering. *Journal of Global Positioning Systems* 7 (1), 81–90.
- Wang, J.-G., Gopaul, N., Scherzinger, B., 2009. Simplified algorithms of variance component estimation for static and kinematic GPS single point positioning. *Journal of Global Positioning Systems* 8 (1), 43–52.
- Wanninger, L., 2009a. Editing of GNSS observations with WaRINEX. URL [www.wasoft.de/wrn/index.html](http://www.wasoft.de/wrn/index.html)
- Wanninger, L., 2009b. GNSS baseline processing program Wa1. URL <http://www.wasoft.de/wa1/index.html>
- Weinmann, M., Jutzi, B., 2011. Fully automatic image-based registration of unorganized TLS data. In: Lichti, D. D., Habib, A. F. (Eds.), *ISPRS Workshop Laser Scanning 2011*. Vol. XXXVIII-5/W12 of ISPRS Archives. pp. 55–60.
- Weinmann, M., Weinmann, M., Hinz, S., Jutzi, B., 2011. Fast and automatic image-based registration of TLS data. *ISPRS Journal of Photogrammetry and Remote Sensing* 66 (6), S62–S70.
- Welsch, W., 1975. Über eine allgemeine reduzierende Gewichtsmatrix zur Elimination von Orientierungsunbekannten. *Zeitschrift für Geodäsie, Geoinformation und Landmanagement* 100 (2), 83–86.
- Welsch, W., Heunecke, O., Kuhlmann, H., 2000. Auswertung geodätischer Überwachungsmessungen. In: Möser, M., Müller, G., Schlemmer, H., Werner, H. (Eds.), *Handbuch Ingenieurgeodäsie*. Wichmann, Heidelberg, p. 507.



- Wieser, A., 2002. Robust and fuzzy techniques for parameter estimation and quality assessment in GPS: PhD thesis. Shaker, Aachen.
- Wilkinson, B. E., Mohamed, A. H., 2009. Ground based LiDAR georeferencing using dual GPS antenna attitude. In: Proceedings of the ION 2009 International Technical Meeting. pp. 375–383.
- Wilkinson, B. E., Mohamed, A. H., Dewitt, B. A., Seedahmed, G. H., 2010. A novel approach to terrestrial lidar georeferencing. *Photogrammetric Engineering & Remote Sensing* 76 (6), 683–690.
- Williams, J. A., 2001. A system for multiple view 3D acquisition and registration incorporating statistical error models. Phd thesis, Queensland University of Technology, Brisbane, Qld.
- Williams, J. A., Bennamoun, M., 2001. Simultaneous registration of multiple corresponding point sets. *Computer Vision and Image Understanding* 81 (1), 117–142.
- Woschitz, H., 2009. Test statischer Eigenschaften ausgewählter Neigungssensoren. *tm - Technisches Messen* 76 (10), 465–473.
- Wu, J. T., Wu, S. C., Hajj, G. A., Bertiger, W. I., Lichten, S. M., 1993. Effects of antenna orientation on GPS carrier phase. *Manuscripta geodaetica* 18 (2), 91–98.
- Wübbena, G., Bagge, A., Schmitz, M., 2001. RTK networks based on Geo++<sup>®</sup> GNSMART: concepts, implementation, results. In: ION GPS 2001: Proceedings of the 14th International Technical Meeting of the Satellite Division of the Institute of Navigation. p. 11.
- Wübbena, G., Schmitz, M., Menge, F., Böder, V., Seeber, G., 2000. Automated absolute field calibration of GPS antennas in real-time. In: ION GPS 2000: Proceedings of the 13th International Technical Meeting of the Satellite Division of the Institute of Navigation. p. 10.
- Yang, Y., Gao, W., Zhang, X., 2010. Robust Kalman filtering with constraints: A case study for integrated navigation. *Journal of Geodesy* 84 (6), 373–381.
- Zaddach, S., 2010. Laserscans und georeferenziertes 3D-Umgebungsmodell: Teilprojekt im Projekt BERTA: Beschreibung und Korrektur von GNSS-Mehrwegeeffekten mittels Ray-Tracing und Software-Empfängern (unveröffentlicht).
- Zeimetz, P., Kuhlmann, H., 2008. On the accuracy of absolute GNSS antenna calibration and the conception of a new anechoic chamber. In: Proceedings of the FIG Working Week 2008. p. 16.
- Zhang, Z., 1994. Iterative point matching for registration of free-form curves and surfaces. *International Journal of Computer Vision* 13 (2), 119–152.
- Zogg, H.-M., Lienhart, W., Nini, D., 2009. Advances in total station design for highest accuracy and performance. In: Grün, A., Kahmen, H. (Eds.), *Optical 3-D Measurement Techniques IX*. Vol. I. pp. 191–200.
- Zoller+Fröhlich GmbH, 2007. Technical data imager 5006: Version 1.0.5.
- Zoller+Fröhlich GmbH, 2009. Z+f imager<sup>®</sup> 5006(i,h): Manual - profiler mode: V 1.30.



## A. Supplementary material

### A.1. Representation of rotation

In this section is introduced the matrix representation using Euler angles which is used throughout this thesis. For other representations and rotations sequences such as quaternions or angle-axis representation the reader is referred to, e. g., Nüchter (2009). The Euler representation of rotation is based on the three rotation angles  $\omega$ ,  $\varphi$  and  $\kappa$  around the  $x$ -,  $y$ - and  $z$ -axis of a Cartesian coordinate system, respectively. The rotation matrices around the axes,  $\mathbf{R}(\cdot)$ , are defined as follows (Lichti and Skaloud, 2010, p. 84)

$$\mathbf{R}(\omega) = \begin{bmatrix} 1 & 0 & 0 \\ 0 & \cos(\omega) & \sin(\omega) \\ 0 & -\sin(\omega) & \cos(\omega) \end{bmatrix}, \quad (\text{A.1})$$

$$\mathbf{R}(\varphi) = \begin{bmatrix} \cos(\varphi) & 0 & -\sin(\varphi) \\ 0 & 1 & 0 \\ \sin(\varphi) & 0 & \cos(\varphi) \end{bmatrix} \text{ and} \quad (\text{A.2})$$

$$\mathbf{R}(\kappa) = \begin{bmatrix} \cos(\kappa) & \sin(\kappa) & 0 \\ -\sin(\kappa) & \cos(\kappa) & 0 \\ 0 & 0 & 1 \end{bmatrix}. \quad (\text{A.3})$$

The concatenation of  $\mathbf{R}(\cdot)$  results in the overall 3D rotation

$$\begin{aligned} \mathbf{R}(\omega, \varphi, \kappa) &= \mathbf{R}(\kappa) \cdot \mathbf{R}(\varphi) \cdot \mathbf{R}(\omega) \\ &= \begin{bmatrix} \cos(\varphi) \cdot \cos(\kappa) & \cos(\omega) \cdot \sin(\kappa) + \sin(\omega) \cdot \sin(\varphi) \cdot \cos(\kappa) \\ -\cos(\varphi) \cdot \sin(\kappa) & \cos(\omega) \cdot \cos(\kappa) - \sin(\omega) \cdot \sin(\varphi) \cdot \sin(\kappa) \\ \sin(\varphi) & -\sin(\omega) \cdot \cos(\varphi) \\ \sin(\omega) \cdot \sin(\kappa) - \cos(\omega) \cdot \sin(\varphi) \cdot \cos(\kappa) \\ \sin(\omega) \cdot \cos(\kappa) + \cos(\omega) \cdot \sin(\varphi) \cdot \sin(\kappa) \\ \cos(\omega) \cdot \cos(\varphi) \end{bmatrix}. \end{aligned} \quad (\text{A.4})$$

### A.2. General remark on estimation of transformation parameters

This section is a brief reminder on different approaches for the estimation of transformation parameters, in particular, within matching algorithms. The two approaches outlined in the following are the use of least-squares adjustment with conditions (also known as GHM) and approaches based on SVD. Other methods which are especially popular in the computer vision community are introduced by Eggert et al. (1997). In general, they are equivalent to the previous mentioned methods except for the rotation representations (Euler notation or Quaternions) and their mathematical derivation of the solution (SVD or different eigensystem analysis). For a detailed discussion the reader is referred to, e. g., Nüchter (2009, Chapter 4).

Commonly in geodesy, the transformation problem, i. e., the estimation of transformation parameters, is solved by means of GHM (e. g., Bleich and Illner, 1989, Grün and Akca, 2005, Gühring, 2002). In general, the functional model of GHM is non-linear in the transformation problem (Eq. 2.7). Therefore, a linearisation of the functional model is necessary and good start values for the unknown parameters are required. The stochastic model of the GHM allows for the individual stochastic information of corresponding tie points. A closed-form

solution for the estimation of the transformation parameters within a GHM by means of iterative calculations is presented by Bleich and Illner (1989). Through this closed-form solution is given the general coordinate transformation (affine transformation) considering nine parameters (rotation, translation and scale factors for each coordinate component). The application of parametric restrictions on the three scale factors leads to the well-known 3D Helmert transformation with seven parameters. Due to the use of approximate start values, the numerical setting in the linearised functional model is updated in each iteration step.

For SVD based approaches (e.g., Umeyama, 1991, Williams and Bennamoun, 2001), including the use of the generalised Procrustes analysis technique (e.g., Beinat and Crosilla, 2002, Grafarend and Awange, 2003), the SVD of a  $3 \times 3$  matrix for the estimation of the unknown transformation parameters is required. Neither linearisation of equation systems and inversion of the normal equations (like in the least-squares approaches) nor a priori values for the unknown parameters are required for this method (Beinat and Crosilla, 2002). The weighted Procrustes algorithm to solve the non-linear 3D datum transformation (seven parameter datum transformation) is discussed by Grafarend and Awange (2003). Stochastic information for the corresponding tie points in both coordinate systems can be considered within this approach. It is noteworthy that SVD based approaches are convenient to be implemented and, thus, heavily used in iterative matching algorithms (e.g., ICP algorithm). In registration tasks of 3D point clouds SVD based approaches are widely used due to usually high numbers of corresponding point pairs.

### A.3. Review of laser scanner calibration

This section provides a brief review of current state of research in the field of laser scanner calibration. Calibration approaches can be applied for either single components or the entire laser scanner as one system to determine parameters which describe the systematic errors. The component calibration (e.g., of the ranging unit or axis misalignments) is typically performed in a sequential order under laboratory conditions, whereas the system calibration can be carried out under experimental conditions or during project execution. The latter is referred to as on-the-job calibration. Therein, the parameters are not inevitably physically interpretable. Furthermore, any parameter variation over time has not to be separately investigated when on-the-job calibrations are applied (Dorninger et al., 2008). Research studies on laser scanner calibration have been reported for instance by Abmayr (2010), Abmayr et al. (2005, 2009), Bae and Lichti (2007), Chow et al. (2011), Gottwald (2008), Gottwald et al. (2009), Lichti (2007, 2009, 2010), Reshetyuk (2010b) and Schulz (2007).

Abmayr et al. (2005, 2009) as well as Abmayr (2010) report on the sensor model and basic calibration methods for the AM-CW laser scanner of type Imager by Z+F. The similarities of the laser scanner to total stations are used to determine the common axis errors. Furthermore, the authors address the combined calibration and registration of the previously mentioned laser scanner and a digital camera. Schulz (2007) reports on calibration and comprehensive investigations of a laser scanner from the same manufacturer regarding precision and accuracy of the distance and angle measurements as well as instrumental and non-instrumental errors.

Lichti (2007) proposes a laser scanner self-calibration method utilising signalised points. In the mathematical model, systematic errors in angle and range observations are modelled using these observations, which are expressed as a function of the unknown exterior orientation, object point coordinates and additional parameters. The error model covers those components which are physically interpretable and empirically identified. To avoid the necessary identification of signalised points and make use of the dense 3D data, Bae and Lichti (2007) used the above-mentioned mathematical model with manually selected planar surface patches instead of signalised control points. More recently, Chow et al. (2011) published a comparative study of point-based versus plane-based self-calibration. Further topics in this paper are model identification and parameter correlation. The laser scanners under test are one pulsed TOF and a AM-CW one. The authors' test results are that both calibration approaches comparably perform for the four most common errors of laser scanners. The question of angle parametrisation in the self-calibration of laser scanners is discussed by Lichti (2009). Furthermore,

Lichti (2010) intensively studies the sources of correlation in laser scanner self-calibration for a basic additional parameter set. The author recommends a measurement design to reduce parameter correlations. A unified approach to self-calibration of laser scanners is proposed by Reshetyuk (2010b). His approach aims to reduce correlations between the estimated parameters. To fulfil this aim a least-squares adjustment is used which treats the parameters as stochastic by assigning appropriate weights to them.

Gottwald (2008) and Gottwald et al. (2009) discuss the assessment and calibration of laser scanners. The authors state the necessity for standardised specifications for an objective laser scanner system comparison and point out the progress of the development of a policy for TLS. Two assessment procedures are presented. On the one hand, field check procedures, which aim to provide simple on-site system checks for the user. On the other hand, standardised laboratory assessments which intend to ease the comparability of assessment results, laser scanner specifications and relevant calibration aspects.

#### A.4. Partial derivatives of the single antenna motion model

Dropping the  $k$  subscript and the  $+$  superscript for ease of notation, the partial derivatives of the transition matrix in Eq. 5.7 are given as follows

$$\left. \frac{\partial X^{G,o}}{\partial \kappa^L} \right|_{\hat{\mathbf{x}}_k^+} = R1 \cdot \left( \hat{r} \cdot \sin(\hat{\varphi}) - \hat{r} \cdot \cos\left(\frac{\hat{s}_{ltd}}{\hat{r}}\right) \right) - R2 \cdot \left( \hat{r} \cdot \cos(\hat{\varphi}) + \hat{r} \cdot \sin\left(\frac{\hat{s}_{ltd}}{\hat{r}}\right) \right), \quad (\text{A.5})$$

$$\left. \frac{\partial Y^{G,o}}{\partial \kappa^L} \right|_{\hat{\mathbf{x}}_k^+} = R2 \cdot \left( \hat{r} \cdot \sin(\hat{\varphi}) - \hat{r} \cdot \cos\left(\frac{\hat{s}_{ltd}}{\hat{r}}\right) \right) + R1 \cdot \left( \hat{r} \cdot \cos(\hat{\varphi}) + \hat{r} \cdot \sin\left(\frac{\hat{s}_{ltd}}{\hat{r}}\right) \right), \quad (\text{A.6})$$

$$\begin{aligned} \left. \frac{\partial X^{G,o}}{\partial r} \right|_{\hat{\mathbf{x}}_k^+} &= R1 \cdot \left( \sin\left(\frac{\hat{s}_{ltd}}{\hat{r}}\right) + \cos(\hat{\varphi}) - \frac{\hat{s}_{ltd} \cdot \cos\left(\frac{\hat{s}_{ltd}}{\hat{r}}\right)}{\hat{r}} \right) \\ &\quad - R2 \cdot \left( \cos\left(\frac{\hat{s}_{ltd}}{\hat{r}}\right) - \sin(\hat{\varphi}) + \frac{\hat{s}_{ltd} \cdot \sin\left(\frac{\hat{s}_{ltd}}{\hat{r}}\right)}{\hat{r}} \right), \end{aligned} \quad (\text{A.7})$$

$$\begin{aligned} \left. \frac{\partial Y^{G,o}}{\partial r} \right|_{\hat{\mathbf{x}}_k^+} &= R2 \cdot \left( \sin\left(\frac{\hat{s}_{ltd}}{\hat{r}}\right) + \cos(\hat{\varphi}) - \frac{\hat{s}_{ltd} \cdot \cos\left(\frac{\hat{s}_{ltd}}{\hat{r}}\right)}{\hat{r}} \right) \\ &\quad + R1 \cdot \left( \cos\left(\frac{\hat{s}_{ltd}}{\hat{r}}\right) - \sin(\hat{\varphi}) + \frac{\hat{s}_{ltd} \cdot \sin\left(\frac{\hat{s}_{ltd}}{\hat{r}}\right)}{\hat{r}} \right), \end{aligned} \quad (\text{A.8})$$

$$\left. \frac{\partial X^{G,o}}{\partial \varphi} \right|_{\hat{\mathbf{x}}_k^+} = R2 \cdot \hat{r} \cdot \cos(\hat{\varphi}) - R1 \cdot \hat{r} \cdot \sin(\hat{\varphi}), \quad (\text{A.9})$$

$$\left. \frac{\partial Y^{G,o}}{\partial \varphi} \right|_{\hat{\mathbf{x}}_k^+} = -R1 \cdot \hat{r} \cdot \cos(\hat{\varphi}) - R2 \cdot \hat{r} \cdot \sin(\hat{\varphi}), \quad (\text{A.10})$$

$$\left. \frac{\partial X^{G,o}}{\partial s_{ltd}} \right|_{\hat{\mathbf{x}}_k^+} = R1 \cdot \cos\left(\frac{\hat{s}_{ltd}}{\hat{r}}\right) + R2 \cdot \sin\left(\frac{\hat{s}_{ltd}}{\hat{r}}\right), \quad (\text{A.11})$$

$$\left. \frac{\partial Y^{G,o}}{\partial s_{ltd}} \right|_{\hat{\mathbf{x}}_k^+} = R2 \cdot \cos\left(\frac{\hat{s}_{ltd}}{\hat{r}}\right) - R1 \cdot \sin\left(\frac{\hat{s}_{ltd}}{\hat{r}}\right) \text{ and} \quad (\text{A.12})$$

with

$$R1 = (\cos(\hat{\kappa}^L) \cdot \cos(\kappa^G) - \sin(\hat{\kappa}^L) \cdot \sin(\kappa^G)) \text{ and} \quad (\text{A.13})$$

$$R2 = (\cos(\hat{\kappa}^L) \cdot \sin(\kappa^G) + \cos(\kappa^G) \cdot \sin(\hat{\kappa}^L)). \quad (\text{A.14})$$



## B. Specifications of the used sensors in this thesis

### B.1. Terrestrial laser scanner Zoller + Fröhlich Imager 5006

Table B.1.: Technical data Z+F IMAGER 5006. Summary of important manufacturer specifications.  
Comprehensive information can be found in Zoller+Fröhlich GmbH (2007).

Ambiguity interval	79 m			
Data acquisition rate	up to 500000 points/s			
	vertical	horizontal		
Field of view	310 °	360 °		
Resolution deflection unit	0.0018 °	0.0018 °		
Accuracy deflection unit (rms)	0.007 °	0.007 °		
Resolution range	0.1 mm			
	Reflectivity	10 %	20 %	100 %
	10 m	1.2 mm	0.7 mm	0.4 mm
Range noise <sup>[a]</sup> at	25 m	3.0 mm	2.0 mm	1.0 mm
	50 m	7.5 mm	4.0 mm	2.5 mm
Built-in inclinometer range / resolution	±1.5 °		0.001 °	
Operation temperature range	0 °C to 40 °C			

<sup>[a]</sup>rms for data acquisition rate of 127000 points/s

### B.2. Inclinometer Schaevitz LSOC-1 °

Table B.2.: Technical data Schaevitz LSOC-1°. Summary of important manufacturer specifications.  
Comprehensive information can be found in Althen GmbH (2010).

Range	±1 °
Full range output (FRO) <sup>[b]</sup>	±5 VDC
Resolution	0.1 ″
Non-linearity <sup>[c]</sup>	0.05 % FRO (max)
Cross-axis sensitivity <sup>[d]</sup>	0.1 % FRO (max)
Zero offset <sup>[e]</sup>	±0.05 VDC (max)
Operation temperature range	-18 °C to +70 °C

<sup>[b]</sup>Full range output is defined as the full angular excursion from positive to negative, i. e.,  $\pm 90^\circ = 180^\circ$ .

<sup>[c]</sup>Non-linearity is determined by the method of least-squares.

<sup>[d]</sup>Cross-axis sensitivity is the output of unit when tilted to full range angle in cross-axis.

<sup>[e]</sup>Zero offset is specified under static conditions with no vibration inputs.

### B.3. GNSS equipment

Table B.3.: Specifications and parameters of GNSS equipments used in the experiments.

	Reference station (P8)	Antennas in p <sup>d</sup>		Antenna in p <sup>o</sup>
Receiver	..... Javad TRE G3TH Delta.....			
Serial	00081	00346		00082
Board	TRE G3T 3	TRE G3TH 4		TRE G3T 3
Version	3.1.1 Oct,05,2009	3.3.0 Mar,03,2011		3.1.6 Apr,27,2010
Receiver settings	..... No use of external clock/frequency.....			
	..... No code smoothing.....			
	..... No multipath reduction applied.....			
	..... Recording of external events with data rate of 12.5 Hz.....			
Antenna	LEIAR25.R3	LEIAX1202GG NONE	JAV GRANT-G3T	LEIAX1202GG
	LEIT		NONE	NONE
Serial	08430002	08400142	00434	08400137
Antenna calibration	..... Individual robot calibration by Institut für Erdmessung (IfE), Hannover, Germany.....			
Cable length	20 m	..... 3 m.....		5 m
Connector	..... TNC.....			

The PCV pattern of the Javad GrAnt G3T GNSS antenna (serial 00434) for the GPS frequency L1 and L2 is depicted in Fig. B.1. The 3D rectangular plots clearly show the dependency of the PCV pattern on elevation and azimuth. Four sharp maxima can be recognized (cf. arrows in Fig. B.1(a)), which are caused by the geometry of the antenna element itself and also by the geometrical dimension of the antenna housing. The L1 PCV corrections (Fig. B.1(a)) have a magnitude of 2–4 mm for mean elevation angles greater than 45° and rise to 6 mm for elevation angles below 45°. On L2 (Fig. B.1(b)) a similar behaviour can be identified. The maximum differences in elevation dependent PCV are 9 mm. The PCO up-component is 49.98 mm for L1 and 45.10 mm for L2, respectively, up to 5 times greater than the pattern.

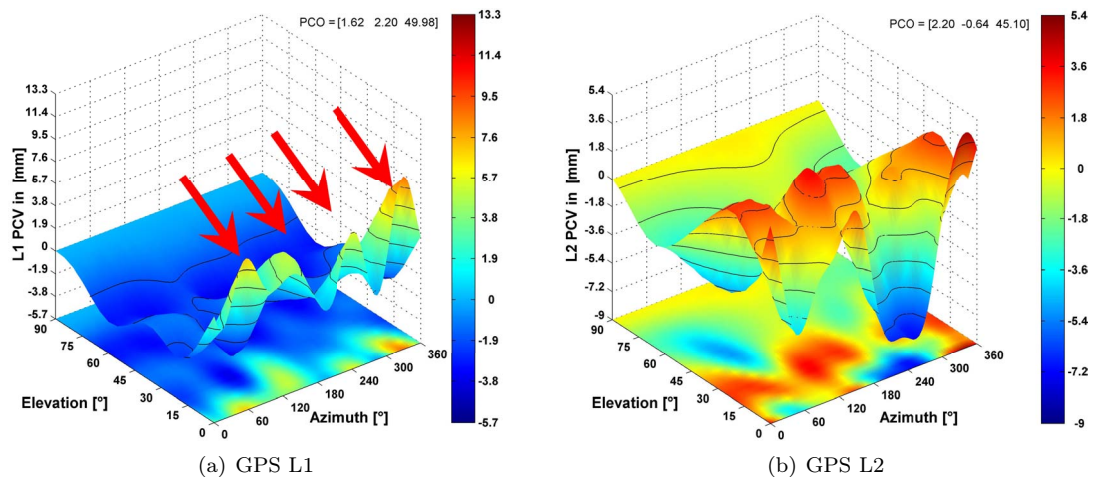


Figure B.1: Individual PCC of GPS frequencies for the Javad GrAnt G3T antenna (serial 00434).



## Curriculum vitae

### Personal information

---

Name	Jens-André Paffenholz
Date of birth	07. January 1981
Place of birth	Munich, Germany

### Working experience

---

07/2012 – present	Research staff, Institute of Cartography and Geoinformatics, Gottfried Wilhelm Leibniz Universität Hannover, Hanover, Germany
10/2006 – 06/2012	Research staff, Geodetic Institute, Engineering Geodesy and Geodetic Data Analysis Section Gottfried Wilhelm Leibniz Universität Hannover, Hanover, Germany
07/2011 – 09/2011	Research associate, Department of Spatial Sciences, Photogrammetry and Laser Scanning Research Group (Dr. K.-H. Bae) Curtin University, Perth, Western Australia, Australia

### Education and training

---

10/2006 – 09/2012	PhD student, Geodetic Institute, Engineering Geodesy and Geodetic Data Analysis Section Gottfried Wilhelm Leibniz Universität Hannover, Hanover, Germany
10/2002 – 09/2006	Graduate Engineer for Geodesy and Geoinformatics (German Diplom), Gottfried Wilhelm Leibniz Universität Hannover, Hanover, Germany
05/2002 – 07/2002	Internship, Surveying office Behrmann and Picht, Hanover, Germany
07/2001 – 03/2002	Basic military service, Munster, Germany
02/1994 – 06/2001	Grammar school Herzog-Ernst-Gymnasium (German Abitur (A-levels)), Uelzen, Germany

## Acknowledgement

An dieser Stelle möchte ich denjenigen danken, die mich während der Anfertigung dieser Arbeit begleitet und auf vielfältige Weise unterstützt haben.

Mein ganz besonderer Dank gilt Herrn Prof. Dr.-Ing. Hansjörg Kutterer. Er hat mir die Möglichkeit eröffnet mich intensiv mit der Thematik auseinanderzusetzen. Insbesondere danke ich Herrn Kutterer für die stets konstruktiven und intensiven Diskussion sowie die Möglichkeit zum Einstieg in die wissenschaftliche Arbeit am Geodätischen Institut unmittelbar nach dem Studium.

Herrn Prof. Dr.-Ing. Andreas Eichhorn und Herrn Prof. Dr.-Ing. Steffen Schön möchte ich für die Übernahme der Korreferate sowie die wertvollen Anregungen nach der Durchsicht der Arbeit danken. Frau Prof. Dr.-Ing. Monika Sester danke ich für die Übernahme des Prüfungsvorsitzes.

Ein weiterer großer Dank gebührt den Kolleginnen und Kollegen vom Geodätischen Institut, die mich während meiner knapp 6-jährigen Zeit am Institut begleitet haben. Ich habe stets die familiäre und freundliche Atmosphäre geschätzt, so dass mir der Abschied schwer gefallen ist. Ausdrücklich nennen möchte ich an dieser Stelle Herrn Dr.-Ing. Hamza Alkhatib, der mir in unzähligen Diskussion zum Thema Filterung, auch gerade in der heißen Phase, stets mit Rat und Tat zur Seite stand und immer wieder motivierende Worte fand. Weiterhin möchte ich Herrn Dr.-Ing. Harald Vennegeerts für die sehr fruchtbare und unkomplizierte Zusammenarbeit danken, insbesondere mit Blick auf die vielen praktischen Messungen mit "unserem" gemeinsamen Messgerät.

Einen ganz speziellen Dank möchte ich an dieser Stelle an Herrn Dr. Kwang-Ho Bae richten. Kwang-Ho und seine Kollegen haben mir einen unvergesslichen und interessanten, wissenschaftlichen Austausch am anderen Ende der Welt ermöglicht. Auch danke ich Kwang-Ho für seine unermüdliche Unterstützung bei der Fertigstellung der Arbeit nach meiner Rückkehr nach Hannover.

Für die Unterstützung in Sachen GNSS-Equipment und Referenzstationsdaten bei den zahlreichen praktischen Messungen bedanke ich mich bei Herrn Prof. Dr.-Ing. Steffen Schön vom Institut für Erdmessung. Namentlich möchte ich weiterhin Tobias Kersten und Nico Lindenthal nennen und mich für die sehr unkomplizierte Zusammenarbeit und das entgegengebrachte Engagement bedanken.

Ein Dank gilt auch den Studenten, die mich durch Ihre Abschlussarbeiten während meiner Zeit am Geodätischen Institut unterstützt haben. Phillip Brieden sei besonders für das erstellte virtuelle Modell des Laserscanners gedankt.

Meinen Eltern Elke und Josef danke ich für die Förderung und mentale Unterstützung in den letzten Jahren.

Mein abschließender Dank geht an meine Lebensgefährtin Katrin, die mir stets Rückhalt und Kraft gegeben hat. Nun freue ich mich riesig auf unseren neuen, gemeinsamen Lebensabschnitt :-)!

# Wissenschaftliche Arbeiten der Fachrichtung Geodäsie und Geoinformatik der Leibniz Universität Hannover

*(Eine vollständige Liste der Wiss. Arb. ist beim Geodätischen Institut, Nienburger Str. 1, 30167 Hannover erhältlich.)*

- Nr. 275 SCHMIDT, Ralph: Automatische Bestimmung von Verknüpfungspunkten für HRSC-Bilder der Mars Express-Mission (Diss. 2008)
- Nr. 276 HAUNERT, Jan-Henrik: Aggregation in Map Generalization by Combinatorial Optimization (Diss. 2008)
- Nr. 277 NEUMANN, Ingo: Zur Modellierung eines erweiterten Unsicherheitshaushaltes in Parameterschätzung und Hypothesentests (Diss. 2009)
- Nr. 278 WEITKAMP, Alexandra: Brachflächenrevitalisierung im Rahmen der Flächenkreislaufwirtschaft (Diss. 2009)
- Nr. 279 HEUWOLD, Janet: Automatische auflösungsabhängige Anpassung von Bildanalyse-Objektmodellen am Beispiel Straßen (Diss. 2009)
- Nr. 280 KOCH, Christian: Extraction of Mercury's tidal signal and libration amplitude from synthetic laser altimeter data sets (Diss. 2009)
- Nr. 281 GITLEIN, Olga: Absolutgravimetrische Bestimmung der Fennoskandischen Landhebung mit dem FG5-220 (Diss. 2009)
- Nr. 282 ELING, Dirk: Terrestrisches Laserscanning für die Bauwerksüberwachung (Diss. 2009)
- Nr. 283 DOLD, Christoph: Ebenenbasierte Verfahren für die automatische Registrierung terrestrischer Laserscans (Diss. 2010)
- Nr. 284 RIPPERDA, Nora: Rekonstruktion von Fassadenstrukturen mittels formaler Grammatiken und Reversible Jump Markov Chain Monte Carlo Sampling (Diss. 2010)
- Nr. 285 KATTERFELD Christiane: Interoperables Geodaten-basiertes E-Learning (Diss. 2010)
- Nr. 286 JARECKI, Focke: Spurkreuzungspunktdifferenzen zur Validierung satellitengradiometrischer Messungen (Diss. 2010)
- Nr. 287 SCHRAMM, Matthias: Unüberwachte lineare spektrale Entmischung mit Anwendungen für Baumdichteabschätzungen in semiariden Regionen Afrikas (Diss. 2010)
- Nr. 288 ALSAYEL, Mohammed Y.: Towards Standardizing International Boundary Determination and Quality Consequences on surveying and Mapping (Diss. 2010)
- Nr. 289 TAVAKKOLI S., Seyed Mohammad: Multi-Temporal Classification of Crops Using ENVISAT ASAR Data (Diss. 2011)
- Nr. 290 VENNEGEERTS, Harald: Objektraumgestützte kinematische Georeferenzierung für Mobile-Mapping-Systeme (Diss. 2011)
- Nr. 291 BULATOV, Dimitri: Textured 3D reconstruction of urban terrain from UAV-borne video sequences (Diss. 2011)
- Nr. 292 GROTE, Anne: Automatic road network extraction in suburban areas from aerial images (Diss. 2011)
- Nr. 293 ALOBEID, Abdalla: Assessment of Matching Algorithms for Urban DSM Generation from Very High Resolution Satellite Stereo Images (Diss. 2011)
- Nr. 294 FANG, Xing: Weighted Total Least Squares Solutions for Applications in Geodesy (Diss. 2011)
- Nr. 295 WEGNER, Jan Dirk: Detection and height estimation of buildings from SAR and optical images using conditional random fields (Diss. 2011)
- Nr. 296 GÖPFERT, Jens : Snakes for Adapting GIS Road and River Objects to Airborne Laser Scanning Data (Diss. 2011)
- Nr. 297 MUHLE, Daniel: Gegenseitige Orientierung von Mehrkamerasystemen mit nicht überlappendem Sichtfeld (Diss. 2011)
- Nr. 298 SIRIBA, David Nyangau: Conflation of Provisional Cadastral and Topographical Datasets (Diss. 2012)
- Nr. 299 HELMHOLZ, Petra: Verifikation von Ackerland- und Grünlandobjekten eines topographischen Datensatzes mit monotonen Bildern (Diss. 2012)
- Nr. 300 DENG, Zhiguo: GPS Meteorology with Single Frequency Receivers (Diss. 2012)
- Nr. 301 ZEIBLER, Maik: Zur Ermittlung von Bodenrichtwerten bei fehlenden Kaufpreisen unbebauter Grundstücke (Diss. 2012)
- Nr. 302 PAFFENHOLZ, Jens-André: Direct geo-referencing of 3D point clouds with 3D positioning sensors (Diss. 2012)

*Die Arbeiten werden im Rahmen des wissenschaftlichen Schriftenaustausches verteilt und sind nicht im Buchhandel erhältlich. Der Erwerb ist zu einem Stückpreis von € 25,- bei den herausgebenden Instituten möglich.*

